

CHARM AND STRANGENESS IN QUARK-GLUON PLASMA  
HADRONIZATION

by

Michal Petran

---

A Dissertation Submitted to the Faculty of the

DEPARTMENT OF PHYSICS

In Partial Fulfillment of the Requirements  
For the Degree of

DOCTOR OF PHILOSOPHY

In the Graduate College

THE UNIVERSITY OF ARIZONA

2013

THE UNIVERSITY OF ARIZONA  
GRADUATE COLLEGE

As members of the Dissertation Committee, we certify that we have read the dissertation prepared by Michal Petran entitled Charm and strangeness in quark-gluon plasma hadronization and recommend that it be accepted as fulfilling the dissertation requirement for the Degree of Doctor of Philosophy.

Date: 5 November 2013

---

Johann Rafelski

Date: 5 November 2013

---

Sean Fleming

Date: 5 November 2013

---

Ken Johns

Date: 5 November 2013

---

Michael Shupe

Date: 5 November 2013

---

Koen Visscher

Final approval and acceptance of this dissertation is contingent upon the candidate's submission of the final copies of the dissertation to the Graduate College. I hereby certify that I have read this dissertation prepared under my direction and recommend that it be accepted as fulfilling the dissertation requirement.

Date: 5 November 2013

---

Dissertation Director: Johann Rafelski

## STATEMENT BY AUTHOR

This dissertation has been submitted in partial fulfillment of requirements for an advanced degree at the University of Arizona and is deposited in the University Library to be made available to borrowers under rules of the Library.

Brief quotations from this dissertation are allowable without special permission, provided that accurate acknowledgment of source is made. Requests for permission for extended quotation from or reproduction of this manuscript in whole or in part may be granted by the head of the major department or the Dean of the Graduate College when in his or her judgment the proposed use of the material is in the interests of scholarship. In all other instances, however, permission must be obtained from the author.

SIGNED: Michal Petran

## DEDICATION

*... to my parents, Ludmila and Petr Petran.*

*And also to you — thanks for reading.*

## TABLE OF CONTENTS

LIST OF FIGURES . . . . .	7
ABSTRACT . . . . .	8
CHAPTER 1 QUARK-GLUON PLASMA IN THE LABORATORY . . . . .	10
1.1 Particle production in heavy-ion collisions . . . . .	10
1.1.1 Quark-gluon plasma – a new phase of matter . . . . .	10
1.1.2 Statistical hadronization model . . . . .	12
1.2 Strangeness and charm production and freeze-out . . . . .	15
1.2.1 Origin of strangeness and charm . . . . .	15
1.2.2 Statistical hadronization of charm . . . . .	17
1.2.3 Estimated charm abundance at RHIC and LHC . . . . .	17
CHAPTER 2 PHYSICS OF STRANGENESS AND CHARM HADRONIZATION . . . . .	20
2.1 Hadron ratios as flavor probes . . . . .	20
2.2 Strangeness overabundance and hadronization conditions at RHIC . .	22
2.3 Hadronization at LHC . . . . .	24
2.3.1 Does SHM describe particle production at LHC? . . . . .	24
2.3.2 Centrality independence and chemical equilibrium of light quarks . . . . .	28
2.3.3 Fit stability, omitted resonances and strange quark mass at hadronization . . . . .	32
2.4 Charm production and hadronization . . . . .	34
CHAPTER 3 SUMMARY AND FUTURE PLANS . . . . .	41
3.1 List of attached publications . . . . .	45
APPENDIX A MULTISTRANGE PARTICLE PRODUCTION AND THE STATISTICAL HADRONIZATION MODEL . . . . .	46
APPENDIX B STRANGENESS PRODUCTION IN AU–AU COLLISIONS AT $\sqrt{s_{NN}} = 62.4$ GeV . . . . .	52
APPENDIX C UNIVERSAL HADRONIZATION CONDITION IN HEAVY ION COLLISIONS AT $\sqrt{s_{NN}} = 62$ GeV AND AT $\sqrt{s_{NN}} = 2.76$ TeV . . .	59

TABLE OF CONTENTS – *Continued*

APPENDIX D HADRON PRODUCTION AND QUARK–GLUON PLASMA HADRONIZATION IN PB–PB COLLISIONS AT $\sqrt{s_{NN}} = 2.76$ TeV . . . . .	65
APPENDIX E INTERPRETATION OF STRANGE HADRON PRODUC- TION AT LHC . . . . .	87
APPENDIX F SHARE WITH CHARM . . . . .	95
APPENDIX G CHARM DECAY AS A SOURCE OF MULTISTRANGE PARTICLES . . . . .	136
REFERENCES . . . . .	142

## LIST OF FIGURES

Figure 1.1	Heavy-ion collision evolution . . . . .	11
Figure 1.2	The effect of phase space occupancy and fugacity factor . . . . .	14
Figure 1.3	Charm phase space occupancy as a function of total charm $N_{c\bar{c}}$	18
Figure 1.4	$D^0$ meson $p_{\perp}$ -spectrum from central Pb–Pb collisions at LHC	19
Figure 2.1	Hadron ratios from SPS to LHC . . . . .	21
Figure 2.2	SHM fit to data from Pb–Pb collisions at $\sqrt{s_{NN}} = 2.76$ TeV .	26
Figure 2.3	The entropy yield at LHC and RHIC as a function of centrality	27
Figure 2.4	Statistical significance profile of $\gamma_q$ . . . . .	28
Figure 2.5	Centrality dependent SHM parameters fitted to data from LHC compared to RHIC . . . . .	30
Figure 2.6	Physical properties of the hadronizing QGP fireball at RHIC62 and LHC . . . . .	31
Figure 2.7	Screenshot of SHARE with CHARM webpage . . . . .	36
Figure 2.8	$\chi^2$ profile of fits to LHC data for different charm amount $N_{c\bar{c}}$ .	38
Figure 2.9	$D^0$ yield as a function of $N_{c\bar{c}}$ and $T_{\text{charm}}/T$ . . . . .	40

## ABSTRACT

This dissertation presents a theoretical study of soft hadron production in relativistic heavy-ion collisions. The aim is to explore the principles governing the hadronization of the expanding quark-gluon plasma (QGP) fireball, and to understand its properties. Strange hadron production and strangeness abundance in the QGP help us to look before the instant of hadronization. Consideration of entropy and charm production further enhances the reach back in time to the first instances of the heavy ion collision.

Much of the ongoing effort is to demonstrate the validity of a QGP hadronization model which describes the particle production data accurately and thus allows us to carry out the above research program. We begin with performing a centrality dependent study of multistrange hadrons from Au–Au collisions at  $\sqrt{s_{NN}} = 62.4$  GeV, data obtained at the Relativistic Heavy Ion Collider (RHIC). We show that the statistical hadronization model (SHM) well describes particle production in QGP hadronization. For all centralities, the particle production conditions are compatible with the earlier proposed critical hadronization pressure suggesting a set of universal hadronization conditions of QGP.

Heavy-ion collisions at the Large Hadron Collider (LHC) present a new challenge for SHM in describing particle production at TeV energy scales. We show that the chemical non-equilibrium model gives a good description of the hadron production in Pb–Pb collisions at  $\sqrt{s_{NN}} = 2.76$  TeV not only in central collisions, where the equilibrium model struggled to describe the baryon to meson ratio, but consistently as a function of centrality. Moreover, the model parameters, such as chemical freeze-out temperature, assume expected values suggested by results from previous studies at lower energies. The quark-gluon plasma fireball hadronizes at the same universal hadronization conditions, that is a common critical pressure, entropy and energy

density.

At LHC energies, a significant amount of charm is expected to be produced in the initial hard parton scattering processes. It is therefore crucial to incorporate charm into the present description of particle production. We present a new tool, an upgraded SHARE with CHARM program, that quantifies the effect of charm on the yield of lighter hadrons and physical properties of the hadronizing fireball. In addition to light flavors ( $u, d, s$ ), SHARE with CHARM describes charm hadron production and decays of charm hadrons. We observe, that according to present experimental results, charm decays mainly affect the yields of multistrange particles.

This dissertation begins with an introduction to the particle production in heavy-ion collisions and SHM framework, followed by a summary of results that are either published or submitted to peer-reviewed journals and others which are published as conference proceedings. Reprints of the publications are attached to the dissertation as appendices. Each appendix is prefaced with a short summary of presented results, and my contribution to these works is described.

## CHAPTER 1

### QUARK-GLUON PLASMA IN THE LABORATORY

#### 1.1 Particle production in heavy-ion collisions

##### 1.1.1 Quark-gluon plasma – a new phase of matter

In matter around us, only colorless combinations of strongly interacting elementary particles, quarks and gluons, are present. In the Early Universe, however, all matter was sufficiently hot and dense so that quarks and gluons were free and formed a new phase of matter we refer to as ‘quark-gluon plasma’ (QGP). The QGP has been under active investigation in past decades [1]. Studying QGP in laboratory experiments aims to answer fundamental questions about the structure of matter. This requires exploration of collective phenomena of the strongly interacting medium and understanding of the transition between this new QGP phase of matter and the regular matter that emerges in a process called hadronization.

In heavy-ion collisions at relativistic energies, at first a dense partonic matter is created. Such strongly interacting matter at high enough energy density dissolves into a thermal gas of quarks and gluons, the state we refer to as quark-gluon plasma. When left to expand and cool down, the quarks bind into colorless combinations of three quarks ( $qqq$ ) called baryons and quark-antiquark ( $q\bar{q}$ ) states called mesons. The process the quark-gluon plasma undergoes while freezing-out the color degree of freedom is called ‘hadronization’. It has been of particular interest to many for several decades and is to this dissertation as well. The description of hadronization in strong coupling limit leads to phase space dominance model for particle production. This statistical hadronization model (SHM) has been successfully used to describe hadron production in high energy particle collisions, in particular heavy-ion

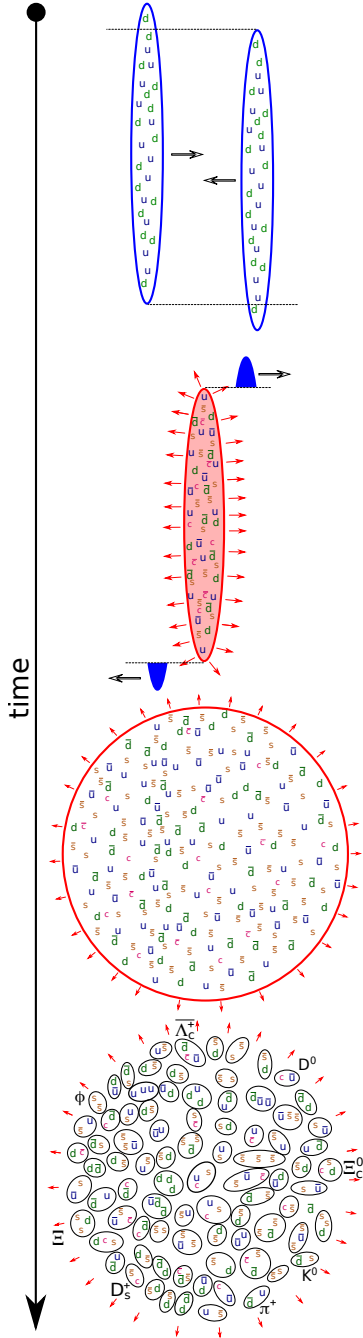


Figure 1.1: Schematic heavy-ion collision evolution.

collisions, in conditions where we expect the creation of quark-gluon plasma.

The main stages of such collisions are depicted in Figure 1.1. In the laboratory frame of a collider experiment, the Lorentz contracted ions collide. The initial hard parton scattering is the dominant mechanism of heavy ( $c, b, t$ ) quark production. A droplet of QGP forms, thermalizes and expands. During the expansion and cool-down, light quarks ( $u, d, s$ ) are produced abundantly, and heavy quarks are carried by the medium outwards from the collision center. When the conditions of the QGP fireball reach a critical point, the fireball hadronizes. After this point, quarks are present only in newly produced bound states, hadrons.

The confinement of quarks and gluons in hadrons is a phenomenon investigated in the context of the theory of strong interactions, quantum chromo-dynamics (QCD). It is not the topic of this dissertation; however, quarks and gluons interact in the QGP. Because the coupling constant of QCD,  $\alpha_s$ , changes as a function of energy scale in the interactions, only at high momentum transfer ( $\gg 1$  GeV) is it small enough to allow the use of perturbative theory methods. At low momentum

transfer where hadronization takes place, the perturbative expansion does not apply. In the limit of strong coupling, we have to rely on phenomenological models, such as SHM. SHM enables us to study and understand the properties of the QGP fireball, the hadronization conditions at which the color degree of freedom freezes-out, and the connection between the chemistry of the plasma and emerging hadrons arises.

### 1.1.2 Statistical hadronization model

The statistical hadronization model aims to describe hadron production in heavy-ion collisions given thermal parameters of the particle source, whether or not deconfinement has been achieved. Given a set of common thermal parameters, hadronization temperature  $T$ , system volume  $V$  and chemical potentials  $\mu$ , the phase space of all hadrons is populated. Below we present the essence of SHM, showing the necessary steps to calculate the hadron yields using statistical methods. More detailed description is presented in Section 2 of Appendix F and a thorough derivation can be found in [2].

We work in grand-canonical limit when describing the phase space of produced particles. Each hadron species  $i$  is thus described in SHM by the distribution

$$n_i \equiv n_i(E_i) = \frac{1}{\Upsilon_i^{-1} \exp(E_i/T) + S}, \quad S = \begin{cases} +1 & \text{Fermi-Dirac distribution} \\ 0 & \text{Boltzmann approximation} \\ -1 & \text{Bose-Einstein distribution.} \end{cases} \quad (1.1)$$

where the hadron energy  $E_i = \sqrt{m_i^2 + p_i^2}$ ,  $T$  is the temperature of the source,  $\Upsilon_i$  is the fugacity and  $S$  distinguishes the appropriate distribution for fermions, bosons and Boltzmann approximation.

The introduction of the temperature  $T$  of the source means that we assume produced particles to be in kinetic, often called ‘thermal’, equilibrium, but not necessarily in chemical equilibrium. The fugacity  $\Upsilon_i$  describes the chemical potential

of the  $i$ -th hadron based on its constituent quark content. The total fugacity of a hadron  $i$  is a product of constituent quark ( $u, d, s, c$ ) fugacities,

$$\Upsilon_i = \prod_{f=u,d,s,c} \Upsilon_f. \quad (1.2)$$

Fugacity of each quark flavor  $\Upsilon_f$  is usually further decomposed into a product of two factors, the phase space occupancy  $\gamma_f$ , and chemical potential factor  $\lambda_f$ .

$$\Upsilon_f = \gamma_f \lambda_f. \quad (1.3)$$

The fugacity factor  $\lambda$  relates to quark chemical potential  $\mu_f$  of each quark flavor  $f$  as

$$\lambda_f = e^{\mu_f/T} \quad (1.4)$$

It can be shown that for anti-particles (anti-quarks),  $\gamma_{\bar{f}} = \gamma_f$  and  $\lambda_{\bar{f}} = \lambda_f^{-1}$  [2].

The simplest and most commonly used SHM approach assumes that all hadron phase space populations reach an equilibrium abundance, which is equivalent to fixing all  $\gamma$ 's to unity. The introduction of phase space occupancies  $\gamma_f \neq 1$  originates from the recognition that it takes considerable time to re-equilibrate flavor abundance. In the scenario of very dynamical, sudden QGP hadronization [3], the number of available quarks of each flavor to be distributed among final state hadrons is given by the conditions in QGP at hadronization. Bearing in mind that equilibrium abundance in the quark phase does not have to be the same as chemical equilibrium abundance of valence quarks in the hadrons, we have to allow for the chemical non-equilibrium. Note that if the hadron abundances were indeed in absolute chemical equilibrium, this general approach allows the phase space occupancies  $\gamma_f$  to converge to unity. As we will show in Chapter 2, this is not the case.

The parameters  $\gamma_f$  controlling the number of  $q_f, q_{\bar{f}}$  quark pairs of flavor  $f$ , as we just explained, is responsible for what one calls, *absolute* chemical equilibrium. The parameter  $\lambda_f$  describes the *relative* chemical equilibrium, that is the difference of quarks and anti-quarks  $q_f - q_{\bar{f}}$  in the system. The effects of  $\lambda$  and  $\gamma$  are schematically

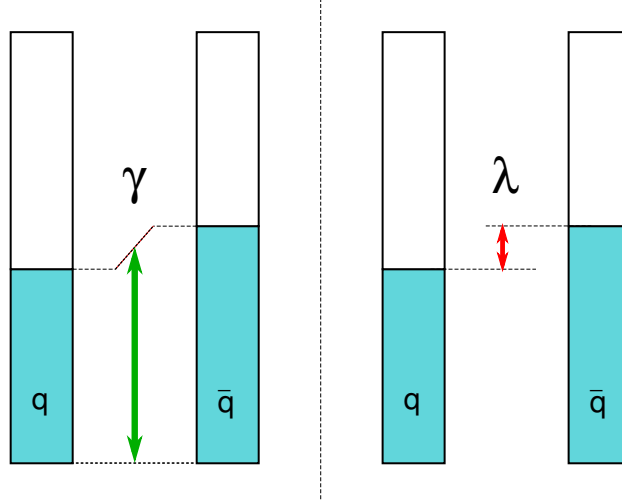


Figure 1.2: Illustration of  $\gamma$  and  $\lambda$  controlling quark abundance. The phase space occupancy  $\gamma$  controls the population of quarks  $q$  and antiquarks  $\bar{q}$  (left); the fugacity factor  $\lambda$  controls the  $q - \bar{q}$  difference (right).

depicted in Figure 1.2. The phase space occupancy  $\gamma$  describes the number of quark-antiquark pairs present in the system, whereas  $\lambda$  describes the difference between the quarks and antiquarks of the same flavor [4].

For a hadron  $i$  composed of  $N_u, N_d, N_s$  and  $N_c$  up, down, strange and charm quarks and  $N_{\bar{u}}, N_{\bar{d}}, N_{\bar{s}}$  and  $N_{\bar{c}}$  anti-quarks respectively, the fugacity can be expressed as:

$$\Upsilon_i = (\gamma_u^{N_u+N_{\bar{u}}} \lambda_u^{N_u-N_{\bar{u}}}) (\gamma_d^{N_d+N_{\bar{d}}} \lambda_d^{N_d-N_{\bar{d}}}) (\gamma_s^{N_s+N_{\bar{s}}} \lambda_s^{N_s-N_{\bar{s}}}) (\gamma_c^{N_c+N_{\bar{c}}} \lambda_c^{N_c-N_{\bar{c}}}) \quad (1.5)$$

Given the temperature  $T$  and fugacities of all flavors, the hadron yield in a given volume  $V$  can be calculated by integrating the distribution (Eq.1.1) over the phase space:

$$\langle N_i \rangle = g_i V \int \frac{d^3 p}{(2\pi)^3} n_i, \quad (1.6)$$

where  $g_i$  is the hadron spin degeneracy  $g = (2J + 1)$ . For a massive particle, Eq.1.6 can be numerically evaluated to any desired precision when expressed as a series of

modified Bessel functions of the second kind

$$\langle N_i \rangle = \frac{g_i V T^3}{2\pi^2} \sum_{n=1}^{\infty} \frac{(\pm 1)^{n-1} \Upsilon_i^n}{n^3} \left( \frac{nm_i}{T} \right)^2 K_2 \left( \frac{nm_i}{T} \right). \quad (1.7)$$

This is widely used in SHM implementations including the program we developed, SHARE, which I upgraded with a CHARM calculation module, and tuned it for LHC (see Appendix F), and which was used to produce the results presented.

As discussed so far, the observation of all particles of type  $i$  is required to determine the total volume  $V$  at hadronization. However, we work with RHIC and LHC results, which were obtained in mid-rapidity range. Thus we study  $d\langle N_i \rangle/dy$  and accordingly determine a volume parameter  $dV/dy$ . This is a 3-dimensional freeze-out hypersurface of the 4-dimensional domain generating particles within  $-0.5 < y < 0.5$  domain. This dissertation does not relate  $dV/dy$  to a geometric and/or dynamical interpretation.

Once we obtain a set of statistical parameters  $dV/dy, T, \gamma_i$ , and  $\lambda_i$  from a best fit to experimental data, we can evaluate within SHM all and any hadron yield and the physical properties of the QGP at hadronization, the latter by summing the contributions of all emerging hadrons carrying away the energy, entropy, and other properties.

## 1.2 Strangeness and charm production and freeze-out

### 1.2.1 Origin of strangeness and charm

The colliding nuclei contain only a very small fraction of the second family quarks, strange or charm. The dominant production mechanisms of these two flavors in relativistic heavy-ion collisions are qualitatively different. Both flavors are produced in pairs  $s + \bar{s}$  and  $c + \bar{c}$  in the early stage of a heavy-ion collision in hard parton scattering. Upon thermalization, the initial fireball temperature is of the order of 300 – 600 MeV [1], rapidly decreasing during the fireball expansion. There is

a qualitative difference in the subsequent behavior of strange and charm quarks, because during the evolution of the QGP fireball, its temperature falls between the strange and charm quark mass  $m_s < T^{QGP} < m_c$ , where  $T = 140 \text{ MeV} < T^{QGP} < T_{initial}^{QGP} \sim 600 \text{ MeV}$ .

1. The strange quark mass of  $m_s = 95 \pm 5 \text{ MeV}/c^2$  [5] is lower than the QGP temperature. This allows a significant additional amount of strangeness to be produced in thermal gluon fusion processes during the expansion of the fireball, which greatly enhances the total yield of strangeness available at hadronization [6]. QGP can achieve chemical equilibrium, which implies  $\gamma_s > 1$  in the hadron phase.
2. Due to the high mass of charm flavor compared to the QGP laboratory temperature,  $m_c = 1275 \pm 25 \text{ MeV}/c^2$  [5], virtually all charm is produced in the early hard parton scattering processes. Depending on the total amount of charm produced, or rather its density in the fireball, it can undergo re-annihilation during the fireball expansion, as long as  $\gamma_c > 1$ . In general, this is a slow process compared to strangeness. We cannot expect charm to be in absolute chemical equilibrium in QGP, and hence not in the hadron phase either. It is therefore necessary to introduce the charm phase space occupancy factor  $\gamma_c$  which we expect to be  $\gamma_c \gg 1$  at hadronization.

One of the objectives of this dissertation is to quantify the effect of charm hadrons production and decay on the final measured particle abundances and hence we focus on the amount of charm present at the end of the fireball expansion, at hadronization. We use as a measure of charm abundance the total charm, i.e., the number of charm and anticharm quarks  $N_{c\bar{c}} = (c + \bar{c})$  present at hadronization. Although the charm is described by the equations introduced in Section 1.1.2 the same way as the other flavors with  $\gamma_c$  and  $\lambda_c$  as parameters, it is more intuitive to evaluate  $\gamma_c$  given the value of  $N_{c\bar{c}}$ , which thus becomes a model parameter.

There are two reasons to allow a separate charm hadronization temperature  $T_{\text{charm}}$ :

1. Charm quarks may not completely follow the kinetic equilibrium within QGP in the first pre-hadronization stage.
2. Due to their relatively large binding, charm hadrons can preform earlier in the QGP and thus the final abundances is controlled by a higher chemical freeze-out temperature  $T_{\text{charm}}$ .

### 1.2.2 Statistical hadronization of charm

In the statistical model approach, the number of charm (and anticharm) quarks is distributed among the charm hadron states according to the relative abundance of other flavors present. Following the approach of [7], given  $N_{c\bar{c}}$  and all other model parameters, we solve for charm phase space occupancy  $\gamma_c$

$$\begin{aligned}
\langle N_{c\bar{c}} \rangle &= \gamma_c \left( \gamma_q \langle N_{qc}^{eq} \rangle + \gamma_s \langle N_{sc}^{eq} \rangle + \gamma_q^2 \langle N_{qqc}^{eq} \rangle + \gamma_s \gamma_q \langle N_{cqs}^{eq} \rangle + \gamma_s^2 \langle N_{ssc}^{eq} \rangle \right) \\
&+ \gamma_c^2 \left( \langle N_{cc}^{eq} \rangle + \gamma_q \langle N_{ccq}^{eq} \rangle + \gamma_s \langle N_{ccs}^{eq} \rangle \right) \\
&+ \gamma_c^3 \langle N_{ccc}^{eq} \rangle,
\end{aligned} \tag{1.8}$$

where  $\langle N_{12(3)}^{eq} \rangle$  is the statistical equilibrium yield of a meson with quark content ‘12’ or a baryon with quark content ‘123’.

As Figure 1.3 shows, the charm phase space occupancy  $\gamma_c$  increases very rapidly as  $\gamma_c \simeq 16N_{c\bar{c}}^{0.8}$ , reaching  $\gamma_c = 100 - 500$  for the  $D^0$  meson data inspired range of  $N_{c\bar{c}}$  and  $\gamma_c > 1000$  for the scaling charm pair production cross section estimate.

### 1.2.3 Estimated charm abundance at RHIC and LHC

At the time of this dissertation preparation, the total charm cross-section of  $d\sigma_{c\bar{c}}/dy|_{y=0} = 175 \pm 12 \pm 23 \mu\text{b}$  has been measured at RHIC and has been shown to scale with the number of binary collisions [9]. Multiplying the cross-section

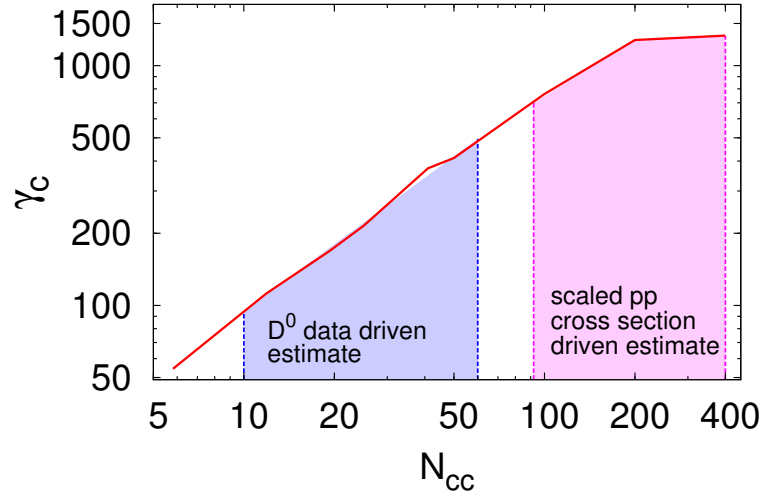


Figure 1.3: Charm phase space occupancy as a function of total charm  $N_{c\bar{c}}$  present at hadronization in 0–20% centrality Pb-Pb collisions at  $\sqrt{s_{NN}} = 2.76$  TeV. In this example,  $\gamma_c$  is computed using  $T_{\text{charm}} = T$ .

with the number of binary collisions in a central Au–Au collision at 200 GeV ( $N_{\text{bin}} = 1012 \pm 59$  [10]) and normalizing by the total inelastic cross-section in  $pp$  collisions, the estimated total charm abundance is

$$N_{c\bar{c}}^{\text{RHIC}} = N_{\text{bin}} \frac{d\sigma_{cc}^{NN}/dy}{d\sigma_{\text{total}}^{pp}/dy} \simeq 8.6. \quad (1.9)$$

Based on the statistical hadronization of charm with  $T_{\text{charm}} = T$ , the theoretical  $D^0$  meson yield we obtain is compatible with the experimental data  $dN_{D^0}/dy = 3.4 \pm 0.32$  (stat.)  $\pm 0.28$  (syst.) [11] for 0–10% centrality Au-Au 200 GeV collisions, .

No charm hadron yield has yet been measured in heavy-ion collisions at LHC. An estimate may be based on the incomplete  $p_{\perp}$ -spectrum of  $D^0$  meson [8], see Figure 1.4, where the low  $p_{\perp}$  bins are yet to be resolved and the spectrum extrapolated to  $p_{\perp} = 0$ . We extrapolate the spectrum without the missing points to estimate a range of  $D^0$  yield  $dN_{D^0}/dy \in (1.3, 9.0)$ . Considering the statistical hadronization of charm, this corresponds to  $N_{c\bar{c}}^{\text{LHC}} \in (6, 45)$ , see corresponding domain of  $\gamma_c$  in Figure 1.3. From the charm production cross section measurement in  $pp$  collisions, the estimated amount of charm produced in a central Pb–Pb collision at LHC is much

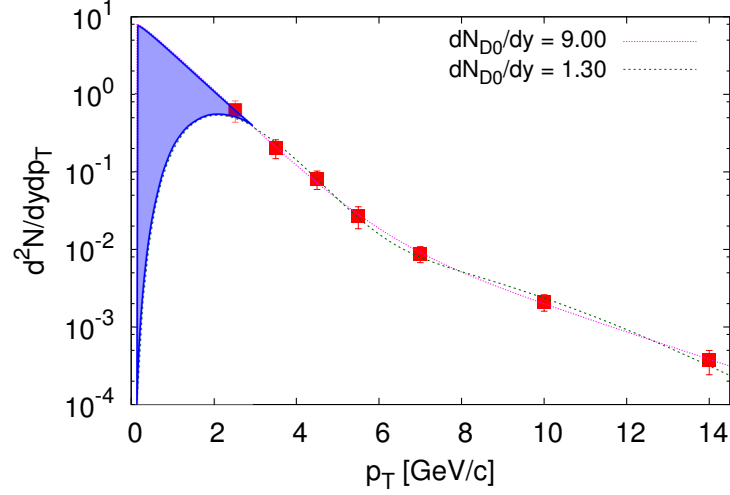


Figure 1.4: Shaded area shows a domain of extrapolation of the  $D^0$  meson  $p_{\perp}$ -spectrum from central Pb–Pb collisions at  $\sqrt{s_{NN}} = 2.76$  TeV, data points measured by the ALICE experiment [8].

higher,  $N_{c\bar{c}} = 246 \pm 154$ , where the large uncertainty originates in the uncertainty of the total charm cross section. The relevant domain of  $\gamma_c$  is shown in Figure 1.3. It is important to remember that the charm abundance estimate based on  $D^0$  yield is directly related to the charm yield at hadronization, whereas the theoretical based calculation reflects the amount of charm produced in the initial stages of the collision. The discrepancy between the two may be due to the annihilation of  $c\bar{c}$  pairs during the fireball expansion.

## CHAPTER 2

### PHYSICS OF STRANGENESS AND CHARM HADRONIZATION

This chapter summarizes results that are presented in detail in the appended publications, and which are referenced as appropriate throughout this chapter. The presentation follows the time line of my research work and its publication of the past years.

#### 2.1 Hadron ratios as flavor probes

The QGP flavor content is imprinted on the hadron distribution. Strangeness rich QGP leads to the production of more strange and even more multistrange particles. One can describe all measured hadron yields fitting them with a complex multi-parameter SHM model. However, as a first step, we choose a different simplified approach (see Appendix A), in which we explore hadron production at RHIC at  $\sqrt{s_{NN}} = 62.4$  GeV testing in the process the consistency of SHM. Consideration of specific ratios of hadrons rather than their individual yields removes the dependence on most model parameters. Consider the following ratio:

$$\begin{aligned} \frac{\Xi}{\phi} &\equiv \sqrt{\frac{\Xi^-(ssd) \Xi^+(\bar{s}\bar{s}\bar{d})}{\phi(s\bar{s}) \phi(s\bar{s})}} = \sqrt{\frac{\gamma_s^4 \gamma_q^2 \lambda_s^2 \lambda_s^{-2} \lambda_q \lambda_q^{-1}}{\gamma_s^4 \lambda_s^2 \lambda_s^{-2}}} \left( \frac{dV_{\Xi}}{dy} \right) \left( \frac{dV_{\phi}}{dy} \right)^{-1} f(T, m_{\Xi}, m_{\phi}) \\ &= \gamma_q f(T, m_{\Xi}, m_{\phi}). \end{aligned} \tag{2.1}$$

In this form, by taking a ratio of the same number of hadrons in the denominator and in the numerator, we remove the dependence on overall normalization; in Eq. 2.1, the overall normalization is volume per unit rapidity  $dV/dy$ . Because both hadron species originate from one QGP fireball source,  $dV_{\Xi}/dy = dV_{\phi}/dy$ . Multiplying a particle with its antiparticle causes the fugacity factors (or equivalently the

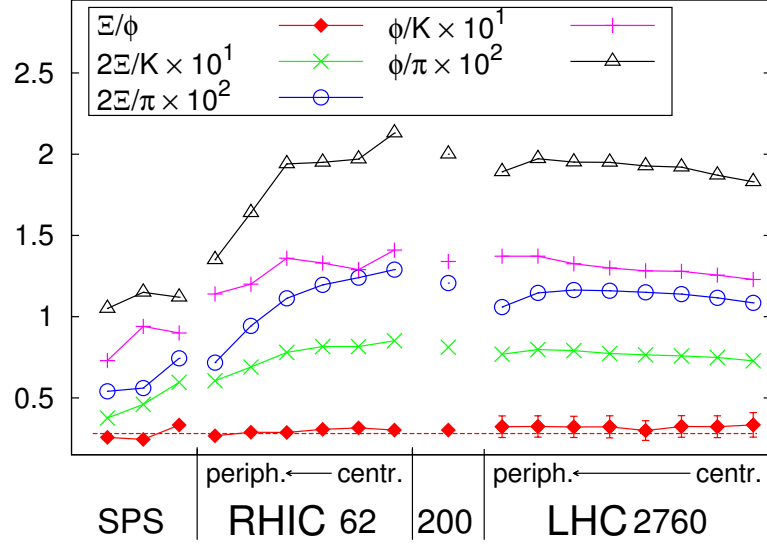


Figure 2.1: Hadron ratios at different heavy-ion experiments from SPS to LHC.

chemical potentials) to cancel. Finally, by choosing specific hadron species, we can eliminate dependence on different powers of phase space occupancies; in Eq. 2.1, the dependence on  $\gamma_s$  vanishes. The  $\Xi/\phi$  ratio is then directly proportional to  $\gamma_q$  and a function of the hadronization temperature  $T$  and the mass of  $\Xi$  and  $\phi$ . Note that the yield of  $\Xi$  is a sum of the  $\Xi$  and higher mass resonances with the same quark content with  $\Xi(1530)^-$  as the second most significant contribution. Looking at this ratio as a function of reaction energy and centrality enables us to study primarily the model parameter,  $\gamma_q$ , and to some degree  $T$ , independently of the other parameters,  $dV/dy$ ,  $\gamma_s$ ,  $\lambda_s$ ,  $\lambda_q$ , as is indicated in the second form of Eq. 2.1.

Data shown in Figure 2.1 from various heavy-ion experiments ranging from GeV to TeV energies demonstrate that  $\Xi/\phi$  as defined by Eq. 2.1 is constant over the whole range of energy, and at different centralities. This implies that  $\gamma_q$  and  $T$  describing all these data sets will be similar. The remarkable universality of the  $\Xi/\phi$  ratio also validates the SHM model. A different result is obtained from the study of ratios proportional to  $\gamma_s$  which change significantly even at one energy,

e.g., 62.4 GeV, but different centralities. This implies the need for strangeness phase space occupancy  $\gamma_s$  as a strongly variable model parameter. This result is obtained by considering the ratio of

$$\Xi/K \equiv \sqrt{\frac{\Xi^-(ssd) \Xi^+(\bar{s}\bar{s}\bar{d})}{K^+(u\bar{s}) K^-(s\bar{u})}} \propto \gamma_s, \quad (2.2)$$

which increases by 50% for RHIC 62.4 GeV as a function of centrality. Even more pronounced functional dependence (factor of 2) is observed in Figure 2.1 for ratios proportional to  $\gamma_s^2$ , such as

$$\Xi/\pi \equiv \sqrt{\frac{\Xi^-(ssd) \Xi^+(\bar{s}\bar{s}\bar{d})}{\pi^+(u\bar{d}) \pi^-(d\bar{u})}} \propto \frac{\gamma_s^2}{\gamma_q}, \quad (2.3)$$

where  $\gamma_q$  is fixed to a common value by the constant  $\Xi/\phi$  ratio. This implies that strangeness reaches different levels of equilibration depending on the available collision energy and the reaction volume size (and therefore lifespan) of the QGP fireball. With a clear need for  $\gamma_s$  for proper description of hadron production in heavy-ion collisions, we effectively ruled out the chemical equilibrium model with all  $\gamma$ 's fixed to unity. We established not only on a theoretical, but now also on an experimental basis, that strangeness is not chemically equilibrated in the observed hadron yields. This result confirms and extends the first analysis of relativistic heavy-ion collision experimental data based on the SHM principles [12].

## 2.2 Strangeness overabundance and hadronization conditions at RHIC

Considering all the available data from Au–Au collisions at  $\sqrt{s_{NN}} = 62.4$  GeV [13], we have enough constraints to perform a global fit to these data within the SHM framework. In Appendix B, we perform a detailed analysis using the yield of  $\pi^\pm$ ,  $K^\pm$ ,  $K_S^0$ ,  $p^\pm$ ,  $\phi$ ,  $\Lambda$ ,  $\bar{\Lambda}$ ,  $\Xi^\pm$  and  $\Omega^\pm$  as a function of centrality. We use the number of participating nucleons  $N_{\text{part}}$  as a measure of centrality characterizing the impact factor of the collision, see Ref. [14] for centrality measure overview. We overcome

the problem of the data reported in incompatible centrality bins by interpolating each hadron species with a power law in the form

$$\frac{dN_i(N_{\text{npart}})}{dy} = a_i N_{\text{npart}}^{b_i} + c_i, \quad (2.4)$$

where the parameters  $a_i, b_i, c_i$  are fitted to best describe the centrality dependence of particle  $i$ . This very precise empirical description enables us to perform an SHM fit to all the particle species for arbitrary centrality.

It is noteworthy that the publication of experimental multistrange particle data [13] included a semi-equilibrium fit to the data, constrained however by  $\gamma_s < 1, \gamma_q = 1$ . Our analysis with the semi-equilibrium model (fixed  $\gamma_q = 1$ ) of the same data set and unconstrained parameter  $\gamma_s$  values leads to compatible results only for peripheral collisions, where  $\gamma_s$  converges to values below unity. For central, head-on collisions, the measured strange hadron yields correspond to  $\gamma_s > 1$ , an overpopulated strangeness phase space. The hadronization temperature assuming semi-equilibrium approach converges to  $T^{\text{semi}} \simeq 160$  MeV.

When we release the light quark phase space occupancy  $\gamma_q$  and fit the data within the non-equilibrium model, we find that the light quark phase space is also overpopulated. This is described by the centrality independent value  $\gamma_q \simeq 1.6$ . The centrality independence is expected from the analysis of the  $\Xi/\phi$  ratio shown in the previous Section 2.1, assuming that the hadronization temperature  $T$  is constant. In full non-equilibrium model, strangeness is even further from the absolute equilibrium value reaching  $\gamma_s = 2.2$  for the most central collisions.

Another very important aspect of the SHM fit shown is the opportunity we have to examine the physical properties of the bulk at hadronization. We expect the same hadronization conditions of the bulk irrespective of the relativistic heavy-ion collision origin and experimental setup leading to the QGP fireball, e.g., determining the volume and the initial collision energy. The physical properties of the bulk, the energy density  $\varepsilon$ , the pressure  $P$ , and the entropy density  $\sigma$  are of particular

interest in the the study of QGP hadronization. All three vary significantly as a function of centrality in the semi-equilibrium model, whereas in the chemical non-equilibrium approach these bulk properties are virtually constant for all centralities. This result strongly supports the non-equilibrium SHM variant within the context of the universal QGP hadronization conditions hypothesis. We cannot exclude fitting the RHIC 62 GeV data with the semi-equilibrium model based on the fit quality, as the large data uncertainties are tolerant enough to accommodate  $\gamma_q = 1$ . However, the non-equilibrium is clearly preferred on physics grounds; it leads to compatible physical properties of different size fireballs at break-up.

A critical hadronization pressure  $P = 82 \text{ MeV}/\text{fm}^3$  has been proposed for heavy-ion collisions at SPS energies [15]. We find the same hadronization pressure for all centralities within the non-equilibrium SHM fit at a CM energy almost 4 times higher than the top SPS energy and for fireballs spanning more than an order of magnitude in reaction volume. This suggests that the intensive bulk properties we evaluated for this system: critical hadronization pressure  $P = 82 \text{ MeV}/\text{fm}^3$ , energy density  $\varepsilon = 0.50 \text{ GeV}/\text{fm}^3$ , and entropy density  $\sigma = 3.3 \text{ fm}^{-3}$ , are in fact nearly universal hadronization conditions for QGP created in heavy-ion collisions.

## 2.3 Hadronization at LHC

### 2.3.1 Does SHM describe particle production at LHC?

A naïve semi-equilibrium SHM fit has been presented together with the preliminary data from 0–20% central Pb–Pb collisions at  $\sqrt{s_{NN}} = 2.76 \text{ TeV}$  measured by the ALICE experiment [16]. The ALICE experiment has higher precision tracking than RHIC, which leads to smaller experimental data uncertainties. The simple fit presented in [16] yields inconsistencies when fitting different hadron species, creating the impression in the community that SHM does not work at LHC. This impression was caused by the constrained  $\gamma_s < 1, \gamma_q = 1$  semi-equilibrium model, which does

not agree (as it does at RHIC) with all particle production data from heavy-ion collision at LHC energy. The largest reported inconsistency is the ratio of protons to pions  $p/\pi$ . Recalling the method from Section 2.1, we see that according to the quark content, this ratio has to be proportional to  $p/\pi \propto \gamma_q$ . In Appendix C, we successfully fit the same data as in [16], applying the non-equilibrium SHM that allows  $\gamma_q$  to vary, permitting also  $\gamma_s > 1$ . The correct experimental value of  $p/\pi$  ratio is a natural outcome of the fit with a value of  $\gamma_q \simeq 1.6$ , as predicted in [17]. Similarly to RHIC results confirming the need for  $\gamma_s > 1$ , at this point the LHC results require both  $\gamma_q > 1$  and  $\gamma_s > 1$ . Moreover, as Figure 2.2 shows, the non-equilibrium model accurately describes all hadron production from central to peripheral collisions that is over 5 orders of magnitude in their yields, where the most variable parameters as a function of centrality are the normalization  $dV/dy$  and strangeness phase space occupancy  $\gamma_s$ .

We complement the preliminary data from the central Pb–Pb collisions with centrality dependent yields of  $\pi^\pm$ ,  $K^\pm$  and  $p^\pm$  from [18] and ratios  $\phi/K$ ,  $\Lambda/\pi$  and  $K^{0*}/K^-$  from [19]. We perform a centrality dependent analysis with a focus on the hadronization conditions at an energy 45 times higher than RHIC 62, the previous system we analyzed. In order to unify the centrality binning, we use four centrality bins in which  $K^{0*}/K^-$  is reported. We match the other data by taking the average of two neighboring points.

This centrality analysis reveals that the main difference from RHIC 62 is a 4 times larger volume of the hadronizing fireball, see Figure 2.5 below. Hadronization temperature  $T$  is found to be a few MeV lower for most central collisions; baryochemical potential is difficult to quantify, but is of the order of 1 MeV. The strangeness phase space, while showing a large overpopulation, is 20% lower than expected based on RHIC 200 results analysis and extrapolation [17]. Those results suggest a long lifespan of the fireball created at LHC, allowing strangeness to annihilate to a lower final abundance. The intensive properties at freeze-out are very similar to those

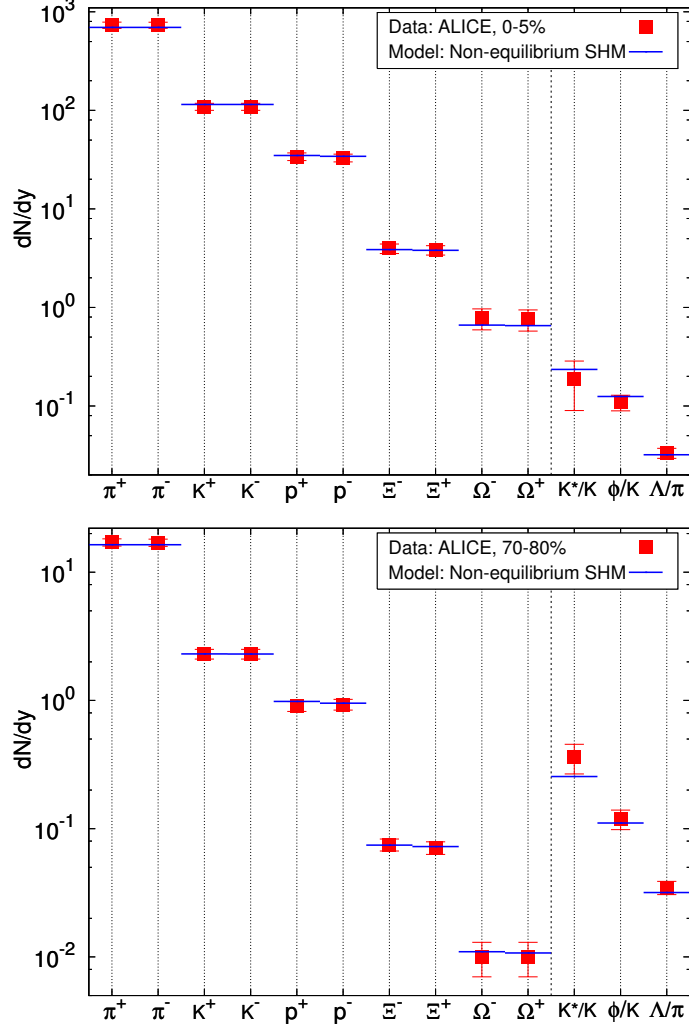


Figure 2.2: Non-equilibrium SHM fit to experimental data from 0–5% and 70–80% centrality Pb–Pb collisions at  $\sqrt{s_{NN}} = 2.76$  TeV measured by the ALICE experiment. Note that the model describes particle yields from  $dN/dy \sim 1000$  to  $dN/dy \sim 0.01$ .

at RHIC: pressure  $P = 82 \pm 8$  MeV/fm<sup>3</sup>, energy density  $\varepsilon = 0.50 \pm 0.05$  GeV and entropy density  $\sigma = 3.35 \pm 0.30$  fm<sup>-3</sup>. This result confirms the existence of universal hadronization conditions of the QGP fireball, which we introduced in the previous Section 2.2 and Appendix B.

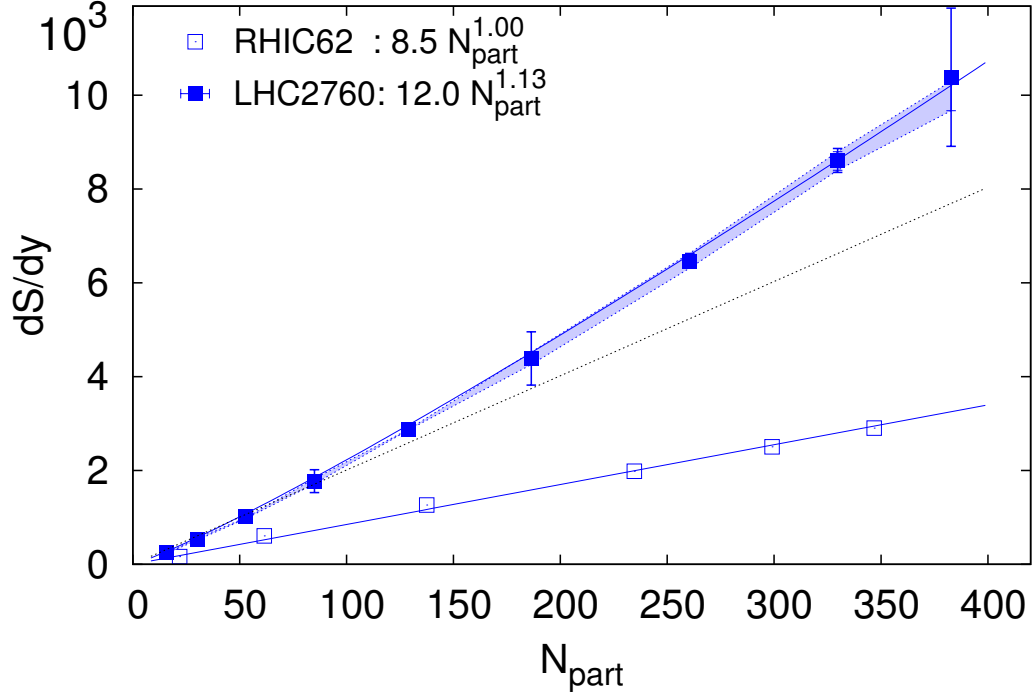


Figure 2.3: The entropy yield at LHC and RHIC as a function of centrality. The black dotted line shows a linear growth, which is to be compared with the top LHC line.

In Figure 2.3 we show an unexpected behavior of the entropy content of the fireball. The entropy yield of the QGP fireball at LHC increases more steeply with the number of participants than the linear behavior seen at RHIC 62, which implies an additional entropy production mechanism proportional to centrality of the collision. At the present time, we suspect charm re-annihilation in the QGP and charm decays after hadronization to be the extra omitted entropy production mechanism, a phenomenon we plan to explore as an application of SHARE with CHARM program we developed, see Appendix F.

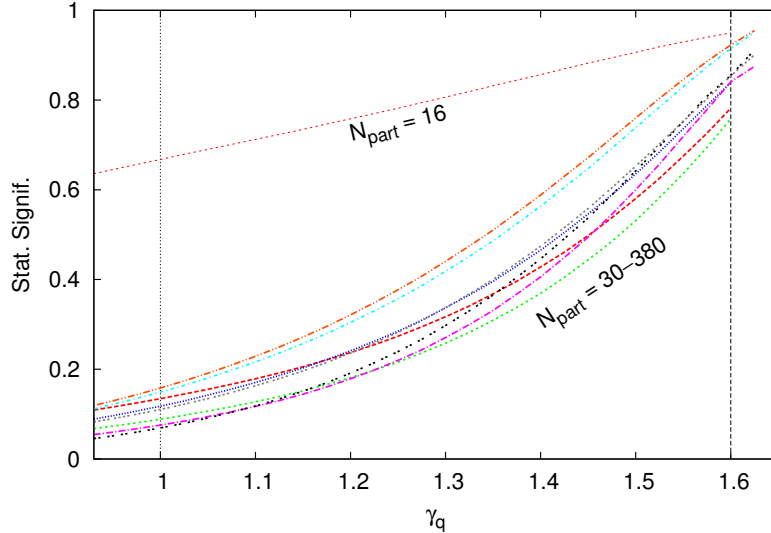


Figure 2.4: Statistical significance profile of the best fit to data from Pb–Pb collisions at  $\sqrt{s_{NN}} = 2.76$  TeV as a function of  $\gamma_q$  for all studied centrality bins.

### 2.3.2 Centrality independence and chemical equilibrium of light quarks

In Appendix D, we present a detailed comprehensive centrality dependent analysis of hadron production in Pb–Pb collisions from LHC. We complement the data set used in the first analysis presented in Appendix C with multistrange baryons  $\Xi$  and  $\Omega$  and unify centrality binning using the interpolation method developed for RHIC data analysis discussed earlier in Section 2.2. This enables us to perform a detailed non-equilibrium SHM analysis in 9 centrality bins and to discuss and reject the alternative models.

We thoroughly compare fits to the data with three SHM equilibrium variants; equilibrium ( $\gamma_s = \gamma_q = 1$ ), semi-equilibrium ( $\gamma_s \neq 1, \gamma_q = 1$ ), and non-equilibrium ( $\gamma_s \neq 1, \gamma_q \neq 1$ ). Recall that the equilibrium model has been proven inapplicable already at RHIC energies. The more precise LHC data clearly prefers non-equilibrium with  $\gamma_q \simeq 1.6$ , as we expect based on the constant  $\Xi/\phi$  ratio, which keeps the same value at RHIC and LHC, see Figure 2.1. We show the necessity of  $\gamma_q > 1$  by eval-

uating the statistical significance profile as a function of  $\gamma_q$  shown in Figure 2.4. This result clearly shows; first, that  $\gamma_q = 1$  has no special meaning for the model and has the lowest confidence level; and second, that the highest confidence level corresponds to the value of  $\gamma_q$  near its critical value of Bose-Einstein condensation of  $\pi^0$  defined by

$$\gamma_q^{crit} = \exp\left(\frac{m_{\pi^0}}{2T}\right). \quad (2.5)$$

The only qualitatively different behavior is the most peripheral bin we analyze, 70–80% ( $N_{\text{npart}} \simeq 16$ ), for which the  $\chi^2$  of the fit is more tolerant to  $\gamma_q < 1.6$ . One can infer that in peripheral collisions, for example, surface contribution could play an important role [20].

With prescribed  $\gamma_q = 1$ , the total  $\chi^2$  of the fit increases by a factor of 4 as compared to  $\gamma_q \sim 1.63$ , confirming the need for  $\gamma_q$  as a free model parameter. Although one can argue that adding a free parameter to a model automatically improves fit to the data, it is noteworthy that releasing only  $\gamma_s$  does not improve the fit decisively, as does releasing and fitting  $\gamma_q$  and  $\gamma_s$ . On the other hand, we have already presented arguments based on the study of particle ratios that  $\gamma_s \neq 1$ , see Section 2.1 and Appendix A. We thus conclude that  $\gamma_q \neq 1$  is required as well.

We further exclude models in which the hadron abundance evolve strongly after hadronization (for example the annihilation process  $p+\bar{p} \rightarrow$  pions) on the grounds of wrong centrality dependence. We find that equilibrium SHM complemented by such ‘afterburner’ does not describe the data adequately. The main challenge of this effort has been the measured ratio of  $p/\pi = 0.046$  compared to the factor of 1.5–1.9 larger value predicted by the equilibrium SHM [21], which could be reduced via the  $p\bar{p}$  annihilation. Although the posthadronization interactions can explain this isolated data point in central collisions, they have two huge challenges to overcome before becoming a viable model. First, the annihilation interactions are highly centrality dependent; the ratio increases to  $p/\pi = 0.058$  already in 20–30% ( $N_{\text{npart}} = 186$ ) centrality bin [22], which is in contradiction by 3 standard deviations with the

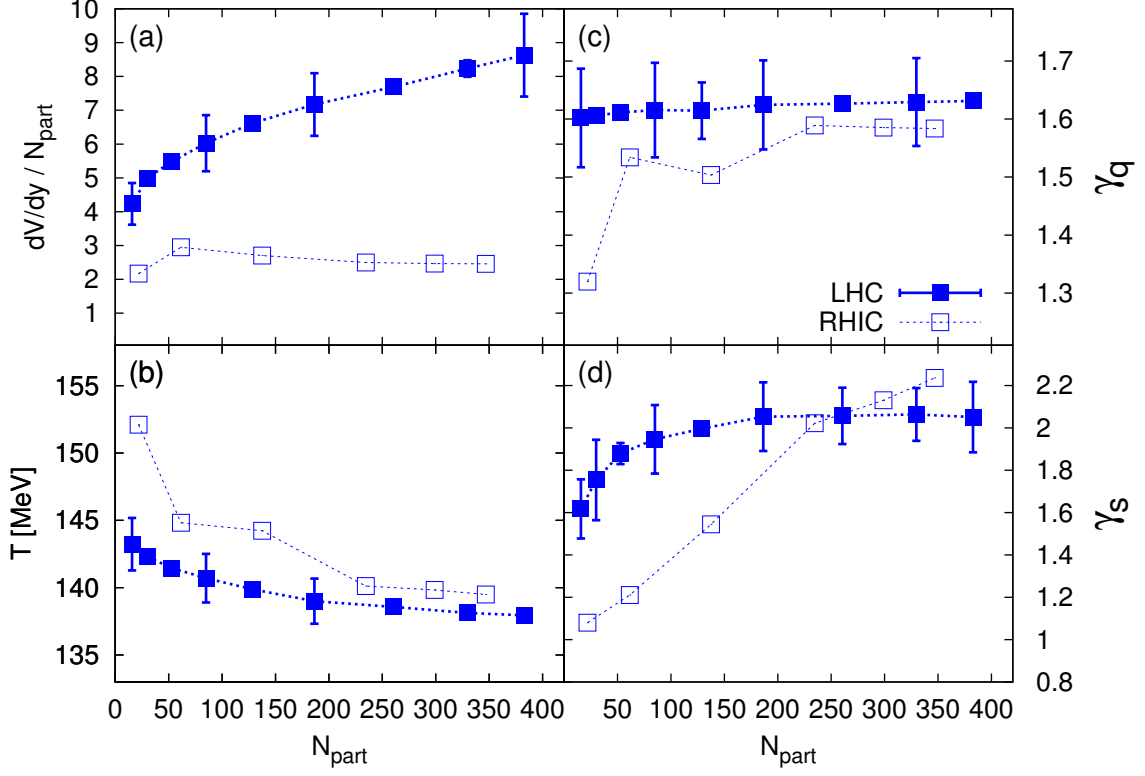


Figure 2.5: SHM parameters obtained by fitting the data from Pb–Pb collisions at  $\sqrt{s_{NN}} = 2.76$  TeV from LHC (Appendix D) compared to RHIC 62 (Appendix B). Volume normalized to number of participants in panel (a), freeze-out temperature  $T$  in panel (b), light quark phase space occupancy  $\gamma_q$  in panel (c) and strangeness phase space occupancy  $\gamma_s$  in panel (d).

experimentally measured centrality independent  $p/\pi$  ratio. Second, while solving the ‘proton anomaly’ with baryon-antibaryon annihilation, the posthadronization interactions cause a new anomaly in the equilibrium model value of  $\Xi$  yield, which is depleted by these interactions disagreeing further with the experimental data.

Having excluded other model approaches, we return to elaborate on the results of SHM non-equilibrium analysis. In Figure 2.5, we show a comparison of centrality dependent non-equilibrium SHM parameters for LHC and RHIC62. Panel (a) shows the volume per unit rapidity normalized to the number of participating nucleons

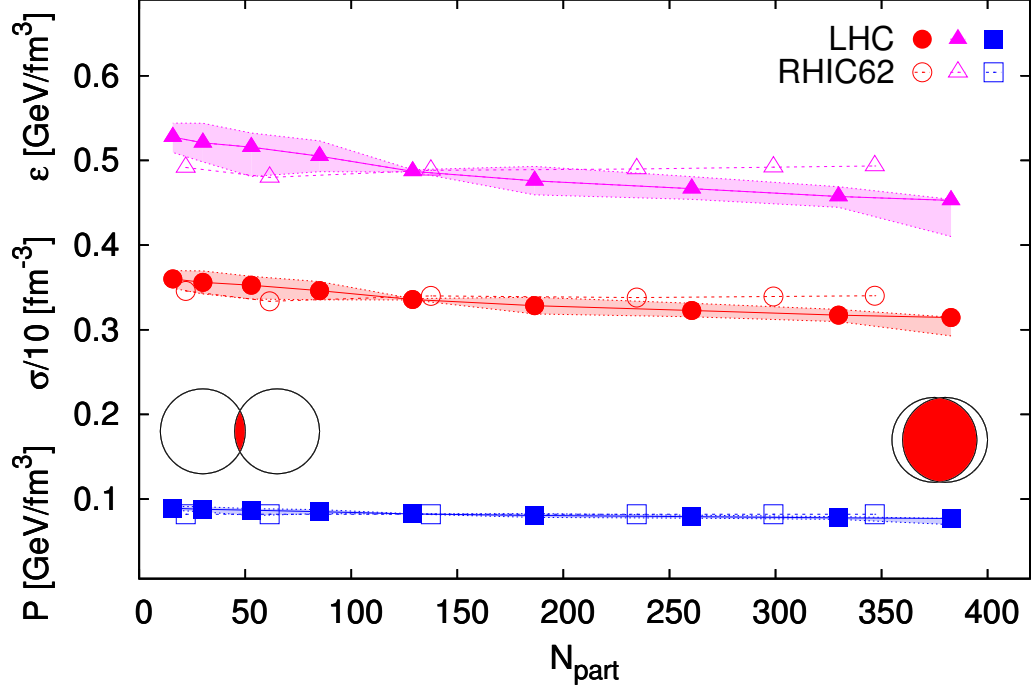


Figure 2.6: Physical bulk properties of the hadronizing QGP fireball from RHIC62 and LHC, critical pressure  $P$ , energy density  $\varepsilon$ , and entropy density  $\sigma$ , as a function of centrality.

$(dV/dy)/N_{\text{npart}}$ ; we note the rise with centrality. The freeze-out temperature  $T$  (panel (b) of Figure 2.5) is very close in the two environments, RHIC and LHC. We observe a temperature drop of a few MeV, which we associate with deeper supercooling of a more dynamically expanding fireball at the LHC energy. However, it is possible that systematic differences in detector properties (ALICE vs. STAR) are the origin of this difference, which is within the fit error. The light quark phase space occupancy  $\gamma_q$  (panel (c) of Figure 2.5) saturates earlier, i.e., for more peripheral systems at LHC. The strangeness reaches a steady level of equilibration for relatively small systems ( $N_{\text{npart}} \gtrsim 50$ ), as seen in the value of the strangeness phase space occupancy  $\gamma_s \rightarrow 2$ .

As data in Figure 2.1 show, hadron ratios proportional to  $\gamma_s$  are also almost

constant at LHC compared to lower energy experiments. This behavior is consistent with the resulting chemical parameters of the SHM fit; in particular the strangeness phase space saturates at  $\gamma_s \simeq 2$  already for rather peripheral collision,  $N_{\text{part}} \geq 50$ , see Figure 2.5(d). This shows that the high initial energy density fireball (increasing greatly the final volume  $V$ ) lives sufficiently long for strangeness to establish a stable chemical equilibrium in the QGP. This QGP equilibrium of strangeness implies chemical non-equilibrium of produced hadrons [2].

In Appendix D, we further evaluate the physical bulk properties of the QGP fireball at LHC and compare them to our previous results from RHIC. New additional data and finer centrality binning are compatible with results also shown in Appendix C further confirming the conclusion that quark-gluon plasma created in heavy-ion collisions at TeV energies hadronizes at nearly the same universal hadronization conditions as at RHIC (and therefore also SPS), see Figure 2.6.

### 2.3.3 Fit stability, omitted resonances and strange quark mass at hadronization

In Appendix E, we study new ALICE data and the physical stability of our fit, and therefore the physics reliability, of the chemical non-equilibrium SHM fits, that we presented above and in Appendices C and D. We first confirm that the newly published final data of  $K_S^0$ ,  $\Lambda$ ,  $\Xi$  and  $\Omega$  agree practically exactly with our presented interpolations and estimates. Furthermore, we perform a fit with finite hadron resonance widths, which in general can cause a shift in computed particle yields due to resonances being created more abundantly below their central mass. We find the calculation with and without finite widths to be virtually the same, except for an overall normalization change which is compatible within the fit errors of our earlier work.

Detailed inspection of the individual fitted data points reveals that the only systematic difference between the model and the experimental yield is for  $\Lambda$  (e.g.,  $\Lambda = 17 \pm 2$  in the 10–20% centrality bin) which is systematically underpredicted:

the model value is a little over 1 standard deviation below the experimental point for all centralities. This may mean that the deviation is due to a systematic centrality independent omission in our model. We explore the Particle Data Book [5] seeking a 2-star (\*\*) resonance that, upon inclusion in the SHARE particle list, could serve as a significant source of  $\Lambda$ . We identify  $\Sigma(1560)$  as a potential candidate. The charged states  $\Sigma(1560)^\pm$  have been observed with  $6\sigma$  signal; however, the neutral state  $\Sigma(1560)^0$  has not been confirmed by an independent experiment. This resonance has only one decay channel  $\Sigma(1560) \xrightarrow{100\%} \Lambda\pi$ ; it is light enough and likely has spin  $3/2$ , so it could be produced abundantly enough to provide the missing source of  $\Lambda$ . After including the  $\Sigma(1560)$  and its decay in the particle list, the subsequent SHM fit converges to the same SHM parameter values. The only change is a significantly lower  $\chi^2$ , because the  $\Lambda$  yield is now fitted within  $1/2$  standard deviation below the experimental point, and thus contributes significantly less towards the total  $\chi^2$ .

After establishing the fit compatibility with the new final data and fit stability against finite resonance width, and against an addition to the hadron mass spectrum, we turn to address strangeness conservation during a sudden hadronization process. We evaluate the observed strangeness in hadrons and match it to the strangeness in QGP. We offer two possible extreme scenarios:

1. Strangeness is chemically equilibrated in the QGP created in central collisions. This, however, requires the strange quark to acquire an effective mass of  $m_s = 299 \text{ MeV}/c^2$ .
2. Strange quark has its PDG mass  $m_s = 140 \text{ MeV}/c^2$  (at the relevant scale  $\mu \simeq 2\pi T = 0.9 \text{ GeV}$ ) and strangeness phase space in the QGP is undersaturated with  $\gamma_s^{QGP} = 0.77$ .

Further analysis may bring these two scenarios together by, e.g., incorporation of QCD many body interactions and/or longitudinal expansion strangeness dilution.

## 2.4 Charm production and hadronization

With a large yield of charm expected in heavy-ion collisions at LHC, hadronization of charm becomes a new necessary feature to be accounted for in the SHM. For this purpose, we developed and present a tool in Appendix F: SHARE with CHARM. It builds on the success of its predecessors, SHAREv1 [23] and SHAREv2 [24]. SHARE was developed at the Department of Physics of the University of Arizona in collaboration with Cracow and Montreal. The first release, SHAREv1 [23], introduced hadron yields and yield calculations for the light ( $u, d, s$ ) quarks. SHAREv2 [24] added calculation of event-by-event fluctuations and has been widely used within the community as a tool for many publication results. SHARE with CHARM (SHAREv3) described in Appendix F now enhances the powerful implementation of SHM with charm capabilities and provides an effective tool for SHM studies of particle production in the LHC era. The program is publicly available at <http://www.physics.arizona.edu/~gtshare/SHARE/share.html> for download together with operation instructions. For the SHARE with CHARM website screenshot, see Figure 2.7.

SHARE with CHARM is designed to address the following questions:

- What number of charm quarks is present at hadronization?
- Is charm hadron production in heavy-ion collisions described by SHM?
- Does charm freeze-out at the same temperature as other hadrons?
- Are the physical properties of the hadronizing fireball affected by a non-negligible amount of charm present at hadronization?

SHARE with CHARM will help to answer all of the above questions once charm hadron yield data from heavy-ion collisions at LHC become available. Currently, we have implemented in the program all 3-star (\*\*\*) and 4-star (\*\*\*\*) hadrons and resonances, we also included states that were not yet confirmed experimentally, but must exist for symmetry reasons of the quark model, such as  $\Omega_{ccc}^{++}$ , a bound

state of three charm quarks ( $ccc$ ). Creating a charm hadron decay table is an even more challenging task. Considering the high number (a few hundred in some cases) of decay channels with comparable branching ratios, we have to include all decay channels with a relative branching ratio over  $10^{-4}$ , sometimes  $10^{-5}$ , when no dominant channel is present. Oftentimes, due to their high mass, charm hadrons decay into four, five or more daughter particles. For many of the decay final multiparticle states, an isospin symmetric decay product state may not have been observed, because some of them are very challenging to measure experimentally. We add these into the charm decay tree, as they are the most likely candidates of unobserved decay channels allowing the sum of branching ratios to add to one.

As an example of this procedure, consider one of the dominant and measured decay channels of  $\Lambda_c^+$ :

$$\Lambda \rightarrow p\bar{K}^0\pi^0 \quad \text{BR} = (3.3 \pm 1.0)\%. \quad (2.6)$$

We add in the decay table a channel symmetric to this one with the same branching ratio

$$\Lambda \rightarrow n\bar{K}^0\pi^+ \quad \text{BR} = (3.3 \pm 1.0)\%, \quad (2.7)$$

even though this channel was not experimentally observed. The decay channels added by hand and the relatively large uncertainties of the branching ratios introduce an intrinsic uncertainty into our CHARM module, which is therefore subject to future refinement as more precise data inputs become available in the future PDG releases and as additional theoretical constraints are recognized.

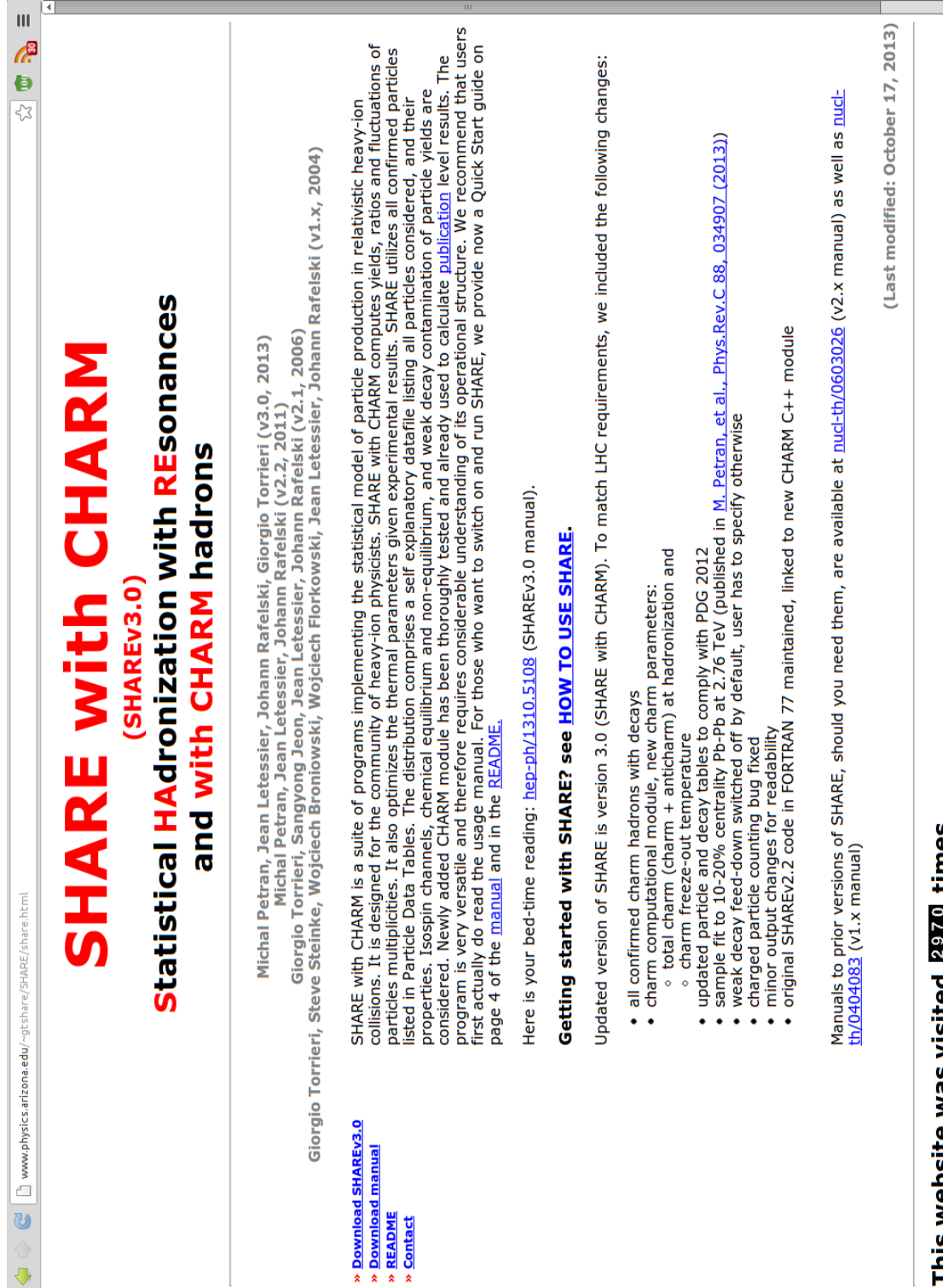


Figure 2.7: Screenshot of SHARE with CHARM webpage.

The new input files and the external CHARM program module are responsible for charm hadron yields calculation based on the thermal parameters set by SHARE. The two parameters specific to charm are: the total number of charm and anticharm quarks  $N_{c\bar{c}} = c + \bar{c}$ ; and the ratio of charm hadronization temperature to the freeze-out temperature of light hadrons  $T_{\text{charm}}/T$ . The CHARM module then calculates the charm feed-down into hadron yields, solves for  $\gamma_c$  and feeds all information back into SHARE for subsequent calculations.

In Appendix G, we present the immediate effects of charm hadronization for a range of produced charm  $N_{c\bar{c}}$  based on the estimates described above in Section 1.2.3. In central Au–Au collisions at  $\sqrt{s_{NN}} = 200$  GeV at RHIC, there is relatively little charm,  $N_{c\bar{c}} = 8.6$ . We find the effect on SHM fit with charm is small at RHIC in terms of modification of both final fit parameters and physical bulk properties of the hadronizing fireball. The effect is well within the experimental errors of the data available for this system.

For LHC, we base our study on the two charm production estimates mentioned in Section 1.2.3; that is the charm production cross section scaling indicating  $N_{c\bar{c}} = 246 \pm 154$  (large error due to  $pp$  charm cross section uncertainty), and the incomplete  $D^0$  meson  $p_{\perp}$ -spectrum consistent with  $N_{c\bar{c}} = 10 - 60$ . During this study, we fit the non-charm hadron data from LHC used in our previous work (see Appendix D), while prescribing a fixed amount of charm in the range of  $N_{c\bar{c}} \in (0, 400)$ . This way we cover the range of charm production up to the forthcoming energy upgrade of LHC. In this preliminary exploration, we kept the charm hadronization temperature equal to that of other hadrons.

The charm hadron feed-down represents, in general, a different pattern of hadron species production. We test if the non-charm data from LHC, which we collected for Appendix D, constrain the charm abundance through the charm decay pattern. For each centrality we calculated a  $\chi^2$  profile in  $N_{c\bar{c}}$ . As a result, we obtain a range of compatible  $N_{c\bar{c}}$  for each centrality that does not contradict the non-charm

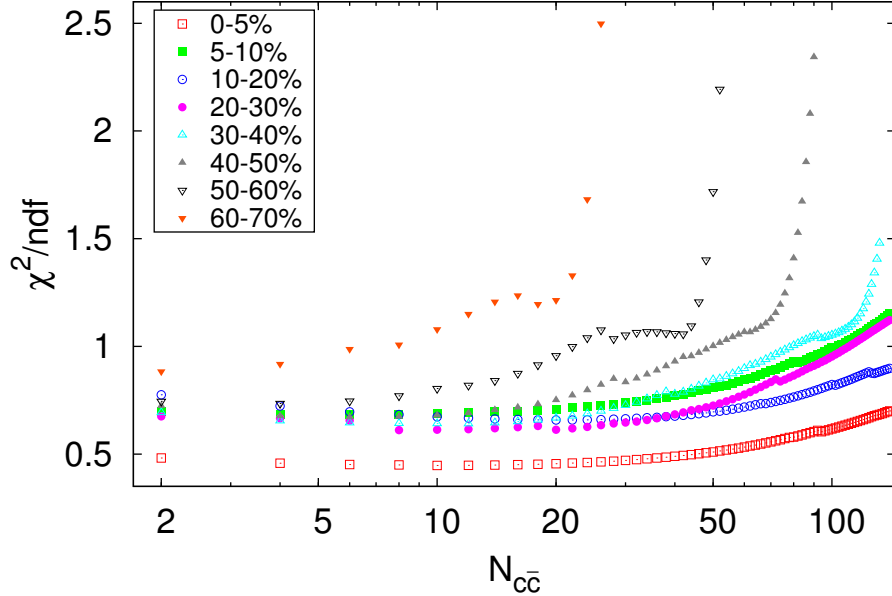


Figure 2.8:  $\chi^2$  profile of fits to non-charm data from Pb–Pb collisions at  $\sqrt{s_{NN}} = 2.76$  TeV from LHC (analyzed in Appendix D) as a function of total charm present at hadronization  $N_{c\bar{c}} = c + \bar{c}$ .

hadron data, see Figure 2.8. For instance, in the 50–60% centrality bin,  $N_{c\bar{c}} < 50$  is compatible with the data; whereas the more peripheral bin 60–70% suggests a tighter limit,  $N_{c\bar{c}} < 25$ . However, no clear minima of the  $\chi^2$  function in the compatible  $N_{c\bar{c}}$  ranges are observed. We conclude that in absence of a directly measured charm hadron yield, charm decay hadron yields impose only a weak constraint on the total amount of charm, and that future data are likely to be compatible with our current SHM results.

We observe that charm hadron yields scale with  $N_{c\bar{c}}$ . While  $D^0(c\bar{u})$  meson scales almost linearly, the yield of, for instance,  $\Xi_{cc}^{++}(ccu)$  is proportional to  $N_{c\bar{c}}^2$ . Recalling that a yield is proportional to one power of  $\gamma_f$  for every constituent (anti)quark of flavor  $f$ , we can attribute this proportionality to  $\gamma_c$  assuming large values, and thus playing a dominant role in charm hadron yield calculation. The yields of single

charm hadrons are well described within our framework irrespective of the  $T_{\text{charm}}$  value. This effect is further discussed below, see also Figure 2.9. A more complete test of SHM with charm comes when several multicharm hadrons will have been measured.

Further, we reach the same conclusion as [7], that charm decays can be a significant source of multistrange particles. This is primarily caused by the enhanced strangeness present in the fireball at hadronization making it very likely for a charm quark to bind to a strange quark, thus enhancing relative yield of hadrons containing a combination of  $cs$  (anti)quarks, e.g.,  $c\bar{s}$ , or  $csq$ . Charm quark in most cases decays weakly into a strange quark (by emitting a  $W^+$ ) hence creating a multistrange particle. On an example of  $\Xi^-(ssd)$ , we show that already for  $N_{c\bar{c}} \simeq 30$  (15  $c\bar{c}$  pairs), charm feed-down contribution to the yield of  $\Xi^-$  is of the same order of magnitude as the experimental uncertainty of the yield measurement, in this case 7%. Therefore, even a very conservative estimate of charm abundance at hadronization makes a significant contribution to the yield of multistrange particles, namely  $\Xi(ssq)$ ,  $\phi(s\bar{s})$ , and  $\Omega(sss)$ .

We also evaluated the physical bulk properties in the presence of charm and we observed a slow decrease as  $N_{c\bar{c}}$  increases, with charm decays serving as an extra source of particles replacing direct contribution. However, the magnitude of this decrease is found to be insignificant compared to other sources of uncertainties of the fireball physical properties. We have checked that including charm in the SHM calculation does not contradict our previously established universality of hadronization conditions.

Without availability of experimental charm yield data, we used a fake charm hadron data point to ensure proper program operation and to test  $N_{c\bar{c}}$  sensitivity. With  $dN_{D^0}/dy = 5 \pm 1$ , SHARE with CHARM successfully converges to a value of  $N_{c\bar{c}} \simeq 21.5$  for various initial parameter values, which implies stable behavior. We further explore the  $D^0$  yield sensitivity to the charm freeze-out temperature  $T_{\text{charm}}$

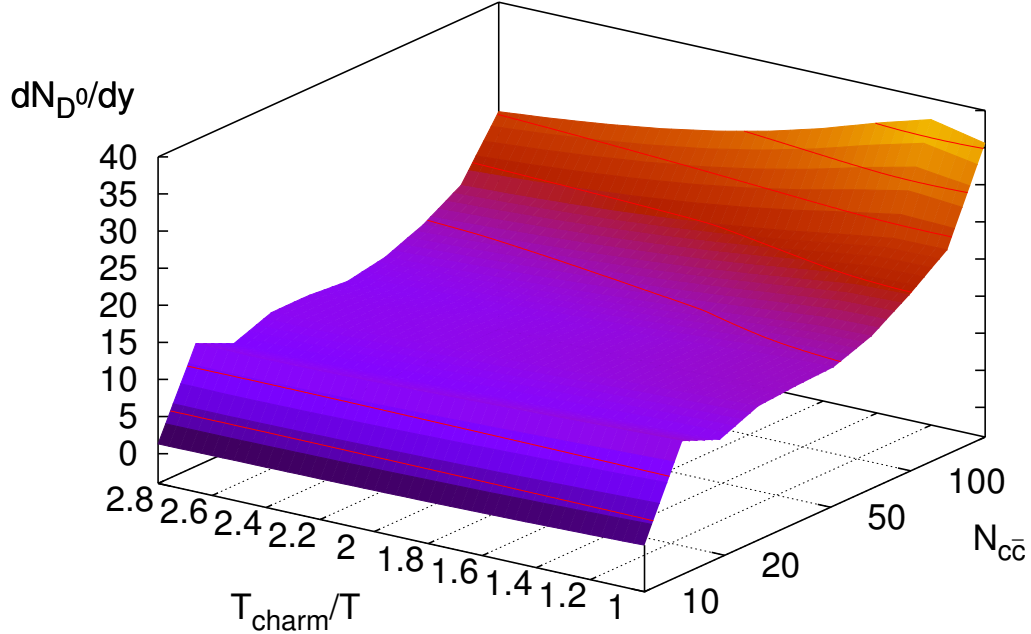


Figure 2.9:  $D^0$  yield as a function of charm abundance at hadronization  $N_{c\bar{c}}$ , and ratio of charm hadronization temperature to that of other flavors  $T_{\text{charm}}/T$ . Solid lines on the surface depict constant yield of  $D^0$ .

and the total charm  $N_{c\bar{c}}$  in Figure 2.9. We can see that the higher hadronization temperature is at a given  $N_{c\bar{c}}$ , the lower is the yield of  $D^0$ . This is so since the relative abundance of heavier multicharm hadrons increases with an increase in  $T_{\text{charm}}$ .

We believe that the new tool, SHARE with CHARM, offers comprehensive analysis of hadron production and properties of quark-gluon plasma at hadronization in contemporary heavy-ion collision experiments including the forthcoming LHC upgrade. It offers an easy to use, yet very flexible implementation of the statistical hadronization model including  $u, d, s$  and now  $c$  quark content. We expect SHARE with CHARM being used extensively in the coming years as charm hadron yield data from LHC should soon become available. At the time of writing this dissertation the most important result obtained with SHARE with CHARM is that universality of hadronization conditions is not affected by the charm feed into hadron abundances.

## CHAPTER 3

### SUMMARY AND FUTURE PLANS

In research leading to this dissertation, we studied particle production from quark-gluon plasma hadronization within the statistical hadronization model. Multi-strange particle ratios, such as  $\Xi/\phi$ , are effective probes of the quark chemistry of the hadronizing fireball imprinted in the measured hadron yields. SHM is confirmed by that  $\Xi/\phi$  ratio is a constant in many heavy-ion collision experiments for a wide range of collision energy and centrality. Variation of other ratios we showed implies different level of strangeness equilibration achieved during the fireball expansion, thus confirming chemical non-equilibrium variant of SHM as the only viable model of hadron production in relativistic heavy-ion collisions.

Fitting data from RHIC 62 within the statistical hadronization model framework with  $\gamma_s$  as a free parameter reveals that strangeness phase space is overpopulated in most central collisions. Due to the large uncertainties of hadron data we cannot exclude the semi-equilibrium model (fixed  $\gamma_q = 1$ ) based alone on the fit quality, even though the fit clearly prefers the non-equilibrium, where for all centralities,  $\gamma_q$  converges to a value near condensation of  $\pi^0$ ,  $\gamma_q \simeq 1.6$ , and the fireball hadronizes at a temperature of  $T = 140$  MeV. However, the non-equilibrium SHM approach results in the same hadronization conditions as previously observed at high energy SPS collision, suggesting both universal hadronization conditions of QGP and applicability of non-equilibrium SHM.

Analysis of preliminary data from Pb–Pb collisions at  $\sqrt{s_{NN}} = 2.76$  TeV reported by the ALICE experiment at LHC confirms the hypothesis of universal hadronization conditions. We find that at the 45 times higher energy than the previously studied system at RHIC 62, the quark-gluon plasma created in heavy-ion collisions freezes-

out at the same universal hadronization conditions. This result holds also as a function of collision centrality.

Detailed analysis of the full set of data shows that at LHC energy, the experimental  $p/\pi$  ratio can be described by our non-equilibrium SHM variant. LHC data is precise enough to confirm the necessity of including the light quark phase space occupancy  $\gamma_q > 1$  as a model parameter. The measured ratio of  $p/\pi$  is a natural outcome of the fit with  $\gamma_q \simeq 1.6$ . No other consistent explanation has been presented up to this date; when applied consistently, posthadronization interactions do not explain all hadron species, nor do they result in a correct description of the  $p/\pi$  ratio as a function of centrality.

Non-equilibrium SHM describes all available data from Pb–Pb collisions at LHC energy with high accuracy across all reported centralities, spanning 5 orders of magnitude of hadron yields at LHC alone. We confirm the universal hadronization conditions of the QGP fireball. For the most central collisions, we find a hadronization temperature of  $T = 138 \text{ MeV}$ , lower than the hadronization temperature at RHIC 62,  $T = 140 \text{ MeV}$ , for central collisions. We attribute the decrease to more supercooling of the fireball due to the more dynamical expansion, as the higher energy content implies a longer-lived fireball, which also gives enough time for strangeness to reach a steady level of QGP equilibration. This is reflected among hadrons by a saturation of  $\gamma_s \simeq 2$  for wide range of centrality. Strangeness conservation during a sudden hadronization allows us to understand better the chemical equilibrium conditions of strangeness in the QGP phase. Matching the QGP Fermi gas strangeness distribution with parameters resulting from the fit to hadron data with the observed strangeness in the hadrons, we conclude that the strange quark either acquires an effective mass of  $m_s = 299 \text{ MeV}/c^2$ , or the strangeness is undersaturated in the QGP with  $\gamma_s^{QGP} \simeq 0.77$ . These bulk QGP properties require further investigation.

At LHC energy, it is estimated that a large amount of charm is produced. The  $D^0 p_\perp$ -spectrum suggests the total amount of  $c+\bar{c}$  quarks ranges between  $10 < N_{c\bar{c}} <$

60  $c + \bar{c}$ . Scaling of the charm production cross section measured in  $pp$  collisions suggest a much higher number,  $100 < N_{c\bar{c}} < 400$ . Since charm is predominantly produced in the initial hard parton scattering processes overpopulating the thermal phase space significantly, annihilation of  $c\bar{c}$  pairs can be expected during the fireball expansion making the two estimates compatible, a point in need of future theoretical investigation. The upgraded program, SHARE with CHARM, is designed to study the effect of charm abundance on hadronization conditions in a range covering the two estimates mentioned above and beyond.

At RHIC 200 GeV, the reported yield of charm is  $N_{c\bar{c}} = c + \bar{c} = 8.6$  and charm effects on hadronization remain hidden within the large experimental hadron yield uncertainties. Without any charm hadron yield measured in Pb–Pb collisions at LHC, we can study today for each centrality, which range of  $N_{c\bar{c}}$  is compatible with the non-charm data we have. Charm decay feed-down is found to be a weak constraint for  $N_{c\bar{c}}$ . We observe, however, that charm decays are a non-negligible source of multistrange hadrons, such as  $\Xi$  or  $\phi$ . The contribution of charm decays in the total yield of multistrange hadrons is comparable at LHC to the small experimental uncertainty already for rather small amount of charm,  $N_{c\bar{c}} \simeq 30$ .

The SHM numerical computation program, SHARE with CHARM, needs as experimental input a charm hadron invariant yield to determine the amount of charm present at hadronization. With more charm hadron yield data, we can determine if charm hadronizes at the same or a different temperature  $T_{\text{charm}}$  than the other flavors. We made SHARE with CHARM publicly available expecting it to become a useful tool in the future to the heavy-ion community, once charm data become available.

Several future research directions have become possible as a result of this dissertation and/or due to data becoming available. I intend to address the following questions in the near future:

**Beam Energy Scan at RHIC** To complete the study of the universal hadroniza-

tion conditions of the quark-gluon plasma, we intend to study the particle production data from the Beam Energy Scan experimental program at RHIC. Detailed analysis of this data within the non-equilibrium SHM framework will test the universal hadronization conditions hypothesis. We hope to identify a reaction energy threshold for QGP creation, i.e., deconfinement.

**Charm dynamics in QGP fireball expansion** The estimated amount of charm created in the initial stages of heavy-ion collisions at LHC is well above the charm content of the fireball at hadronization suggested by the  $D^0$  data. Resolution of this discrepancy between preliminary results requires a detailed modeling of charm evolution during the fireball expansion.

**Entropy at LHC** Charm annihilation during the fireball expansion may be the omitted additional source of entropy at LHC. Detailed modeling of flavor dynamics during the fireball expansion will reveal how much additional entropy can be created by charm annihilation after charm is created in the initial hard parton scattering processes. This will help explaining the value of strangeness over entropy ratio  $s/S$  as a function of centrality at LHC.

**$c, s$  – flavor hadronization dynamics** Because at LHC the fireball volume is so large, strange and charm quarks could undergo complex evolution in QGP towards the end of QGP expansion and hadronization. For example, distillation phenomena of both strangeness and charm need to be considered.

**Flavor chemistry and flavor symmetry** The precision of the LHC heavy-ion data may enable us to study the  $u$  and  $d$  quark flavors separately. This will test the  $u$ - $d$  production symmetry in the QGP fireball. Flavor is one of the important riddles of particle physics. Only in QGP can we study deconfined flavors of the first and the second elementary particle family in a large volume.

### 3.1 List of attached publications

- Appendix A (5 pages) — M. Petran, J. Rafelski, Phys.Rev. C **82** (2010) 011901, DOI:10.1103/PhysRevC.82.011901
- Appendix B (6 pages) — M. Petran, J. Letessier, V. Petracek, J. Rafelski, proceedings of Strangeness in Quark Matter (SQM), 18-24 September 2011, Cracow, Poland  
Acta Phys.Polon.Supp. 5 (2012) 255-262  
DOI:10.5506/APhysPolBSupp.5.255
- Appendix C (5 pages) — M. Petran, J. Rafelski, Phys. Rev. C 88, 021901(R) (2013), DOI:10.1103/PhysRevC.88.021901
- Appendix D (20 pages) — M. Petran, J. Letessier, V. Petracek, J. Rafelski, Phys. Rev. C 88, 034907 (2013), DOI:10.1103/PhysRevC.88.034907
- Appendix E (6 pages) — M. Petran, J. Letessier, V. Petracek, J. Rafelski, Pending publication as proceedings of Strangeness in Quark Matter (SQM), 22-27 July 2013, Birmingham, UK in IOP Conference series  
E-print available as: arXiv:1309.6382 [hep-ph]
- Appendix F (39 pages) — M. Petran, J. Letessier, J. Rafelski, G. Torrieri, Pending publication in Computer Physics Communications  
E-print available as: arXiv:1310.5108 [hep-ph]
- Appendix G (4 pages) — M. Petran, J. Letessier, V. Petracek, J. Rafelski, Pending publication as proceedings of Strangeness in Quark Matter (SQM), 22-27 July 2013, Birmingham, UK, in IOP Conference series  
E-print available as: arXiv:1310.2551 [hep-ph]

## APPENDIX A

### MULTISTRANGE PARTICLE PRODUCTION AND THE STATISTICAL HADRONIZATION MODEL

M. Petran, J. Rafelski, Phys.Rev. C **82** (2010) 011901

DOI:10.1103/PhysRevC.82.011901

#### Summary

In this work, we have motivated the SHM method of studying the multistrange hadrons, primarily  $\Xi$  and  $\phi$ . Their ratio  $\Xi/\phi$  (as defined by Eq. 1 of the paper) is within SHM proportional to the light quark phase space occupancy  $\gamma_q$ . This ratio remains constant over a wide range of energy and centrality values confirming the SHM and the value of  $\gamma_q$  as being constant. Other ratios also proportional to the strangeness phase space occupancy  $\gamma_s$  (such as  $\Xi/\pi$ ) vary, as can be expected, from system to system. This implies that strangeness at hadronization is out of chemical equilibrium. We must allow  $\gamma_s \neq 1$  to achieve proper description of particle production in heavy-ion collisions. This result rules out the absolute chemical equilibrium among produced hadrons. Furthermore, all hadron data from Au–Au collisions at  $\sqrt{s_{NN}} = 62.4$  GeV at RHIC are well described with the chemical non-equilibrium SHM. Seeing the  $\Xi/\phi$  ratio being constant, we predict it to hold also for heavy-ion collisions at LHC and this prediction is now confirmed.

During the preparation of this manuscript, I was guided into SHM calculations and was responsible for the result analysis and preparation of all figures. I prepared a draft, which has been discussed and revised with my advisor, Johann Rafelski, before submission and during the referee process. I estimate the published version contains about 30% of my original text.

## Multistrange particle production and the statistical hadronization model

Michal Petráň<sup>1,2</sup> and Johann Rafelski<sup>1</sup>

<sup>1</sup>*Department of Physics, University of Arizona, Tucson, Arizona 85721*

<sup>2</sup>*Department of Physics, Czech Technical University, Břehova 7, 11519 Praha 1*

(Received 9 December 2009; revised manuscript received 17 May 2010; published 26 July 2010)

We consider the chemical freeze-out of  $\Xi$ ,  $\bar{\Xi}$ , and  $\phi$  multistrange hadrons within a statistical hadronization model inspired approach. We study particle yields across a wide range of reaction energy and centrality from NA49 at the Super Proton Synchrotron (SPS) and the Solenoidal Tracker at RHIC (STAR) experiments. We constrain the physical conditions present in the fireball source of strange hadrons and anticipate results expected at the Large Hadron Collider (LHC).

DOI: [10.1103/PhysRevC.82.011901](https://doi.org/10.1103/PhysRevC.82.011901)

PACS number(s): 24.10.Pa, 12.38.Mh, 13.60.Rj, 25.75.-q

*Introduction*—We study multistrange hadron production in the context of the quark-gluon plasma (QGP) formation in relativistic heavy ion collisions [1]. Given the relatively small reaction cross sections of multistrange hadrons in hadron matter, the observed yields of  $\Xi(qss)$ ,  $\bar{\Xi}$ ,  $\Omega(sss)$ ,  $\bar{\Omega}$ ,  $\phi(s\bar{s})$  [2–7] are considered probes of the earliest stage of the QGP-fireball hadronization.

The yields of these particles were considered previously within a global approach (see, e.g., Ref. [8]). Here we show that it is possible to analyze multistrange hadron yields alone. When this is done we find that multistrange and nonstrange hadrons share the same freeze-out condition. We will discuss the meaning of this discovery in the following, addressing the dynamics of hadronization. We also address the forthcoming Large Hadron Collider (LHC) effort to measure multistrange hadron yields in high multiplicity  $pp$  [9], and soon after, in  $A + A$  reactions.

QGP hadronic particle production yields are usually considered within the statistical hadronization model (SHM) [10–12]. SHM has been successful in describing (strange) hadron production in heavy ion collisions for different colliding systems and energies. These results showing successful global fits of particle yields in the SHM framework inspired us to study multistrange hadron yields alone in this separate analysis for the purpose of (i) establishing that SHM is appropriate for describing yields of these particles, (ii) assessing if their yields are consistent with the established bulk matter properties of the QGP fireball, thus testing the single freeze-out hypothesis for particles with large and small hadron reaction cross sections, and (iii) understanding better how the future LHC results may help arrive at a distinction between SHM model approaches.

*SHM Models*—We begin by introducing the three principal SHM approaches:

- (i) Taking the view that SHM has a limited theoretical foundation, one can seek *simplicity* in an effort to obtain a qualitative description of the yields for all hadrons with just a small number of parameters. An additional attraction is that this assumption leads to a model with chemical equilibrium hadron yields is explored. The main result of this approach is that the hadronization in high-energy heavy ion collisions at the Relativistic Heavy Ion Collider (RHIC) requires  $T \geq 175$  MeV

and this high value is close to the lattice crossover temperature, between the deconfined and hadron phases [13,14].

- (ii) To arrive at a precise description of the bulk properties, such as the strangeness and entropy content of the hadron fireball, we need a precise capability to extrapolate hadron yields to unobserved kinematic domains and particle types. This is achieved by introducing statistical occupancy parameters  $\gamma_i > 1, i = q, s$ . Within this approach there is good systematic behavior of physical observables as a function of collision conditions such as energy or centrality [8,15–19]. The yields of hadrons are, in general, found not to be in chemical equilibrium,  $\gamma_i \neq 1$ ; the hadronization temperature is found near to  $T \simeq 140$  MeV.

While this value of  $T$  can be further away from the deconfinement crossover domain, this is where chiral symmetry restoration is achieved [13,20] and QGP is transformed into hadrons. Moreover, in this approach the variation of the freeze-out temperature with a baryochemical potential parallels the slope seen in the lattice data. Another important outcome of this approach is that a fit to the data offers a good statistical significance. The results obtained can be interpreted in terms of a dynamical picture of nearly chemically equilibrated QGP, decaying into free streaming hadrons. The high intrinsic QGP entropy content explains why equilibrated QGP turns into chemically overpopulated (oversaturated) hadronic gas (HG) phase space—the fast breakup of QGP means that the emerging hadrons do not have the opportunity to re-establish chemical equilibrium in the HG phase.

- (iii) The *single freeze-out* and/or *strangeness nonequilibrium* model has, as the main objective, a statistically significant description of hadron yields achieved with minimal effort. Only strangeness chemical nonequilibrium is allowed. This is often enough to produce a decent data fit and to assure that all particles can be formed at the same physical condition [21–25]. The main result of this approach is a hadronization temperature near  $T \simeq 160$  MeV, which agrees with Hagedorn temperature [26,27].

*Particle ratios of interest*—We must include in our theoretical consideration of multistrange hadron yields the contributing yield of decaying hadron resonances. Within SHM these individual yields generally depend on several parameters. The phase-space occupancy  $\gamma_q$  scales particle yields according to the light quark content and a similar parameter  $\gamma_s$  refers to the strange quark content. Temperature  $T$  quantifies the size of the accessible phase space. The baryochemical potential  $\mu_B$  differentiates baryons from antibaryons and strange chemical potential  $\mu_S$  does the same for strangeness. There is also a potential  $\mu_{13}$  related to a different number of up and down quarks that is constrained by proton and neutron asymmetry in colliding nuclei and the overall yield is normalized by a volume parameter  $V$ .

By considering the ratio

$$\frac{\Xi}{\phi} \equiv \sqrt{\frac{\Xi^+ \Xi^-}{\phi \phi}} \simeq \gamma_q f(T), \quad (1)$$

we eliminate in good approximation most of the SHM parameter dependencies since (i) by taking the product of a particle and antiparticle, we eliminate baryochemical potential  $\mu_B$  as well as strange chemical potential  $\mu_S$ , (ii) we also eliminate the strange quark phase-space occupancy  $\gamma_s$  because the strange and antistrange quark content in the numerator and denominator is the same, and (iii) The overall normalization is eliminated by the fact that we have the same number of hadrons in the ratio numerator and denominator.

The  $\Xi/\phi$  ratio depends on the probability of finding a nonstrange  $d, \bar{d}$  quark at the formation of  $\Xi^-(dss)$  and  $\Xi^+(\bar{d}\bar{s}\bar{s})$ , respectively. This is expressed by the light quark phase-space occupancy  $\gamma_q$ . Furthermore, temperature  $T$  controls the magnitude of

$$f(T) \simeq \sum_i \frac{g_i}{3} \left( \frac{m_{\Xi_i}}{m_\phi} \right)^{3/2} e^{-\frac{m_\phi - m_{\Xi_i}}{T}}, \quad (2)$$

the (nonrelativistic) phase-space ratio of  $\Xi^-$  and  $\phi$ .  $\Xi(1321)$  is always a decay product of  $\Xi^*(1530)$ . Thus aside from the ground state  $i = 1$ :  $\Xi(1321)$ ,  $g_1 = 2$  one must include in the sum the  $\Xi^*(1530)$ ,  $g_2 = 4$  resonance. Consideration of this special yield ratio parallels the earlier effort made to identify  $\gamma_s/\gamma_q$  in Ref. [28].

We extend our considerations to include single strange  $K^+(u\bar{s})$ ,  $K^-(\bar{u}s)$  mesons and triple strange  $\Omega^-(sss)$ ,  $\Omega^+(\bar{s}\bar{s}\bar{s})$  baryons considering the ratios

$$\frac{\Xi}{K} \equiv \sqrt{\frac{\Xi^+ \Xi^-}{K^+ K^-}} = \gamma_s f_1(T); \quad \frac{\Omega}{\phi} = \sqrt{\frac{\Omega^+ \Omega^-}{\phi \phi}} = \gamma_s f_2(T). \quad (3)$$

Given the quark content, both  $\Xi/K$  and  $\Omega/\phi$  are proportional to strange quark yield [i.e., the strange quark phase-space occupancy  $\gamma_s$  and a function  $f_i(T)$ ].

The arguments leading to Eq. (1) and Eq. (3) are strictly valid only in the Boltzmann approximation. Considering quantum statistics, there is some residual dependence of  $f(T)$  on the chemical parameters, involving higher powers of  $\gamma_q$  for the ratio  $\Xi/\phi$  Eq. (1), and higher powers of  $\gamma_s$  for the ratio  $\Xi/K$

Eq. (3). To estimate the magnitude of the quantum statistics effect we calculate the actual particle ratios with SHARE2 [11] using both quantum and Boltzmann statistics. We find that the Boltzmann approximation we used overestimates  $\Xi/\phi$  by 0.25%, which is always negligible. For  $\Xi/K$ , we find that it is overestimated by the Boltzmann approximation by up to 4%, the relatively larger effect is due to the relatively low mass of the kaon. Since the experimental error is much greater we continue to consider the simple theoretical Boltzmann yields. When in the following we consider ratios involving pions, all results are obtained using SHARE2, which accounts for resonance decays and all yields can be obtained using quantum statistics.

*Experimental data*—We consider  $4\pi$  data from the CERN-SPS NA49 experiment, and for the STAR experiment at RHIC the acceptance rapidity interval is  $|y| < 0.5$ ; therefore at RHIC we use the yield per unit of rapidity  $dN/dy$  and omit the differential  $dy$  when referring to relative yields. For the  $\phi$  meson we consider the recently published data from STAR [2] and the updated data from NA49 [3]. We collected the necessary data for  $\Xi$  and  $\Xi$  baryons from Refs. [4–6].

We do not use NA49 158 GeV results since these experimental results do not allow us to interpolate the different centrality bins used to measure different multistrange particle yields. We cannot simply combine data from different centrality bins having seen the variation of yields with centrality (that is  $\gamma_s$ ). The STAR 62 experiment provides data in several centrality bins, defined as a percentage of the most central collisions: Data from the most central collisions are found in the centrality 0–5% interval and the most peripheral collision results presented are in the 70–80% bin. The relation to  $N_{\text{part}}$  and/or impact parameter  $b$  is discussed in Ref. [7].

We use recent data for  $K^\pm$  mesons from STAR experiments at both  $\sqrt{s_{NN}} = 200$  and 62.4 GeV from Ref. [7]. For the SPS NA49 data we use yields from Refs. [29,30].

We note that different centrality bins are often chosen for different particle types. To be able to form particle ratios in a common centrality interval, we interpolate or extrapolate, that is, fit individual yields as a function of the number of participants using a simple functional form  $f(N_{\text{part}}) \equiv a \cdot N_{\text{part}}^b + c$ . We show the fit parameters  $a$ ,  $b$ , and  $c$  in Table I and compare the experimental results and the fit in Fig. 1.

TABLE I. Fit parameters used to determine particle yields for incompatible centrality bins using  $f(N_{\text{part}}) \equiv a \cdot N_{\text{part}}^b + c$  (see text for details).

	a	b	c
$\pi^-$	$4.179 \times 10^{-1}$	1.072	$7.107 \times 10^{-1}$
$\pi^+$	$4.247 \times 10^{-1}$	1.048	$6.422 \times 10^{-1}$
$K^+$	$5.433 \times 10^{-2}$	1.111	$-1.014 \times 10^{-1}$
$K^-$	$4.812 \times 10^{-2}$	1.107	$-3.859 \times 10^{-2}$
$\Xi^-$	$1.228 \times 10^{-3}$	1.247	$-4.678 \times 10^{-3}$
$\Xi^+$	$8.978 \times 10^{-4}$	1.221	$9.390 \times 10^{-4}$
$\phi^0$	$4.162 \times 10^{-3}$	1.203	$-9.311 \times 10^{-3}$

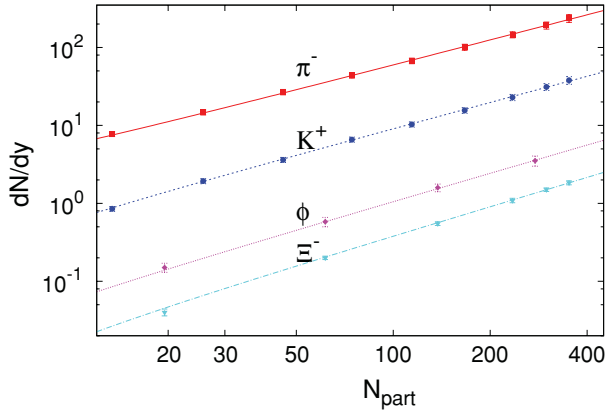


FIG. 1. (Color online) Data points (full symbols) of particle yields used in the analysis and their respective fitted centrality dependence.

*Particle ratios*—After this preparation we can form ratios of particle yields as shown in Fig. 2 and Table II. We note that the  $\Xi/\phi$  relative yield does not change much over a wide range of energies and centralities, in contrast to the individual hadron yields which enter the ratio. The average value of all available data points is  $\Xi/\phi = 0.281$  with an error at 15% level.

The remarkable result, the constancy of  $\Xi/\phi$ , means that at SPS and RHIC energies the mechanisms and conditions at which double-strange particles are produced are very similar and that, according to Eq. (1), there is a constraint between the values of  $\gamma_q$  and  $T$ , which we now explore in Fig. 3 where we show in the  $T, \gamma_q$  plane the theoretical SHM results as lines for a constant ratio  $\Xi/\phi$ . These values are obtained using SHARE2 and varying  $\gamma_q$  and  $T$ , with all other model parameters fixed to reasonable physical values. In this way we also confirm once again the analytical formula Eq. (2).

We limit the magnitude of  $\gamma_q$  by a critical value of light quark phase-space occupancy  $\gamma_q^{\text{crit}}$ .  $\gamma_{\pi^0} \equiv \gamma_q^2 \leq (\gamma_q^{\text{crit}})^2 = \exp(m_{\pi^0}/T)$ , which is the condition where the pion phase-space distribution function diverges for  $m_{\pi^0} = 135 \text{ MeV}/c^2$ . The experimental values  $\Xi/\phi \simeq 0.281 \pm 15\%$  are found consistent with all SHM models in that for  $\gamma_q = 1$  we find

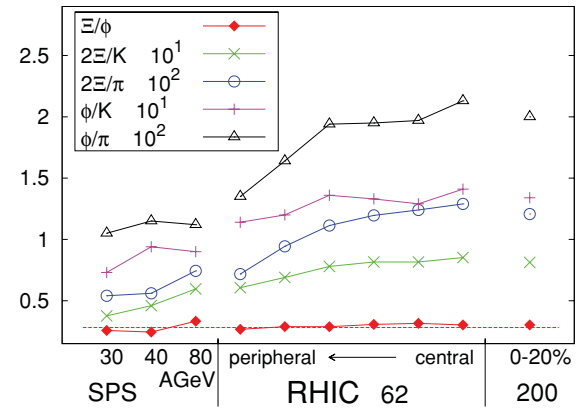


FIG. 2. (Color online) Data points of  $\Xi/\phi$  Eq. (1),  $\Xi/K$  Eq. (3),  $\Xi/\pi$  and  $\phi/\pi$  Eq. (4). The straight line for  $\Xi/\phi = 0.281$ .

the value  $T = 170 \pm 10 \text{ MeV}$ , and for  $\gamma_q \rightarrow 1.63$  a value  $T \rightarrow 140 \text{ MeV}$ .

*Test of SHM models*—We have seen that hadronization of  $\Xi$  and  $\phi$  is consistent with the three different SHM models, but there is an interesting constraint between  $T, \gamma_q$  arising from the constancy of the relative  $\Xi$  and  $\phi$  yield. We see also in Fig. 2 that the variation of  $\Xi/K$  is significant, it changes by a factor of 2.3 in the entire data range. Considering that we already established by the study of  $\Xi/\phi$  that the hadronization temperature does not vary, this indicates that there is a variation of the  $\gamma_s$  value by a factor of about 2.3 in the data range. We conclude that a fixed value  $\gamma_s = 1$  cannot be chosen. This rules out the SHM model (a). We also note that this argument can be made in the same way considering the variation of the other ratios in Fig. 2 (e.g.,  $\Xi/\pi$  and  $\phi/K$ ).

SHM results for  $\Xi/K$  and  $\Omega/\phi$  in the  $T, \gamma_s$  plane are shown in Fig. 4, obtained by the same method as before (i.e., using SHARE with other SHM parameters fixed at an appropriate value. For a given  $\Xi/K$  and/or  $\Omega/\phi$  a slight  $\gamma_q$  dependence remains since there are unrelated resonances decaying into  $K$  (and to a lesser degree  $\Xi$ ). Thus we present for each fixed value of  $\Xi/K$  two extremes  $\gamma_q = 1$  and  $\gamma_q = \gamma_q^{\text{crit}}$ . The effect

TABLE II. Values of ratios  $\Xi/\phi$  Eq. (1),  $\Xi/K$  Eq. (3), and  $\Xi/\pi$  and  $\phi/\pi$  Eq. (4) obtained from the data and the resulting estimated uncertainty in  $\gamma_s$  and  $\gamma_q$ , respectively. When symbol “E” is shown in the error column, the data ratio is a result of the interpolation and/or extrapolation needed to account for different centrality bins.

Experiment	Centrality	$\Xi/\phi \times 10$	$\delta\gamma_q$	$\Xi/K \times 10^2$	$\delta\gamma_s$	$\Xi/\pi \times 10^3$	$\phi/K \times 10$	$\phi/\pi \times 10^2$
STAR 62	0–5%	3.04	E	4.19	9.6%	6.22	1.38	2.04
STAR 62	5–10%	3.00	E	4.08	9.2%	6.20	1.36	2.06
STAR 62	10–20%	2.94	E	4.06	9.3%	5.98	1.38	2.04
STAR 62	20–40%	2.88	12.5%	3.79	E	5.48	1.32	1.91
STAR 62	40–60%	2.85	14.6%	3.38	E	4.65	1.18	1.63
STAR 62	60–80%	2.49	19.3%	2.84	E	3.45	1.14	1.38
STAR 200	0–20%	3.02	11.8%	4.06	12.9%	6.04	1.34	$2.54^{+0.21}_{-0.09}$ <sup>a</sup>
SPS 80 AGeV	7%	3.33	24.5%	3.04	22.7%	2.60	0.83	0.88
SPS 40 AGeV	7%	2.45	42.1%	1.89	18.0%	3.23	0.78	0.83
SPS 30 AGeV	7%	2.57	66.5%	1.85	24.3%	2.10	0.63	0.72

<sup>a</sup>For STAR 200  $\phi/\pi$  considering Fig. 14 in Ref. [2] we give an average of data for centralities up to 50%.

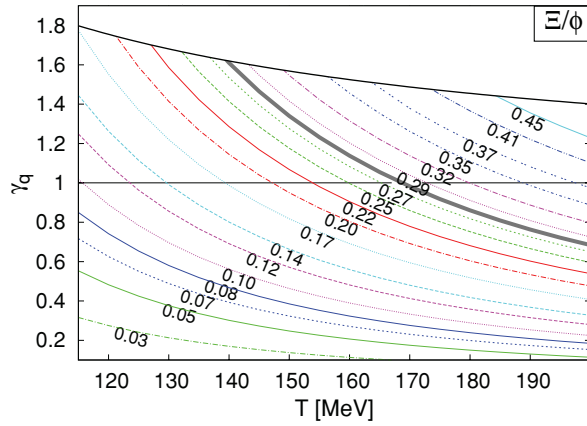


FIG. 3. (Color online) Lines of a constant given ratio Eq. (1)  $\Xi/\phi \in [0.03, 0.45]$  in the  $T, \gamma_q$  plane. The lines for  $\gamma_q = 1$  and  $\gamma_q = \gamma_q^{\text{crit}}$  are presented by solid black lines. The average result, 0.281, of all SPS and RHIC experiments is highlighted by a thick gray line. As this ratio is considered constant, this line indicates the prediction of the LHC results.

is depicted in Fig. 4(a) in terms of two lines shown by the same line type.

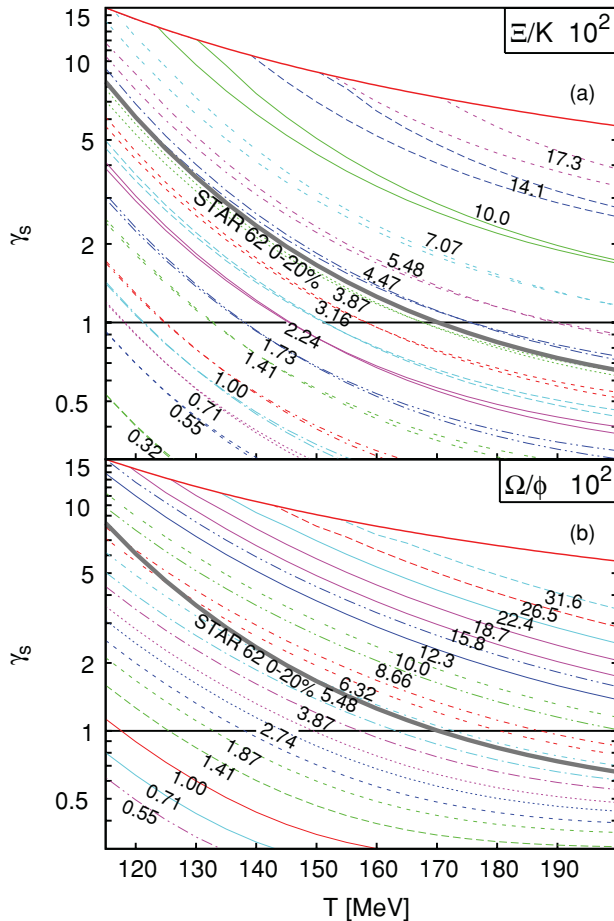


FIG. 4. (Color online) Lines of constant ratio  $\Xi/K$  (a) and  $\Omega/\phi$  (b). Experimental data from most central 0–20% STAR 62 are indicated by a thick line which in the bottom frame (b) shows our prediction. See text for more detail.

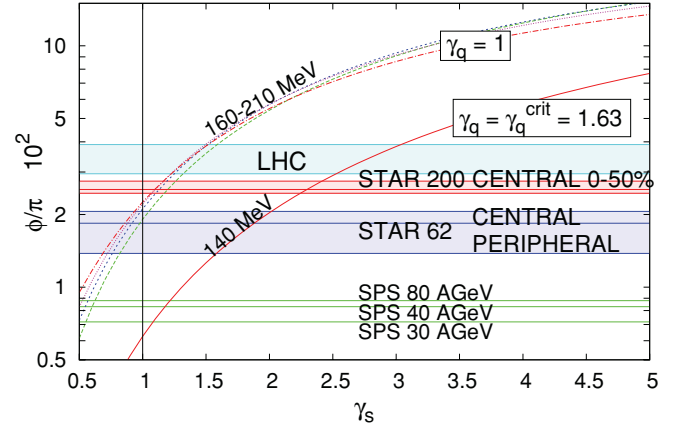


FIG. 5. (Color online) The relative  $\phi/\pi$  Eq. (4) yield as a function of  $\gamma_s$  in several hadronization scenarios, see text. The vertical solid black line shows the chemical equilibrium with  $\gamma_s = 1$ . For experimental data see Table II. Predicted values for LHC are indicated in blue.

Note that similarly as for  $\gamma_q$ , there is a critical value for  $\gamma_s$  based on the Bose-Einstein condensation of the  $\eta$  meson ( $\eta = 0.55(u\bar{u} + d\bar{d}) + 0.45s\bar{s}$  [31,32]). The large values of  $\gamma_s$  can be relevant to the future LHC results. To compare theory and experiment we show the thick 0–20% STAR 62 line and by looking at the bottom frame of Fig. 4 we obtain the prediction  $5.5 \times 10^{-2} < \Omega/\phi < 7.0 \times 10^{-2}$ , the variation due to the variability of hadronization temperature.

To further elaborate the validity of models (b) and (c) we show on the right in Table II the ratios  $\Xi/\pi$ ,  $\phi/K$  and  $\phi/\pi$ , where

$$\frac{\Xi}{\pi} \equiv \sqrt{\frac{\Xi^- \Xi^+}{\pi^- \pi^+}}; \quad \frac{\phi}{K} \equiv \sqrt{\frac{\phi \phi}{K^- K^+}}; \quad \frac{\phi}{\pi} \equiv \sqrt{\frac{\phi \phi}{\pi^- \pi^+}}. \quad (4)$$

The experimental  $\Xi/\pi$  and  $\phi/\pi$  relative yields vary by a factor  $\simeq 3.5$  in both cases. In Fig. 5 we show the  $\phi/\pi$  ratio and compare it to theory as a function of  $\gamma_s$  at a fixed given  $T$ . Model (b) with  $T \simeq 140$ ,  $\gamma_q = \gamma_q^{\text{crit}}$  implies that the different experimental results correspond to  $1 < \gamma_s < 2.4$ . These values are consistent with the large value of  $\gamma_q = \gamma_q^{\text{crit}} \simeq 1.6$ . However, for  $\gamma_q = 1$ , several fixed  $T$  lines nearly coincide in the interesting range  $210 \geq T \geq 160$  MeV. This means that the growth in the yield of  $\phi$  is nearly compensated by the growth in the  $\pi$  multiplicity. It will be very interesting to see how LHC results will line up in this presentation since we see that the high-energy RHIC results even at  $\gamma_q = 1$  imply  $\gamma_s > 1$ . A value  $\gamma_s > 1$  is incompatible with the picture of strangeness production in hadron collisions and implies the presence of a strangeness dense QGP phase as a source of hadrons.

*Behavior at LHC*—As already remarked the ratio  $\Xi/\phi \simeq 0.28$  is firmly constrained and cannot change. Even under the extreme LHC conditions we expect that this ratio will be the same as at RHIC. However, considerable changes can be expected for the other (multi)strange particle ratios that were discussed earlier [33,34]. Here we will mainly address the  $\phi/\pi$  ratio.

When we accept the premise that entropy and strangeness are conserved during the hadronization, we can predict values of the phase-space occupancy  $\gamma_s$  in chemical semiequilibrium and nonequilibrium models for the LHC. We expect a 20% increased value of strangeness over entropy  $s/S \simeq 0.037$  [34]. For the two models under consideration ( $T = 140$  MeV,  $\gamma_q = \gamma_q^{\text{critical}}$  and  $170$  MeV,  $\gamma_q = 1$ ) this value suggests [33]  $\gamma_s/\gamma_q \simeq 1.55$ . The expected  $\phi/\pi$  ratio is  $2.95 \times 10^{-2}$  and  $3.90 \times 10^{-2}$  for the two models as indicated by the boundaries of the LHC band in Fig. 5. Experimental results of this magnitude require  $\gamma_s > 1$  and concludes in favor of chemical nonequilibrium, the still ongoing discussion of chemical equilibrium models.

*Summary and conclusion*—We find that the relative particle yield  $\Xi/\phi$  is practically constant as a function of centrality and the reaction energy at RHIC and SPS. We find that these particles, despite their small reaction cross-sections are emerging at the same hadronization condition as all bulk particles. This result was anticipated [35] for a fast expanding QGP fireball, which undercools and rapidly breaks apart (hadronizes) and was used extensively in single hadronization models [16,18,19,22].

Variation in the ratio  $\Xi/K$  (and thus also  $\phi/K \propto \gamma_s/\gamma_q$ ) implies a variation in strange phase-space occupancy  $\gamma_s$ , in agreement with the expectation that strangeness production grows with energy and the centrality of the collision. This experimental result is incompatible with the chemical equilib-

rium model (a), for which also the parameter  $\gamma_s$  is fixed to 1 by definition.

Considering further the yields  $\Xi/\pi$  and  $\phi/\pi$ , consistency with the bulk matter particle production rates is arrived at within the chemical nonequilibrium model (b) with  $\gamma_q > 1$  and  $\gamma_s > 1$ . These values imply that the observed strange hadrons yields are above chemical equilibrium, a feature predicted to be signature for hadronization of a QGP fireball [36]. The expected further increase of  $\gamma_s > 1$  at LHC implies a further increase of the  $\phi/\pi$  ratio, providing a clear distinction between chemical nonequilibrium model (b) and semi-equilibrium model (c).

Our results show that the yields of all multistrange hadrons available today are (1) compatible with the SHM picture of hadron formation, (2) are well described by current chemical nonequilibrium hadronization models in the parameter domain obtained from the other hadron yields, and (3) these data are incompatible with the chemical equilibrium single-freeze-out SHM. A critical test of our approach is that in LHC ion experiments the  $\Xi/\phi$  ratio remains the same as was observed at SPS and RHIC.

*Acknowledgments*—JR would like to thank Z.L. Matthews and O. Villalobos Baillie of Birmingham University and CERN-ALICE collaboration for interesting discussions. This work was supported by a grant from the US Department of Energy, DE-FG02-04ER41318.

- 
- [1] A. R. Timmins (STAR Collaboration), *Nucl. Phys. A* **830**, 829c (2009).
- [2] B. I. Abelev (STAR Collaboration), *Phys. Lett. B* **673**, 183 (2009).
- [3] C. Alt (NA49 Collaboration), *Phys. Rev. C* **78**, 044907 (2008).
- [4] C. Alt (NA49 Collaboration), *Phys. Rev. C* **78**, 034918 (2008).
- [5] J. Adams (STAR Collaboration), *Phys. Rev. Lett.* **98**, 062301 (2007).
- [6] J. Speltz, Ph.D. thesis, Institut Pluridisciplinaire Hubert Curien, Strasbourg, France, 2006.
- [7] B. I. Abelev (STAR Collaboration), *Phys. Rev. C* **79**, 034909 (2009).
- [8] I. Kuznetsova, J. Letessier, and J. Rafelski, *Acta Phys. Pol. B* **40**, 1013 (2009).
- [9] Z. L. Matthews (ALICE Collaboration), *J. Phys. G: Nucl. Part. Phys.* **37**, 094048 (2010).
- [10] J. Letessier and J. Rafelski, *Camb. Monogr. Part. Phys. Nucl. Phys. Cosmol.* **18**, 1 (2002).
- [11] G. Torrieri *et al.*, *Comput. Phys. Commun.* **167**, 229 (2005); **175**, 635 (2006).
- [12] F. Becattini and R. Fries (2009), [arXiv:0907.1031](https://arxiv.org/abs/0907.1031).
- [13] Z. Fodor and S. D. Katz (2009), [arXiv:0908.3341](https://arxiv.org/abs/0908.3341).
- [14] P. Braun-Munzinger and J. Wambach, *Rev. Mod. Phys.* **81**, 1031 (2009).
- [15] G. Torrieri and J. Rafelski, *New J. Phys.* **3**, 12 (2001).
- [16] J. Rafelski, J. Letessier, and G. Torrieri, *Phys. Rev. C* **72**, 024905 (2005).
- [17] J. Letessier and J. Rafelski, *Phys. Rev. C* **73**, 014902 (2006).
- [18] J. Letessier and J. Rafelski, *Eur. Phys. J. A* **35**, 221 (2008).
- [19] J. Rafelski and J. Letessier, *J. Phys. G* **36**, 064017 (2009).
- [20] R. Gupta (2009), [arXiv:0912.1374](https://arxiv.org/abs/0912.1374).
- [21] F. Becattini, J. Cleymans, A. Keranen, E. Suhonen, and K. Redlich, *Phys. Rev. C* **64**, 024901 (2001).
- [22] W. Broniowski and W. Florkowski, *Phys. Rev. C* **65**, 064905 (2002).
- [23] F. Becattini, M. Gazdzicki, A. Keranen, J. Manninen, and R. Stock, *Phys. Rev. C* **69**, 024905 (2004).
- [24] F. Becattini, J. Manninen, and M. Gazdzicki, *Phys. Rev. C* **73**, 044905 (2006).
- [25] F. Becattini and J. Manninen, *J. Phys. G* **35**, 104013 (2008).
- [26] R. Hagedorn and J. Ranft, *Nuovo Cimento Suppl.* **6**, 169 (1968).
- [27] R. Hagedorn and J. Rafelski, *Phys. Lett. B* **97**, 136 (1980).
- [28] J. Rafelski and J. Letessier, *Nucl. Phys. A* **715**, 98 (2003).
- [29] C. Alt *et al.* (NA49 Collaboration), *Phys. Rev. C* **77**, 024903 (2008).
- [30] S. V. Afanasiev (NA49 Collaboration), *Phys. Rev. C* **66**, 054902 (2002).
- [31] V. Uvarov, *Phys. Lett. B* **511**, 136 (2001).
- [32] J.-W. Li and D.-S. Du, *Phys. Rev. D* **78**, 074030 (2008).
- [33] I. Kuznetsova and J. Rafelski, *Eur. Phys. J. C* **51**, 113 (2007).
- [34] J. Letessier and J. Rafelski, *Phys. Rev. C* **75**, 014905 (2007).
- [35] J. Rafelski and J. Letessier, *Phys. Rev. Lett.* **85**, 4695 (2000).
- [36] M. Jacob and J. Tran Thanh Van, *Phys. Rep.* **88**, 321 (1982), see p. 331 ff.

## APPENDIX B

### STRANGENESS PRODUCTION IN AU–AU COLLISIONS AT

$$\sqrt{s_{NN}} = 62.4 \text{ GeV}$$

M. Petran, J. Letessier, V. Petracek, J. Rafelski, proceedings of Strangeness in Quark Matter (SQM), 18-24 September 2011, Cracow, Poland

Acta Phys.Polon.Supp. 5 (2012) 255-262

DOI:10.5506/APhysPolBSupp.5.255

#### Summary

We explore hadron production at RHIC in Au–Au collisions at  $\sqrt{s_{NN}} = 62.4 \text{ GeV}$ . We performed a fit to all available data as a function of centrality including multi-strange particles using the chemical non-equilibrium SHM, allowing  $\gamma_s \neq 1$  and  $\gamma_q \neq 1$ . We show that our model describes the data better (with significantly lower  $\chi^2$ ) than previous efforts seen in literature, for instance compared to the constrained  $\gamma_s < 1, \gamma_q = 1$  semi-equilibrium model fit presented in reference [3] of our publication. We find overpopulation of strangeness,  $\gamma_s > 1$  for large enough system volume in central collision. We have confirmed the same hadronization conditions, pressure  $P = 82 \text{ MeV/fm}^3$ , energy density  $\varepsilon = 0.5 \text{ GeV/fm}^3$ , and entropy density  $\sigma = 3.3 \text{ fm}^{-3}$ , that were found for the high SPS energy and other RHIC energies (reference [7] of the publication). This led to a hypothesis of universal hadronization conditions in all heavy-ion collision experiments, in particular also at that time not yet available LHC. This prediction has been now confirmed.

After presenting these results at Strangeness in Quark Matter 2011 conference, I prepared a draft, which was then revised with my co-authors. I estimate about 50% of the publication to be my original text.

# STRANGENESS PRODUCTION IN Au–Au COLLISIONS AT $\sqrt{s_{NN}} = 62.4$ GeV\*

MICHAL PETRÁŇ<sup>a,b</sup>, JEAN LETESSIER<sup>a,c</sup>, VOJTĚCH PETRÁČEK<sup>b</sup>  
JAN RAFELSKI<sup>a</sup>

<sup>a</sup>Department of Physics, University of Arizona, Tucson, Arizona 85721, USA

<sup>b</sup>Czech Technical University in Prague

Faculty of Nuclear Sciences and Physical Engineering, Czech Republic

<sup>c</sup>Laboratoire de Physique Théorique et Hautes Energies

Université Paris 6, Paris 75005, France

*(Received January 2, 2012)*

We obtain strangeness production as function of centrality in a statistical hadronization model analysis of all experimental hadron production data in Au–Au collisions at  $\sqrt{s_{NN}} = 62.4$  GeV. Our analysis describes successfully the yield of strange and multi-strange hadrons recently published. We explore condition of hadronization as a function of centrality and find universality for the case of chemical non-equilibrium in the hadron phase space corresponding to quark-gluon plasma (QGP) in chemical equilibrium.

DOI:10.5506/APhysPolBSupp.5.255

PACS numbers: 24.10.Pa, 12.38.Mh, 25.75.-q, 13.60.Rj

## 1. Experimental data

The statistical hadronization model (SHM) is known to successfully describe hadron yields in a variety of experiments at different energies [1, 2]. Recently, new results on the yields of strange and multi-strange hadrons at  $\sqrt{s_{NN}} = 62.4$  GeV have been published [3]. This data together with previously published non-strange particle yields [4] and  $\phi$  meson measurement [5] provides a new opportunity to reevaluate hadronization conditions in  $\sqrt{s_{NN}} = 62.4$  GeV collisions.

Heavier multistrange particles are more rarely produced and therefore to assure that statistical errors are small, they are often presented in wider centrality bins than non-strange particles. In order to study all particle yields as a function of centrality, we have to account for the different centrality

---

\* Presented at the Conference “Strangeness in Quark Matter 2011”, Kraków, Poland, September 18–24, 2011.

binning. We associate each bin with average number of participants  $N_{\text{part}}$ . Then, we fit hadron yield as a function of  $N_{\text{part}}$  using a power law,

$$f(N_{\text{part}}) = a N_{\text{part}}^b + c, \quad (1)$$

where  $a, b$  and  $c$  are free parameters fitted and shown in Table I. We see, as expected, that particles are always more numerous than their respective anti-particles. However for the  $\Omega$ , we had only three data points and three free parameters of the interpolating function from Eq. (1). Therefore, we fixed  $c = 0$  and fitted the other two. This fit, with one degree of freedom, gave us a qualitatively similar function as for the other particles.

TABLE I

Particle yields power fit parameters (as defined by Eq. (1)) used to describe particle yields as function of centrality. For  $\Omega$ ,  $c = 0$  is assumed.

	$a$	$b$	$c$
$\pi^-$	$3.756 \times 10^{-1}$	1.098	$-2.330 \times 10^{-2}$
$\pi^+$	$3.788 \times 10^{-1}$	1.094	$-5.768 \times 10^{-2}$
$K^+$	$4.769 \times 10^{-2}$	1.141	$-2.002 \times 10^{-1}$
$K^-$	$4.188 \times 10^{-2}$	1.138	$-1.165 \times 10^{-1}$
$K_s^0$	$5.068 \times 10^{-2}$	1.074	$-2.341 \times 10^{-1}$
$p^+$	$3.972 \times 10^{-2}$	1.125	$-9.963 \times 10^{-2}$
$p^-$	$3.404 \times 10^{-2}$	1.024	$-8.573 \times 10^{-2}$
$\phi^0$	$4.162 \times 10^{-3}$	1.203	$-1.311 \times 10^{-3}$
$\Lambda$	$1.772 \times 10^{-2}$	1.154	$-1.025 \times 10^{-2}$
$\bar{\Lambda}$	$1.045 \times 10^{-2}$	1.125	$1.764 \times 10^{-2}$
$\Xi^-$	$1.434 \times 10^{-3}$	1.197	$-1.415 \times 10^{-2}$
$\bar{\Xi}^+$	$7.693 \times 10^{-4}$	1.231	$-1.765 \times 10^{-3}$
$\Omega$	$1.266 \times 10^{-5}$	1.720	0
$\bar{\Omega}$	$3.985 \times 10^{-6}$	1.879	0

## 2. SHM fit including multistrange hadrons

We performed a cross check of SHARE [1], the thermal model implementation we used, with three other codes currently in use by other groups using the compiled data in [2]. We tested our model on the data set from Au–Au collision at  $\sqrt{s_{NN}} = 200$  GeV from STAR and obtained both yields and thermal parameters within 5% from the values in [2].

Rather than hadron ratios studied in [3], we decided to fit hadron yields, which require a common volume  $dV/dy$  of the source. We complemented the data set with identified hadrons ( $\pi^\pm$ ,  $K^\pm$ ,  $p^\pm$ ) from [4] and  $\phi$  yield

from [5]. Furthermore, we require the conservation of charge per baryon  $(Q - \bar{Q})/(B - \bar{B}) = 0.39 \pm 0.01$  and strangeness  $(s - \bar{s})/(s + \bar{s}) = 0 \pm 0.05$  with a few percent error to account for the detector acceptance and efficiency.

As was also pointed out in [3], the experimental particle yields are subject to an important inconsistency: for all centralities, the yield of  $K_s^0$  is smaller than both  $K^+$  and  $K^-$  (lowest of three corresponding lines in the left panel of figure 1). In general, at finite baryon density, we expect  $K^+ < K^0 < K^-$ . Interestingly, the missing  $K_s^0$  are associated with yields of  $\Lambda, \bar{\Lambda}$  in that these three particle types had the largest contributions to the total  $\chi^2$  of the fit. The choice to include or exclude them from the fit did not change the values of the SHM parameters we obtained.

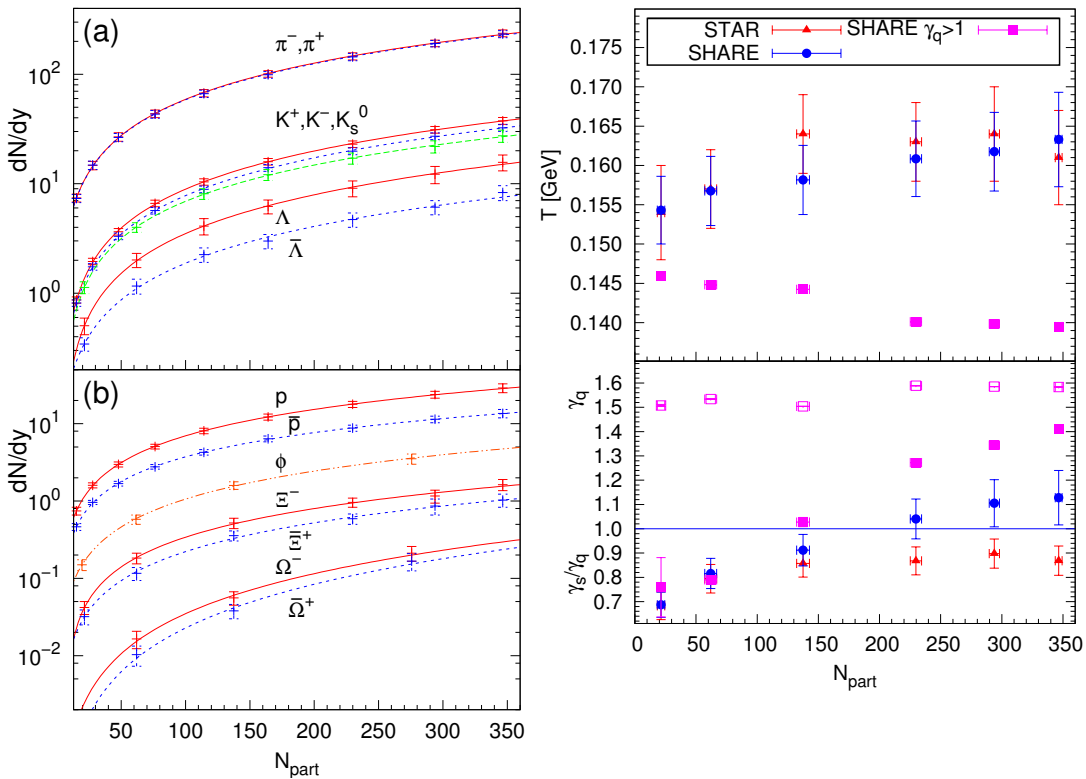


Fig. 1. Left panel: Particle yields as a function of number of participants with respective interpolating functions. Right panel: Top panel depicts chemical freeze-out temperature  $T$  as a function of the number of participants  $N_{\text{part}}$ . Triangles (red) are a copy of the results in [3], circles (blue) describe our fit of the same data set in semi-equilibrium model with  $\gamma_q \equiv 1$ ,  $\gamma_s \neq 1$  and squares (purple) are non-equilibrium model  $\gamma_i \neq 1$ ,  $i = q, s$ . Bottom panel shows the strangeness phase space occupancy compared to the light quark phase space occupancy ratio  $\gamma_s/\gamma_q$  for different models. Open squares (purple) show the values of  $\gamma_q$  for the non-equilibrium model.

It is interesting to note that the three neutral particle types have the same V-type charged particle decay and that there is an overlap in kinematic ID of the decay channels. For this reason, we fitted instead the yield of  $\Lambda + \bar{\Lambda} + 2 K_s^0$  which does not have this ambiguity. Considering the smallness of the required shift from more numerous  $K_s^0$  to  $\Lambda, \bar{\Lambda}$  we also fitted the ratio  $\bar{\Lambda}/\Lambda$ . These two data points replace the three raw yields and proved to be consistent with all other particle yields. Assuming that other particles fix the source volume, this procedure incurs minimal loss of data information.

We expected that our SHM fit with  $\gamma_q = 1$  should reproduce results of [3]. And indeed, we obtain compatible chemical freeze-out temperature  $T$  (top right panel of figure 1). However, we find that the strangeness phase space is strongly overpopulated, which is reflected by  $\gamma_s > 1$  (bottom right panel of figure 1) contrary to results published by STAR. After we found this discrepancy, we learned from the authors that in [3]  $\gamma_s < 1$  has been forced. This, of course, completely invalidates the conclusions of this work. This also resolves the myth that the yields of  $\phi \propto \gamma_s^2$  are inconsistent with SHM.

As a next step, we considered the chemical non-equilibrium with  $\gamma_i \neq 1$ ,  $i = q, s$ . This approach allows that aside of the strangeness phase space also the light  $q = u, d$  quark phase space, when observed on hadron side, to be out of equilibrium. To preserve the number of degrees of freedom, we fitted the pressure  $P \simeq 82 \text{ MeV}/\text{fm}^3$ , which is the value of critical hadronization pressure found in SHM fits to other experiments [7].

The chemical non-equilibrium SHM fit results in an even more pronounced strangeness yield enhancement,  $\gamma_s \rightarrow 1.5$  at central rapidity, an over-population of the light quark phase space  $\gamma_q \simeq 1.6$ , and a lower freeze-out temperature  $T \simeq 142 \text{ MeV}$ . Another important feature of this approach is that the parameter errors in the fit decreased dramatically compared to the semi-equilibrium model. In the right bottom panel of figure 1, the centrality dependence of these parameters is shown and the errors on  $\gamma_q$  and  $\gamma_s$  for chemical non-equilibrium are within the size of the symbols. We note that the SHM fits at all centralities have confidence level above 60%.

### 3. Hadronization conditions

In the non-equilibrium SHM approach there appears to be universal hadronization condition as function of centrality, which can be seen in figure 2 top two panels on the left. Apart from the constant pressure  $P \simeq 82 \text{ MeV}/\text{fm}^3$ , obtained at other RHIC energies [7], which value was used in non-equilibrium fits and found consistent with the new data, the entropy density at hadronization stays at constant universal value  $\sigma \simeq 3.3 \text{ fm}^{-3}$ . Similarly, the energy density is constant at  $\varepsilon \simeq 0.48 \text{ GeV}/\text{fm}^3$ . A universal value of statistical properties at hadronization as function of centrality [8]

supports the notion of a new phase of matter, the quark-gluon plasma undergoing a sudden break up transition to hadrons which free stream, as the chemical non-equilibrium model assumes. On the other hand, in the semi-equilibrium hadronization model, both entropy and energy density grow nearly proportional to the number of participants. There is no physical understanding of this behavior.

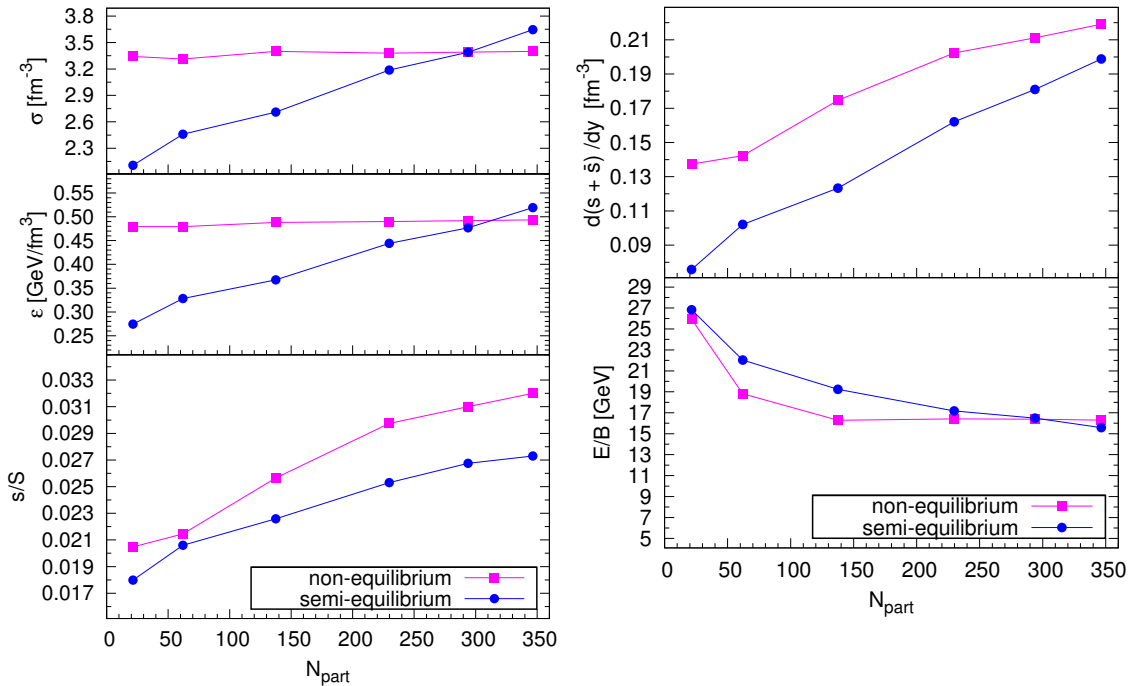


Fig. 2. Left panel: Going from top to bottom, centrality dependence of entropy density, energy density ( $\sigma$  and  $\epsilon$  respectively) and strangeness per entropy ratio  $s/S$ . Right panel: Going from top to bottom, centrality dependence of the strangeness rapidity density and energy per baryon.

We see, in the left bottom panel of figure 2, that in SHM non-equilibrium fit, the ratio of strangeness  $s$  to entropy  $S$  approaches for most central collisions the QGP expectation  $s/S = 0.031$ . The relative yield of strangeness is systematically smaller in the SHM semi-equilibrium fit. In the right panel of figure 2, we see at the top that strangeness density increases with centrality, in agreement with the expectation that the largest system can approach the QGP yield. Moreover, we see that in the SHM non-equilibrium model, we always find a much greater strangeness yield compared to the SHM semi-equilibrium. The effect is quite large at small centrality, where the entropy contents differ most, see the left top panel.

Another interesting result in non-equilibrium SHM is the constancy for  $N_{\text{part}} > 130$  of hadronization energy per baryon  $E/B$  seen in the bottom right panel of figure 2. Moreover, we find that the fraction of the available energy in the collision is universal among other systems and collision ener-

gies. We find,  $E/B_{\text{most central}} = 16.5 \text{ GeV} \simeq 0.25 \times 62.4 \text{ GeV} = \frac{1}{4}\sqrt{s_{NN}}$ . This result is the same as at the lower SPS energies. It says that the stopping of baryon number is 4 times more effective than the stopping of energy. Only at small centralities the stopping of energy and baryon number seems to converge to a common value resulting in  $E/B_{\text{most peripheral}} \rightarrow \frac{1}{2}\sqrt{s_{NN}}$ .

#### 4. Conclusions

We revisited the statistical hadronization fit of particle yields from Au–Au collisions at  $\sqrt{s_{NN}} = 62.4 \text{ GeV}$  recently updated with the yields of multi-strange hadrons. We obtained qualitatively different fit from the one published by the STAR Collaboration [3] which was done with the constraints  $\gamma_q = 1$  and  $\gamma_s < 1$  and which fails to resolve yields of all multistrange particles. They also show a very good confidence level at all centralities. Our results show that the hadron strangeness phase space is overpopulated  $\gamma_s > 1$  from semi-central  $N_{\text{part}} = 150$  to most central collisions  $N_{\text{part}} = 350$ . We allowed the light quark phase space,  $\gamma_q \neq 1$ , to be out of equilibrium as well and the new fit to the experimental data works for multistrange hadrons and has much smaller errors. However, given that  $K_s^0$  were inconsistent with the yields of charged hadrons, we did fit  $\Lambda + \bar{\Lambda} + 2K_s^0$ . We conclude that the non-equilibrium model shows appropriate and universal behavior of bulk physical properties (entropy, energy, strangeness and the stopped energy per baryon) as a function of centrality, *i.e.*, as a function of system size [7].

Laboratoire de Physique Théorique et Hautes Energies, LPTHE, at University Paris 6, is supported by CNRS as Unité Mixte de Recherche, UMR7589. This work was supported by the grant LC07048 and LA08015 from the Czech Ministry of Education and the grant from the U.S. Department of Energy, DE-FG02-04ER41318.

#### REFERENCES

- [1] G. Torrieri *et al.*, *Comput. Phys. Commun.* **167**, 229 (2005); **175**, 635 (2006).
- [2] F. Becattini, P. Castorina, A. Milov, H. Satz, *Eur. Phys. J.* **C66**, 377 (2010).
- [3] M.M. Aggarwal *et al.* [STAR Collaboration], *Phys. Rev.* **C83**, 024901 (2011).
- [4] B.I. Abelev *et al.* [STAR Collaboration], *Phys. Rev.* **C79**, 034909 (2009).
- [5] B.I. Abelev *et al.* [STAR Collaboration], *Phys. Rev.* **C79**, 064903 (2009).
- [6] M. Petran, J. Rafelski, *Phys. Rev.* **C82**, 011901 (2010).
- [7] J. Rafelski, J. Letessier, *J. Phys. G* **36**, 064017 (2009).
- [8] J. Rafelski, J. Letessier, G. Torrieri, *Phys. Rev.* **C72**, 024905 (2005).

## APPENDIX C

### UNIVERSAL HADRONIZATION CONDITION IN HEAVY ION COLLISIONS AT $\sqrt{s_{NN}} = 62$ GeV AND AT $\sqrt{s_{NN}} = 2.76$ TeV

M. Petran, J. Rafelski, Phys. Rev. C 88, 021901(R) (2013)  
DOI:10.1103/PhysRevC.88.021901

#### Summary

As the first data from Pb–Pb collisions at  $\sqrt{s_{NN}} = 2.76$  TeV from LHC has become available, we study the first results in four overlapping centrality bins. The first important result is that the non-equilibrium SHM describes all available data from LHC with high accuracy despite smaller data errors compared to RHIC. We estimate small baryochemical potential  $\mu_B \simeq 1.5$  MeV. Following the model-independent approach presented in Appendix A, we recall that  $p/\pi \propto \gamma_q$ . The experimental value of  $p/\pi$  is a natural outcome of a fit with  $\gamma_q \simeq 1.6$ . For the first time, the data is precise enough to exclude directly SHM variants that require light quarks ( $q = u, d$ ) in equilibrium, i.e.  $\gamma_q = 1$ . Moreover, our fits to the data show the same bulk physical properties of the hadronizing fireball as at RHIC 62, despite the 45 times higher energy and 4 times larger hadronization volume in most central collisions. In other words, we establish universal hadronization conditions of QGP in all contemporary heavy-ion collision experiments. This means that bulk critical pressure  $P$ , energy density  $\varepsilon$ , and entropy density  $\sigma$  are found to be in essence the same.

I was responsible for experimental data assembly, all calculations, evaluation of results and figures for this publication. I prepared the original draft of the publication, which was later revised based on fruitful comments of J. Rafelski and in response to the referee reports before it was accepted for publication. I estimate the article contains 70% of my original text.

## Universal hadronization condition in heavy ion collisions at $\sqrt{s_{NN}} = 62$ GeV and at $\sqrt{s_{NN}} = 2.76$ TeV

Michal Petráň and Johann Rafelski

*Department of Physics, The University of Arizona, Tucson, Arizona 85721, USA*

(Received 4 March 2013; revised manuscript received 25 April 2013; published 16 August 2013)

We obtain a detailed description of all available hadron multiplicity yields in central Pb-Pb collisions at the CERN Large Hadron Collider (LHC) measured in the rapidity interval  $|y| < 0.5$ . We find that the hadronization of the fireball at the LHC occurs at nearly identical intensive physical bulk conditions for all centralities similar to those already seen at the Brookhaven National Laboratory Relativistic Heavy Ion Collider.

DOI: [10.1103/PhysRevC.88.021901](https://doi.org/10.1103/PhysRevC.88.021901)

PACS number(s): 25.75.Nq, 24.10.Pa, 12.38.Mh

*Introduction and motivation.* We extend the successful description of central rapidity particle yields in a single freeze-out model [1,2] to characterize the physical properties of the hadronizing fireball. We consider, as an example, a supercooled quark-gluon plasma (QGP) disintegrating into hadrons, which can scatter but can preserve the stable particle abundance. Therefore, hadron particle multiplicities directly characterize the properties of the fireball. Final state hadrons are, thus, produced according to the accessible phase space with otherwise equal reaction strength. Accordingly, the particle yields are described by the chemical non-equilibrium statistical hadronization model (SHM) [3].

In this SHM implementation within the SHAREV2.2 program, the yields of particles are given the chemical freeze-out temperature  $T$  and overall normalization  $dV/dy$  (matching the presentation of the experimental data available as  $dN/dy$ ). We include phase-space occupancies  $\gamma_q, \gamma_s$  for light ( $q = u, d$ ) and strange  $s$  quark flavors, respectively, and we account for the small asymmetry between particles and antiparticles by fugacity factors  $\lambda_q, \lambda_s$  and the light quark asymmetry  $\lambda_{I3}$ . These parameters enter the distribution function as  $f_i(\varepsilon, T, \gamma_i, \lambda_i) = 1/(\gamma_i^{-1} \lambda_i^{\pm 1} e^{\varepsilon/T} + S)$  for flavor  $i$ , where  $S = -1, 0, +1$  for bosons, Boltzmann distribution, and fermions, respectively. We refer the reader to Sec. 2 of Ref. [4] for further discussion of the above parameters.

Our discussion addresses, evaluates, and compares the CERN Large Hadron Collider (LHC) Pb-Pb experimental results available at  $\sqrt{s_{NN}} = 2760$  GeV and the Brookhaven National Laboratory Relativistic Heavy Ion Collider (RHIC) Au-Au results available at  $\sqrt{s_{NN}} = 62.4$  GeV. We show that the chemical non-equilibrium SHM works at the LHC in the 0–20% centrality. This is so, since in the chemical non-equilibrium SHM approach, we allow the quark pair yield parameter  $\gamma_q > 1$  for light quarks; this is the key difference from the simpler equilibrium SHM. The rationale for  $\gamma_q \neq 1$  originates in the high entropy density of QGP at hadronization compared to the hadron phase space in which the color degree of freedom is frozen. In case the fireball disintegrates faster than the time necessary to equilibrate the yield of light quarks bound in hadrons, the value  $\gamma_q > 1$  must arise.

In case the fireball disintegrates faster than the time necessary to equilibrate the yield of light quarks bound in hadrons, either the value  $\gamma_q > 1$  arises, or one must consider

a dynamical volume growth as a path for absorbing the excess entropy of the QGP source. However, this second option requires a much longer life span of the particle source than supported by the two pion correlation data [5,6] and, thus, is experimentally excluded: The observed LHC total life span ( $\tau_f \simeq 10$  fm/c [6]) favors very fast, or sudden, hadronization [7,8]. In this situation, the chemical non-equilibrium approach must also be applied to the light quark abundance, which introduces the light quark phase-space occupancy  $\gamma_q$ . This proposal, made for the high-energy CERN Super Proton Synchrotron (SPS) data [9,10], also helped to improve the understanding of RHIC200 hadron rapidity yield results [11] and allowed a consistent interpretation of such data across the full energy range at the SPS and RHIC200 [12].

The equilibrium SHM fits, which arbitrarily set  $\gamma_q = 1$  [13, 14], describe hadron yields at the LHC with relatively large total  $\chi^2$ . This chemical equilibrium SHM disagrees at the LHC across many particle yields, but the greatest issue is the “proton anomaly,” which makes it impossible to fit the  $p/\pi = 0.046 \pm 0.003$  ratio [14] along with the multistrange baryons  $\Xi$  and  $\Omega$ .

We will show that intensive QGP bulk properties are nearly exactly equal to those found at the RHIC for all four collision centralities we analyze. We will discuss in depth the main extensive bulk property difference we find, which is the entropy  $dS/dy$  growth with energy and centrality.

*Fit to most central collisions.* Within the chemical non-equilibrium SHM, we have, by allowing for baryon-antibaryon asymmetry, seven independent statistical model parameters reduced by two constraints: (a) The isospin fugacity factor  $\lambda_{I3}$  is constrained by imposing the charge per baryon ratio ( $\langle Q \rangle - \langle \bar{Q} \rangle$ )/( $\langle B \rangle - \langle \bar{B} \rangle$ )  $\simeq 0.38$ , present in the initial nuclear matter state at the initial instant of the collision; (b) for each value of  $\lambda_q$ , strangeness fugacity  $\lambda_s$  is evaluated by imposing the strangeness conservation requirement  $\langle s \rangle - \langle \bar{s} \rangle \simeq 0$ . By considering the particle-antiparticle symmetry at the LHC, the four key parameters are the hadronization volume  $dV/dy$ , the temperature  $T$ , and the two phase-space occupancies  $\gamma_q$  and  $\gamma_s$ . The seventh parameter is light quark fugacity  $\lambda_q$ .

We use, as input to our fit, the hadron yield data in the 0–20% centrality bin as presented in Ref. [15] where a fit to this data set for the case of chemical equilibrium ( $\gamma_s = \gamma_q = 1$ ) is shown. For comparison and demonstration

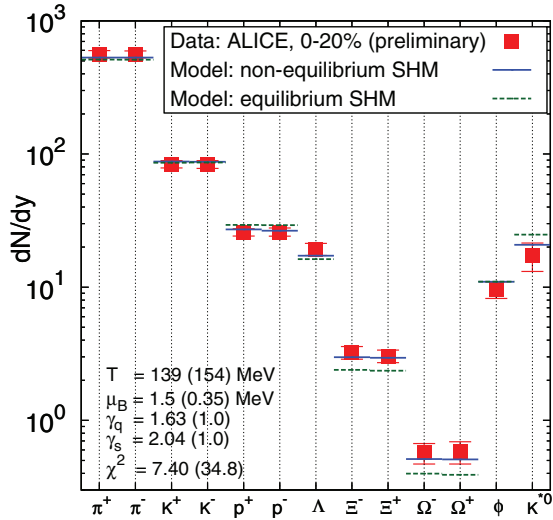


FIG. 1. (Color online) The non-equilibrium SHM fit is indicated by (blue) solid horizontal lines overlaying for all the LHC-ALICE (preliminary) data available in a 0–20% centrality bin (red squares). The chemical equilibrium fit is indicated by (green) dashed lines with model parameters presented in parentheses.

of method compatibility, the chemical equilibrium model fit (dashed lines in Fig. 1) is shown with a large  $\chi^2 = 34.8$ . In both approaches, we fit the same data, the decrease in  $\chi^2$  by a factor of nearly 5 is due to chemical non-equilibrium, i.e.,  $\gamma_q \neq 1$ ,  $\gamma_s \neq 1$ . We determine the best light quark fugacity factor  $\lambda_q = 1.00359$ , which corresponds to the baryochemical potential  $\mu_B \simeq 1.5$  MeV, and we apply strangeness and charge per baryon conservation by fitting them as two additional data points. The result of our 0–20% centrality bin fit is shown in Fig. 1 and in the upper section of the third column of Table I. We compare our present results to our recent analysis [16] of Au-Au collisions at  $\sqrt{s_{NN}} = 62.4$  GeV at RHIC62, shown in the second column of Table I.

TABLE I. The top section shows chemical non-equilibrium SHM fit parameters  $dV/dy$ ,  $T$ ,  $\gamma_q$ ,  $\gamma_s$ , and  $\chi_{\text{total}}^2$  with number of data less number of parameters (ndf) obtained in each centrality bin. Errors are a fit-stability estimate obtained with a  $K^\pm$  yield shifted within the experimental error; the underlying statistical fit error is negligible. The bottom section presents fireball bulk properties in each bin: energy density  $\varepsilon$ , pressure  $P$ , entropy density  $\sigma$ , strangeness per entropy content  $s/S$ , and entropy at LHC2760 compared to RHIC62  $S_{\text{LHC}}/S_{\text{RHIC}}$ . The centrality that defines number of participants  $N_{\text{part}}$  values is adopted from Ref. [20].

	RHIC62		LHC2760		
Centrality	0–5%	0–20%	20–40%	40–60%	60–80%
$\langle N_{\text{part}} \rangle$	346	308	157	68.8	22.6
$dV/dy$ (fm <sup>3</sup> )	853	$2455 \pm 146$	$1169 \pm 9$	$406 \pm 3$	$102 \pm 7$
$T$ (MeV)	139.5	$138.6 \pm 1.1$	$137.6 \pm 0.03$	$140.5 \pm 0.04$	$143.2 \pm 0.08$
$\gamma_q$	1.58	$1.627 \pm 0.007$	$1.633 \pm 0.0002$	$1.616 \pm 0.003$	$1.60 \pm 0.02$
$\gamma_s$	2.24	$2.04 \pm 0.04$	$2.01 \pm 0.12$	$1.83 \pm 0.08$	$1.70 \pm 0.09$
$\chi_{\text{total}}^2/\text{ndf}$	0.38/5	7.40/8	2.93/5	3.58/5	5.43/5
$\varepsilon$ (GeV/fm <sup>3</sup> )	0.493	$0.466 \pm 0.018$	$0.441 \pm 0.012$	$0.488 \pm 0.010$	$0.536 \pm 0.025$
$P$ (MeV/fm <sup>3</sup> )	82.0	$79.1 \pm 2.8$	$75.5 \pm 1.5$	$82.2 \pm 1.3$	$90.2 \pm 4.0$
$\sigma$ (fm <sup>-3</sup> )	3.40	$3.23 \pm 0.11$	$3.07 \pm 0.07$	$3.36 \pm 0.06$	$3.65 \pm 0.13$
$s/S$	0.0322	$0.0296 \pm 0.0002$	$0.0289 \pm 0.0014$	$0.0277 \pm 0.0009$	$0.0267 \pm 0.0011$
$S_{\text{LHC}}/S_{\text{RHIC}}$		3.05	2.66	2.18	1.52

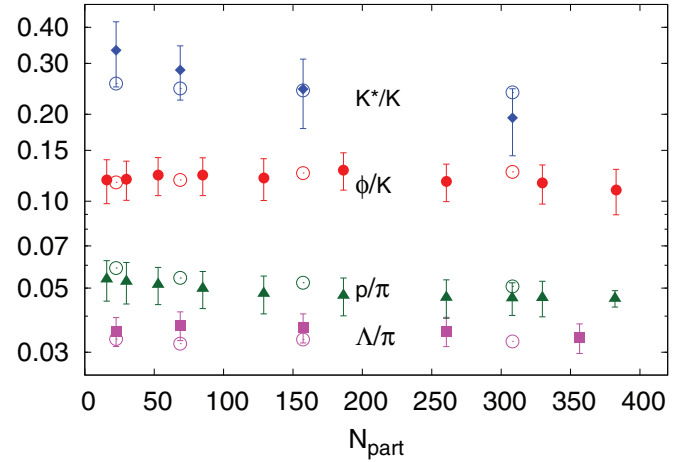


FIG. 2. (Color online) Experimental data (full symbols) and model predicted (open circles) for particle ratios as a function of centrality. See text for discussion of data and results.

*More peripheral centralities.* We extend our study to more peripheral collisions at the LHC by using a much smaller data set, complemented by two assumptions as follows:

- (i) We consider the three ratios  $K^{*0}/K^-$ ,  $\Lambda/\pi \equiv 2\Lambda/(\pi^- + \pi^+)$ , and  $\phi/K^-$  as presented in Ref. [17] and which we show in Fig. 2 with full symbols. We fit these ratios in three centrality bins, 20–40%, 40–60%, and 60–80% in which  $K^*/K$  and  $\Lambda/\pi$  have experimental data points. We take the average of two neighboring  $\phi/K$  data points to use this ratio as input to our fit in the intermediate centrality. This is consistent with the claim that  $\phi/K$  is constant over all centralities and has been claimed independent of centrality in Ref. [17].
- (ii) To obtain overall normalization, we complement the ratios with charged particle rapidity density  $dN_{\text{ch}}/dy$ . Based on our fit of 0–20% centrality data, we see that

the ratio of charged particle rapidity to pseudorapidity density is  $(dN_{\text{ch}}/dy)/(dN_{\text{ch}}/d\eta) = 1.115$ . We multiply data from Ref. [18] by this factor and use the resulting  $dN_{\text{ch}}/dy$  as an additional data point that determines the value of fireball volume  $dV/dy$ . The input multiplicity data is presented in Fig. 3.

- (iii) We include the yields of  $\pi^\pm$ ,  $K^\pm$ , and  $p^\pm$  as presented in Ref. [19] and shown in Fig. 3. Similar to the  $\phi/K$  ratio, we use the averages of yields in two neighboring centrality bins as input.

We fit the three centrality bins of the LHC2760 data by using the eight data points and the two conservation laws, which fix  $\lambda_s$  and  $\lambda_{13}$ . Therefore, we have five degrees of freedom as seen in Table I in the fourth through sixth columns. All studied centralities show reasonable  $\chi^2/\text{ndf} \leq 1.1$ . We find remarkably similar statistical parameters for all four LHC centrality bins.

We compare the outcome of the fit by showing the three input ratios  $K^{*0}/K^-$ ,  $\Lambda/\pi$ , and  $\phi/K^-$  and  $p/\pi$  in Fig. 2. All data are well fitted, including both yields of  $p$  and  $\pi$  from Ref. [19], which implies good description of their ratio  $p/\pi$  evaluated from the individual yields.

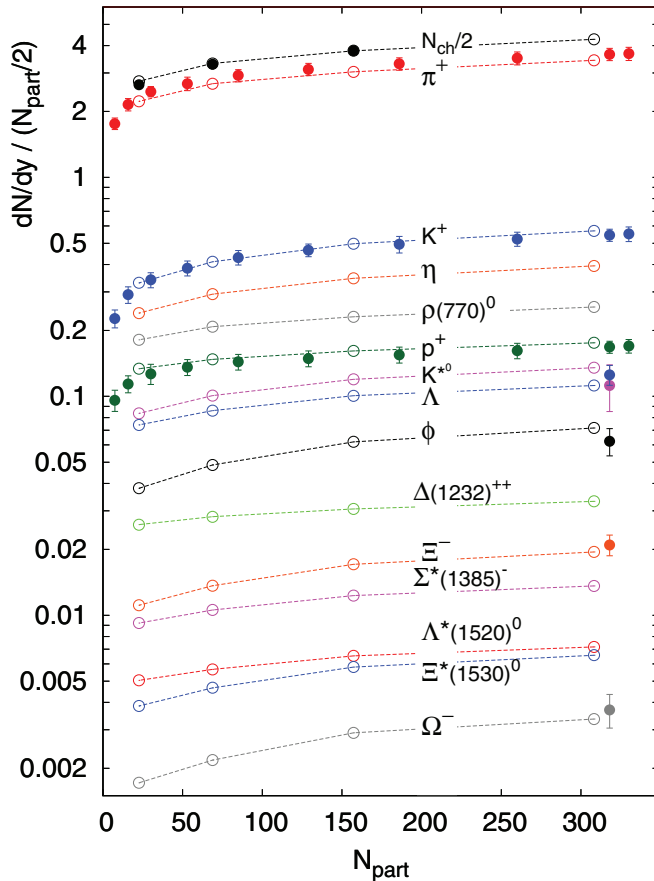


FIG. 3. (Color online) Predicted particle yields per participant pair as a function of centrality. Open symbols represent our model predictions; lines guide the eye. We show experimental data for the 0–20% bin as full symbols with an offset.

The predicted particle yields normalized by  $N_{\text{part}}/2$  are shown in Fig. 3 where, in consideration of particle-antiparticle symmetry, only one of the isospin multiplets is shown. The  $\pi$ ,  $K$ , and  $p$  yields are fitted values, whereas, the other particle yields are predictions. In Fig. 3 on the right boundary, we indicate the experimental input for the 0–20% bin with an offset to assure visibility of the small differences between fit and experimental data. We show the input multiplicity  $(dN_{\text{ch}}/dy)/(N_{\text{part}}/2)$  and fit result in Fig. 3. Both are exactly overlapping for the three peripheral bins since this is the most precise input data.

*Hadronization conditions.* Despite a change by a factor of 45 in the reaction energy by comparing the RHIC and the LHC and the wide range of centrality, the only quantity among the statistical parameters shown in Table I that significantly changes is  $dV/dy$ . This suggests that we should look closer at the intensive bulk physical properties of the fireball: The emitted hadrons not only carry the above-discussed charge, baryon number, or strangeness away from the fireball, but also, e.g., carry the thermal energy  $dE/dy$  obtained by summing the energy content of all produced particles, observed and predicted.

The bulk thermal energy density at hadronization  $\varepsilon$  defined by  $\varepsilon \equiv (dE/dy)/(dV/dy)$  is of direct interest. Similarly, we evaluate the entropy  $dS/dy$ , pressure  $P$ , and total yield of strangeness  $ds/dy \equiv d(q_s + \bar{q}_s)/2 dy$ . These properties of the fireball at hadronization are shown in the bottom section of Table I where, in the first column, for simplicity, we omit the symbol  $d/dy$ .

As one can see by comparing the second and third columns of Table I, the intensive properties of the RHIC62 fireball at hadronization, i.e.,  $\varepsilon$ ,  $P$ ,  $\sigma$ , and  $s/S$ , are practically identical to the here evaluated case of LHC2760, and this continues across all considered centralities as seen in the fourth through sixth columns of Table I. We show a comparison of  $\varepsilon$ ,  $P$  as a function of centrality between the LHC (solid symbols) and the RHIC (open symbols) in the bottom part of Fig. 4. The difference between the LHC and the RHIC can easily be attributed to the fit uncertainties since the intensive quantities are proportional to a high power of statistical parameters.

Hadronization volume  $dV/dy$  does not characterize the early stage of a collision; this information is available in the entropy content at hadronization  $dS/dy \propto dV/dy$ , which presents a more accurate view of the prehadronization processes that created the fireball. For an ideally flowing and expanding QGP, most of the observed entropy yield  $dS/dy$  of a fireball is created early in the collision. In the top panel of Fig. 4, we see that, at the LHC,  $dS/dy \propto N_{\text{part}}^{-1.173}$ , the rise is faster than linear. For comparison, note that, at the RHIC, the entropy yield rises almost linearly with  $N_{\text{part}}$ . The last row of Table I shows the enhancement of entropy at the LHC compared to the RHIC  $S_{\text{LHC}}/S_{\text{RHIC}}$ . The enhancement decreases as a function of centrality from  $\sim 3$  to  $\sim 1.5$ , which implies an additional entropy production mechanism proportional to centrality at the LHC.

Strangeness per entropy  $s/S \equiv (ds/dy)/(dS/dy)$  is of particular interest in the source fireball since both entropy and

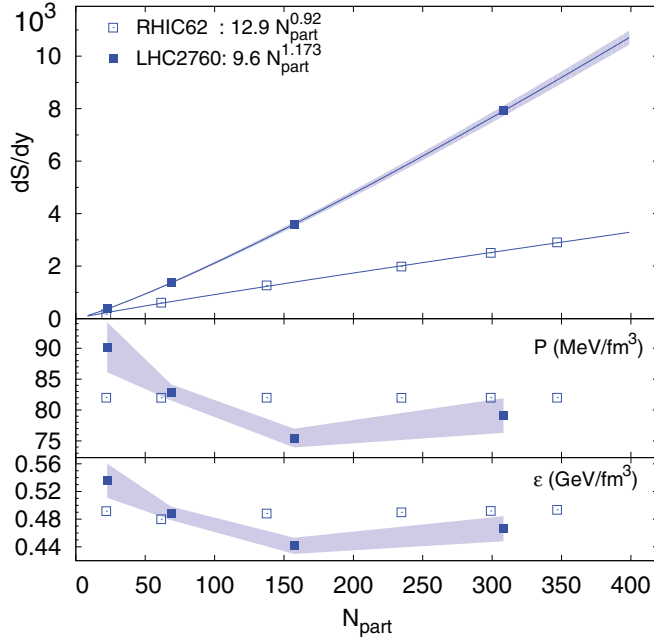


FIG. 4. (Color online) The top panel shows the entropy content of the fireball at the LHC (full symbols) and the RHIC (open symbols) as a function of centrality. The bottom part shows pressure  $P$  and energy density  $\epsilon$  at hadronization with the same symbols for the LHC and the RHIC as in the top panel, for values, see Table I.

strangeness yields are nearly preserved in the hadronization process, but the production of strangeness occurs after most of the entropy is created. Up to a well-studied proportionality factor,  $s/S$  is the ratio of strange quark abundance to total quark and gluon abundance, which makes up the entropy in the bulk. Therefore,  $s/S$  measures the degree of chemical equilibration in the QGP. We observe a constant value of  $s/S \simeq 0.03$  (see Table I), which is in agreement with theoretical expectations for the strange quark mass  $m_s \simeq 100$  MeV [21].

*Comments and conclusions.* The LHC2760 experimental environment has opened a new opportunity to investigate the hadron production mechanisms in detail. Precise particle tracking near the interaction vertex in the ALICE removes the need for off-line corrections of weak interaction decays, and at the same time, vertex tracking enhances the efficiency of track identification by considerably increasing the precision of the particle yield measurement [13,15]. All LHC experimental results we considered were obtained in this way by the ALICE experiment for Pb-Pb collisions at  $\sqrt{s_{NN}} = 2.76$  TeV, limited to the central unit of rapidity interval  $-0.5 < y < 0.5$ .

In this new experimental environment, we show the necessity to introduce the final-state hadron chemical non-equilibrium, which well describes all experimental results obtained in the Pb-Pb collisions at  $\sqrt{s_{NN}} = 2.76$  TeV from the LHC. As Fig. 1 shows,  $\gamma_q \simeq 1.6$  (non-equilibrium of light quarks) allows for describing the ratio  $p/\pi = 0.046 \pm 0.003$  [13,14] together with yields of multistrange baryons  $\Xi$  and  $\Omega$ .

Another approach to describe the data that include the “anomalous” proton yield at the LHC involves chemical

equilibrium hadronization at relatively high  $T$  followed by hadron interactions [22,23]. We note the chemical equilibrium SHM yields at hadronization in Fig. 1, which overpredicts proton yield and, at the same time, underpredicts both  $\Xi$  and  $\Omega$ . Any alternate data explanation must come to terms with this situation, thus, it must deplete protons and enhance both  $\Xi$  and  $\Omega$ , and at the same time, the ratio  $p/\pi$  must remain practically constant. This is difficult, as we now discuss, by looking closer at the results of Refs. [22,23]:

- (i) In Fig. 1 of Ref. [22], we see that if and when equilibrium style hadronization occurs and leads to high  $T$ , the necessary posthadronization reactions deplete protons and  $\Xi$  and enhance  $\Omega$ . This means that the already too small yield of  $\Xi$  is further depleted and disagrees gravely with experiment.
- (ii) The measured  $p/\pi$  ratio in the 0–5% centrality bin can be made consistent with posthadronization proton-antiproton annihilation [23]. This fine-tunes the model parameters and, as a result, for the 20–30% centrality bin, Ref. [23] reports increased  $p/\pi = 0.058$ .
- (iii) For peripheral collisions, the model predicts yet less annihilation and, thus, a  $p/\pi$  ratio that approaches the equilibrium SHM value, which is twice as large as experiment. Although the experiment for  $p/\pi$  seen in Fig. 2 is a constant for all centralities, Ref. [23], thus, predicts a rapid variation by about factor of 2.

These arguments lead to the conclusion that posthadronization interactions are inconsistent with the experimental data of baryon yields at the LHC. On the other hand, our chemical non-equilibrium SHM at the LHC produces a high confidence level fit  $\chi^2/\text{ndf} = 7.4/8 < 1$ . Prior SPS and RHIC data analyses [11,12,16] have already strongly favored a chemical non-equilibrium variant of SHM. The implied sudden hadronization picture is perfectly consistent with the anisotropic flow of quarks that lead to the final hadron momentum distribution azimuthal asymmetry (see, e.g., Ref. [24]).

Moreover, we find that the LHC and RHIC results are quite consistent in our approach, and we obtain the same hadronization condition  $(\epsilon, P, \sigma)$  at the LHC as previously reported at the RHIC, which, in turn, agrees with high-energy SPS [12]. The energy density of hadronizing matter is  $0.50 \pm 0.05$  GeV/fm<sup>3</sup>, which is about 3.3 times the energy density of nuclear matter, and the pressure is  $P = 82 \pm 8$  MeV/fm<sup>3</sup> =  $(158 \pm 4 \text{ MeV})^4$  as seen in the bottom part of Fig. 4, and which has been proposed in Ref. [25]. The bottom part of Table I also shows that the entropy density is constant:  $\sigma = 3.35 \pm 0.30$  fm<sup>-3</sup> for both experiments and all centralities.

These typical QGP properties, which include  $s/S \rightarrow 0.03$ , mean that, at the LHC, the source of hadrons is a chemically equilibrated strangeness saturated QGP fireball. Furthermore, the universal hadronization condition assures that hadron production cannot be viewed anymore as being due to successive particle emission or to proceed via the equilibrated hadron gas phase.

This work was supported by a grant from the US Department of Energy, Grant No. DE-FG02-04ER41318.

- [1] M. Rybczyński, W. Florkowski, and W. Broniowski, *Phys. Rev. C* **85**, 054907 (2012).
- [2] W. Broniowski and W. Florkowski, *Phys. Rev. Lett.* **87**, 272302 (2001).
- [3] G. Torrieri, S. Steinke, W. Broniowski, W. Florkowski, J. Letessier, and J. Rafelski, *Comput. Phys. Commun.* **167**, 229 (2005); G. Torrieri, S. Jeon, J. Letessier, and J. Rafelski, *ibid.* **175**, 635 (2006).
- [4] J. Rafelski, *Eur. Phys. J. Spec. Top.* **155**, 139 (2008).
- [5] L. P. Csernai, M. I. Gorenstein, L. L. Jenkovszky, I. Lovas, and V. K. Magas, *Phys. Lett. B* **551**, 121 (2003).
- [6] K. Aamodt (ALICE Collaboration) *et al.*, *Phys. Lett. B* **696**, 328 (2011).
- [7] L. P. Csernai and I. N. Mishustin, *Phys. Rev. Lett.* **74**, 5005 (1995).
- [8] J. Rafelski and J. Letessier, *Phys. Rev. Lett.* **85**, 4695 (2000).
- [9] J. Letessier and J. Rafelski, *Phys. Rev. C* **59**, 947 (1999).
- [10] J. Letessier and J. Rafelski, *Int. J. Mod. Phys. E* **09**, 107 (2000).
- [11] J. Rafelski, J. Letessier, and G. Torrieri, *Phys. Rev. C* **72**, 024905 (2005).
- [12] J. Letessier and J. Rafelski, *Eur. Phys. J. A* **35**, 221 (2008).
- [13] B. Abelev (ALICE Collaboration), Proceedings from Physics of the LHC 2012 Conference (unpublished).
- [14] B. Abelev (ALICE Collaboration) *et al.*, *Phys. Rev. Lett.* **109**, 252301 (2012).
- [15] M. Ivanov (ALICE Collaboration), *Nucl. Phys. A* **904–905**, 162c (2013).
- [16] M. Petran, J. Letessier, V. Petracek, and J. Rafelski, *Acta Phys. Pol. B Proc. Suppl.* **5**, 255 (2012).
- [17] S. Singha (ALICE Collaboration), *Nucl. Phys. A* **904–905**, 539c (2013).
- [18] K. Aamodt (ALICE Collaboration) *et al.*, *Phys. Rev. Lett.* **106**, 032301 (2011).
- [19] B. Abelev (ALICE Collaboration) *et al.*, arXiv:1303.0737.
- [20] B. Abelev (ALICE Collaboration) *et al.*, arXiv:1301.4361.
- [21] I. Kuznetsova and J. Rafelski, *Eur. Phys. J. C* **51**, 113 (2007).
- [22] J. Steinheimer, J. Aichelin, and M. Bleicher, *Phys. Rev. Lett.* **110**, 042501 (2013).
- [23] I. A. Karpenko, Y. M. Sinyukov, and K. Werner, *Phys. Rev. C* **87**, 024914 (2013).
- [24] U. W. Heinz and R. Snellings, *Annu. Rev. Nucl. Part. Sci.* **63**, 123 (2013).
- [25] J. Rafelski and J. Letessier, *J. Phys. G* **36**, 064017 (2009).

## APPENDIX D

### HADRON PRODUCTION AND QUARK–GLUON PLASMA HADRONIZATION IN Pb–Pb COLLISIONS AT $\sqrt{s_{NN}} = 2.76$ TeV

M. Petran, J. Letessier, V. Petracek, J. Rafelski, Phys. Rev. C 88, 034907 (2013)  
DOI:10.1103/PhysRevC.88.034907

#### Summary

This paper extends the analysis of hadron production data in Pb–Pb collisions at  $\sqrt{s_{NN}} = 2.76$  TeV obtained by the ALICE experiment at LHC. We include multistrange baryons  $\Xi$  and  $\Omega$  to the data set. Using interpolation of experimental results, we present a finer centrality binning of all available particle yields with non-equilibrium SHM. For comparison purposes, the semi-equilibrium and equilibrium SHM fits are also shown. We confirm the conclusion of Appendix C, that  $\gamma_q > 1$  is necessary in order to describe all the measured yields within the experimental uncertainty.

We address in more detail the  $p/\pi$  ratio, which is naturally fitted within our chemical non-equilibrium SHM. A mechanism incorporating posthadronization hadron interactions, namely proton-antiproton annihilation has been proposed (see publication references [30,42–46]). We show that posthadronization interactions alter yields of all other particles and while describing the proton yield, they create large discrepancy in the multistrange baryon yields. Moreover, these interactions produce centrality dependent  $p/\pi$ , whereas the experimental  $p/\pi$  ratio is nearly constant as a function of centrality.

We further report that at LHC, the expanding QGP reaches a steady equilibrium

level of both light and strange quark flavors. This follows given the constant light quark phase space occupancy  $\gamma_q \simeq 1.6$  for all centralities and the strangeness phase space occupancy  $\gamma_s$ , which even for relatively small systems created in peripheral collisions has a value of  $\gamma_s \simeq 2$ . This  $\gamma_s$  value is 20% below expectation based on the RHIC data analysis (reference [41] of the publication). This is why we found in Appendix E  $\gamma_s^{QGP} \sim 0.8$ . This also contributes to lower than expected strangeness over entropy ratio  $s/S \simeq 0.030$ . We also report chemical freeze-out temperature  $T = 138$  MeV, 2 MeV lower compared to similar centrality at RHIC. We interpret this as a supercooling of the more dynamically expanding QGP fireball. However, the difference is within error of RHIC results.

Some of the data we used in the analysis were still preliminary. During the review process of this paper, final yields of  $K_S^0$ ,  $\Lambda$ ,  $\Xi$  and  $\Omega$  were published (references [61,62] of the publication). We have confirmed (see section IV.F: Update of our publication) that the final centrality dependent data is compatible with all our results in the paper.

Preparation of this article took a considerable amount of time. I was responsible for the data collection and calculations, which were checked by my collaborator, J. Letessier. I analyzed the results and prepared all figures for publication and an original manuscript draft. The text was then extended several times by all co-authors including added results before and one revision during the referee review process. The published version contains about 70% of my original text.

# Hadron production and quark-gluon plasma hadronization in Pb-Pb collisions at $\sqrt{s_{NN}} = 2.76$ TeV

Michal Petráň,<sup>1,2</sup> Jean Letessier,<sup>3</sup> Vojtěch Petráček,<sup>2</sup> and Johann Rafelski<sup>1,4</sup>

<sup>1</sup>*Department of Physics, The University of Arizona, Tucson, Arizona 85721, USA*

<sup>2</sup>*Czech Technical University in Prague, Faculty of Nuclear Sciences and Physical Engineering*

<sup>3</sup>*Laboratoire de Physique Théorique et Hautes Energies, Université Paris 6, Paris 75005, France*

<sup>4</sup>*Theory Division of Physics Department, CERN, CH-1211 Geneva 23, Switzerland*

(Received 8 March 2013; revised manuscript received 16 August 2013; published 20 September 2013)

We show that all central rapidity hadron yields measured in Pb-Pb collisions at  $\sqrt{s_{NN}} = 2.76$  TeV are well described by the chemical nonequilibrium statistical hadronization model (SHM), where the chemically equilibrated quark-gluon plasma source breaks up directly into hadrons. SHM parameters are obtained as a function of centrality of colliding ions, and we compare CERN Large Hadron Collider (LHC) results with Brookhaven National Laboratory Relativistic Heavy Ion Collider (RHIC) results. We predict yields of unobserved hadrons and address antimatter production. The physical properties of the quark-gluon plasma fireball particle source show universality of hadronization conditions at LHC and RHIC.

DOI: [10.1103/PhysRevC.88.034907](https://doi.org/10.1103/PhysRevC.88.034907)

PACS number(s): 25.75.Nq, 24.10.Pa, 12.38.Mh

## I. INTRODUCTION AND MOTIVATION

Our interest in the multiparticle production process in ultra-relativistic heavy-ion collisions originates in the understanding that the transverse momentum integrated rapidity distributions are insensitive to the very difficult to fully characterize transverse evolution dynamics of the hot fireball source [1]. A successful description of central rapidity particle yields in a single freeze-out model [2,3] are used here to characterize the properties of the hadronizing quark-gluon-plasma (QGP) fireball. The QGP breakup, as modeled within the statistical hadronization model (SHM), assumes equal reaction strength in all hadron particle production channels. Therefore, the phase-space volume determines the hadron yields. SHM has been described extensively before and we refer the reader to SHARE manuals [4] for both further theoretical details and numerical methods. Here we apply SHM to study particle production in Pb-Pb collisions at  $\sqrt{s_{NN}} = 2.76$  TeV (LHC2760), a new energy domain an order of magnitude higher than previously explored in Au-Au collisions at  $\sqrt{s_{NN}} = 200$  GeV (RHIC200).

We begin by demonstrating that the chemical nonequilibrium SHM variant describes the experimental LHC-ion data with high accuracy. This finding disagrees with claims that SHM alone does not describe the particle multiplicity data obtained in relativistic heavy-ion collisions at LHC [5,6]. In the chemical nonequilibrium SHM approach, we allow quark pair yield parameter  $\gamma_q$  for light quarks, a feature we presented as a necessary model refinement for the past 15 yr [7–9]. We demonstrate the general model validity in our numerical approach by showing correspondence of chemical equilibrium SHM results with other fits to the LHC data. This demonstrates that several SHM programs, which had years to mature and evolve, are compatible in their data tables of hadronic resonance mass spectra and decay patterns. However, only our extended SHARE code includes advanced features, such as chemical nonequilibrium of all quark yields, differentiation of up and down quarks, evaluation of fireball physical properties, and the capability to constrain the fit by imposing physical properties on the particle source.

To demonstrate that our chemical nonequilibrium SHM works at LHC, we show in the left-hand side of Fig. 1 our fit to the 0%–20% centrality data, shown in the second column of Table I, recently presented and studied by the experiment ALICE [5,6]. Only in this one instance we consider the relatively wide centrality trigger of 0%–20% to compare directly with the earlier analysis effort. As can be seen in the left-hand side of Fig. 1, our nonequilibrium SHM approach describes these data with  $\chi^2/\text{ndf} = 9.5/9 \simeq 1$ . We see in the Fig. 1(a) inset that the chemical equilibrium SHM works poorly,  $\chi^2/\text{ndf} = 64/11 \simeq 6$ , which is the same finding and conclusion as in Refs. [5,6].

While the equilibrium SHM disagrees at LHC across many particle yields the most discussed data point is the  $p/\pi = 0.046 \pm 0.003$  ratio [6], a point we study in more detail in Sec. III B. Our work shows that the inability of the equilibrium SHM alone to fit the experimental value of the  $p/\pi$  ratio does not mean that all variants of SHM do not describe particle production in heavy-ion collisions at LHC. One of the key findings of this work is that the chemical nonequilibrium SHM variant without any additional posthadronization evolution provides an excellent description of all data. We also argue that the present-day hybrid models, that is, models that combine SHM results with posthadronization hadron yield evolution, need to address key features of the data such as quasiconstancy of the  $p/\pi$  ratio as a function of centrality of the heavy-ion collision and the abundance of multistrange baryons.

The chemical nonequilibrium results for the 5%–10% centrality bin (containing interpolated data, open symbols) is shown for comparison in the right-hand panel of Fig. 1. The fit has the same set of particles as the 0%–20% centrality bin; however, we must fit here three ratios for which data are directly (or by interpolation) available, and we use a more recent set of proton, pion, and kaon data. Definition of the model and some technical details about how we obtain results seen in Fig. 1 follow below; the fitted data are shown in the fourth column of Table I. The Fig. 1(c) shows the SHM parameters and  $\chi^2$  for all three variants. Comparing the SHM parameters on left- and right-hand sides of Fig. 1 we see a large

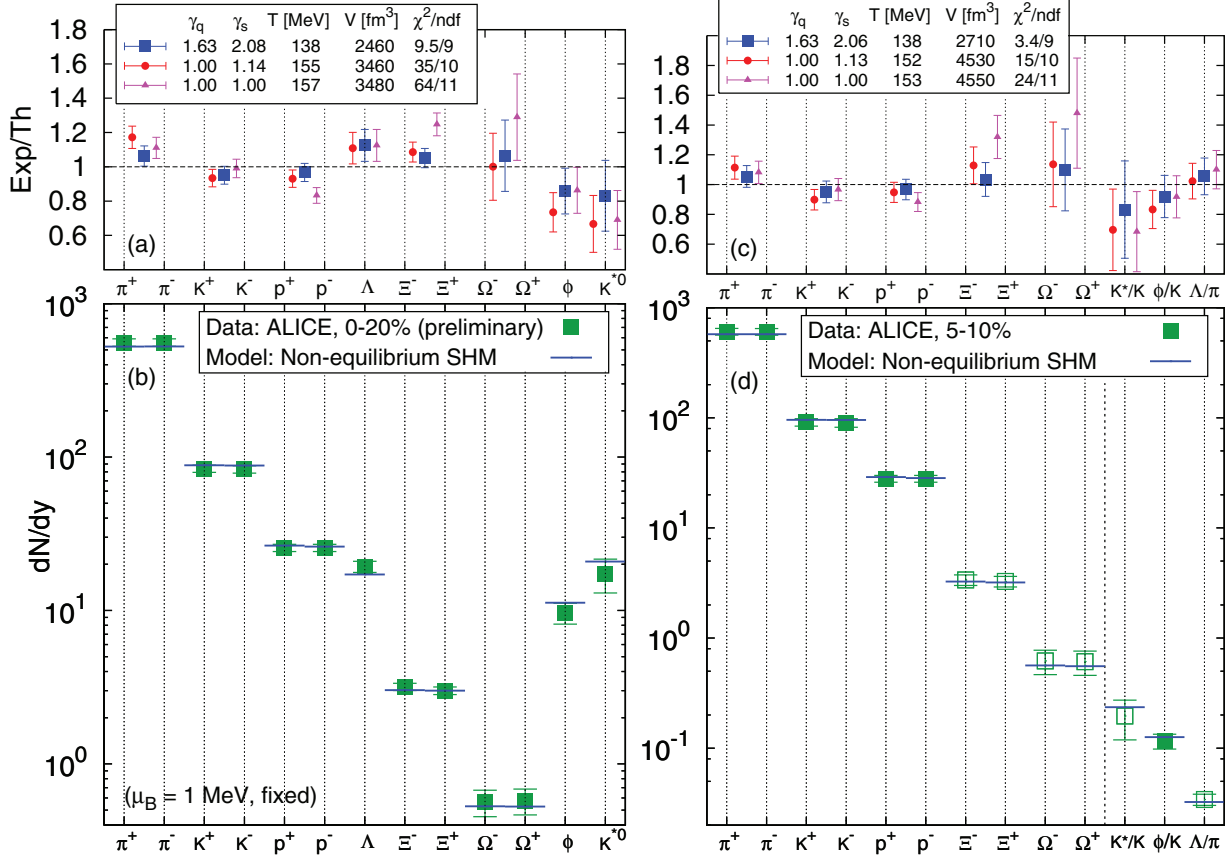


FIG. 1. (Color online) SHM fit to experimental data measured by the ALICE experiment in Pb-Pb collisions at  $\sqrt{s_{NN}} = 2.76$  TeV for 0%–20% centrality [panels (a) and (b) on the left-hand side] and for 1/4 of this range, 5%–10% [panels (c) and (d) on the right-hand side]. The input set of particle types is the same as can be seen in particle listing on the ordinates of panels (b) and (d); in panel (d) also particle yield ratios are used. In the panels (b) and (d) comparison of SHM chemical nonequilibrium fit (horizontal line) with data is shown. The experimental data are shown as solid squares; in the panel (d) the interpolated experimental data are shown with open symbols (see Appendix for details). Panels (a) and (c) show the ratio of model values to experimental data for the three SHM variants and present the key parameter values for chemical nonequilibrium (solid squares), chemical semiequilibrium (solid circles), and chemical equilibrium (solid triangles). For readability, antiparticles are omitted in panels (a) and (c).

change in  $V$  expected for different centralities. We see that use of finer centrality binning and more mature data sample reduces  $\chi^2$  for all SHM variants.

As Fig. 1 shows and we discuss below in detail, the chemical nonequilibrium SHM works perfectly at LHC, resulting in a high confidence level. This could be predicted considering prior CERN Super Proton Synchrotron (SPS) and RHIC data analyses [10–12], which strongly favor chemical nonequilibrium variant of SHM. Moreover, the chemical nonequilibrium SHM has a dynamical physical foundation in sudden breakup of a QGP fireball, we are not aware of a dynamical origin of the simple chemical equilibrium SHM because no dynamical computation of relativistic heavy-ion scattering achieves the chemical equilibrium condition without introduction of an unknown particle, cross sections, etc. Furthermore, as we discuss in Sec. III C, we obtain hadronization universality across a wide collision energy range: Comparing RHIC62 with LHC2760 we show that the fireball source of particles is nearly identical and consistent with chemically equilibrated QGP fireball. Given this result, the chemical nonequilibrium

SHM variant is validated across a wide energy range, while the chemical equilibrium SHM [13–18] is invalidated by the LHC data and this conclusion can be extended across different reaction energies because there is no reason why a model should work only sporadically.

We have now shown that the chemical nonequilibrium is the necessary ingredient in the SHM approach to the process of hadronization of a QGP fireball. The nonequilibrium SHM was proposed when first strange hadron multiplicity results were interpreted more than 20 yr ago [19]. The yield of strange hadrons indicated that the number of quark pairs present had to be modified by a factor  $\gamma_s$ ; the source of strangeness is not populating the final-state hadrons with the yields expected from the hadronic chemical equilibrium, a point of view widely accepted today. At SPS energies, for which this model was originally conceived, the production of strangeness did not yet saturate the QGP phase space; that is, strangeness was out of chemical equilibrium both in the QGP fireball source with  $\gamma_s^Q < 1$  and thus also in the final hadronic state with also  $\gamma_s^H < 1$ . The distinction of QGP as

TABLE I. Table of data points we use as input for SHM fits; hadron yields ( $dN/dy$ ) and ratios at midrapidity  $|y| < 0.5$  for different centralities. The header of the table defines the centrality bins in three different ways. Centrality as a function of  $N_{\text{part}}$  is taken from [29]. Errors are combined systematic and statistical errors added in quadratures where systematic errors are, in general, dominant and statistical errors are negligible. Values in brackets are interpolated data. See Appendix for details about data sources and how data are rebinned.

Centrality	0%–20%	0%–5%	5%–10%	10%–20%	20%–30%	30%–40%	40%–50%	50%–60%	60%–70%	70%–80%
$\langle N_{\text{part}} \rangle$	308	382.8	329.7	260.5	186.4	128.9	85.0	52.8	30.0	15.8
$dN_{\text{ch}}/d\eta$	$1601 \pm 60$	$1294 \pm 49$	$966 \pm 37$	$649 \pm 23$	$426 \pm 15$	$261 \pm 9$	$149 \pm 6$	$76 \pm 4$	$35 \pm 2$	
$\pi^+$	$562 \pm 36$	$733 \pm 54$	$606 \pm 42$	$455 \pm 31$	$307 \pm 20$	$201 \pm 13$	$124 \pm 8$	$71 \pm 5$	$37 \pm 2$	$17.1 \pm 1.1$
$\pi^-$	$560 \pm 34$	$732 \pm 52$	$604 \pm 42$	$453 \pm 31$	$306 \pm 20$	$200 \pm 13$	$123 \pm 8$	$71 \pm 4$	$37 \pm 2$	$17.0 \pm 1.1$
$K^+$	$84 \pm 5.4$	$109 \pm 9$	$91 \pm 7$	$68 \pm 5$	$46 \pm 4$	$30 \pm 2$	$18.3 \pm 1.4$	$10.2 \pm 0.8$	$5.1 \pm 0.4$	$2.3 \pm 0.2$
$K^-$	$84 \pm 5.7$	$109 \pm 9$	$90 \pm 8$	$68 \pm 6$	$46 \pm 4$	$30 \pm 2$	$18.1 \pm 1.5$	$10.2 \pm 0.8$	$5.1 \pm 0.4$	$2.3 \pm 0.2$
$K^{*0}$	$17.3 \pm 4.2$									
$K^{0*}/K$		$(188 \pm 98)$	$(196 \pm 77)$	$(209 \pm 54)$	$(227 \pm 59)$	$(247 \pm 64)$	$(269 \pm 70)$	$(295 \pm 77)$	$(326 \pm 85)$	$(361 \pm 94)$
$p$	$25.9 \pm 1.6$	$34 \pm 3$	$28 \pm 2$	$21.0 \pm 1.7$	$14.4 \pm 1.2$	$9.6 \pm 0.8$	$6.1 \pm 0.5$	$3.6 \pm 0.3$	$1.9 \pm 0.2$	$0.90 \pm 0.08$
$\bar{p}$	$26.0 \pm 1.8$	$33 \pm 3$	$28 \pm 2$	$21.1 \pm 1.8$	$14.5 \pm 1.2$	$9.7 \pm 0.8$	$6.2 \pm 0.5$	$3.7 \pm 0.3$	$2.0 \pm 0.2$	$0.93 \pm 0.09$
$\phi$	$9.6 \pm 1.4$									
$\phi/K$		$109 \pm 20$	$116 \pm 18$	$117 \pm 17$	$128 \pm 19$	$120 \pm 20$	$123 \pm 18$	$123 \pm 19$	$119 \pm 18$	$119 \pm 21$
$\Lambda$	$19.3 \pm 2.0$									
$\Lambda/\pi$		$(33.3 \pm 3.9)$	$(34.2 \pm 4.0)$	$(35.3 \pm 4.1)$	$(36.4 \pm 4.3)$	$(37.0 \pm 4.3)$	$(37.1 \pm 4.4)$	$(36.8 \pm 4.3)$	$(36.0 \pm 4.2)$	$(34.7 \pm 4.1)$
$\Xi^-$	$323 \pm 35$	$(397 \pm 44)$	$(337 \pm 37)$	$(258 \pm 28)$	$(176 \pm 19)$	$(116 \pm 13)$	$(71.6 \pm 7.9)$	$(40.7 \pm 4.5)$	$(19.6 \pm 2.2)$	$(7.5 \pm 0.8)$
$\bar{\Xi}^+$	$304 \pm 33$	$(382 \pm 42)$	$(327 \pm 36)$	$(253 \pm 28)$	$(176 \pm 19)$	$(118 \pm 13)$	$(73.7 \pm 8.1)$	$(42.3 \pm 4.7)$	$(20.3 \pm 2.2)$	$(7.1 \pm 0.8)$
$\Omega^-$	$57 \pm 10$	$(78 \pm 19)$	$(62 \pm 16)$	$(45 \pm 11)$	$(29 \pm 7)$	$(18 \pm 4)$	$(10 \pm 3)$	$(5.4 \pm 1.4)$	$(2.5 \pm 0.6)$	$(1.0 \pm 0.3)$
$\bar{\Omega}^+$	$58 \pm 11$	$(76 \pm 18)$	$(61 \pm 15)$	$(45 \pm 11)$	$(29 \pm 7)$	$(18 \pm 4)$	$(10 \pm 3)$	$(5.5 \pm 1.4)$	$(2.5 \pm 0.6)$	$(1.0 \pm 0.3)$

the initial and the final hadron phase-space domain for  $\gamma_s$  was also modeled [20]. It is important to always remember that hadron phase-space nonequilibrium can arise from a QGP fireball with strangeness in chemical equilibrium, because, in general, the QGP and hadron phase-space strangeness densities are greatly different. Moreover, it is quite possible that a not-yet-in-chemical equilibrium QGP, which is the higher density phase, produces an equilibrated hadron yield. This can, however, happen only accidentally and variation of reaction energy or collision centrality shows this.

Another nonequilibrium parameter  $\gamma_c$ , similar to  $\gamma_s$ , was introduced very soon after  $\gamma_s$  to control the charm final-state phase space [20], and it has been widely adopted in consideration of a strong charm yield overabundance above chemical hadron gas equilibrium. Note that both strangeness and charm flavors are therefore assumed to have been produced in a separate and independent process before hadronization, and note further that each of the production mechanisms, in this case, is different, with charm originating in first parton collisions and strangeness being also abundantly produced in secondary thermalized gluon fusion reactions. At the end of QGP expansion, these available and independently established strangeness and charm particle supplies are distributed into available final-state phase-space cells, which is the meaning of SHM in a nutshell.

The full chemical nonequilibrium is introduced by means of the parameter  $\gamma_q \neq 1$ . This situation arises when the source of hadrons disintegrates faster than the time necessary to reequilibrate the yield of light quarks present. The two-pion correlation data provide experimental evidence that favors a rapid breakup of QGP with a short time of hadron production [21] and thus favors very fast, or sudden, hadronization

[22,23]. In this situation, a similar chemical nonequilibrium approach must be applied to the light quark abundance, introducing the light quark phase-space occupancy  $\gamma_q$ . This proposal made for the high-energy SPS data [7,8], helped improve the understanding of RHIC200 hadron rapidity yield results [10], and allowed a consistent interpretation of these data across the full energy range at SPS and RHIC200 [11].

For more than a decade we have made continued effort to show that a high-quality (low  $\chi^2$ ) and simple (no need for hybrid models) description of hadron abundances emerges using chemical nonequilibrium SHM. However, the *recognition* of the necessity of light quark ( $u, d$ ) chemical nonequilibrium, i.e.,  $\gamma_q \neq 1$ , remains sparse, despite the consistency of this approach with the two-pion correlation results, which provides additional evidence for fast hadronization [21]. The recent steady advances of lattice QCD [24–27] favors QGP hadronization at a temperature below the once-preferred  $T_c = 165$  MeV temperature. As already noted, the equilibrium SHM variant imposing  $\gamma_q = 1$  light quark chemical equilibrium [13–18] produces (relatively dense) particle chemical freeze-out near  $T = 155$  MeV. Such freeze-out assumes, on one hand, in the present context a relatively high QGP hadronization temperature and, on the other hand, requires as a complement an “afterburner” describing further reaction evolution of some particles. As we argue in Sec. III B, such a “hybrid” model does not result in a viable description of the precise ALICE experimental data.

This is the case since the LHC2760 experimental environment has opened a new experimental opportunity to investigate in detail the SHM hadron production model. Precise particle tracking near the interaction vertex in the ALICE experiment removes the need for off-line corrections of weak interaction

decays, and at the same time vertex tracking is enhancing the efficiency of track identification, increasing considerably the precision of particle yield measurement [5,28]. All data used in the present work were obtained in this way by the LHC-ALICE experiment for Pb-Pb collisions at  $\sqrt{s_{NN}} = 2.76$  TeV, limited to the central unit of rapidity interval  $-0.5 < y < 0.5$ . The experimental particle yield results are reported in different collision centrality bins according to the geometric overlap of colliding nuclei, with the “smallest,” e.g., 0%–5% centrality bin corresponding to the nearly fully overlapping geometry of the colliding nuclei. The collision geometry model [29] relates the centrality trigger to the number of participating nucleons  $N_{\text{part}}$ , which we use as our preferred centrality variable in what follows.

Section II presents our general method and approach to the particle multiplicity data analysis. Following a brief summary of the SHM methods in Sec. II A, we describe in Sec. II B our centrality study of particle production based on the following data: For the 0%–20% centrality bin, we obtain the preliminary data from [5,28]. For the centrality study of particle production, we present in Table I the final yields of  $\pi^\pm$ ,  $K^\pm$ , and  $p^\pm$  as presented in Ref. [30]. The preliminary ratio  $\phi/K$  is from Ref. [31]; these seven data points are binned in the same centrality bins and are used as presented. However, several other particle types require rebinning with interpolation and, at times, extrapolation, which is further discussed in Appendix. The (preliminary) data input into this rebinning for  $K^{*0}/K^-$  and for  $2\Lambda/(\pi^- + \pi^+)$  are also taken from Ref. [31]. Using the preliminary enhancement factors of  $\Xi^-$ ,  $\Xi^+$ ,  $\Omega^-$ ,  $\Omega^+$  shown in Refs. [32,33], combined with yields of these particles for  $p$ - $p$  reactions at  $\sqrt{s_{NN}} = 7$  TeV as presented in Ref. [34], we obtain the required yield input; see Appendix. In Sec. II C, we present particles both fitted and predicted by SHM, including antimatter clusters.

In Sec. III, we discuss the key physics outcome of the fits, i.e., the resulting SHM parameters as a function of centrality. We compare to the equilibrium approach in Sec. III A. We discuss the differences seen between the SHM variants and compare our results to our analysis of Au-Au collisions at  $\sqrt{s_{NN}} = 62.4$  GeV at RHIC62, because it is a system we analyzed in detail recently [12]. We obtain the bulk physical properties—energy density, entropy density, and pressure—as a function of centrality in Sec. III C, where we also address strangeness and entropy yields. This study is made possible because all SHM parameters are determined with minimal error in consideration of the precise experimental particle multiplicity result. We discuss how our results relate to the lattice-QCD study of QGP properties in Sec. III D. We close our paper with a short summary and discussion of all results in Sec. IV.

## II. SHM AND PARTICLE PRODUCTION

### A. Generalities

We use here SHM implementation within the SHARE program [4]. The SHM describes the yields of particles given the chemical freeze-out temperature  $T$  and overall normalization  $dV/dy$  (as the experimental data are available as  $dN/dy$ ). We account for the small asymmetry between

particles and antiparticles by fugacity factors  $\lambda_q$ ,  $\lambda_s$  and the light quark asymmetry  $\lambda_{I3}$ ; see Ref. [4]. We further note that it is not uncommon to present the particle-antiparticle asymmetry employing the baryochemical and strangeness chemical potentials defined by

$$\mu_B = 3T \ln \lambda_q \quad \text{and} \quad \mu_S = T \ln(\lambda_q/\lambda_s), \quad (1)$$

the “inverse” definition of  $\mu_S$  with reference to  $\lambda_s$  has historical origin and is a source of frequent error.

For each value of  $\lambda_q$ , strangeness fugacity  $\lambda_s$  is evaluated by imposing the strangeness conservation requirement  $\langle s \rangle - \langle \bar{s} \rangle \simeq 0$ . From now on, we omit the bra-kets indicating grand canonical average of the corresponding summed particle yield. The isospin fugacity factor  $\lambda_{I3}$  is constrained by imposing the charge per baryon ratio present in the initial nuclear-matter state at the initial instant of the collision. We achieve this objective by fitting these conservation laws along with particle yield data, using the following form:

$$\frac{s - \bar{s}}{s + \bar{s}} = 0.00 \pm 0.01, \quad (2)$$

$$\frac{Q - \bar{Q}}{B - \bar{B}} = 0.38 \pm 0.02. \quad (3)$$

We believe that implementing conservation laws as data points with errors accounts for the possibility that particles escape asymmetrically from the acceptance domain.

In the LHC2760 energy regime, there is near symmetry of particle and antiparticle sector; thus, the chemical potentials are hard to quantify. Therefore, the two constraints Eqs. (2) and (3) alone were not sufficient to achieve smooth behavior of the chemical potentials as a function of centrality. We therefore impose as a further constraint a constant baryon number stopping per participating nucleon in the midrapidity region in the following form:

$$\frac{b - \bar{b}}{N_{\text{part}}} = 0.0054 \pm 1\%. \quad (4)$$

We selected condition (4) because this was the variable that emerged in unconstrained fits as being most consistent. The value we selected is our estimate based on convergence without constraint to this value at several centralities. The alternative to this approach would have been to take a constant value of  $\mu_B$  across centrality. While this produces a good-enough fit as well, this approach was poorly motivated: The unconstrained fit results produced a rather random-looking distribution of  $\mu_B$  across centrality and thus did not present any evidence pointing towards a specific choice for  $\mu_B$ . While the actual method of fixing matter-antimatter asymmetry is extraneous to the main thrust of this paper, the value of  $\mu_B$  is of some relevance when considering predictions for antinuclei which we present further below.

Our considerations include the already described phase-space occupancy parameters  $\gamma_s$  and  $\gamma_q$ , where the light quarks  $q = u, d$  are not distinguished. We do not study  $\gamma_c$  here; in other words, we do not include in the present discussion the charm degree of freedom. We note that there is no current experimental  $p_\perp$ -integrated charmed hadron yield information available from Pb-Pb collisions at LHC. The integration of the

phase-space distribution is not yet possible owing to uncertain low transverse momentum yields.

Thus, in the LHC2760 energy domain, we have at most  $7 - 3 = 4$  independent statistical model parameters: seven parameters— $dV/dy$ ,  $T$ ,  $\lambda_q$ ,  $\lambda_s$ ,  $\lambda_{I3}$ ,  $\gamma_q$ , and  $\gamma_s$ —constrained by the three conditions—Eqs. (2)–(4)—to describe within SHM approach many very precise data points spanning in yield across centrality more than 5 orders of magnitude. We show for comparison results obtained setting arbitrarily  $\gamma_q = 1$  (chemical semiequilibrium fit, comprising 6 parameters – 3 constraints) and then  $\gamma_q = \gamma_s = 1$  (chemical equilibrium fit, 5 parameters – 3 constraints).

Absolute yields of hadrons are proportional to one power of  $\gamma_q$  for each constituent light quark (or antiquark) and one power of  $\gamma_s$  for each strange quark (or antiquark). For example,  $\gamma_q$  enters nonstrange baryon-to-meson ratios in the following manner:

$$\frac{\text{baryon}(qqq)}{\text{meson}(q\bar{q})} \propto \frac{\gamma_q^3}{\gamma_q^2} F(T, m_{\text{baryon}}, m_{\text{meson}}), \quad (5)$$

where  $q$  stands for either  $u$  or  $d$  quark and  $F$  is the integral over all particle momenta of the phase-space distribution at freeze-out temperature. We always use exact form of relativistic phase-space integrals. For strange hadrons, we must replace  $\gamma_q$  with  $\gamma_s$  for each constituent  $s$  (and/or  $\bar{s}$ ) quark. Experimentally measured light baryon-to-meson ratios (such as  $p/\pi$ ) strongly depend on the value of  $\gamma_q$  in a fit. Similarly,  $\Lambda(qqs)/\pi(q\bar{q}) \propto \gamma_s$  is very sensitive to the value of  $\gamma_s$ .

The value of  $\gamma_q$  is bound by appearance of a pion condensate which corresponds to a singularity in the pion Bose-Einstein distribution function reached at the condition

$$\gamma_q^{\text{crit}} = \exp\left(\frac{m_{\pi^0}}{2T}\right). \quad (6)$$

This numerically works out for  $T = 138$ – $160$  MeV to be in the range  $\gamma_q^{\text{crit}} = 1.63$ – $1.525$ . However, there is a much more lax limit on the range of  $\gamma_s$ ; strangeness can increase very far before a particle condensation phenomenon limit is reached for the  $\eta$  meson.

## B. Centrality study

The input hadron yield data used in the fit to the 0%–20% centrality bin is shown in the second column of Table I. The fit to this data set for the case of chemical equilibrium, where one forces  $\gamma_s = \gamma_q = 1$ , was done in Ref. [28], choosing a fixed value  $\mu_B = 1$  MeV. In a first step, we compare to these results and follow this approach. However, we consider it necessary to apply strangeness and charge per baryon conservation by fitting Eqs. (2) and (3) as two additional data points determining the corresponding values of chemical parameters  $\mu_S$ ,  $\mu_{I3}$ , a procedure omitted in the report Ref. [28], where  $\mu_S = \mu_{I3} = 0$  was set. Naturally, the effect of this improvement is minimal, but it assures physical consistency. We show the values of  $\chi_{\text{total}}^2$  in Fig. 2; see the large open symbols. The wider range of  $N_{\text{part}}$  corresponding to the centrality bin 0%–20% is shown in Fig. 2 as horizontal uncertainty bars.

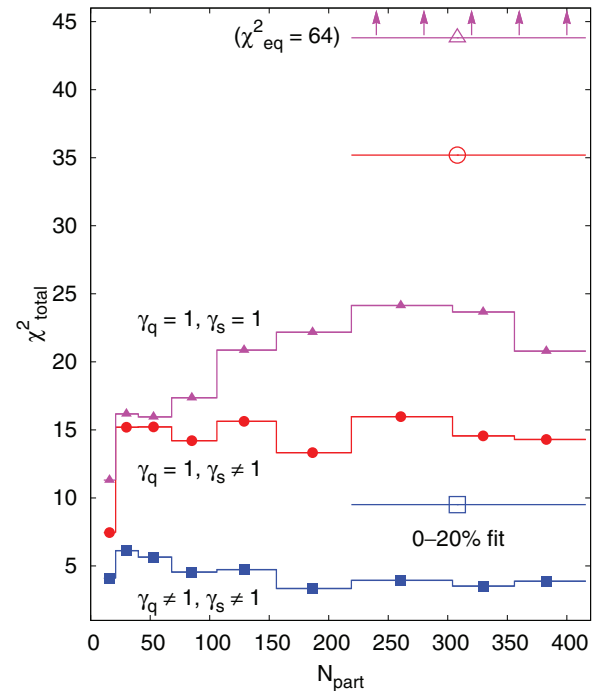


FIG. 2. (Color online) Total  $\chi^2$  as a function of centrality, as indicated in the figure, for the total equilibrium ( $\gamma_q = \gamma_s = 1$ ,  $\text{ndf} = 11$ ), for the semiequilibrium ( $\gamma_q = 1$ ,  $\gamma_s \neq 1$ ,  $\text{ndf} = 10$ ), and for chemical nonequilibrium ( $\gamma_q \neq 1$ ,  $\gamma_s \neq 1$ ,  $\text{ndf} = 9$ ) SHM. Open symbols represent the total  $\chi^2$  for the 0%–20% centrality bin depicted in Figs. 1(a) and 1(b). The number of degrees of freedom for the three cases, respectively, is  $\text{ndf} = 11, 10, 9$ . (The value of equilibrium SHM in the 0%–20% bin has been shifted down by 20 to fit in the figure.)

In our detailed centrality-dependent analysis, we use data in nine finer centrality bins, which we show in the 3rd to 11th and last column of Table I. The bins are classified according to the average number of participants  $N_{\text{part}}$  as a measure of centrality. This is a model value originating in the experimentally measured pseudorapidity density of charged particles  $dN_{\text{ch}}/d\eta$  [29], which we state in the third row of Table I. We consider the consistency in Fig. 3: The experimentally measured  $dN_{\text{ch}}/d\eta$  in the relevant participant bins [30] is shown by square symbols, as well as our SHM results for rapidity density of charged particles  $dN_{\text{ch}}/dy$  emerging directly from QGP (i.e., primary charged hadrons) and the final yield of charged hadrons, as fed by the decay of hadronic resonances. In all cases, we show, in Fig. 3, the yield per pair of interacting nucleons using the model value  $N_{\text{part}}$ . While the primary charged hadron rapidity yield (solid circles) is well below the pseudorapidity density  $dN_{\text{ch}}/d\eta$  of charged hadrons (solid squares), the final rapidity yield  $dN_{\text{ch}}/dy$  after strong decays (solid triangles) is well above it. This result,  $dN_{\text{ch}}/dy > dN_{\text{ch}}/d\eta$ , is consistent with dynamical models describing the momentum spectra, which account for the production of charged particles that are not identified by experiments [1].

In Fig. 3, we see that about 50% of charged hadronic particles are produced by strong decays of heavier resonances. We show, in Fig. 4, the ratio of primarily produced yield to

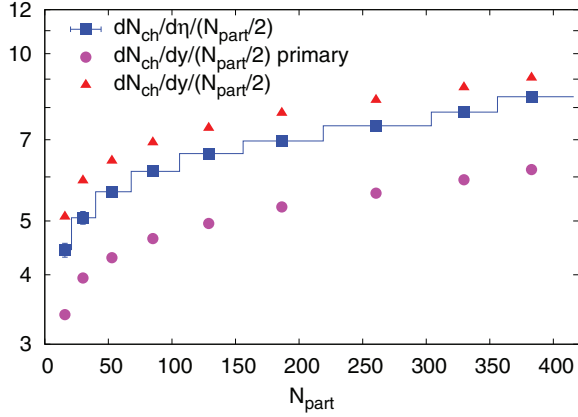


FIG. 3. (Color online) Experimental charged-particle yield pseudorapidity density  $dN/d\eta$  (blue squares), and geometric model relating to charged-particle rapidity density  $dN/dy$  of only primary particles (violet circles) and including feed from strongly decaying resonances (red triangles) per participant pairs  $N_{\text{part}}/2$ .

the total yield for different particle species in the expected range of hadronization temperatures. The dominant fraction, almost 80%, of  $\pi$  and  $p$  yield originates from decaying resonances. This result demonstrates the difficulty that one encounters in the interpretation of transverse momentum spectra which must account for the decays and is thus, in a profound way, impacted by collective flow properties of many much heavier hadrons [1–3]. Conversely, this means that one can perform a convincing analysis of transverse momentum distribution only for hadrons, which do not have a significant feed from resonance decays, such as  $\Omega$  or  $\phi$ . This finding is the reason why we study the  $p_{\perp}$  integrated yields of hadrons in exploration of the physics of the fireball particle source. Moreover, we believe that “blast-wave” model fits to  $p_{\perp}$  hadron spectra are only meaningful for the  $\Omega$  or  $\phi$  hadrons.

The centrality binning, which differs for the different particles considered, requires us to use several interpolated and even some slightly extrapolated experimental results, which

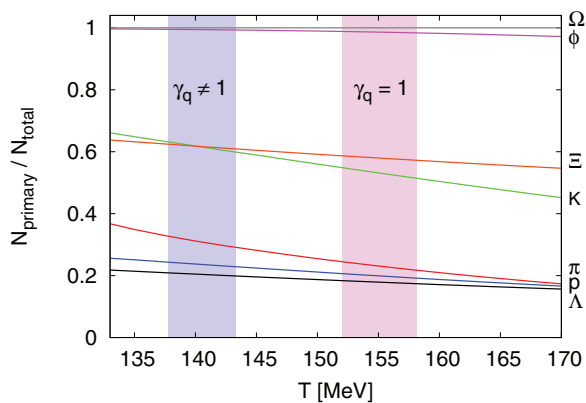


FIG. 4. (Color online) Fraction of primary hadrons produced, normalized by their final yield, which consists of primary produced hadrons and the feed from strong decaying resonances, for particles indicated in the right margin, as a function of hadronization temperature in single freeze-out model.

procedure we discuss in depth below and in Appendix. In our fits, we choose to use the centrality bins with the largest number of directly determined experimental data, minimizing the potential error originating in our multipoint interpolation. A few particles appear more than once in our data set (as a yield and/or in a ratio). However, to prevent duplicity, we always fit every particle measured just once.

To show that the finer centrality binning matters, we have already shown the 5%–10% centrality bin [which contains only close extrapolation; see open symbols in Figs. 1(b) and 1(d)]. The fit has the same set of particles as the 0%–20% centrality bin seen in Figs. 1(a) and 1(c), however, some of these particles enter the finer binned fit in ratios. If the outcome of the fit as a function of centrality is even a small variation in fitted parameters (other than normalization, i.e., volume), we expect and we find that the 5%–10% centrality bin, which describes a much smaller participant  $N_{\text{part}}$  range, leads to smaller  $\chi^2$  compared to the wide 0%–20% case. However, the stability of the fit parameters implies that much of the improvement is attributable to the revision in the input data set. The 0%–20% fit is based on preliminary data [28], whereas 5%–10% includes more recent final data [30] (see Appendix for details). For chemical nonequilibrium SHM an improvement of  $\chi^2$  by a factor of 4 is found for both preliminary 0%–20% and more recent final data set in 5%–10% bin as compared to chemical equilibrium SHM, thus favoring our simple nonequilibrium hadronization model.

We perform a fit to the entire data set with all three SHM approaches and compare the resulting  $\chi^2$  as a function of  $N_{\text{part}}$  in Fig. 2. The solid squares represent the chemical nonequilibrium SHM ( $\gamma_q \neq 1$ ,  $\gamma_s \neq 1$ ), the solid circles represent the semiequilibrium SHM ( $\gamma_q = 1$ ,  $\gamma_s \neq 1$ ), and solid triangles represent the full equilibrium SHM ( $\gamma_q = \gamma_s = 1$ ). The range of centrality is indicated by the horizontal bars. Considering most central bins, we note in Fig. 2 that allowing  $\gamma_q \neq 1$  can reduce the total  $\chi^2$  of the fit by more than a factor of 3 compared to semiequilibrium and more than a factor of 5 comparing full nonequilibrium with full equilibrium.

As a last step, we verify if there is a special value of the parameter  $\gamma_q$  of particular importance. To this end, we have evaluated the  $\chi^2/\text{ndf}$  of the fit as a function of a given fixed  $\gamma_q$  within a range  $\gamma_q \in (0.95, \gamma_q^{\text{crit}})$ . This  $\chi^2$  profile curves, seen in Fig. 5, all pass  $\gamma_q = 1$  smoothly; therefore,  $\gamma_q = 1$  has no special importance for the SHM. However, fits to data in all centralities decrease in  $\chi^2$  as  $\gamma_q$  increases; they all point to best-fit value of  $\gamma_q$  near the critical value of Bose-Einstein condensation given by Eq. (6).

The most peripheral bin (70%–80%,  $N_{\text{part}} = 15.8$ ) analyzed here requires further discussion as it shows in Fig. 5 a different behavior and in particular a considerably lower  $\chi^2$  when  $\gamma_q \rightarrow 1$ . For this peripheral centrality bin the procedure we use to interpolate data of  $\Xi$ ,  $\Omega$ ,  $\Lambda/\pi$ , and  $K^*/K$  assigns a narrow peripheral centrality range to these experimental data points obtained for a much greater centrality domain spanning a participant range which is considerably wider. This can be a problem because within the wider centrality range the experimental results change rapidly with participant number. Therefore, our extrapolation towards the edge of the experimental data centrality range may introduce a fit

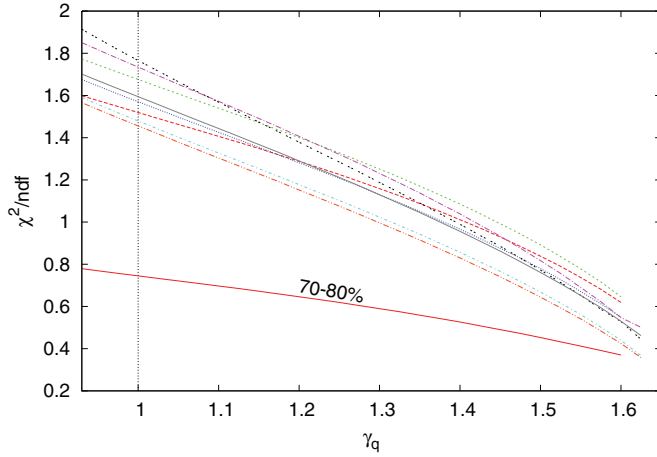


FIG. 5. (Color online)  $\chi^2/\text{ndf}$  profile as a function of  $\gamma_q$  for all studied centralities.

aberration; here it happens that the created data are less incompatible with equilibrium SHM variants when  $\gamma_q \rightarrow 1$ . We do not believe that there is any issue with the result of the fit for  $\gamma_q \rightarrow 1.6$  we discuss in this work. A different approach, in which we recombine the bins rather than interextrapolate, was presented in Ref. [35].

### C. Particle yields

We compare input to the resulting particle yields graphically in Fig. 6. We fit 13 particles, counting antiparticles, which in the figure cannot be visually distinguished as an independent input or output data, and ratios  $\Lambda/\pi$ ,  $K^*/K$ , and  $\phi/K$ . For these ratios, the relevant yield outputs  $\Lambda$ ,  $K^*$ , and  $\phi$  are shown. Direct comparison of the input  $\Lambda/\pi$ ,  $K^*/K$ , and  $\phi/K$  ratios to the output is presented in Fig. 7; note that the  $\phi/K$  ratio is available as an experimental data point in all centrality bins. The fitted output yields are stated also in the top portion of Table II, and ratios are given just below, allowing for comparison with the input values.

Our fit results appear as open circles in Fig. 6, at times completely overlaying the input data (solid symbols). For the  $\Lambda$ , the dotted line guides the eye, because the actual fit is to the ratio  $\Lambda/\pi$  shown in Fig. 7; no absolute  $\Lambda$  data are available. In the absence of absolute yields, only the open circles, i.e., the fitted values, are shown in Fig. 6. A similar situation arises with  $\phi$  and  $K^*$ , where data are not available, but we fit  $\phi/K$  and  $K^{0*}/K$ . One can see that SHM-generated results follow closely both the experimental data available and the interpolation dashed lines for each particle and that each interpolation curve passes through the experimental data points shown as full symbols or, at worst, the error bars if these are larger than the symbol.

Even so, we note in Fig. 6 that our interpolation for  $\Omega$  shows a slightly different systematic shape (dashed line) compared the fit results (open symbols) or the behavior of the other particles. In other words, we see that other particles “predict” the yield of  $\Omega$  that follows the centrality dependence of other particles, while the four data points lead to a centrality distribution that is slightly different. More precise  $\Omega$  data will,

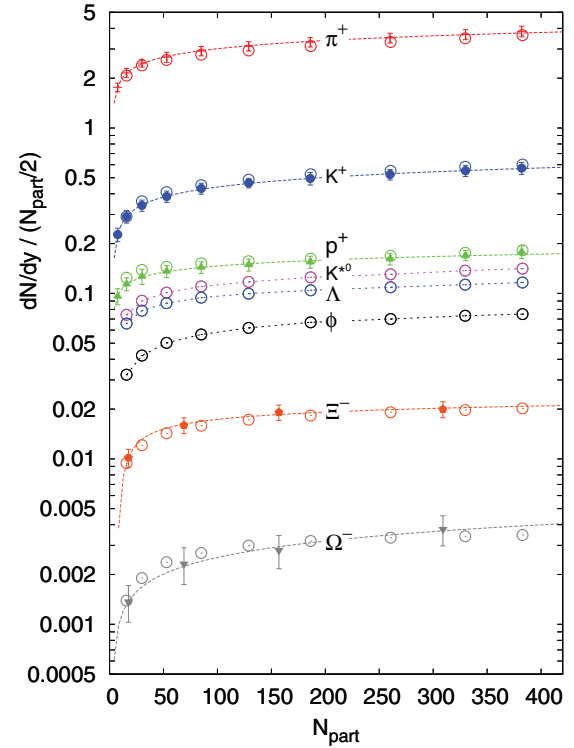


FIG. 6. (Color online) Solid symbols are the experimental data points. Open symbols represent the outcome for our chemical nonequilibrium SHM fit to LHC2760 as a function of centrality, i.e.,  $N_{\text{part}}$ . Dashed lines are the outcome of our data interpolation of experimental yields available (see Appendix). Dotted lines connecting  $\Lambda$ ,  $K^*$ , and  $\phi$  SHM output values are presented to guide the eye; because ratios of these particles were used in our fit, the data are shown in Fig. 7.

without any doubt, offer a resolution to this slight tension in our interpolation. The hadron yields we find are also stated in Table II. Aside from the yields, we show there frequently

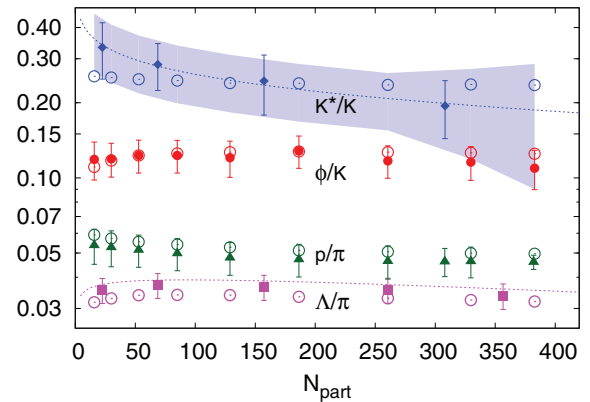


FIG. 7. (Color online) Solid symbols, experimental data with errors for  $K^*/K$ ,  $\phi/K$ , and  $\Lambda/\pi$  as a function of centrality, i.e., number of participants  $N_{\text{part}}$ . Lines are the interpolation (respectively, extrapolation) except for the case  $\phi/K$ , where dotted line guides the eye. Open circles represent the resulting fit value for each ratio. The (blue) shaded band shows the error input used obtaining the interpolated values of  $K^*/K$  ratio.

TABLE II. Table of hadron yield output. The header of the table defines the centrality bins in three different ways. The top section of the table shows fitted yields  $dN/dy$  of hadrons entering the fit at LHC2760 obtained in the chemical nonequilibrium SHM. Next are three ratios that are actually included in the fit (rather than the yields of  $\Lambda$ ,  $K^{0*}$ ,  $\phi$ ), followed by the ratios of hadron yields that can be formed from the stated results, stated here for convenience of the reader. In the two lower sections of the table, there are predicted yields of yet-unmeasured hadrons, and at the very bottom we show predicted yields of light antinuclei scaled up by factor 1000 (and by  $10^6$  for antihelium). Note that yield of matter particles is nearly the same.

Centrality bin ( $N_{\text{part}}$ )	0%–20%	0%–5%	5%–10%	10%–20%	20%–30%	30%–40%	40%–50%	50%–60%	60%–70%	70%–80%
$dN_{\text{ch}}/dy$	1312	1732	1433	1075	729	474	294	169	88.7	40.2
$\pi^+$	525	696	574	431	292	190	118	68.0	35.8	16.4
$\pi^-$	525	696	575	430	292	189	118	68.1	35.9	16.4
$K^+$	88.4	115	96.0	71.8	49.0	31.4	19.2	10.8	5.41	2.30
$K^-$	88.1	114	95.5	72.1	48.7	31.5	19.1	10.8	5.37	2.30
$p$	26.5	34.9	29.0	22.0	15.1	10.1	6.45	3.82	2.08	0.982
$\bar{p}$	26.1	34.2	28.4	21.6	14.8	9.89	6.30	3.72	2.02	0.953
$K^{0*}$	20.8	27.0	22.6	17.0	11.7	7.56	4.68	2.67	1.36	0.587
$\phi$	11.2	14.4	12.1	9.12	6.23	3.99	2.40	1.33	0.632	0.255
$\Lambda$	17.2	22.3	18.6	14.2	9.73	6.43	4.00	2.31	1.18	0.520
$\Xi^-$	3.03	3.86	3.25	2.49	1.70	1.11	0.674	0.377	0.181	0.0745
$\bar{\Xi}^+$	3.00	3.80	3.22	2.43	1.68	1.08	0.664	0.371	0.179	0.0726
$\Omega^- 10^3$	529	663	561	435	297	193	115	62.6	28.5	11.0
$\bar{\Omega}^+ 10^3$	527	654	560	421	295	186	114	62.1	28.4	10.7
$\Lambda/\pi 10^3$	32.7	32.0	32.4	33.0	33.4	33.9	34.0	33.9	32.9	31.7
$K^{0*}/K 10^3$	236	235	237	236	239	240	245	248	252	255
$\phi/K 10^3$	127	125	126	127	128	127	125	123	117	111
$\phi/\pi^- 10^3$	21.4	20.6	21.0	21.2	21.4	21.1	20.3	19.5	17.6	15.6
$K^-/\pi^- 10^3$	168	165	166	167	167	167	162	158	150	141
$p/\pi^+ 10^3$	50.4	50.2	50.5	51.0	51.8	53.2	54.8	56.2	58.0	60.0
$\Xi/\pi 10^3$	5.76	5.55	5.65	5.79	5.84	5.86	5.71	5.53	5.06	4.55
$\Omega/\pi 10^3$	1.007	0.952	0.976	1.010	1.019	1.019	0.973	0.920	0.795	0.671
$K^{0*}/\pi 10^3$	39.6	38.8	39.3	39.5	40.0	39.9	39.7	39.2	37.8	35.9
$p/K$	0.300	0.303	0.302	0.306	0.309	0.322	0.336	0.354	0.385	0.426
$\eta$	61.0	79.7	66.3	49.8	33.9	21.9	13.4	7.64	3.90	1.72
$\rho(770)^0$	38.9	51.3	42.5	32.1	21.9	14.5	9.14	5.35	2.87	1.34
$\omega(782)^0$	35.1	46.4	38.4	29.0	19.8	13.1	8.28	4.85	2.61	1.22
$\Delta(1232)^{++}$	4.98	6.57	5.46	4.15	2.86	1.92	1.23	0.734	0.402	0.191
$\Sigma^*(1385)^-$	2.08	2.70	2.26	1.72	1.18	0.785	0.492	0.284	0.146	0.065
$\Lambda^*(1520)$	1.09	1.41	1.18	0.907	0.625	0.418	0.264	0.153	0.0795	0.0355
$\Xi^*(1530)^-$	1.02	1.30	1.09	0.84	0.58	0.378	0.230	0.129	0.0626	0.0258
${}^2\bar{\text{H}} 10^3$	74.7	98.1	81.9	62.6	43.6	29.4	19.5	11.8	6.53	3.16
${}^3\bar{\Lambda} 10^3$	0.478	0.601	0.506	0.397	0.279	0.191	0.128	0.0773	0.0415	0.0193
${}^3\bar{\text{H}} 10^3$	1.64	2.13	1.79	1.39	0.983	0.677	0.468	0.290	0.166	0.083
${}^3\bar{\text{He}} 10^3$	1.64	2.14	1.79	1.39	0.986	0.679	0.469	0.291	0.166	0.083
${}^4\bar{\text{He}} 10^6$	5.87	7.57	6.41	5.04	3.64	2.56	1.85	1.18	0.697	0.362

quoted ratios of particle yields; e.g., we find  $p/\pi^+ \simeq 0.05$ . We return to discuss this ratio in Sec. III B.

Figure 7 has the largest differences between theory and experiment. In case of the  $\Lambda/\pi$  ratio, we see a systematic within error bar underprediction at all centralities. For  $K^*/K$ , we see within the error bar a different slope of the fit as a function of centrality. The question can be asked if these differences of fit and results indicate some not-yet-understood physics contents. However, we are within the error bars and such data-fit difference must be expected and is allowed given a large data sample and potential for experimental refinement of these two preliminary data sets involving  $K^*$  and  $\Lambda$ . We recall

that at RHIC200, the  $K^*/K$  ratio was 10%–15% smaller and agrees with current ALICE results within the error margin [36]. We also note that we did not yet study how the charmed hadron decay particles influence the fit.

Predictions for the six hadron yields— $\eta$ ,  $\rho^0$ ,  $\Delta(1232)^{++}$ ,  $\Lambda^*(1520)$ ,  $\Sigma^*(1385)^-$ ,  $\Xi^*(1530)^0$ —are shown in Fig. 8 as a function of centrality; these results are stated in the lower portion of Table II. We further show five different species of (strange) antimatter, from antideuteron to anti- $\alpha$ , including antihypertriton, appropriately scaled to fit into Fig. 8. Our predictions of these composite objects should serve as a lower limit of their production rates: Fluctuation in the QGP

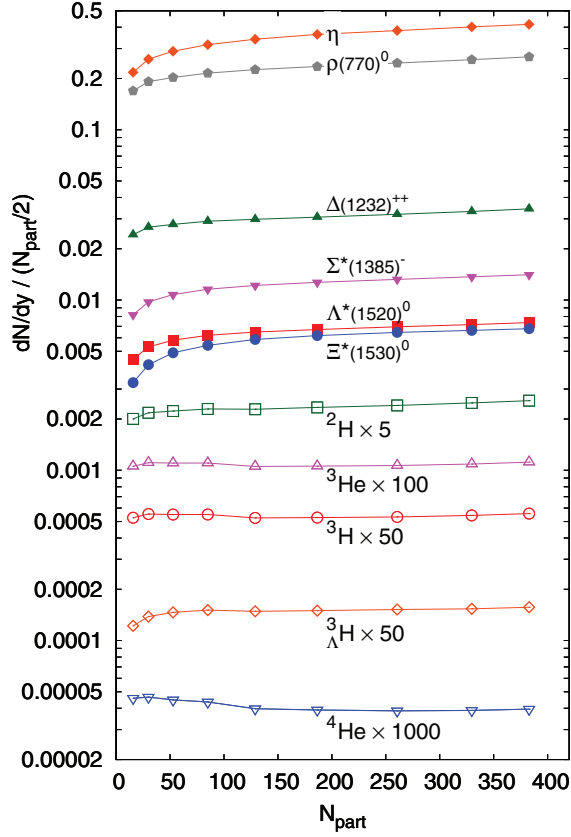


FIG. 8. (Color online) Particles predicted by the chemical nonequilibrium SHM fits. Predictions for hadron yields (solid symbols) are above antinuclei yield predictions (open symbols), which have been multiplied by suitable factors. Lines guide the eye; points are actual predictions for each of the nine centralities we analyzed.

homogeneity at hadronization and recombinant formation after hadronization may add contributions to the small SHM yield; see here the corresponding RHIC result [37].

### III. PARTICLE SOURCE AND ITS PROPERTIES

#### A. Statistical parameters

In Fig. 9, we depict the LHC2760 statistical parameters as a function of collision centrality and compare these LHC2760 results with those we have obtained at RHIC62 [12], shown with open symbols. In all three panels of Fig. 9, we show parameter errors evaluated by SHAREV2 [4] employing the MINOS minimization routine. One can see that the parameter values for chemical nonequilibrium are defined better than for the case with  $\gamma_q = 1$ .

We present LHC2760 hadronization parameters for the nonequilibrium SHM case also in the top section of Table III. In Fig. 9(a), we see the particle source volume  $dV/dy$ , in Fig. 9(b) the chemical freeze-out temperature  $T$ , and in Fig. 9(c) the phase-space occupancies; the different variants are distinguished by superscripts “neq” (nonequilibrium, that is,  $\gamma_q \neq 1, \gamma_s \neq 1$ ), “seq” (semiequilibrium,  $\gamma_q = 1, \gamma_s \neq 1$ ), and “eq” (equilibrium,  $\gamma_q = 1, \gamma_s = 1$ ). To compare with the

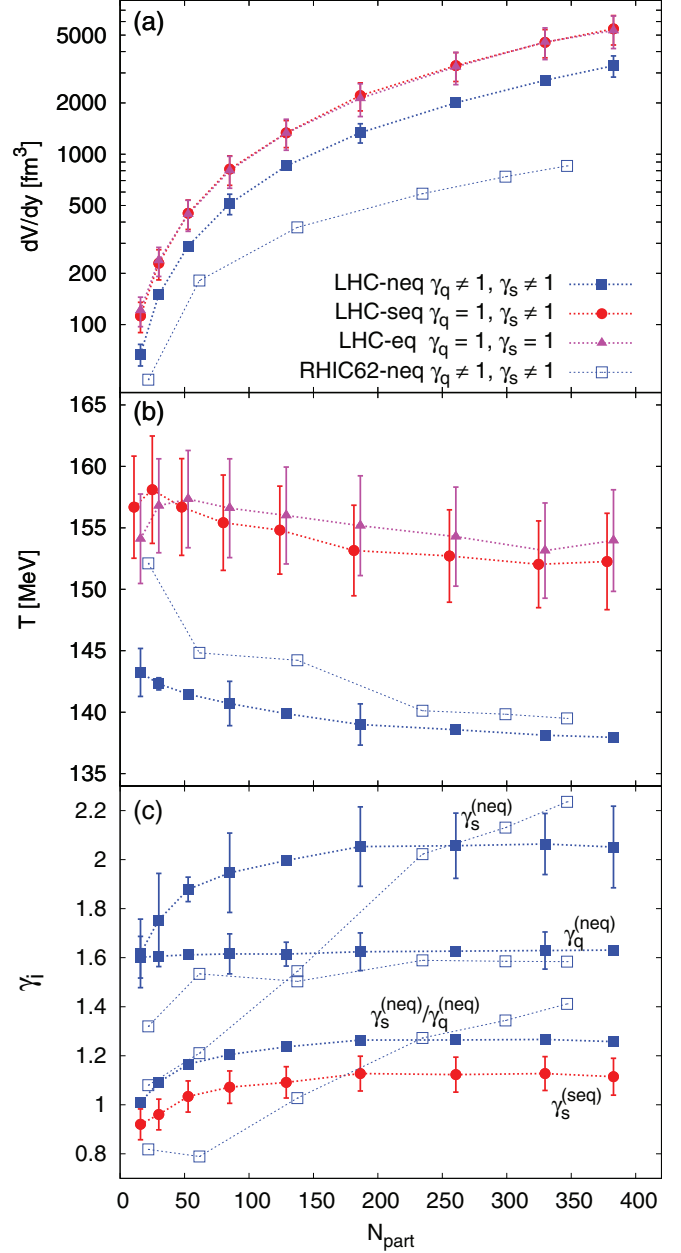


FIG. 9. (Color online) SHM parameters as a function of centrality, i.e., number of participants  $N_{\text{part}}$ , presented for the three different levels of chemical equilibrium, and compared to the chemical nonequilibrium SHM RHIC62 results (open symbols, dashed lines). All lines guide the eye. From top to bottom: (a)  $dV/dy$  (note that the volume for both equilibrium and semiequilibrium SHM variants is so close that symbols overlap); (b)  $T$ , the chemical freeze-out temperature (semiequilibrium symbols are offset to separate them from equilibrium); (c) phase-space occupancies  $\gamma_s^{(\text{neq})}$ ,  $\gamma_q^{(\text{neq})}$ , and for comparison with equilibrium  $\gamma_s^{(\text{seq})}$ ; we also present  $\gamma_s^{(\text{neq})}/\gamma_q^{(\text{neq})}$ .

semiequilibrium SHM variant, we show the ratio  $\gamma_s^{(\text{neq})}/\gamma_q^{(\text{neq})}$ , a ratio which helps to quantify the strangeness to light quark enhancement. This is to be directly compared with the semiequilibrium strangeness phase-space occupancy  $\gamma_s^{(\text{seq})}$ , given fixed  $\gamma_q^{(\text{seq})} = 1$ .

TABLE III. The top section shows chemical nonequilibrium SHM fit parameters  $dV/dy$ ,  $T$ ,  $\gamma_q$ ,  $\gamma_s$ , and  $\chi_{\text{total}}^2$  with ndf (number data less number of parameters) obtained in each centrality bin. For error discussion, see text in Sec. III C. The bottom section presents fireball bulk properties in each bin: energy density  $\varepsilon$ , pressure  $P$ , entropy density  $\sigma$ , strangeness per entropy content  $s/S$ , entropy at LHC2760 compared to RHIC62,  $S_{\text{LHC}}/S_{\text{RHIC}}$ , and net baryon number per entropy ratio  $b/S$ .

Centrality ( $N_{\text{part}}$ )	0%–20%	0%–5%	5%–10%	10%–20%	20%–30%	30%–40%	40%–50%	50%–60%	60%–70%	70%–80%
$dV/dy$ (fm <sup>3</sup> )	2463 ± 6	3304 ± 469	2715 ± 81	2003 ± 47	1337 ± 173	853.9 ± 5.9	512.2 ± 70.1	289.4 ± 5.5	149.8 ± 5.0	66.9 ± 9.7
$T$ (MeV)	138.3 ± 0.0	138.0 ± 0.0	138.1 ± 0.0	138.6 ± 0.0	139.0 ± 1.7	139.9 ± 0.0	140.7 ± 1.8	141.5 ± 0.0	142.3 ± 0.5	143.2 ± 2.0
$\gamma_q$	1.63 ± 0.00	1.63 ± 0.00	1.63 ± 0.08	1.63 ± 0.00	1.62 ± 0.08	1.62 ± 0.05	1.62 ± 0.08	1.61 ± 0.00	1.61 ± 0.00	1.60 ± 0.09
$\gamma_s$	2.08 ± 0.00	2.05 ± 0.17	2.06 ± 0.13	2.06 ± 0.13	2.05 ± 0.16	2.00 ± 0.01	1.95 ± 0.16	1.88 ± 0.05	1.75 ± 0.19	1.62 ± 0.14
$\chi_{\text{total}}^2/\text{ndf}$	9.51/9	3.87/9	3.52/9	3.94/9	3.35/9	4.73/9	4.55/9	5.65/9	6.13/9	4.09/9
$\varepsilon$ (GeV/fm <sup>3</sup> )	0.462	0.453	0.457	0.467	0.476	0.487	0.505	0.516	0.521	0.527
$P$ (MeV/fm <sup>3</sup> )	78.5	77.1	77.7	79.1	80.5	82.3	85.1	86.8	87.9	89.2
$\sigma$ (fm <sup>-3</sup> )	3.20	3.14	3.17	3.23	3.28	3.36	3.46	3.53	3.56	3.60
$s/S$	0.0299	0.0295	0.0297	0.0297	0.0298	0.0294	0.0290	0.0284	0.0272	0.0257
$S_{\text{LHC}}/S_{\text{RHIC}}$	3.07	3.23	3.10	2.93	2.75	2.56	2.33	2.06	1.74	1.27
$b/S \times 10^4$	1.37	2.00	2.08	2.19	2.30	2.45	2.61	2.81	3.06	3.57

For the LHC2760 data, the SHM forcing chemical equilibrium of light quarks (i.e.,  $\gamma_q = 1$  with either  $\gamma_s = 1$  or  $\gamma_s \neq 1$ ) have a very similar volume  $dV/dy$  and similar chemical freeze-out  $T$ , as shown in Figs. 9(a) and 9(b), respectively, with nearly overlapping lines for  $dV/dy$ . In the nonequilibrium approach,  $dV/dy$  is reduced by about 20%–25% and the freeze-out temperature  $T$  by 10% compared to the equilibrium SHM variant. Compared to the RHIC62 results [12] (open symbols) the LHC2760 volume  $dV/dy$  is up to a factor 4 larger while the LHC hadronization temperature  $T$  is 2–5 MeV lower. Thus, given equal number of participants  $N_{\text{part}}$  at RHIC62 and LHC2760, the much larger particle multiplicity  $dN/dy$  requires in consideration of the universal hadronization condition [35] considerably increased transverse dimension of the fireball at the time of hadronization, which we find within our SHM interpretation of hadron production data. We understand this growth of particle multiplicity (and therefore volume) as being attributable to a greater transverse fireball expansion, driven by the greater initial energy density formed in a LHC2760 heavy-ion collision. This corresponds to a greater initial pressure necessary for the matter expansion to the same bulk hadronization conditions as already found at RHIC. The small but systematic decrease of the freeze-out temperature at LHC2760 compared to RHIC62 may be an indication of a greater supercooling caused by the more dynamical LHC expansion.

The freeze-out temperature  $T$  at LHC2760 decreases when considering more central collisions; see Fig. 9(b). In the hadronization scenario used in this work, this can be interpreted as being attributable to a deeper supercooling of the most central and most energetic collision systems. We can extrapolate the freeze-out temperature to  $N_{\text{part}} = 0$  in the figure to set an upper limit on hadronization temperature at LHC2760,  $T_{\text{had}} \rightarrow 145 \pm 4$  MeV, applicable to a small (transverse size) fireball. This, then, is the expected hadronization temperature without supercooling. Excluding, in Fig. 9(b), the most peripheral  $T$ -fit point for RHIC62, which does not have a good confidence level, we see that  $T$  at RHIC62 converges towards the same maximum value as we found at LHC2760,

thus confirming the determination of  $T_{\text{had}}$  as the common hadronization temperature without supercooling.

We show the phase-space occupancies  $\gamma_q, \gamma_s$  in Fig. 9(c). We note that the LHC2760 fit produces nearly a constant  $\gamma_q$  as a function of centrality. However,  $\gamma_s$  (and respectively  $\gamma_s/\gamma_q$ ) decreases for more peripheral collisions towards unity, suggesting that these flavors approach the same level of chemical equilibrium for systems of small transverse size. A similar situation for peripheral collisions was observed for RHIC62. However, at RHIC62, we see a strong centrality dependence of  $\gamma_s$  and, hence,  $\gamma_s/\gamma_q$ . This rapid rise of the RHIC62  $\gamma_s$  as a function of centrality can be attributed to the buildup of strangeness in QGP formed at RHIC62, which is imaged in the later produced strange hadron yield. Note that, omitting the most peripheral RHIC62 point, the peripheral  $\gamma_q$  is nearly the same as at LHC2760. The small difference can be attributed to the smaller allowed value of  $\gamma_q$  for the slightly higher value of  $T$  seen at RHIC62.

We have executed all our fits allowing for the presence of the chemical potentials [Eq. (1)] characterizing the slight matter-antimatter asymmetry present at LHC2760. The quality of the fit is not sufficiently improved including effectively one extra parameter ( $\mu_B$ , because  $\mu_S$  is fixed by strangeness conservation) to assure that the unconstrained results for  $\mu_B$  are convincing. As mentioned in Sec. II A, we smooth the centrality dependence of  $\mu_B$  by introducing baryon stopping fraction at midrapidity, that is, imposing Eq. (4) as an additional data point, a value that we saw a few times in the data without introducing this constraint. This constraint leads to the chemical potentials  $\mu_B$  and  $\mu_S$  presented in Fig. 10, with the baryochemical potential  $1 \leq \mu_B \leq 2.3$  MeV and  $\mu_S = 0.0 \pm 0.5$  MeV for all centralities, values an order of magnitude smaller than at RHIC62 and RHIC200. As we can see, even with the constraint, there are two centralities which do not agree with the trend set by the other seven data points.

Data shown in Fig. 10 are not defined well enough to argue that we see a decrease of baryochemical potential with increasing centrality, because this outcome could be the result of the bias we introduced. However, we think that

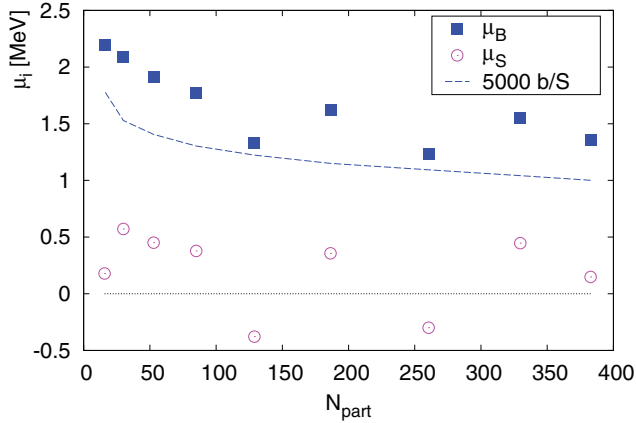


FIG. 10. (Color online) Scatter plot of fitted chemical potentials. The dashed line shows net baryon number over entropy  $b/S$  scaled with 5000.

for the most central collisions at LHC2760 there is some indication that  $\mu_B \simeq 1.5$  MeV. The dashed line in Fig. 10 indicates the resultant baryon per entropy,  $b/S$ , scaled with 5000, these values are also seen in Table III. This is a first estimate of this important result needed for comparison with the conditions prevailing in the big-bang early universe, where  $b/S \simeq 3.3 \times 10^{-11}$  [38].

### B. $p/\pi$ ratio and chemical (non-)equilibrium

The key difference between the three SHM approaches are the values of  $\gamma_{q,s}$ , as seen in Fig. 9(c). In Sec. II A, we argued that the baryon-to-meson ratio, e.g.,  $p/\pi$ , is directly proportional to  $\gamma_q$  and this can be used to distinguish between the three SHM approaches. This ratio is a big problem for the equilibrium SHM [6]. We wish now to quantify this result within our approach and to show that, within the chemical nonequilibrium SHM, the problem is solved.

For this purpose, we redo all fits but making this ratio more explicit in the data analysis. Specifically, first we evaluate the  $p/\pi$  ratio based on the yields of  $p$  and  $\pi$  seen in Table I

$$\frac{p}{\pi} \equiv \frac{p + \bar{p}}{\pi^- + \pi^+}. \quad (7)$$

We estimate the error of the  $p/\pi$  ratio by adopting the relative error of  $p/\pi$  from [6], that is, 6.5%. We include this new data point, the  $p/\pi$  ratio, in the fit. Note that this increases the relative importance of  $p$  and  $\pi$  compared to the other particles included in the fit. Open symbols in Fig. 11(a) depict the data and solid symbols show the resulting output values obtained when we refit with enlarged data set that includes the  $p/\pi$  ratio. There is a minimal change in statistical parameters and physical properties of the fireball which we do not restate. In Fig. 11(b), we show  $\chi^2_{\text{total}}$ .

Even with the increased importance of  $p/\pi$ , the chemical nonequilibrium SHM works very well. However, SHM with fixed  $\gamma_q = 1$  have increased difficulties describing this ratio; that is, there is systematic 1.5–2 s.d. difference of the fit result and data and the value of  $\chi^2_{\text{total}}$  is large. When compared to the  $\chi^2_{\text{total}}$  obtained without the added  $p/\pi$  in Fig. 2, the

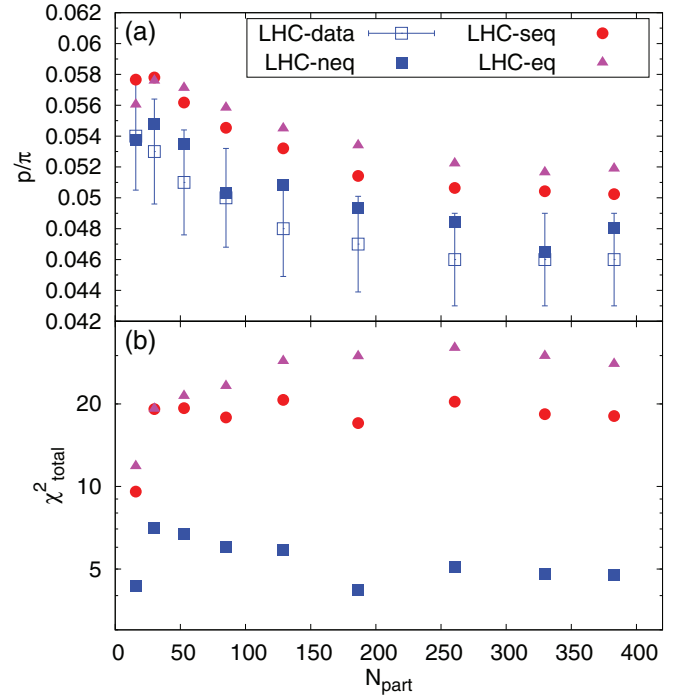


FIG. 11. (Color online) (a) Data and SHM description of  $p/\pi$  ratio fitted together with all other data within the three SHM approaches as a function of centrality. (b) Resulting  $\chi^2_{\text{total}}$  for the three variants. See Sec. III B for details.

nonequilibrium variant shows nearly the same values of  $\chi^2_{\text{total}}$  for all centralities, the  $p/\pi$  ratio is a natural outcome of the nonequilibrium approach. However, SHM approaches with  $\gamma_q = 1$  show additional systematic increase in  $\chi^2$  by a factor of  $\sim 1.3$ – $1.5$  for all centralities. This means that the  $p/\pi$  data are in conflict with the hypothesis  $\gamma_q = 1$ . This demonstrates that the hypothesis of chemical equilibrium of light quarks is incompatible with the baryon-to-meson ratio at LHC2760 and  $\gamma_q \simeq 1.6$  is needed to describe the LHC data. This finding is in agreement with the RHIC200 data [39], where the importance of the  $p/\pi$  ratio was noted.

To compare  $p/\pi$  ratio with our predictions, recall that the picture of universal hadronization condition with universal hadronization pressure  $P = 82 \pm 5$  MeV has been advanced by our group [11,35,40]. For this favored hadronization condition, the  $p/\pi$  ratio is predicted in Table II of Ref. [41] to be  $p/\pi = 0.047 \pm 0.002$ , which agrees practically exactly with the experimental result shown in Fig. 11(a). The ALICE collaboration [30] considers and discusses the mechanism of chemical equilibrium hadron production followed by posthadronization interactions [42–46], specifically proton-antiproton annihilation, to justify the small  $p/\pi$  ratio, as compared to the result of equilibrium SHM alone. However, the annihilation mechanism was proposed based on preliminary data available in a single centrality bin 0%–20%, whereas our work includes more recent and centrality-dependent experimental results [30], allowing a far more conclusive study of the annihilation model.

Aside from  $p\bar{p}$  annihilation, there are  $p\bar{p}$  formation events. The significantly larger abundance (and therefore also density)

of heavy mesons compared to nucleons (see Table II) implies that mesons can be an effective source of nucleon pairs in reactions such as  $p + \bar{p} \longleftrightarrow \rho + \omega$  and many other relevant reactions; see Table II in Ref. [47]. ALICE collaboration notes, that  $p/\pi$  ratio modification after annihilation should disappear in most peripheral collisions owing to smaller volume. We now quantify this effect showing how this fade-out of the annihilation effect would work as a function of centrality. We show that, given the constant  $p/\pi$  ratio in a wide range of centralities [Fig. 11(a)], the effect of posthadronization change of  $p/\pi$  ratio must be negligible.

To establish the centrality dependence of posthadronization nucleon yield changing reactions, we evaluate the total number of  $p\bar{p}$  annihilation events. This number is obtained by integrating annihilation rate over history of the posthadronization matter expansion,

$$N_{\text{annih}} = \int dt N_{\bar{p}}(t) \rho_p(t) \sigma_{\text{annih}} v, \quad (8)$$

where  $v$  is the relative velocity of  $\bar{p}$  and  $p$ . The three-dimensional dilution of the density can be modeled as

$$\rho_p(t) = \frac{\rho_p^h}{(1 + \langle v_{\text{flow}} \rangle t / \langle L \rangle)^3}, \quad \langle L \rangle \simeq [(dV/dy)/(4\pi/3)]^{1/3}, \quad (9)$$

where  $\langle L \rangle$  is the magnitude of the fireball size, and  $\langle v_{\text{flow}} \rangle \simeq 0.6-1c$  is the velocity of the fireball expansion, in both cases averaged over the fireball complex three-dimensional geometry.

The initial density at time of hadronization is obtained from our hadronization study:

$$\rho_p(t_h) \equiv \rho_p^h \simeq \rho_p^h \equiv \frac{dN_p/dy}{dV/dy}. \quad (10)$$

In a wide range of low relative energies, which are relevant here, the event cross section is [48]

$$\sigma_{\text{event}} \equiv \sigma_{\text{annih}} v/c \simeq 46 \text{ mb}. \quad (11)$$

Neglecting the depletion of nucleons [i.e.,  $N_{\bar{p}}(t) \simeq N_{\bar{p}}^h$ ], we find, combining Eq. (8) with Eq. (9), the ratio of annihilated (anti)protons to their total yield  $N_{\text{annih}}/N_{\bar{p}}^h$  and proton mean path before it annihilates  $L_{\text{event}}$ :

$$\frac{N_{\text{annih}}}{N_{\bar{p}}^h} = \frac{\langle L \rangle}{2 \langle v_{\text{flow}}/c \rangle L_{\text{event}}}, \quad L_{\text{event}} = \frac{1}{\sigma_{\text{event}} \rho_p^h}. \quad (12)$$

The upper three lines, in Fig. 12, show  $L_{\text{event}}$  for the three models of hadronization (equilibrium, semiequilibrium, and nonequilibrium) as a function of centrality. The colored band in Fig. 12 represents the error originating from the freeze-out temperature  $T$  uncertainty (see Fig. 9). Note that the nonequilibrium model has much smaller parameter errors, so  $L_{\text{event}}$  is defined more precisely. The event reaction cross section for annihilation is well measured and nearly constant, thus it does not introduce any additional uncertainty to  $L_{\text{event}}$ . The bottom three lines, in Fig. 12 (semiequilibrium and equilibrium lines overlap, because  $dV/dy$  is very similar in these two cases), show how the size  $\langle L \rangle$  of the system changes as a function of centrality. Especially for peripheral

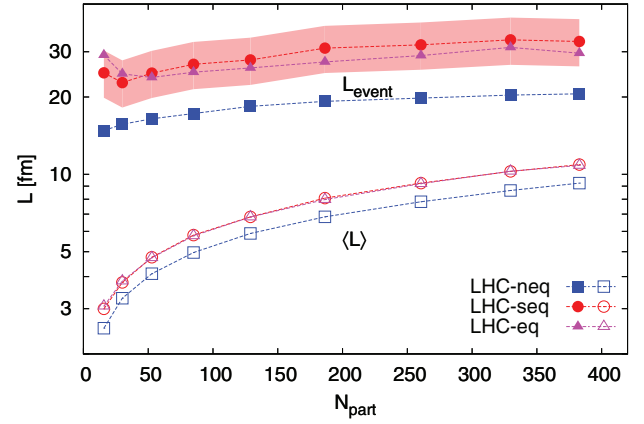


FIG. 12. (Color online) Solid symbols, antiproton annihilation event path  $L_{\text{event}}$  for the three SHM models as a function of centrality; open symbols, fireball size scale  $\langle L \rangle$ . The shaded error band represents error margin originating from the uncertainty of  $T$  (semi)equilibrium SHM. For readability, we omit much smaller error bands for nonequilibrium SHM.

collisions, we see that  $\langle L \rangle \ll L_{\text{event}}$ . The ratio of both length scales provides a measure of the fraction of protons that can be annihilated.

As seen in Fig. 12, from central to semiperipheral ( $N_{\text{part}} \simeq 85$ ) collisions, the ratio of both lengths nearly doubles. This means that the annihilation fraction drops in semiperipheral collisions to about half of the most central value. However, the measured ratio  $p/\pi$  is nearly constant over this range, increasing from  $0.046 \pm 0.003$  to  $0.050 \pm 0.003$ . We interpret this as experimental evidence that the net effect of  $p\bar{p}$  formation and annihilation is insignificant. Therefore, the annihilation of  $p\bar{p}$  pairs cannot serve as the explanation of the disagreement between the equilibrium SHM and observed small value of  $p/\pi$  ratio.

Our estimate of the annihilation effect based on Eq. (12) and the result seen in Fig. 12 is consistent with the annihilation effect reported in Ref. [42], where detailed balance reactions forming  $p\bar{p}$  were not considered. In this work,  $p/\pi$  rises to  $p/\pi = 0.058$  already in the 20%–30% centrality bin ( $N_{\text{part}} = 185$ ), which is more than 3 s.d. above experimental data [see Fig. 11(a)]. Another work, Ref. [44], addresses directly our scenario of describing the experimental  $p/\pi$  ratio and shows that with annihilation the required temperature would be  $T = 165 \pm 5$  MeV, while without baryon annihilation a hadronization temperature of  $T = 145 \pm 5$  MeV is required (initial yield from equilibrium SHM). Such models of posthadronization interactions also predict depletion of  $\Xi$  yield and enhancement of  $\Omega$  yield [44–46], which leads to even greater discrepancy between at least one of the multistrange baryons and equilibrium SHM predictions, because these yields as obtained before annihilation are already, in general, below the experimental data [see Figs. 1(a) and 1(c)].

We do not see a scenario that would allow equilibrium SHM with hadronic afterburners to remain a viable model which can explain (a) the reduction of the  $p/\pi$  ratio from the equilibrium SHM value as a function of centrality and (b) the yields of the multistrange baryons at the same time. However,

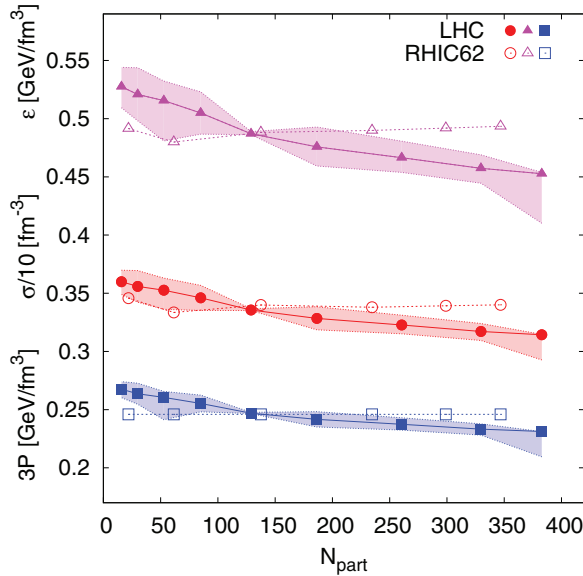


FIG. 13. (Color online) Bulk properties of the fireball as a function of centrality. From top to bottom, energy density  $\epsilon$  (purple triangles), the entropy density  $\sigma$  (red circles), scaled down by factor 10, and the hadronization pressure  $3P$  (blue) squares; LHC2760 values are shown with solid symbols, RHIC62 values are shown with open symbols for comparison. Shaded areas show our estimate of systematic error arising from the uncertainty of  $\gamma_s$ .

the experimental value of  $p/\pi$  ratio was predicted [41]. The experimental result, the almost centrality-independent  $p/\pi$  ratio seen in Fig. 11 (note that the scale is greatly enhanced) is now successfully fitted within nonequilibrium SHM in this work without any modifications to the model or essential change in model parameter values.

### C. Fireball bulk properties

To obtain the bulk physical properties of the source of hadronic particles, we use exactly the same set of particles and the same assumptions about their properties that we employed in the fit procedure. Therefore, the physical properties we determine are consistent with the particle yields that originated our fit. In other words, we sum the energy, entropy, etc., carried away by the observed particles, adding to this observed yield the contributions owing to unobserved particles used in the SHM fit.

The bulk physical properties of the hadronizing fireball, that is, energy, pressure, entropy, and strangeness per entropy content, are shown in the bottom part of Table III and in Fig. 13, where shaded domains show our error estimate. Solid symbols are results of the fit; lines guide the eye. In our SHAREV2 fit with MINOS minimization, the largest uncertainty seen in Table III is the  $\gamma_s$  and  $dV/dy$  error (see Fig. 9); other statistical bulk properties have relatively insignificant errors. As can be seen in Table III, multidimensional fits to data can result in nearly all of the fit error accumulating in the uncertainty of two or even just one parameter. In our fits, we see that the dominant uncertainty is in the volume normalization.

When error is found in a few if not only one parameter, we checked for uncertainty arising within an experimental data stability test. We test how a fit is modified when a small subset of experimental data points is altered arbitrarily but within error. We find that fits comprising input data with such arbitrary modification have, in general, larger errors distributed among all parameters. The convergence of the intensive parameters (e.g.,  $T$ ) in our initial fit suggests only a very small statistical error inherent to the data, while the extensive parameters (e.g.,  $V$ ) show a large error common to particle yield normalization. In this situation, predicted ratios of hadron species should be more precise than their individual errors suggest. This is attributable to the experimental normalization of particle yields being, as this study indicates, strongly correlated. The presence of not vanishingly small error in  $\gamma_s$  could be a signal of additional source of strange hadrons, for example, charm hadron decays.

All fit errors propagate into the properties seen in Fig. 13. Because in Fig. 9 we consider densities, the error in volume does not affect these values. Therefore, by recomputing the properties of the fireball shifting alone the value of  $\gamma_s$  within 1 s.d., we obtain a good error evaluation in the measurement of the bulk physical properties shown in Fig. 13. The point that stands out with very small error is at  $N_{\text{part}} = 130$ . This anomaly is attributable to accidental appearance of a sharp minimum in the highly nontrivial seven-dimensional parameter space.

We are interested in studying the bulk properties of the source of hadrons to test the hypothesis that a QGP fireball was the source of particles observed. For this to be true, we must find appropriate magnitude of bulk properties consistent with lattice results, and at the same time, a variation as a function of centrality that makes good sense. We observe in Fig. 13 a smooth and slow decrease of energy density  $\epsilon$  (top), entropy density  $\sigma$  (middle), and hadronization particle pressure  $P$  (bottom) as a function of centrality. This slow systematic decrease of all three quantities is noted, in particular, comparing to RHIC62 (open symbols), where the properties seem to vary less. This maybe interpreted as an effect of volume expansion at LHC, leading to larger supercooling for larger systems.

The local thermal energy density of the bulk is the source of all particles excluding the expansion flow kinetic energy. The value we find is  $\epsilon \simeq 0.50 \pm 0.05$  GeV/fm<sup>3</sup> in the entire centrality range. Nearly the same value is found within the chemical nonequilibrium approach for RHIC62 [12] and RHIC200 [10]. We note that  $\epsilon$  assumes the smallest value for the most central collisions; see Table III and Fig. 13. The hadronization pressure  $P$  and entropy density  $\sigma$  are also decreasing for more central collisions, which is consistent with our reaction picture of expanding and supercooling fireball; the larger system in central collisions exhibits more supercooling reflected by a decrease of hadronization temperature and the above-mentioned behavior of bulk properties. The error band is (as for  $\epsilon$ ) based on  $\gamma_s$  uncertainty.

In the last row of Table III, we show that entropy yield at LHC2760 is more than 3 times greater than obtained at RHIC62. The entropy yield  $dS/dy$  as a function of participant number is shown in Fig. 14, and the notable feature is that the power-law parametrization displays a nearly linear dependence at RHIC62 while at LHC2760 a strong additional

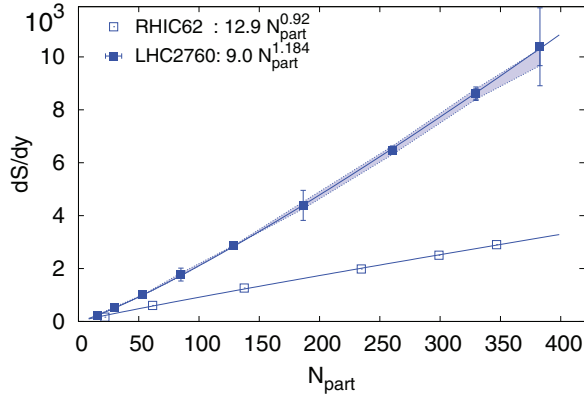


FIG. 14. (Color online) Entropy yield  $dS/dy$  at LHC2760 and at RHIC62 as a function of centrality showing power-law fit parameters in the legend. The colored band represents uncertainty based on  $\gamma_s$  fit uncertainty. Error bars arise from error in the volume  $dV/dy$ .

entropy yield, associated with the faster-than-linear increase, is seen:  $dS/dy \propto N_{\text{part}}^{1.184}$ . Most of the entropy is produced in an initial-state mechanism which remains to be understood and our finding of the nonlinear entropy growth with  $N_{\text{part}}$  adds to the entropy production riddle an important observational result.

However, at LHC2760, one expects a component in the entropy count arising from the inclusion of the decay products of heavy charmed hadrons in the hadron yield. This entropy component is different from entropy produced in initial reactions; this is the entropy arising from hard parton collision production of charm and posthadronization decay of charmed hadrons. It is unlikely that the nonlinearity of the entropy yield is attributable to this phenomenon, as one can easily see that the required charm yield would be very large. We will return, in the near future, to this question. The uncertainty of entropy depicted in Fig. 14 as a shaded band is based alone on  $\gamma_s$  variation, as was obtained for other physical properties in Fig. 13. A further error owing to variance in  $dV/dy$  is shown as a separate error bar. Where it is invisible for the LHC2760, it is hidden in symbol size.

We turn now to study strangeness per entropy  $s/S \equiv (ds/dy)/(dS/dy)$  in the source fireball. We are interested in this quantity because both entropy and strangeness yields are preserved in the hadronization process. Therefore, by measuring  $s/S$ , we measure the ratio of strange quark abundance to total quark and gluon abundance, which determines the source entropy, with a well-known proportionality factor. For the presently accepted small strange quark mass  $m_s(\mu = 2 \text{ GeV}) = 95 \pm 5 \text{ MeV}$  [49], the predicted value shown in Fig. 5 of Ref. [50] is  $s/S \simeq 0.0305 \pm 0.0005$ . Finding this result in our LHC data analysis is necessary to maintain the claim that the source of hadrons is a rapidly disintegrating chemically equilibrated QGP fireball.

In Fig. 15(a), we show the strangeness per entropy  $s/S$  in the source fireball. The solid squares are for the LHC2760, and the open symbols are for RHIC62. We see that  $s/S$  saturates at  $s/S \simeq 0.030$  at LHC2760, a value reached already for  $N_{\text{part}} > 150$ , thus for a smaller number of participating nucleons than we found at RHIC62 and which value remains constant up

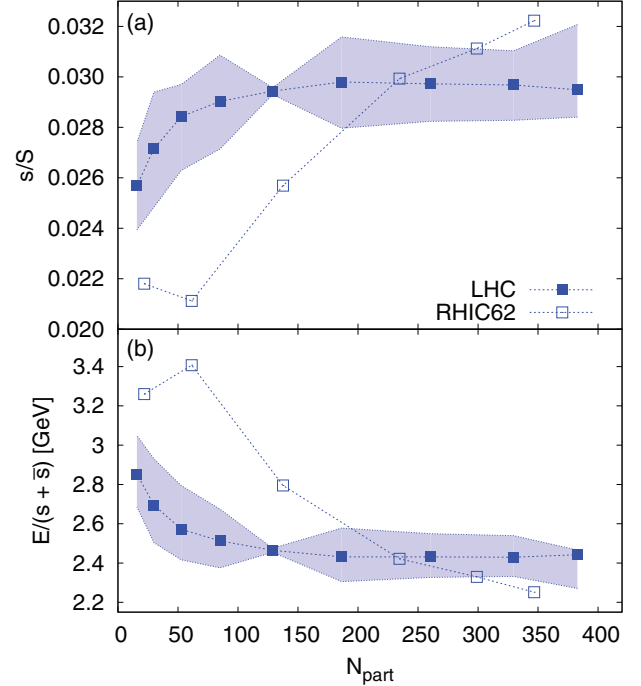


FIG. 15. (Color online) (a) Strangeness per entropy  $s/S$  content of the fireball at LHC2760 (solid squares) and at RHIC62 (open squares) as a function of centrality; (b) the thermal energy cost to make a strange-antistrange quark pair. Colored bands represent uncertainty based on  $\gamma_s$  uncertainty.

to the maximum available  $N_{\text{part}}$ . This agrees with equilibrated QGP hypothesis and suggests that the source of hadrons was under the same conditions for a wide range of centrality.

This constant  $s/S$  value as a function of centrality can be interpreted as an evidence of chemical equilibrium for a QGP source: The strangeness yield normalized to all quark and gluon yield inherent in  $S$  can be constant only if dynamical processes find a chemical balance for the differently sized fireballs. The value  $s/S = 0.03$  is in excellent quantitative agreement with microscopic model of strangeness production and equilibration in QGP [50,51], adopting the latest strange quark mass value. The high QGP strangeness yield oversupplies in hadronization the hadron phase space, resulting in  $\gamma_s \simeq 2$  seen in Fig. 9. Considering the RHIC results shown in Fig. 15(a), we see a slightly higher  $s/S$  saturation limit for most central collisions, though the difference is within the RHIC error band (not shown). It is possible that the  $s/S$  LHC2760 result is 5%–10% diluted owing to inadvertent inclusion in the entropy count of the charm-decay hadrons. It is also of interest to note that at RHIC62,  $s/S$  increases monotonically (discounting the low confidence level most peripheral point) with increasing  $N_{\text{part}}$ , suggesting that the QGP source reaches chemical equilibrium only for most central collisions. At LHC2760 there is such increase for much smaller size fireball corresponding to the smaller collision centrality  $N_{\text{part}} < 150$ .

In Fig. 15(b), we show the thermal energy cost to make a strange quark-antiquark pair. At LHC2760, the energy cost to make a strange pair is practically constant for the wide range of midcentral to central collisions, which confirms that

strangeness in the QGP fireball is in chemical equilibrium at the time of hadronization. The slight increase of the thermal energy cost for small centralities corresponds to the lower yield of strangeness seen in Fig. 15(a). At RHIC62, we see monotonically improving energy efficiency converging to a value slightly below our new LHC2760 result, but well within the error bar at RHIC62 (not shown). The rise of energy cost for smaller systems relates to the fact that a larger and notable fraction of strangeness was produced in first hard-collision processes during the initial stages of the collision which for RHIC62 and LHC2760 results in the higher energy needed to produce one strange-antistrange pair.

#### D. Connection to lattice results and related considerations

Elaborate lattice-QCD numerical computations of QGP-hadron transition regime are available today [24,25] and are comprehensively reviewed in Ref. [26]: the HotQCD collaboration [25] converged for 2 + 1 flavors towards  $T_c = 154 \pm 9$  MeV. The question of how low the value of  $T_c$  can be remains in current intense discussion, as the latest work of Wuppertal–Budapest collaboration [27] suggests a low  $T_c \simeq 145$  MeV. For an expanding QGP with supercooling, this can lead to hadronization below  $T_c \simeq 145$  MeV and near  $T = 140$  MeV. This is indeed the range of values of  $T$  that we find in our chemical nonequilibrium SHM analysis.

A comparison of lattice results with freeze-out conditions is shown in Fig. 16. The two bands near to the temperature axis display the lattice critical temperature in the range  $T_c = 154 \pm 9$  MeV [25] (red online) and  $T_c = 147 \pm 5$  MeV [27] (green online). The symbols show the results of hadronization analysis in the  $T$ - $\mu_B$  plane. We selected here the results for the most central collisions and the heaviest nuclei. The solid (blue) circles are SHARE chemical nonequilibrium results obtained by our group, with result presented in this paper included in the LHC domain and RHIC and SPS results seen, e.g.,

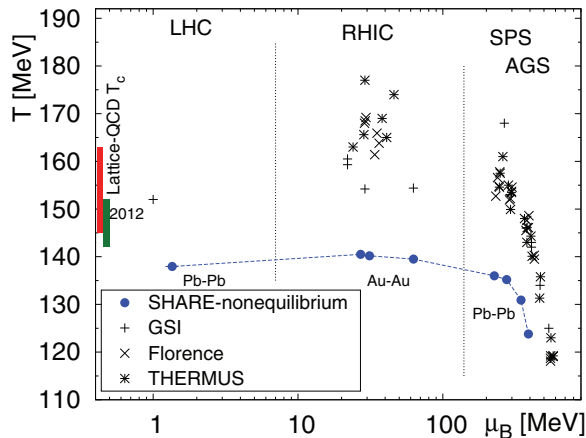


FIG. 16. (Color online) Phase diagram showing current lattice value of critical temperature  $T_c$  calculated by two groups [25,27] and results of this work, as well as our previous results (blue circles) [7,40,52] and results of other groups [6,15,53–58]. Solid circles refer to chemical nonequilibrium; all other symbols refer to fit results with chemical equilibrium of light quarks.

in Refs. [11,40,52]. The LHC2760 freeze-out temperature is in our case clearly below the lattice critical temperature  $T_c$ . As just discussed, this is expected for supercooling followed by sudden hadronization. We show also  $\gamma_q = 1$  results of other groups: GSI [53,54], Florence [15,55,56], THERMUS [57], STAR [58], and ALICE [6]. These results show the chemical freeze-out temperature in numerous cases well above the lattice critical temperature  $T_c$ , which, in essence, means that these SHM calculations are incompatible with lattice calculations.

The two recent lattice results, shown in Fig. 16, challenge the chemical equilibrium hadronization [14] scenario widely used for the past decade, which produces a hadronization temperature above the lattice phase crossover results. Two complementary hypotheses were made in Ref. [14]: (1) there is chemical equilibrium in (2) a long-lived hadron gas phase. Both statements were assumptions without theoretical or experimental evidence “confirmed” by fits to data, which had, even with the large experimental errors, a rather large  $\chi^2$  and thus a negligible confidence level. Therefore, this model needed additional support. Lattice results showing  $T_c = 173 \pm 8$  MeV were often introduced in support of equilibrium-SHM. Such a high  $T_c$  appears, for example, in Fig. 10 of Ref. [59], but reading the text, one sees that it applies to the mathematical case of two light quark flavors on discrete space-time. Allowing for strangeness flavor in QGP, the hadronization temperature must decrease. Therefore, already a decade ago  $T_c = 154 \pm 8$  MeV was the best estimate for 2 + 1 flavors, leading to the consensus range  $T_c = 163 \pm 15$  MeV before continuum limit. Present-day continuum value we estimate to be  $T_c \simeq 150 \pm 7$  MeV combining the two results seen in Fig. 16.

An important requirement for the full chemical nonequilibrium hadronization approach is that in the hadronization process, quark flavor abundances emerge as produced at an earlier and independent stage of fireball evolution. Our analysis relies on hadronization being fast, not allowing a significant modification of the available quark abundances. These quark abundances at LHC in a wide range of centralities and in most central RHIC collisions are near to the QGP chemical equilibrium abundance. For the quark yields to remain largely unchanged during hadronization and after, it is necessary that the transformation from QGP to hadrons (hadronization) occurs suddenly and at a relatively low temperature, near the expected chemical freeze-out point, where particle abundances stop evolving. The two-pion correlation experimental results favor sudden hadronization, which has been seen in the results for a long time [21]. The sudden hadronization model was required for consistency with these results [22,23]. It is associated with chemical nonequilibrium SHM analysis of the data [7,8]. Today, with lattice QCD transition conditions reaching a low- $T$  consensus, the only SHM approach that remains valid is the chemical nonequilibrium.

## IV. DISCUSSION

### A. What is new at LHC

The primary difference between RHIC62 and LHC2760 data is a 4-times-larger transverse volume  $dV/dy$  at

hadronization, as seen in Fig. 9(a). The increase of volume at LHC compared to RHIC, rather than a change of hadronization temperature, shows a common source of hadrons, a signature of QGP formation. The increased volume is in qualitative agreement with the two-pion correlation studies [60]. Given the nearly constant entropy density at hadronization, the growth of volume drives the total entropy yield, which is up to 3.2 times greater at LHC2760 than at RHIC62.

Other differences of LHC2760 compared to RHIC62 are

- (i) an order-of-magnitude-smaller baryochemical potential  $\mu_B \simeq 1.5$  MeV (see Fig. 10);
- (ii) phase-space occupancy  $\gamma_q$  constant as a function of centrality;
- (iii) earlier saturation of  $\gamma_s$  as a function of centrality, and thus  $\gamma_s/\gamma_q$  ratio following the behavior of  $\gamma_s$ .

For comparison, at RHIC62, we have a fast increase of  $\gamma_s$  over the entire range of  $N_{\text{part}}$ , as is shown in Fig. 9(c). The LHC2760 result is interpreted to mean that the QGP fireball is rapidly chemically equilibrated already for small  $N_{\text{part}}$ , while at RHIC62, we must have a large value of  $N_{\text{part}}$ , that is a large volume, and thus large life span, to achieve full strangeness chemical equilibrium in the QGP fireball. The value  $s/S = 0.03$  is in excellent qualitative agreement with microscopic model of strangeness production and equilibration in QGP and the associated predictions of the final-state yield [50,51].

As a comparison of our present work with our predictions [41] shows, the yield of strangeness is  $\sim 20\%$  below our prior expectations. These were motivated by consideration of a very rapidly diluting QGP fireball, wherein the early strangeness QGP equilibrium is preserved and leads to overabundance, above QGP chemical equilibrium at time of hadronization. Such behavior was indicated given the RHIC results showing a steady rise; see Fig. 15(a) for RHIC62. Instead, we find a perfectly equilibrated QGP fireball: The observed value of  $s/S \simeq 0.03$  is expected for a chemically equilibrated QGP fireball near hadronization condition. This equilibrium QGP saturated value  $s/S = 0.03$  is observed for many centralities. Because to obtain our prediction we used  $s/S = 0.037$ , both the value of  $\gamma_s$  and yields of kaons are equally  $\sim 20\%$  suppressed compared to expectation [41], as are other strange particles. How this is possible will be one of the riddles that future data and theoretical modeling will need to address. For us, this strangeness suppression compared to expectation is the most remarkable difference from RHIC data that we have found in this first LHC result analysis.

### B. Centrality dependence

Considering the bulk properties of the fireball at hadronization, the most remarkable finding is that there is so little centrality dependence. This means that at LHC2760 the source of hadrons is a hot drop of energy that varies mainly in volume as we vary the collision geometry. This applies to energy density  $\varepsilon \simeq 0.50 \pm 0.05$  GeV/fm<sup>3</sup>, hadronization pressure  $P$ , and entropy density  $\sigma$  in the entire centrality range; see Table III and Fig. 13. These bulk properties decrease monotonically and slowly and assume the smallest value for the most

central collisions, supporting the reaction picture of expanding and supercooling fireball; the larger system supercools a bit more. Recall that the error bands in Fig. 13 are based on  $\gamma_s$  uncertainty. The one clear centrality dependence of the fireball we find is the rapid rise and early appearance of the strangeness yield saturation seen in Fig. 15(a).

The chemical freeze-out temperature  $T$  decreases by about 3 MeV at all centralities compared to RHIC62; see middle panel in Fig. 9 (we do not consider here the most peripheral RHIC62 result, which has a small confidence level). We believe that this result is related to the need to expand and supercool further the initial energy and entropy rich LHC2760 fireball. The large expanding QGP matter pushes further out, supercooling more and yielding a further reduction in the sudden hadronization temperature. The freeze-out temperature  $T$  increases towards more peripheral collisions [see Fig. 9(b)], which can be explained by the disappearance of supercooling present for the most central and most energetic collision systems. Considering the behavior of both LHC2760 and RHIC62 for  $N_{\text{part}} \rightarrow 0$ , we obtain  $T_{\text{had}} \rightarrow 145 \pm 4$  MeV, applicable to hadronization without supercooling. This value is in good agreement with the latest lattice result [27] for transformation temperature from QGP to hadrons.

The value of temperature and its behavior as a function of centrality and heavy-ion collision energy suggest that produced hadrons emerge directly from a sudden breakup of quark-gluon plasma. The hadron particle density at this low  $T$  is sufficiently low to limit the particle number changing reactions and render these insignificant.  $T = 145\text{--}140$  MeV is at and below the expected QGP phase transition. The presence of chemical nonequilibrium at this low  $T$  means that hadrons did not evolve into this condition, but must have been produced directly from the deconfined phase. This is consistent with the two-pion correlation time parameter, which suggests that particles are produced at a scale which is sudden compared to the size of the system, as is expected for a supercooled QGP state undergoing, e.g., a filamenting breakup at  $T \simeq 140$  MeV, and the result of such dynamics is qualitatively consistent with the features described here [21].

The second-to-last row in Table III shows the ratio of entropy at LHC2760 to RHIC62,  $S_{\text{LHC}}/S_{\text{RHIC}}$ , within the rapidity interval  $-0.5 \leq y \leq 0.5$ . The entropy enhancement factor increases monotonically with centrality, from ratio of 1.27 in the most peripheral bin to ratio 3.23 in the most central bin. This increase requires volume-dependent additional entropy production mechanisms, which are more effective for the more central, larger  $N_{\text{part}}$ , collisions. Such an increase can arise from hard-parton-collision-generated jets, which are better quenched in the larger volume of matter, and, in addition, in abundant charm production, which decays into hadrons and appears as additional hadron multiplicity, i.e., entropy. As long as the additional entropy is generated in early stages of the fireball evolution, this has little impact on SHM method of approach in study of hadronization. For example, the quenching of QCD jets feeds thermal degrees of freedom that can convert a part of its energy into strangeness. However, charm decay is different because it occurs after hadronization. Thus, it needs to be accounted for and/or proved irrelevant. It is possible that a charm-decay entropy-generating mechanism

may be the cause of the slight (5%) strangeness  $s$  over entropy  $S$  dilution at LHC2760 [see Fig. 15(a)].

### C. What we learn about hadronization at LHC

The full chemical nonequilibrium is introduced by the way of the parameter  $\gamma_q \neq 1$ . This allows one to describe a situation in which a source of hadrons disintegrates faster than the time necessary to reequilibrate the yield of light quarks present. The two-pion correlation data provide experimental evidence that favors a rapid breakup of QGP with a short time of hadron production [21], and thus favors very fast, or sudden, hadronization [22,23]. There has been for more than a decade an animated discussion if the parameter  $\gamma_q$  is actually needed with arguments such as simplicity used to invalidate the full chemical nonequilibrium approach.

We have shown that *only* the chemical nonequilibrium SHM describes very well all available LHC2760 hadron production data obtained in a wide range of centralities obtained in the rapidity interval  $-0.5 \leq 0 \leq 0.5$ , and the outcome is consistent with lattice QCD results. We successfully fit the data with  $\chi^2/\text{ndf} < 1$  for all centrality bins, and show a smooth systematic behavior as a function of centrality of both the statistical SHM parameters (see Fig. 9) and bulk physical properties (see Fig. 13) that allow a simple and consistent interpretation. SHM is validated at LHC2760 as it describes precisely yields of different particles in a wide range of collision centrality and which span over more than 5 orders of magnitude; see Fig. 6.

We have shown that it is impossible to fit the ratio  $p/\pi = 0.046 \pm 0.003$  [5,6] together with the other data, when choosing a SHM with  $\gamma_q = 1$ . However,  $p/\pi \simeq 0.05$  is a natural outcome of our chemical nonequilibrium fit where  $\gamma_q \simeq 1.6$ . This result was predicted [41]: Within the chemical nonequilibrium SHM,  $p/\pi|_{\text{prediction}} = 0.047 \pm 0.002$  for  $P = 82 \pm 5 \text{ MeV/fm}^3$  is in agreement with experimental result we discuss here, for most central collisions  $p/\pi|_{\text{ALICE}} = 0.046 \pm 0.003$ .

We have discussed, in Sec. III B, the possibility of the  $p/\pi$  ratio evolving after hadronization and found this scenario to be highly unlikely considering that experimental ratio  $p/\pi$  does not vary in a wide centrality domain. Therefore, the fact that chemical equilibrium SHM variant overpredicts  $p/\pi$  and produces a poor  $\chi^2_{\text{total}}$ , see Fig. 11(b), demonstrates that the chemical equilibrium SHM approach (with or without posthadronization interactions) does not work at LHC2760. Further evidence for the chemical nonequilibrium SHM comes from the universality of hadronization at LHC2760 and at RHIC; see Sec. III C and Ref. [35].

### D. Predicting experimental results

Our prediction of hadron yields [41] required as input the charge particle multiplicity  $dN_{\text{ch}}/dy$ , which normalizes the reaction volume  $dV/dy$ . Further, we assumed strangeness per entropy content  $s/S$ , and the nearly universal hadronization pressure with preferred value  $P = 82 \pm 5 \text{ MeV/fm}^3$ . This is accompanied by the strangeness conservation constraint  $\langle s - \bar{s} \rangle = 0$  and the projectile-target charge to baryon ratio  $Q/B = 0.4$  and, as baryochemical potential cannot yet be

fully defined, an approximate value  $\mathcal{O}(1) \text{ MeV}$ . Using this input with a 5% error, we obtain the most compatible values of  $dV/dy$ ,  $T$ ,  $\gamma_q$ ,  $\gamma_s$  and chemical potentials, and we can evaluate the particle yields along with fireball properties.

We have redone the predictions for  $\sqrt{s_{NN}} = 2.76 \text{ TeV}$  case with the tested and released SHAREV2.2 code and find that the prerelease SHARE predictions in Ref. [41] were made for  $dN_{\text{ch}}/dy = 2150$  and not for  $dN_{\text{ch}}/dy = 1800$ . Therefore, all absolute hadron yields stated in Ref. [41] are normalized to be  $\sim 20\%$  too large, in addition to the strangeness overcount originating in the assumption  $s/S = 0.037 > 0.030$ . The ratios of hadrons with the same strangeness content were correctly predicted.

Applying our prediction method using the updated strangeness value of  $s/S = 0.030$  and a more precise hadronization pressure estimate  $P \simeq 77 \pm 4 \text{ MeV/fm}^3$  results, for  $\sqrt{s_{NN}} = 2.76 \text{ TeV}$ , in the accurate prediction of all hadron particle yields, statistical parameters, and fireball bulk properties, without using as input any individual hadron yield. This validates our approach [41], which can be applied to the forthcoming Pb-Pb collisions at  $\sqrt{s_{NN}} = 5.5 \text{ TeV}$  or in the RHIC beam energy scan. Noting that the multiplicity of produced hadrons is synonymous with entropy of the fireball, this result means that all hadron yields can be predicted within the framework of chemical nonequilibrium SHM using as input the properties of the bulk matter in the fireball.

### E. Conclusions and outlook

We have shown that the nonequilibrium SHM model in the LHC reaction energy range is yielding a very attractive data fit. We have argued that nonequilibrium SHM is today favored by the lattice results, because we must have  $T < T_c$ , and the lattice is moving lower in  $T_c$ ; see  $T_c = 147 \pm 5 \text{ MeV}$  [27]. Only the nonequilibrium SHM range  $T < 145 \text{ MeV}$  remains convincingly compatible, considering the dynamics of the fireball expansion  $\Delta T \equiv T_c - T$  is of magnitude where we would like it for supercooling. Moreover, the chemical nonequilibrium SHM is favored by offering simplicity, as it needs no afterburners. Occam's razor argument (*lex parsimoniae*) can be used to conclude that nonequilibrium SHM is a valid precise description of multihadron production.

The good fit within the realm of nonequilibrium SHM of all observed particles allows us to predict with some confidence the yields of yet-unmeasured hadrons within the chemical nonequilibrium SHM scheme, which are seen in Table II. The question is how stable these yields are when data basis of the fit increases to include new measurement. A small SHM parameter change should be expected also when we refine the theoretical model by adding features, such as inclusion of hadrons from perturbative QCD jets and/or charm hadron decay contribution to hadron yields. We believe that predictions for the primary "stable" hadrons such as  $\eta$  are accurate. However, even the minor changes in SHM parameters can have a relatively large effect, especially for antimatter clusters shown in the bottom part of Table II: In the anti- $\alpha$ , we have 12 antiquarks, and a few % error in understanding their primordial yield is raised to 12th power.

It is quite remarkable that despite a change by a factor of 45 in reaction energy, we find for all centralities at both LHC2760 and RHIC62, that the energy density of hadronizing matter is  $0.50 \pm 0.05$  GeV/fm<sup>3</sup>, as is seen in Fig. 13. In fact, the present-day data favor a systematic decrease of hadronization pressure  $P$  from peripheral towards central collisions as compared to earlier RHIC62 [12], RHIC200 [10] and our preliminary LHC analysis with limited data set [35]. It is possible that the more dynamical expansion of the LHC2760 fireball and deeper supercooling of the fireball are the cause.

We checked that assuming universal hadronization pressure, we could obtain a very good fit to particle data for all centrality LHC2760 data bins. This means that if and when more hadron yield data are available, the decrease in bulk properties with centrality seen in Fig. 13 could easily disappear. Therefore, the presence of a constant critical hadronization pressure [40] could extend from SPS to LHC. We are investigating this hypothesis, as well as the possibility that another quantity governs universality of hadronization. We hope to return to the matter as soon as we have understood better the final-state contributions to hadron yields from charmed hadron decays.

We have shown that the precise hadron yields measured by the ALICE collaboration at LHC2760 have offered a vast new opportunity to explore the properties of the QGP fireball and to understand the dynamics of its evolution and matter production. We are able to quantify the key physical properties at this early stage. With more data becoming available, we expect a significant refinement and improved understanding of both the QGP fireball and mechanisms of matter creation out of the deconfined QGP phase.

### F. Update

We have verified that the new results [61,62] on strange hadron multiplicities which became available at the beginning

of the SQM2013 meeting at the end of July 2013 are fully compatible: The  $K_S$ ,  $\Omega$ , and  $\Xi$  are in remarkable agreement with our here-presented evaluations and  $\Lambda$  yield is as much off as the preliminary  $\Lambda/\pi$  ratio we fitted (see Fig. 7); that is, the theoretical  $\Lambda$  yield is in general about 1.2 s.d. smaller compared to the final experimental  $\Lambda$  yield. Here we note that the presented fits are carried out without taking into account charmed particle decay products, which, beyond the generally enhanced overall hadron multiplicity, produce a non-negligible number of additional strange baryons.

### ACKNOWLEDGMENTS

This work has been supported by a grant from the US Department of Energy, Grant No. DE-FG02-04ER41318; Laboratoire de Physique Théorique et Hautes Energies, LPTHE, at University Paris 6 is supported by CNRS as Unité Mixte de Recherche, UMR7589. J.R. thanks CERN-PH-TH for the hospitality while most of this work was carried out. J.R. thanks members of ALICE collaboration, in particular Karel Safarik, Boris Hippolyte, and Federico Antinori, for many conversations and clarifications.

### APPENDIX: DATA REBINNING

#### 1. Rebinning multistrange hadron yields

Because there is no literature stating explicitly the yields of  $\Xi$  and  $\Omega$  in Pb-Pb collisions, we proceed to obtain these results by unfolding the preliminary enhancement data. We combine the yield of  $\Xi$  and  $\Omega$  produced in  $p$ - $p$  collisions at 7 TeV [34] stated in Table IV and labeled “ $pp$ ” in the third column therein, with the “preliminary” enhancement  $E$  relative to  $p$ - $p$  and normalized to a pair of participating nucleons shown in Ref. [31] and which we also show in the fifth column of Table IV. We generate the first data point for the centrality

TABLE IV. Enhancement of multistrange baryon yields per participant pair relative to  $p$ - $p$  collisions,  $p$ - $p$  yields, and calculated yields in Pb-Pb, which we use as input to our interpolation as a function of  $N_{\text{part}}$ .

Particle	Ref.	Centrality	$\langle N_{\text{part}} \rangle$	$p$ - $p$ data $(dN/dy)_{pp}$ and enhancement $E$	$(dN/dy)_{\text{PbPb}} = E 0.8 (dN/dy)_{pp} (\langle N_{\text{part}} \rangle / 2)$	
$\Xi^-$	[34]	$p$ - $p$	2	$(8.0 \pm 0.7) \times 10^{-3}$		
	[32]	60%–90%	17.6	$E = 1.58 \pm 0.18$	$0.090 \pm 0.010$	
		40%–60%	68.8	$E = 2.48 \pm 0.26$	$0.55 \pm 0.06$	
		20%–40%	157	$E = 2.95 \pm 0.32$	$1.51 \pm 0.17$	
		0%–20%	308	$E = 3.08 \pm 0.33$	$3.08 \pm 0.33$	
$\Xi^+$	[34]	$p$ - $p$	2	$(7.8 \pm 0.7) \times 10^{-3}$		
	[32]	60%–90%	17.6	$E = 1.57 \pm 0.19$	$0.087 \pm 0.011$	
		40%–60%	68.8	$E = 2.56 \pm 0.26$	$0.56 \pm 0.06$	
		20%–40%	157	$E = 3.20 \pm 0.35$	$1.59 \pm 0.17$	
		0%–20%	308	$E = 3.00 \pm 0.32$	$2.91 \pm 0.32$	
$\Omega^-$ $\overline{\Omega}^+$	[34]	$p$ - $p$	2	$(0.67 \pm 0.08) \times 10^{-3}$		
		$p$ - $p$	2	$(0.68 \pm 0.08) \times 10^{-3}$	$\Omega^-$	$\overline{\Omega}^+$
$\frac{(\Omega^- + \overline{\Omega}^+)}{2}$	[32]	60%–90%	17.6	$E = 2.56 \pm 0.53$	$0.012 \pm 0.003$	$0.012 \pm 0.003$
		40%–60%	68.8	$E = 4.57 \pm 0.79$	$0.08 \pm 0.02$	$0.08 \pm 0.02$
		20%–40%	157	$E = 5.23 \pm 0.95$	$0.22 \pm 0.05$	$0.21 \pm 0.04$
		0%–20%	308	$E = 6.97 \pm 1.27$	$0.57 \pm 0.12$	$0.56 \pm 0.12$

bin 0%–20% by averaging the number of participants in the centrality bins from 0% to 20% shown in Table 1 of Ref. [29]. We reduce the yields of both  $\Xi$  and  $\Omega$  by a constant factor of 0.8 to compensate for the difference in collision energy  $\sqrt{s} = 7$  TeV in  $p$ - $p$  collisions and  $\sqrt{s_{NN}} = 2.76$  TeV in Pb-Pb. We obtained the magnitude of this energy correction factor by comparing with the actual yield for the 0%–20% centrality bin given in Ref. [28]. To disentangle the combined yield of  $\Omega + \bar{\Omega}$ , we use the separated  $\Omega$  and  $\bar{\Omega}$  yields from  $p$ - $p$  collisions [34]; see Table IV.

We use the relative errors of the enhancements to estimate the errors of the multistrange baryon yields, that is  $\sim 11\%$  for  $\Xi$  and  $\sim 20\%$  for  $\Omega$ . Our adopted  $\Omega$  error is larger by  $\sim 3\%$  than the error of its yield in the 0%–20% centrality bin [28]. We adopted this slightly increased error to account for a procedure which leads us to estimate the yield of  $\Omega$ ,  $\bar{\Omega}$  based in part on  $\Omega + \bar{\Omega}$  yield. The mathematical operations leading to the yields, the yields, and widths we use are stated in self-explanatory fashion in Table IV.

To account for the different centrality bins for multistrange baryons as compared to  $\pi$ ,  $K$ ,  $p$ , and  $\phi/K$ , we express the centrality bins in terms of average number of participants according to [29] and then interpolate every particle yield  $dN/dy$  available as a function of  $N_{\text{part}}$  with a power law,

$$\frac{dN(N_{\text{part}})}{dy} = a N_{\text{part}}^b + c, \quad (\text{A1})$$

where  $a$ ,  $b$ , and  $c$  are free parameters. The form of the function has no immediate physical motivation; it serves well the purpose of unifying the data across incompatible centrality bins. This method enables us to evaluate the invariant yields for any given  $N_{\text{part}}$ , i.e., arbitrary centrality, and thus enables us to include the multistrange baryon yields in this analysis. Interpolation parameters together with  $\chi^2$  of each particle interpolation are summarized in Table V. For completeness and potential future use, we present also the parametrization of  $\pi^\pm$ ,  $K^\pm$ , and  $p^\pm$  which do not require rebinning. Small values of  $\chi^2/\text{ndf}$  show that our description is accurate in the given interval of  $N_{\text{part}}$ . Interpolation curves are depicted with dashed lines in Fig. 6 for particle yields.

TABLE V. Interpolation parameters of particle yields as defined in Eq. (A1).

Particle	$a$	$b$	$c$	$\chi^2/\text{ndf}$
$\pi^+$	0.725	1.160	-0.890	0.30/7
$\pi^-$	0.724	1.160	-0.864	0.22/7
$K^+$	0.0935	1.187	-0.174	0.07/7
$K^-$	0.0927	1.188	-0.158	0.06/7
$p$	0.0432	1.116	-0.047	0.32/7
$\bar{p}$	0.0502	1.089	-0.088	0.26/7
$\Xi^-$	0.005 52	1.108	-0.043	0.12/1
$\bar{\Xi}^+$	0.007 62	1.049	-0.067	0.70/1
$\Omega^-$	0.000 286	1.324	-0.0006	0.40/1
$\bar{\Omega}^+$	0.000 309	1.308	-0.0011	0.21/1
$K^{*0}/K^-$	See text for details			0.032/1
$\Lambda/\pi$	See text for details			0.0054/1

TABLE VI. Experimentally measured ratios used as input to our interpolation as a function of  $N_{\text{part}}$ .

Ratio	Ref.	Centrality	$\langle N_{\text{part}} \rangle$	Experimental ratio
$K^{*0}/K^-$	[31]	60%–80%	22.6	$0.333 \pm 0.084$
		40%–60%	68.8	$0.285 \pm 0.061$
		20%–40%	157	$0.245 \pm 0.066$
		0%–20%	308	$0.194 \pm 0.051$
$\frac{2\Lambda}{(\pi^- + \pi^+)}$	[31]	60%–80%	22.6	$0.0355 \pm 0.0041$
		40%–60%	68.8	$0.0371 \pm 0.0042$
		20%–40%	157	$0.0365 \pm 0.0042$
		10%–20%	261	$0.0355 \pm 0.0041$
		0%–10%	357	$0.0336 \pm 0.0040$

## 2. Rebinning $K^{*0}/K^-$ , $\Lambda/\pi$ hadron ratios

We include particle ratios  $K^{*0}/K^-$ ,  $\phi/K^-$ , and  $\Lambda/\pi \equiv 2\Lambda/(\pi^- + \pi^+)$  [31]. This adds  $\Lambda$ ,  $K^{*0}$ , and  $\phi$  into our data set. Because in some ratios certain systematic uncertainties of individual yields cancel out, introduction of ratios is reducing the overall error of the global fit. The ratio  $\phi/K$  has an experimental data point in each centrality bin we analyze, removing the need for interpolation or rebinning. Thus, the following addresses only  $K^{*0}/K^-$  and  $\Lambda/\pi$ .

There are four (five) data points for  $K^*/K$  ( $\Lambda/\pi$ ), which we present in Table VI. We describe  $K^*/K$  dependence on  $N_{\text{part}}$  with a power law,

$$\frac{K^*}{K} = f(N_{\text{part}}) = 16.23(N_{\text{part}}^{-0.0034} - 1) + 0.512, \quad (\text{A2})$$

with total  $\chi^2/\text{ndf} = 0.032/1$ . Systematic behavior of  $\Lambda/\pi$  as a function of centrality is qualitatively different from  $K^*/K$  (see Fig. 7); a power law is not sufficient to properly describe the data. We use a sum of two power laws in the form

$$\frac{\Lambda}{\pi} = f(N_{\text{part}}) = -6.79 \times 10^{-5} N_{\text{part}}^{0.848} - 2 N_{\text{part}}^{-0.00135} + 2.03, \quad (\text{A3})$$

with  $\chi^2/\text{ndf} = 0.0054/1$ . In these two cases, the form of the ratio functions has no immediate physical meaning; it is invented to provide an accurate empirical description; note that the bottom of the Table V presents the fit quality of these two ratios.

Interpolation curves are depicted with dashed lines, in Fig. 7, for  $K^*/K$  and  $\Lambda/\pi$  ratios. To assign an error to the interpolated data points, we take the average nearby experimental error for the given particle yield or ratio. However, by extrapolating the  $K^*/K$  ratio to  $N_{\text{part}} = 382$ , we introduce systematic error owing to our choice of the functional form of Eq. (A2). To account for this effect, we multiply the error of  $K^*/K$  by 2 (1.5) in the most (second-most) central bin we analyze as indicated by the shaded area in Fig. 7. As seen in Fig. 6, we also extrapolate  $\Omega$ ,  $\Xi$ , but we do not believe that this adds to the already significant error, considering that our power law interpolation functions describe other hadron yields up to  $N_{\text{part}} = 382$ .

- [1] P. Bozek and I. Wyskiel-Piekarska, *Phys. Rev. C* **85**, 064915 (2012).
- [2] M. Rybczynski, W. Florkowski, and W. Broniowski, *Phys. Rev. C* **85**, 054907 (2012).
- [3] W. Broniowski and W. Florkowski, *Phys. Rev. Lett.* **87**, 272302 (2001).
- [4] G. Torrieri, S. Steinke, W. Broniowski, W. Florkowski, J. Letessier, and J. Rafelski, *Comput. Phys. Commun.* **167**, 229 (2005); G. Torrieri, S. Jeon, J. Letessier, and J. Rafelski, *ibid.* **175**, 635 (2006).
- [5] B. Abelev (ALICE Collaboration), [arXiv:1209.3285](https://arxiv.org/abs/1209.3285) [nucl-ex].
- [6] B. Abelev *et al.* (ALICE Collaboration), *Phys. Rev. Lett.* **109**, 252301 (2012).
- [7] J. Letessier and J. Rafelski, *Phys. Rev. C* **59**, 947 (1999).
- [8] J. Letessier and J. Rafelski, *Int. J. Mod. Phys. E* **9**, 107 (2000); J. Rafelski and J. Letessier, [arXiv:nucl-th/9903018](https://arxiv.org/abs/nucl-th/9903018).
- [9] J. Letessier and J. Rafelski, *Camb. Monogr. Part. Phys. Nucl. Phys. Cosmol.* **18**, 1 (2002).
- [10] J. Rafelski, J. Letessier, and G. Torrieri, *Phys. Rev. C* **72**, 024905 (2005).
- [11] J. Letessier and J. Rafelski, *Eur. Phys. J. A* **35**, 221 (2008).
- [12] M. Petran, J. Letessier, V. Petracek, and J. Rafelski, *Acta Phys. Pol. B Proc. Suppl.* **5**, 255 (2012).
- [13] F. Becattini, M. Bleicher, T. Kollegger, M. Mitrovski, T. Schuster, and R. Stock, *Phys. Rev. C* **85**, 044921 (2012).
- [14] P. Braun-Munzinger, D. Magestro, K. Redlich, and J. Stachel, *Phys. Lett. B* **518**, 41 (2001).
- [15] F. Becattini, P. Castorina, A. Milov, and H. Satz, *Eur. Phys. J. C* **66**, 377 (2010).
- [16] F. Becattini, J. Manninen, and M. Gazdzicki, *Phys. Rev. C* **73**, 044905 (2006).
- [17] P. Braun-Munzinger, K. Redlich, and J. Stachel, in *Quark Gluon Plasma 3*, edited by R. C. Hwa and Xin-Nian Wang (World Scientific, Singapore, 2004), pp. 491–599.
- [18] A. Andronic *et al.*, *Nucl. Phys. A* **837**, 65 (2010).
- [19] J. Rafelski, *Phys. Lett. B* **262**, 333 (1991).
- [20] J. Rafelski, J. Letessier, and A. Tounsi, *Acta Phys. Pol. B Proc. Suppl.* **27**, 1037 (1996).
- [21] L. P. Csernai, M. I. Gorenstein, L. L. Jenkovszky, I. Lovas, and V. K. Magas, *Phys. Lett. B* **551**, 121 (2003).
- [22] L. P. Csernai and I. N. Mishustin, *Phys. Rev. Lett.* **74**, 5005 (1995).
- [23] J. Rafelski and J. Letessier, *Phys. Rev. Lett.* **85**, 4695 (2000).
- [24] G. Endrodi, Z. Fodor, S. D. Katz, and K. K. Szabo, *J. High Energy Phys.* **04** (2011) 001.
- [25] A. Bazavov *et al.*, *Phys. Rev. D* **85**, 054503 (2012).
- [26] O. Philipsen, *Prog. Part. Nucl. Phys.* **70**, 55 (2013).
- [27] S. Borsányi, *Nucl. Phys. A* **904-905**, 270c (2013).
- [28] M. Ivanov (ALICE Collaboration), *Nucl. Phys. A* **904-905**, 162c (2013).
- [29] B. Abelev *et al.* (ALICE Collaboration), [arXiv:1301.4361](https://arxiv.org/abs/1301.4361) [nucl-ex] [Phys. Rev. C (to be published)].
- [30] B. Abelev *et al.* (ALICE Collaboration), [arXiv:1303.0737](https://arxiv.org/abs/1303.0737) [hep-ex] [Phys. Rev. C (to be published)].
- [31] S. Singha (ALICE Collaboration), *Nucl. Phys. A* **904**, 539c (2013).
- [32] D. D. Chinellato (ALICE Collaboration), [arXiv:1211.7298](https://arxiv.org/abs/1211.7298) [hep-ex].
- [33] A. G. Knospe (ALICE Collaboration), *J. Phys. Conf. Ser.* **420**, 012018 (2013).
- [34] B. Abelev *et al.* (A. Large Ion Collider Experiment Collaboration), *Phys. Lett. B* **712**, 309 (2012).
- [35] M. Petrání and J. Rafelski, *Phys. Rev. C* **88**, 021901(R) (2013).
- [36] M. M. Aggarwal *et al.* (STAR Collaboration), *Phys. Rev. C* **84**, 034909 (2011).
- [37] B. I. Abelev (STAR Collaboration), *Science* **328**, 58 (2010).
- [38] M. J. Fromerth, I. Kuznetsova, L. Labun, J. Letessier, and J. Rafelski, *Acta Phys. Pol. B Proc. Suppl.* **43**, 2261 (2012).
- [39] H. Z. Huang and J. Rafelski, *AIP Conf. Proc.* **756**, 210 (2005).
- [40] J. Rafelski and J. Letessier, *J. Phys. G: Nucl. Part. Phys.* **36**, 064017 (2009).
- [41] J. Rafelski and J. Letessier, *Phys. Rev. C* **83**, 054909 (2011).
- [42] I. A. Karpenko, Y. M. Sinyukov, and K. Werner, *Phys. Rev. C* **87**, 024914 (2013).
- [43] R. Rapp and E. V. Shuryak, *Phys. Rev. Lett.* **86**, 2980 (2001).
- [44] Y. Pan and S. Pratt, [arXiv:1210.1577](https://arxiv.org/abs/1210.1577) [nucl-th].
- [45] F. Becattini, M. Bleicher, T. Kollegger, T. Schuster, J. Steinheimer, and R. Stock, [arXiv:1212.2431](https://arxiv.org/abs/1212.2431) [nucl-th].
- [46] J. Steinheimer, J. Aichelin, and M. Bleicher, *Phys. Rev. Lett.* **110**, 042501 (2013).
- [47] C. Amsler, *Rev. Mod. Phys.* **70**, 1293 (1998).
- [48] W. Brueckner *et al.*, *Z. Phys. A: At. Nucl.* **335**, 217 (1990).
- [49] J. Beringer *et al.* (Particle Data Group Collaboration), *Phys. Rev. D* **86**, 010001 (2012).
- [50] I. Kuznetsova and J. Rafelski, *Eur. Phys. J. C* **51**, 113 (2007).
- [51] J. Letessier and J. Rafelski, *Phys. Rev. C* **75**, 014905 (2007).
- [52] J. Rafelski and J. Letessier, *PoS CONFINEMENT* **8**, 111 (2008).
- [53] P. Braun-Munzinger, J. Stachel, J. P. Wessels, and N. Xu, *Phys. Lett. B* **344**, 43 (1995).
- [54] A. Andronic, P. Braun-Munzinger, and J. Stachel, *Nucl. Phys. A* **772**, 167 (2006).
- [55] F. Becattini, M. Gazdzicki, A. Keranen, J. Manninen, and R. Stock, *Phys. Rev. C* **69**, 024905 (2004).
- [56] J. Manninen and F. Becattini, *Phys. Rev. C* **78**, 054901 (2008).
- [57] J. Cleymans, H. Oeschler, K. Redlich, and S. Wheaton, *Phys. Rev. C* **73**, 034905 (2006).
- [58] B. I. Abelev *et al.* (STAR Collaboration), *Phys. Rev. C* **79**, 034909 (2009).
- [59] P. de Forcrand and O. Philipsen, *Nucl. Phys. B* **642**, 290 (2002).
- [60] K. Aamodt *et al.* (ALICE Collaboration), *Phys. Lett. B* **696**, 328 (2011).
- [61] B. Abelev *et al.* (ALICE Collaboration), [arXiv:1307.5530](https://arxiv.org/abs/1307.5530) [nucl-ex].
- [62] B. Abelev *et al.* (ALICE Collaboration), [arXiv:1307.5543](https://arxiv.org/abs/1307.5543) [nucl-ex].

## APPENDIX E

### INTERPRETATION OF STRANGE HADRON PRODUCTION AT LHC

M. Petran, J. Letessier, V. Petracek, J. Rafelski, Pending publication as proceedings of Strangeness in Quark Matter (SQM), 22-27 July 2013, Birmingham, UK, in IOP Conference series

E-print available as: arXiv:1309.6382 [hep-ph]

#### Summary

This publication studies the physical stability of the fit presented in Appendix D in a representative centrality bin 10–20%, for which no data interpolation is necessary. We reproduce the fit from Appendix D with the updated data set. We then run a fit with finite resonance widths, which converges to the same minimum in terms of model parameters and physical bulk properties. This gives us confidence, that we can omit this computationally very intensive feature in our calculations.

The yield of  $\Lambda$  is identified as the main contributor to the total fit  $\chi^2$ ; its model yield is about 1.1 standard deviation below experimental value. However, the model parameters are constrained enough by the rest of the experimental data set, so that the  $\Lambda$  data point does not affect the parameter values, but only increases the total  $\chi^2$  of the fit. The hadron spectrum in our SHM program includes only 3-star (\*\*\*) and 4-star (\*\*\*\*) states from the Review of Particle Physics (publication reference [5]). We explore the influence of an omitted 2-star (\*\*) hadron resonance,  $\Sigma(1560)$ , as an additional source of  $\Lambda$ . When we add  $\Sigma(1560) \rightarrow \Lambda\pi$  to the particle list and decay tree, the fit converges to the same minimum, and the  $\Lambda$  yield is now fitted

within  $1/2$  standard deviation of its experimental value. This finding has prompted an experimental search for this resonance.

We study how well is strangeness conserved at hadronization. From the measured strange hadron yields we know that over 600 strange and antistrange quarks are produced per unit rapidity at hadronization in the most central Pb–Pb collisions. We calculate the total strangeness (i.e. the number of strange and antistrange quarks  $s + \bar{s}$ ) in the QGP phase using the Fermi gas strangeness density and match it to the measured strangeness in hadrons. Assuming the sudden hadronization implying strangeness conservation at hadronization, we report two scenarios: 1) strangeness in the QGP fireball is in equilibrium and the strange quark acquires an effective mass of  $m_s = 299 \text{ MeV}/c^2$  at hadronization; or 2) the strange quark has its PDG mass of  $m_s = 140 \text{ MeV}/c^2$  (at the relevant scale  $2\pi T \simeq 0.9 \text{ GeV}$ ) implying the QGP fireball strangeness to be undersaturated with strangeness phase space occupancy in the plasma  $\gamma_s^{QGP} = 0.77$ .

After presenting these results in a plenary lecture Strangeness in Quark Matter conference, I prepared a draft for the written report. I was responsible for all calculations, result analysis and figure preparation. My co-authors and I revised the text before submission and it contains about 70% of my original text.

# Interpretation of strange hadron production at LHC

M Petráň<sup>1</sup>, J Letessier<sup>2</sup>, V Petráček<sup>3</sup> and J Rafelski<sup>1</sup>

<sup>1</sup> Department of Physics, University of Arizona, Tucson, AZ 85719, USA

<sup>2</sup> Laboratoire de Physique Théorique et Hautes Energies, Université Paris 6, Paris 75005, France

<sup>3</sup> Czech Technical University in Prague, Břehova 7, 115 19 Praha 1, Czech Republic

**Abstract.** We extend the SHM analysis of hadron production results showing here consistency with the increased experimental data set, stability of the fit with regard to inclusion of finite resonance widths and 2-star hyperon resonances. We present new results on strangeness yield as a function of centrality and present their interpretation in terms of QGP inspired model of strangeness abundance in the hadronizing fireball.

## 1. Inclusion of new data

We interpret strange soft hadron multiplicity results obtained in Pb–Pb collisions at  $\sqrt{s_{NN}} = 2.76$  TeV at CERN Large Hadron Collider (LHC). This contribution extends the more detailed presentation of Ref. [1], whereas Ref. [2] provided the related analysis without data inter- or extrapolation. In the results presented here we can use final data for  $K_S^0$ ,  $\Lambda$ ,  $\Xi^\pm$  and  $\Omega^\pm$  [3, 4]. Our fit with these results converges to the same set of thermal parameters as in [1].

Considering limited space and in order to rely solely on directly measured and final experimental results we show here as an example the centrality 10%–20% data bin. In the top two result rows of Table 1, we compare the prior with the present results for statistical parameters. As before  $\Lambda$ -abundance is the dominant contributor to the error as is seen also in direct comparison of input and output results shown in Figure 1. Thus in Table 1 the  $\chi_{\text{tot}}^2$  is found to be greater, yet relatively small given the 9 degrees of freedom.

As seen in the top two rows of results, the differences between these two fits are well within the error. Looking at  $\mu_B$ , recall that we did constrain the value in Ref. [1] by its centrality dependence. Our present result is the outcome of an unconstrained fit for this centrality. This is

**Table 1.** Comparison of non-equilibrium SHM model parameter obtained in fit to 10–20% centrality results for Pb–Pb collisions at  $\sqrt{s_{NN}} = 2.76$  TeV. See text for discussion.

$\Sigma(1560)$	widths	$dV/dy$ [fm <sup>3</sup> ]	$T$ [MeV]	$\mu_B$ [MeV]	$\gamma_q$	$\gamma_s$	$\chi_{\text{tot}}^2$
reported in [1]		$2003 \pm 47$	138.6	$1.23 \pm 0.06$	$1.63 \pm 0.01$	$2.06 \pm 0.13$	3.943
NO	NO	$2033 \pm 105$	138.6	$1.36 \pm 7.94$	$1.63 \pm 0.01$	$2.02 \pm 0.08$	6.599
NO	YES	$1978 \pm 488$	139.3	$1.15 \pm 0.97$	$1.62 \pm 0.19$	$2.00 \pm 0.31$	5.169
YES	NO	$2042 \pm 409$	138.5	$0.49 \pm 0.35$	$1.63 \pm 0.15$	$2.03 \pm 0.25$	4.766
YES	YES	$1976 \pm 398$	139.2	$0.74 \pm 0.09$	$1.62 \pm 0.01$	$2.01 \pm 0.14$	3.472

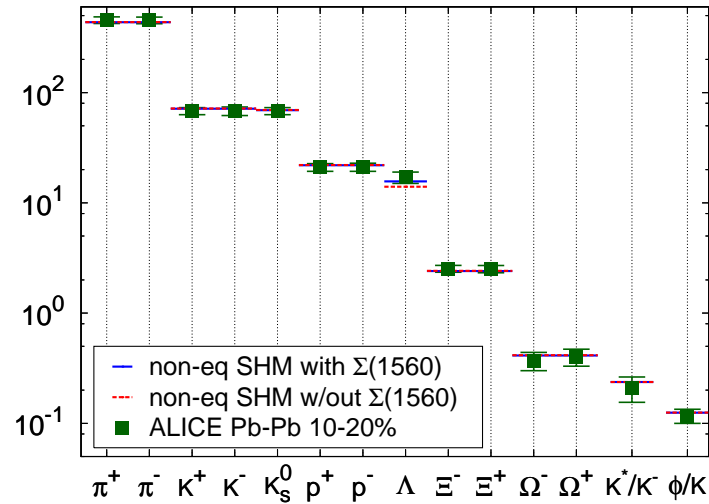


**Figure 1.** (color online) Comparison of non-equilibrium SHM fit with most recent data from Pb–Pb collisions at  $\sqrt{s_{NN}} = 2.76$  TeV for the 10%–20% centrality bin measured by the ALICE collaboration (darkgreen squares), with the 2-star resonance  $\Sigma(1560)$  feeding the yield of  $\Lambda$  (solid blue bars), and without the  $\Sigma(1560)$  feed (red dashed bars).

possible since the added experimental data for  $\Xi^\pm$  and  $\Omega^\pm$  contain a small particle-antiparticle asymmetry even if this is well within the particle yield error bar. The value of  $\mu_B$  we find is near to our earlier expectations; however, the error in  $\mu_B$  is large. There is no error shown for  $T$  since the statistical fit error is much smaller than the precision of the result shown. The error that relates directly to the error of fitted particle yields is found to mainly impact  $dV/dy$  and  $\gamma_s$ . This shows that there are two types of error in the data: a common normalization error for all data points, and a further strange particle normalization error.

The bulk properties of the fireball at hadronization are shown in Table 2. These are presented without an error estimate: the impact of the error in  $dV/dy$  impacts directly the total strangeness yield  $N_{s+\bar{s}}$  and entropy  $S$ . The other three properties that we show, pressure  $P$ , energy density  $\varepsilon$ , trace anomaly  $(\varepsilon - 3P)/T^4$ , are impacted by other statistical parameters but the error of  $\gamma_s$  is the most important. The two top rows are practically equal showing that the additional data, and changes in final data do not impact any of the results and discussion presented in Ref. [1].

## 2. Improving the fit

### 2.1. Influence of hadron resonance width

The SHARE package [6, 7] was developed with the option of allowing the resonance widths presented by the Particle Data Group [5] (PDG) values. The computing time required to allow the resonance widths is significant with fits needing often more than 24h CPU time. The reason for this is that many numerical foldings need to be performed in order to evaluate the total particle yields; see [6] for details. In the past the small change in outcome did not justify the numerical effort. Thus this test has not been performed often.

The third result row in Table 1 shows the statistical parameters obtained allowing for hadron resonance widths. While  $\chi_{\text{tot}}^2$  of the fit slightly decreases and central points of statistical parameters aside of  $T$  agree within error, we note that the error is now more distributed among parameters and the progression is larger indicating slightly less consistency between fit and data.

The fact that there is an increase in  $T$  by  $\delta T = 0.7$  MeV, which is well above statistical error,

is not surprising considering the systematic effect that the resonance widths have on particle yields. Note that to compensate the increase in value of  $T$  the central value of  $dV/dy$  decreased. Another consequence of the slight increase of  $T$  is a slight (1%) increase of the intensive bulk properties  $P$ ,  $\varepsilon$ ,  $(\varepsilon - 3P)/T^4$ , see the third result row in Table 2. The extensive bulk properties directly related to the measured particle yields i.e.  $N_{s+\bar{s}}$  and  $S$  remain unchanged.

### 2.2. $\Sigma(1560)$ as a source of $\Lambda$

The only data point that is not fitted within the 1 s.d. experimental error margin is the yield of  $\Lambda$ . This situation was also discussed in Ref. [1], where the preliminary  $\Lambda/\pi$  ratio was fitted and was systematically under-predicted for all centralities as the only data point standing out with model value just outside the one standard deviation error margin. The newly reported experimental value for 10–20% centrality,  $\Lambda = 17 \pm 2$ , is to be compared to the fitted value,  $\Lambda = 14$ . Inclusion of hadron resonances with their widths discussed above does not improve the fit to the  $\Lambda$  data point.

The question arises if perhaps a contribution to the  $\Lambda$  yield was inadvertently omitted. The SHARE implementation of SHM [6, 7] includes 3-star (\*\*\*) and 4-star (\*\*\*\*) hadron resonances from among all resonances reported by PDG [5]. There are many omitted 2-star (\*\*) resonances. Generally these are so massive that their contribution to particle yields is insignificant. However, we found one exception to this rule, a  $\Sigma(1560)$  which decays into  $\Lambda$  and which would thus systematically increase the  $\Lambda$  yield within the error across all centrality.

The charged states  $\Sigma(1560)^\pm$  have been clearly observed ( $6\sigma$  signal) by two independent experiments [8]. On the other hand, no evidence of  $\Sigma(1560)^0 \rightarrow \Lambda\pi^0$  has been found in a recent crystal ball experiment [9] and hence the resonance remains unconfirmed at (\*\*) level.  $\Sigma(1560)$  quantum numbers have not been measured. Inspired by the close in mass resonance  $\Sigma(1580)\frac{3}{2}^-$  [10], we assign spin  $\frac{3}{2}$  also to  $\Sigma(1560)$ .

Once we include  $\Sigma(1560)$  in the list of hadron states, the new resonance decay feeds the  $\Lambda$  yield by  $\Sigma(1560) \rightarrow \Lambda\pi$  (100%) decay. When we repeat the fit, the resulting statistical model parameters are all almost identical to those without  $\Sigma(1560)$  as is seen in Table 1. This means that the other 13 data points alone constrain enough the fit parameters so that the effect of an omitted resonance simply reduces the  $\chi^2$  without changing other results. This result confirms ‘missing’ resonance hypothesis as the probable origin of the  $\Lambda$  yield underprediction.

In the final result row in Table 1, we consider the finite width of all resonances and the influence of the 2-star  $\Sigma(1560)$  resonance. The overall  $\chi_{\text{tot}}^2$  is decreased by a factor of two, the fitted value of  $\mu_B$  is showing a relatively small error. The main fit error is in overall normalization  $dV/dy$ . The physical bulk properties remain as already obtained and discussed without  $\Sigma(1560)$ .

**Table 2.** Comparison of models (see table 1 for all other details) in terms of physical bulk properties. From left to right, we show pressure  $P$ , energy density  $\varepsilon$ , trace anomaly  $\varepsilon - 3P$  in units of  $T^4$ , total strangeness  $N_{s+\bar{s}}$  and entropy  $S$ .

$\Sigma(1560)$	widths	$P$ [MeV/fm <sup>3</sup> ]	$\varepsilon$ [GeV/fm <sup>3</sup> ]	$(\varepsilon - 3P)/T^4$	$N_{s+\bar{s}}$	$S$
reported in [1]		79.1	0.467	4.77	384	6466
NO	NO	79.2	0.468	4.79	388	6589
NO	YES	82.0	0.483	4.85	385	6593
YES	NO	78.7	0.465	4.78	387	6574
YES	YES	81.7	0.481	4.84	384	6570

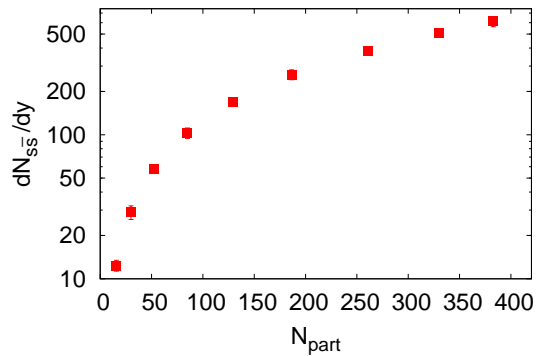


**Figure 2.** (color online) Total strangeness  $dN_{s+\bar{s}}/dy$  produced in Pb–Pb collisions at  $\sqrt{s_{NN}} = 2.76$  TeV as a function of centrality.

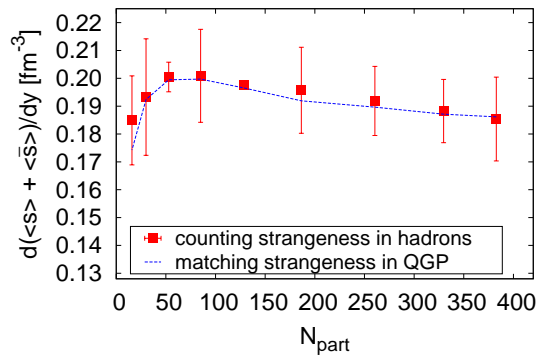


**Figure 3.** (color online)  $s + \bar{s}$  strangeness density per unit rapidity in the hadron phase (red squares), fitted with strangeness in the QGP phase (blue dashed line). See text.

### 3. Strangeness conservation and strange quark mass at hadronization

In the central Pb–Pb collisions at the LHC, an unprecedented amount of strangeness is produced, a total of  $dN_{s\bar{s}}/dy \simeq 600$  strange and anti-strange quarks per unit of rapidity for the most head-on 5% central collisions, see Figure 2. For the peripheral collisions the rise of the total strangeness yield is very rapid, as both the size of the volume and saturation of strangeness production combine. For the more head-on collisions we see a power ( $\sim 1.17$ ) law rise similar to particle interpolation in [1]. Normalization error bar contained in  $dV/dy$  is typically 10% is not shown, only the error from  $\gamma_s$  is shown in Figure 2 (often hidden in the symbol size).

The corresponding total observed strangeness density in the hadron phase is depicted in Figure 3. The uncertainty is evaluated using the relative uncertainty of the model parameter  $\gamma_s$  reported in [1]. Note that the variation in density shown is only about  $\pm 3.5\%$ . Such constancy of the strangeness yield, assuming a recombinant hadronization, should result in strange hadron yield ratios independent of centrality. In Figure 4 the flat line at the bottom is a ratio of two doubly strange particle yields,  $\Xi/\phi$ . Its constancy provides a reference of precision of the argument as this result should be constant [12] even if the strangeness density varies.

The other ratios compare the yield of doubly strange particles with the yield of single strange particles and in one case doubly strange with pions. When strangeness is not saturated as a function of centrality in QGP, one expects an increase in these ratios which we clearly see at lower SPS and RHIC energies. However at LHC a different pattern emerges: there is a bit of increase looking at some of the most peripheral bins which is followed by a slow decrease. The strangeness density shown in Figure 3 mirrors this behavior.

It is of considerable interest to understand if the ‘measured’ strangeness density seen in Figure 3 can be interpreted in terms of sudden hadronization of a QGP fireball. Sudden hadronization implies the conservation of strangeness yield. In sudden hadronization model the volume does not change thus the density in the hadron phase equals that in QGP as well. The chemical freeze-out temperature  $T$  is also the hadronization temperature, i.e. the temperature of QGP breakup. We evaluate the QGP phase strangeness density for a given  $T$  given by integral of Fermi gas strangeness density in the QGP using [11]:

$$s(m_s, T; \gamma_s^{\text{QGP}}) = -\frac{g}{2\pi^2} \left(\frac{T}{\hbar c}\right)^3 \sum_{n=1}^{\infty} (-\gamma_s^{\text{QGP}})^n \frac{1}{n^3} \left(\frac{nm_s}{T}\right)^2 K_2\left(\frac{nm_s}{T}\right), \quad (1)$$

where  $m_s$  is the strange quark mass,  $\gamma_s^{\text{QGP}}$  is the phase space occupancy: here superscript QGP

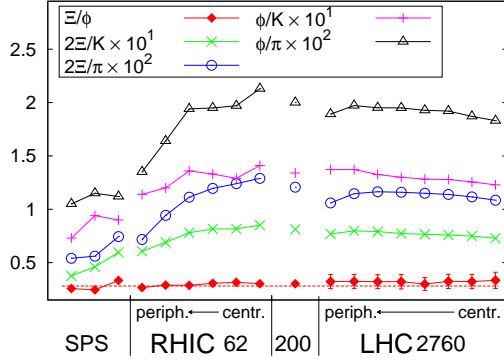


**Figure 4.** Measured particle ratios from relativistic heavy ion collisions across different collisional energies at SPS, RHIC and LHC, and centralities.

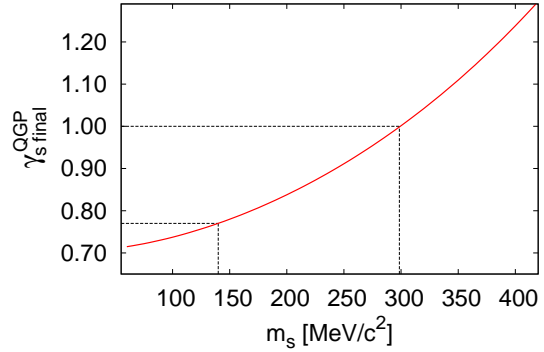


**Figure 5.** (color online) The strangeness phase space occupancy in the QGP phase as defined by Eq. (2) and correlated in the fit to strangeness density with the strange quark mass. See text.

helps to distinguish from that in the hadron phase where we used  $\gamma_s$  without a superscript. The degeneracy  $g = 12 = 2_{\text{spin}} 3_{\text{color}} 2_p$  where the last factor accounts for the presence of both quarks and antiquarks. We will discuss below the reduction in  $s$  due to color-interactions.

In central LHC collisions, the large volume (longer lifespan) suggests that strangeness approaches saturated yield in the QGP. This hypothesis is confirmed by almost constant particle ratios we discussed above, see Figure 4. However, in peripheral collisions, the short lifespan of the fireball may not be sufficient to reach chemical equilibrium. Therefore we introduce a centrality dependent strangeness phase space occupancy  $\gamma_s^{\text{QGP}}(N_{\text{part}})$  which is to be used in Eq.(1).

To model the centrality dependence of  $\gamma_s^{\text{QGP}}(N_{\text{part}})$ , we recall that the lifespan  $\tau$  of the fireball depends on the transverse surface of the fireball and hence the time is proportional to the transverse radius  $\tau \propto r_{\perp}$ . The transverse radius is related to number of participants as  $r_{\perp} \propto N_{\text{part}}^{1/3}$ . Thus, at mid-rapidity, the strangeness production will be assumed to be proportional to  $r_{\perp}^2 \propto N_{\text{part}}^{2/3}$  and modeled by the usual saturating functional form:

$$\gamma_s^{\text{QGP}}(N_{\text{part}}) = \gamma_s^{\text{QGP}} \tanh \left[ \left( \frac{N_{\text{part}}}{N_0} \right)^{2/3} \right]. \quad (2)$$

$\gamma_s^{\text{QGP}}$  is the asymptotic saturation of strangeness phase space in the QGP for large systems and  $N_0$  controls the scale of the fireball transverse size.

We now match the strangeness density measured in the hadron phase shown in Figure 3 with the centrality dependent strangeness density in the QGP, using Eq.(2) in Eq.(1). Our fit to the observed strangeness density is shown in Figure 3. We observe a very strong correlation between  $m_s$  and  $\gamma_s^{\text{QGP}}$ , which we show as a function in Figure 5, while choosing the best  $N_0$  which converges within a narrow interval of  $N_0 \in (11, 14)$ . This shows a quick saturation of  $\gamma_s^{\text{QGP}}(N_{\text{part}})$ , which reaches  $0.95 \gamma_s^{\text{QGP}}$  already for  $N_{\text{part}} \simeq 2N_0 = 30$ .

To choose a set of values of  $(m_s, \gamma_s^{\text{QGP}})$  we consider two cases shown in Figure 5:

- (i) The strangeness in QGP is chemically equilibrated in central collisions,  $\gamma_s^{\text{QGP}} \simeq 1$ . This requires the strange quark to have an effective mass of  $m_s = 299 \text{ MeV}/c^2$  at hadronization;
- (ii) We assume the PDG value of strange quark mass [5]  $m_s \simeq 140 \text{ MeV}/c^2$  at a scale of  $\mu \simeq 2\pi T \simeq 0.9 \text{ GeV}$ . This requires  $\gamma_s^{\text{QGP}} \simeq 0.77$ .

We believe that both approaches can coincide in an improved theoretical description:

- (i) We omitted in Eq. (1) the thermal QCD prefactor which reduces the expected QGP strangeness density due to thermal QCD many body interactions. The typical reduction of  $s$  is by a factor  $(1 - c\alpha_s/\pi)$ . With  $\alpha_s \simeq 0.65$  and  $c \simeq 1$  this effect reduces the QGP density by  $\simeq 20\%$ . The resultant  $\gamma_{s\text{final}}^{\text{QGP}}$  can be 20% larger. This effect is present; we do not know its exact magnitude.
- (ii) The measured value of  $s$  could be reduced from hadronization value by longitudinal dilution of strangeness during matter expansion after hadronization. This effect vanishes in the limit of Bjorken scaling as for every particle that moves out, another particle moves back into the central rapidity acceptance domain. The rapidity plateau has not been demonstrated experimentally for strange hadrons at LHC.

We note that longitudinal dilution by 15% restores strangeness abundance to prior expectations [14]. Both effects would allow  $m_s \simeq 140 \text{ MeV}/c^2$  to be consistent with  $\gamma_{s\text{final}}^{\text{QGP}} \simeq 1$ .

#### 4. Conclusions

The most important result of this analysis is complete stability at 1%-level of results presented in Ref. [1]. This earlier analysis is fully compatible with the latest results [3, 4]. The 1–1.5 s.d. discrepancy of  $\Lambda$  yield systematically below the experimental result inspired us to explore potential  $\Lambda$  sources. We investigated the finite width of all resonances. We found that our fit is very stable and confidence level is slightly improved, however to explain  $\Lambda$  yield we needed the 2-star (\*\*) resonance  $\Sigma(1560)$ , increasing the model yield of  $\Lambda$  to within  $1/2$  s.d. of the experimental yield.  $\Sigma(1560)$  causes no other change in the outcome of our analysis.

We then considered in detail how to interpret the strangeness yield present at hadronization in terms of a QGP inspired model. We considered strangeness conservation during hadronization and concluded that for a fully consistent description we must account for possible reduction of  $s$  by interactions. We then argued that the relatively low hadronization strangeness density could be a consequence of particle dilution in central rapidity region should Bjorken scaling not apply fully. Hadrons from jet quenching and charm decay are produced predominantly in central rapidity domain.

#### Acknowledgments

This work has been supported by a grant from the U.S. Department of Energy, grant DE-FG02-04ER41318, Laboratoire de Physique Théorique et Hautes Energies, LPTHE, at University Paris 6 is supported by CNRS as Unité Mixte de Recherche, UMR7589.

#### References

- [1] M. Petran, J. Letessier, V. Petracek and J. Rafelski, arXiv:1303.2098 [hep-ph].
- [2] M. Petran and J. Rafelski, Phys. Rev. C **88**, 021901 (2013) arXiv:1303.0913 [hep-ph].
- [3] B. Abelev *et al.* [ALICE Collaboration], arXiv:1307.5530 [nucl-ex].
- [4] B. B. ABELEV *et al.* [ALICE Collaboration], arXiv:1307.5543 [nucl-ex].
- [5] J. Beringer *et al.* [Particle Data Group Collaboration], Phys. Rev. D **86**, 010001 (2012).
- [6] G. Torrieri, S. Steinke, W. Broniowski, W. Florkowski, J. Letessier and J. Rafelski, Comput. Phys. Commun. **167**, 229 (2005) [nucl-th/0404083].
- [7] G. Torrieri, S. Jeon, J. Letessier and J. Rafelski, Comput. Phys. Commun. **175**, 635 (2006) [nucl-th/0603026].
- [8] B. T. Meadows, “Hyperons In Production,” In Proceedings *Baryon 1980*, Toronto 1980 pp 283-300
- [9] J. Olmsted *et al.* [Crystal Ball Collaboration], Phys. Lett. B **588**, 29 (2004) [nucl-ex/0308005].
- [10] P. J. Litchfield, Phys. Lett. B **51**, 509 (1974).
- [11] J. Letessier and J. Rafelski, Camb. Monogr. Part. Phys. Nucl. Phys. Cosmol. **18**, 1 (2002).
- [12] M. Petran and J. Rafelski, Phys. Rev. C **82**, 011901 (2010) [arXiv:0912.1689 [hep-ph]].
- [13] K. Aamodt *et al.* [ALICE Collaboration], Phys. Lett. B **696**, 328 (2011) [arXiv:1012.4035 [nucl-ex]].
- [14] J. Rafelski and J. Letessier, Phys. Rev. C **83**, 054909 (2011) [arXiv:1012.1649 [hep-ph]].

## APPENDIX F

### SHARE WITH CHARM

M. Petran, J. Letessier, J. Rafelski, G. Torrieri, Pending publication in Computer Physics Communications

E-print available as: arXiv:1310.5108 [hep-ph]

#### Summary

The predicted charm production at the top LHC heavy-ion collisions called for an upgrade of the SHM implementation, SHAREv2. I upgraded SHARE with a CHARM module, hence SHARE with CHARM, included all charmed 3-star (\*\*\*) and 4-star (\*\*\*\*) hadron states from the current PDG review (publication reference [4]) together with their numerous decay channels. Frequently, the experimentally measured charm decays today have considerable uncertainty, which presents an intrinsic uncertainty in all our results with charm. We also included all decay channels that are suggested by, e.g., the isospin symmetry. assuming that all branching ratios add up to 1.

The new version of the SHARE program adds several new functionalities and provides a common SHM framework for all contemporary heavy-ion experiments. The default settings of the program are tuned for the LHC environment; for example, the omission of all weak decay feed-down, which is possible given enhanced tracking capabilities of the ALICE experiment. We implement the number of charm and anticharm quarks  $N_{c\bar{c}} = c + \bar{c}$  as a new model parameter as well as the ratio of charm to light hadron freeze-out temperature  $T_{charm}/T$ , which allows more flexibility in study of charm hadronization. When an invariant yield of a charm hadron becomes

available, SHARE with CHARM provides the total amount of charm, predicts other charm hadron yields, evaluates any change in bulk physical properties due to charm, and ultimately demonstrates the hypothesis that the statistical hadronization model describes the production of charm hadrons in QGP hadronization.

The publication is a complete detailed user's manual to the SHARE with CHARM that includes description of features introduced in SHAREv1 and SHAREv2 as well as the new capabilities introduced in this release, combined into one concise user's guide.

For the program upgrade, it was necessary to collect charm hadron properties and decay channels, which I compiled into program input files, solving inconsistencies with J. Letessier and J. Rafelski. I was responsible for the CHARM module coding and necessary code modifications of the original SHAREv2 program. J. Letessier helped me test and debug the program. G. Torrieri, the lead author of both previous versions of SHARE, was responsible for testing correct evaluation of fluctuations in the program and revisions of fluctuations related parts of the manual. I prepared the first draft of the program manual, which was revised together with all co-authors. The article submitted for publication contains about 90% of my original draft.

# SHARE with CHARM<sup>☆</sup>

M. Petran<sup>a</sup>, J. Letessier<sup>b,a</sup>, J. Rafelski<sup>a</sup>, G. Torrieri<sup>c,d</sup>

<sup>a</sup>*Department of Physics, The University of Arizona, Tucson, AZ 85721, USA*

<sup>b</sup>*Laboratoire de Physique Théorique et Hautes Energies, Université Paris 6, Paris 75005, France*

<sup>c</sup>*FIAS, J.W. Goethe Universität, 60438 Frankfurt A.M., Germany*

<sup>d</sup>*Pupin Physics Laboratory, Columbia University, 538 West 120<sup>th</sup> Street, NY 10027, USA*

---

## Abstract

SHARE with CHARM program implements the statistical hadronization model description of particle production in relativistic heavy-ion collisions. Given the statistical parameters, it describes yields and thus also yield ratios, and statistical fluctuations of hadrons produced. The program determines the physical bulk properties of the particle source. The program is also allowing these bulk properties to be prescribed as a complement or replacement of some, or all of the statistical hadronization parameters. The program incorporates features seen previously in SHAREv1.x and v2.x and adds the complete treatment of charm hadrons and their decays feeding the hadron yields. The program includes tables of all confirmed hadronic particles including resonances as derived from the latest Particle Data Group tabulation [1], composed of up, down, strange  $u, d, s$  quarks, and extended in the present SHARE release to include hadrons with charm  $c$  quark. The program further contains tables of hadron decays with partial widths, some of charm hadron decays are result of theoretical consideration in absence of direct experimental information. This article provides a complete self-contained manual to the extended SHARE with CHARM program with examples oriented towards recent and forthcoming LHC hadron production results.

*Keywords:* statistical hadronization model, SHM, quark-gluon plasma, QGP, strangeness production, charm production, hadron fluctuations, relativistic heavy-ion collisions, RHIC, LHC

---

## NEW VERSION PROGRAM SUMMARY

*Program Title:* SHARE with CHARM

*Journal Reference:*

*Catalogue identifier:*

*Licensing provisions:* none

*Programming language:* FORTRAN77, C++

*Computer:* PC, Intel 64-bit, 3 GB RAM (not hardware dependent)

*Operating system:* GNU Linux: Ubuntu, Debian, Fedora (not OS dependent)

---

<sup>☆</sup>Work supported by the U.S. Department of Energy, grants DE-FG02-04ER41318 (MP, JL, JR) and DE-FG02-93ER40764 (GT). Laboratoire de Physique Théorique et Hautes Energies, LPTHE, at University Paris 6 is supported by CNRS as Unité Mixte de Recherche, UMR7589. GT acknowledges financial support received from the Helmholtz International Centre for FAIR within the framework of the LOEWE program (Landesoffensive zur Entwicklung Wissenschaftlich-ökonomischer Exzellenz) launched by the State of Hesse.

*RAM:* 615 MB

*Number of processors used:* 1 (single thread)

*Keywords:* SHARE, statistical hadronization model, SHM, quark-gluon plasma, QGP, strangeness production, charm production, hadron fluctuations, relativistic heavy-ion collisions, RHIC, LHC

*Classification:* 11.2, 11.3

*External routines/libraries:* Standard C++ library, CERNLIB library

*Catalogue identifier of previous version:* ADVD\_v2\_0

*Journal reference of previous version:* Comput.Phys.Commun. **175** (2006) 635-649

*Does the new version supersede the previous version?:* Yes

*Nature of problem:* The Understanding of hadron production incorporating the four  $u, d, s, c$  quark flavors is essential for the understanding of the properties of quark-gluon plasma created in relativistic heavy-ion collisions in the large-hadron collider (LHC) energy domain. We describe hadron production by a hot fireball within the statistical hadronization model (SHM) allowing for the chemical nonequilibrium of all quark flavors individually. By fitting particle abundances subject to bulk property constraints in the source, we find the best SHM model parameters. This approach allows to test physical hypotheses regarding hadron production mechanisms in relativistic heavy-ion collisions, physical properties of the source at hadronization and the validity of the statistical hadronization model itself. The abundance of light hadrons made of  $u, d$  and  $s$  constituent quarks [2] and their fluctuations [3] were the core physics contents of the prior releases SHAREv1.x and v2.x respectively. We now consider the hadronization of the heavier charm quarks, a phenomenon of relevance in the analysis of recent and forthcoming LHC results. We introduce bulk matter constraints such as a prescribed charge to baryon ratio originating in the initial state valance  $u$  and  $d$  quark content of colliding nuclei. More generally, all the bulk physical properties of the particle source such as energy, entropy, pressure, strangeness content and baryon number of the fireball at hadronization are evaluated and all of these can be used as fit constraints. The charm quark degree of freedom is handled as follows: given an input number of charm quark pairs at the time of charm chemical freeze-out, we populate charm hadron yield according to rules of statistical hadronization for a prescribed set of parameters associated with the particle source, such as bulk matter fugacities. A separate charm hadronization temperature can be chosen and fitted, and as an option it is possible to make this temperature the same as the fitted hadronization temperature of  $u, d, s$ -quarks. Charm hadron resonances decay feeding ‘stable’ charmed hadrons. These stable charmed hadrons are so short-lived that within current technological detector capabilities practically all their decay products are feeding light hadron yields. These charm decay feeds are changing the abundances of produced hadrons in a pattern that differs from particle to particle.

*Solution method:* SHARE with CHARM builds in its approach upon the numerical method developed for its predecessor, SHARE [2, 3] for the evaluation of the distribution of light ( $u, d, s$ ) hadrons. SHARE with CHARM distributes a prescribed number  $N_{c\bar{c}}$  of charm  $c + \bar{c}$  quarks into individual charmed hadrons applying statistical hadronization rules in a newly added computation module ‘CHARM’ obtaining the yields evaluating appropriate series of Bessel functions. Similarly to light hadrons, the charm hadrons decays are evaluated using pre-existent tables derived from PDG listing [1], proceeding from the heaviest to the lightest particle. The yields of each hadron are obtained using decay branching ratio tables of the mother particle yield – where data was not available, appropriate theoretical model was implemented to assure that all particles decayed with 100% probability. Each of the resultant daughter hadron contributions is added to this  $u, d, s$  hadron yield computed independently for the related set of SHM parameters in the SHARE module. The total yield is subsequently subject to the weak decays (WD) of strange hadrons. A user generated or default WD control file defines what portion of the  $u, d, s$  particle yield decays weekly feeding other particles in turn, and which fraction given the detection capability is observed. Once final observable

hadron yields are so obtained, we compare these with the experimental data aiming in an iteration to find the best set of prescribed SHM parameters for the yield of  $u, d, s$  hadrons observed.. The CHARM module is associated with two new SHM parameters, the charm hadronization temperature  $T_{charm}$  (which can be defaulted to  $T$  obtained for the other  $u, d, s$  hadrons) and the total yield of  $N_{c\bar{c}} = c + \bar{c}$  quarks, called  $N_{c\bar{c}}$ . These and all other SHM parameters are discussed in text.

*Reasons for the new version.\**

Since the release of SHAREv1 in 2004 [2] and SHAREv2 in 2006 [3], heavy-ion collision experiments underwent major development in both detector technology and collision energy. The forthcoming tracker upgrade of STAR at BNL Relativistic Heavy Ion Collider (RHIC) and the current tracking precision of ALICE at CERN Large Hadron Collider (LHC) require upgrades of the SHARE program described below. In the anticipation of significant charm abundance at LHC, SHARE with CHARM allows the study of all charm hadron production. Charm hadron decays are particularly important because they are a significant source of multistrange hadrons. The introduction of charm component of the hadron spectrum into SHM is crucial for correct interpretation of particle production and QGP fireball properties at hadronization in heavy-ion collisions at TeV energy scale. SHARE with CHARM is an easy-to-use program, which offers a common framework for SHM analysis of all contemporary heavy-ion collision experiments for the coming years.

*Summary of revisions:\**

The charm hadron mass spectrum and decays have been fully implemented in the provided program package. We provide a current up-to-date detailed list of charm hadrons and resonances together with their numerous decay channels within the set of fully updated input files that correspond to the present PDG status [1]. Considering the enhanced tracking capabilities of LHC experiments and similar RHIC capability, the default behavior of weak decay feed-down has been updated to not accept any weak feed-down unless specified otherwise by the user. The common framework for all contemporary heavy-ion experiments required an update of the format of the particle list and of the content to correspond to present day PDG. SHARE with CHARM is backward compatible with the previous release, SHAREv2, in terms of calculation capabilities and use of control files. However, SHARE user may need to update and or add individual input file command lines in order to assure that same tasks are performed, considering that defaults, e.g., characterizing weak decays, have been modified. Furthermore quite a few interface improvements have been implemented and are described in detail further in this manual. They allow considerable simplification of control files.

*Running time:* From a few seconds in case of calculating hadron yields and bulk properties given a prescribed set of model parameters, to  $\sim 30$  hours in case of fitting all parameters to experimental data and calculation with finite widths. Sample calculation provided in the program package, which demonstrates the program capabilities other than calculation with finite widths, took just under 2 hours on both 2.1 GHz CPU (2MB L2 cache) laptop and 2.5 GHz CPU (6MB L2 cache) cluster computing node. Simple fit of model parameters to a data set (provided as default in the package) takes about 5 minutes.

## References

- [1] J. Beringer *et al.* [Particle Data Group Collaboration], Phys. Rev. D **86**, 010001 (2012).
- [2] G. Torrieri, S. Steinke, W. Broniowski, W. Florkowski, J. Letessier and J. Rafelski, Comput. Phys. Commun. **167**, 229 (2005) [nucl-th/0404083].
- [3] G. Torrieri, S. Jeon, J. Letessier and J. Rafelski, Comput. Phys. Commun. **175**, 635 (2006) [nucl-th/0603026].

## Quick Start reference

### *Installation*

This section provides a quick reference how to install SHARE with CHARM on most common PC with GNU Linux system, namely we assume `gfortran` and `g++` compilers and `cernlib` installed. If you encounter any problems following this quick guide, please refer to Section 5 for detailed installation guide.

1. In a terminal, navigate into a folder where you want to install SHARE with CHARM and download the package with the command  

```
wget http://www.physics.arizona.edu/~gtshare/SHARE/sharev3.zip
```
2. Unzip the package contents with the command (this will create a new subfolder `sharev3`)  

```
unzip sharev3.zip
```
3. Enter the unpacked folder using  

```
cd sharev3
```

 and compile SHARE with CHARM using  

```
make
```

### *Running SHARE with CHARM*

Once SHARE with CHARM is compiled, it can be run in a terminal with the command  

```
./share
```

If you have not already, it is a good idea to run the program once with the default setup. Individual operations SHARE performs during a run are specified in the file `sharerun.data`. Without any changes to the input files after installation, the program is preset to read the provided input files and to perform a chemical non-equilibrium fit to 10-20% centrality data from Pb–Pb collisions at LHC employing only 2 free parameters  $T$ ,  $V$  – this calculation takes typically less than 10 seconds.

Let us show how to modify the input files in order to perform a semi-equilibrium fit to the same data set instead of the simplified full non-equilibrium. Note that for the purpose of this quick start we do not explain in full detail all inputs that will appear below.

Changing the nature of the fit requires a few steps. We begin by changing the fit output filename (so the old fit is not overwritten), then changing a parameter value, and learning how to include the parameter among those being fitted.

**Changing fit output file name** Looking at the contents of `sharerun.data` in a text editor, the fitting command is the following line

```
CALC FITRATIOS fitTESTne.out
```

It tells SHARE to perform a fit (FITRATIOS) all free parameters to experimental data, and that the output file name is `fit1020ne.out`. The file is overwritten every run. So let us redirect the new output to another file by changing this line to

```
CALC FITRATIOS fitTESTse.out
```

so we have both outputs for comparison. The output filename has to be 13 characters long. Remember to keep two spaces between each word.

**Setting parameter value** Parameter values are set in `thermo.data` file. Open it in a text editor of your choice. Chemical semi-equilibrium is defined by  $\gamma_q = 1$  and thus we need to change the line starting with the parameter name, `gamq`, to read

```
gamq      1 .
```

The format is such that you must remember to keep four spaces after the parameter name and always enter a decimal point even for integer values. The values specified in this input are either fixed parameter values, or the initial fitted parameter values. Final cross check of fits with several different initial parameter values is advisable to fully understand errors and fit stability, i.e., that the fit converges to the same minimum from different starting point(s) in the parameter space and that error is not underestimated.

**Fixing/Fitting a parameter** Parameter ranges for this test run defined in `ratioset.test` file (equivalent to `ratioset.data`, Section 3.1.2). Upon opening the file in a text editor, you will notice that each parameter has a separate line such as the following one for `gams` ( $\gamma_s$ ):

```
gams      0.1      9.      0.1      0
```

In the previous non-equilibrium fit, `gams` was fixed. Parameter with 0 in the last column will be kept constant at the value specified in `thermo.data` file during a fit, whereas parameters with 1 in the last column are to be changed within the allowed range (first two numbers on the line). The different value of  $\gamma_q$  we set in the previous step will result in a new value of  $\gamma_s$ , so let us release `gams` by changing the 0 to 1 on the above quoted line, so the line now reads:

```
gams      0.1      9.      0.1      1
```

demanding that the program finds the best value of  $\gamma_s$  to describe the data.

With the above modifications, running `./share` again will produce a new output file with semi-equilibrium fit (with 3 free parameters,  $T$ ,  $V$  and  $\gamma_s$ ) obtained for the same experimental data defined in the file `LHC1020MI.data`. Note that the resulting fit should have lower CL as other SHM parameters for purpose of this example remain fixed to their optimized full non-equilibrium values.

**Changing experimental data point** Every line in `LHC1020MI.data` contains one data point name, experimental value, statistical and systematic error and whether or not this data point is fitted or only evaluated during a fit. For example, the experimental yield of  $\Lambda = 17 \pm 2$  is defined on the following line:

```
Lm1115zer prt_yield      17.      2.0      0.      1
```

One can change the value from  $17 \pm 2$  to a different one by changing the numbers. The data point can be excluded from the fit by changing the 1 to a 0 in the last column. Similarly to fixing a parameter above, this implies that the experimental value will not be fitted, its theoretical value will be calculated based on the model parameters irrespective of its experimental value.

SHARE with CHARM program is far more capable than the basic operation shown in this Quick Start guide, we refer the reader to the following 30 pages for details about program operation, input file structure, and full description of program capabilities.

## 1. Physics motivation

Strong interaction reactions usually lead to high multiplicity of produced particles. A non-perturbative description of particle production has been proposed originally by Fermi [5] based on statistical ideas and later the model was developed further by considering the reaction volume expansion and realizing that at some point during the expansion, the particle density decreases below the point, where they can interact with each other. This stage is referred to as chemical freeze-out. Next important feature included the hadron resonance mass spectrum significantly increasing the number of states to be populated in the statistical approach. The hadron resonance spectrum implied that the hadronic matter could undergo a phase transition at Hagedorn temperature  $T_H \sim 160$  MeV into a gas of quarks. For the statistical model milestones and more detailed history, see [5] and other references in [2].

Relativistic heavy-ion collisions allow us to create a fireball of matter at very high temperature and density in a laboratory. The objective of the heavy-ion collision program is to study the formation of a deconfined state of matter, the quark–gluon plasma (QGP) and its transition to hadronic matter. The Early Universe has been composed of QGP up until a few microseconds after the Big Bang, when quarks and gluons merged into hadrons, particles that we see around us today. Creation of a small fireball of matter, where quarks and gluons are not bound, would confirm that deconfinement is a property of strong interaction vacuum state. An overview of the matter can be found for example in [6].

The short lifetime and the extreme conditions leave us with indirect observations of the fireball. It is challenging to identify unique probes that allow us to distinguish between a deconfined QGP and a sequence of hadron interactions leading to the final hadron state we observe experimentally. High multiplicity of produced hadrons is a characteristic feature of heavy-ion collisions irrespective of whether or not deconfined state of matter has been achieved during the collision. Specific properties of the final hadron state can distinguish between the two scenarios of hadron production. For details about the differences in the final hadron state see, e.g., [7].

Statistical hadronization model has been used in the past decades to describe hadron production in heavy-ion collisions at CERN Super Proton Synchrotron (SPS) ( $\sqrt{s_{NN}} = 8 - 17$  GeV), RHIC ( $\sqrt{s_{NN}} = 64 - 200$  GeV) and recently at LHC ( $\sqrt{s_{NN}} = 2.76$  TeV) with oftentimes great accuracy. Despite the variety of SHM approaches (chemical equilibria of different flavors, post-hadronization interactions, ...) has a common evolution pattern, at some point during the evolution, the phase space of stable hadrons and resonances is populated as described by their respective statistical distributions. Then, the resonances decay and thus significantly increase the yields of the daughter particles.

Proper model description of the final hadron state yields information about the source of hadrons in relativistic heavy-ion collisions and its properties at the time of hadronization, the transition from the deconfined QGP phase into hadrons. We have compiled an upgraded program ‘SHARE with CHARM’, which produces the final hadron yields and ratios based on intensive parameters of the particle source. We have prepared a package, that takes advantage of already implemented and thoroughly tested program SHAREv2 written in Fortran 77 and we complement it with an external module written in C++ which adds proper description of charm hadron production according to the current status of the field including updated input data tables.

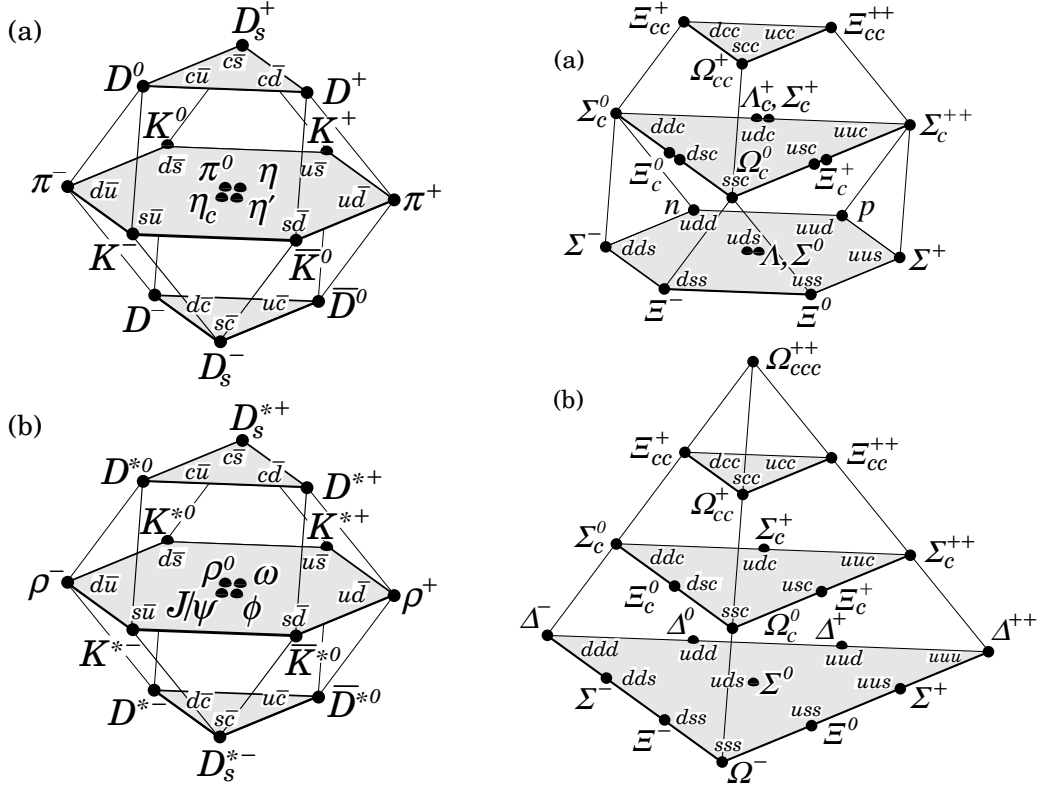


Figure 1: Diagrams showing the 16-plets for the pseudoscalar and vector mesons on the left, where one can see non-charm mesons on the center planes, and diagrams showing the baryon 20-plets (right) made of  $u, d, s$  and  $c$  quarks, where the mass and charm content increases from the base upwards. Figure derived from [1].

For accurate description of the final hadron spectrum, it is necessary to implement a detailed list of hadron states and their decay branching ratios. Seemingly negligible assumptions about both can lead to significant differences in the results of such analysis. Frequent testing and cross-checks with the Particle Data Book [1] and other available programs (see, e.g., [9] and references therein) give us confidence, that the hadron spectrum and decay pattern of hadrons consisting of  $u, d$  and  $s$  quarks are well described in our program. Our hadron mass spectrum involves all \*\*\*\* and \*\*\* resonances. This program update introduces charm mesons depicted in Figure 1 and charm baryons schematically depicted in Figure 1 together with their higher mass \*\*\* and \*\*\*\* resonances.

Particles, that evaporate from a hot boiling quark–gluon ‘soup’ statistically according to the accessible phase space can be described by the SHM. In this scenario, one expects the final hadron state near, but not generally in chemical equilibrium. In the case of more dynamical evolution and sudden hadronization, the final hadron state can be out of chemical equilibrium irrespective of the fireball being or not being chemically equilibrated. Very slow hadronization process, in which all quark flavors have time to (re-)equilibrate in the hadron phase, can also be described statistically, the different scenarios will be reflected by the values of model parameters.

SHARE with CHARM introduces charm hadron production. Most of charm is produced in hard parton scattering very early in the collision. The yield of charm may evolve from the its creation in the initial collision until freeze-out. At high densities, it may be depleted by annihilation, particularly at LHC where high yield and long fireball evolution is expected. We describe statistical hadronization of given number of charm quarks at the time of chemical freeze-out, i.e., hadronization.

Charm quarks are quite massive, about an order of magnitude above the expected freeze-out temperature. Therefore, charm quarks may have on average smaller velocity of expansion than the light ( $u, d, s$ ) quarks and ‘fall behind’. As the size of charm particles is smaller, it is natural to assume a higher decoupling temperature  $T_{charm}$ , a feature we also introduce in this program upgrade and which called for an external CHARM computational module.

SHAREv2 introduced event-by-event fluctuations of particle yields, which further enhanced the model capabilities. They can be used to, e.g., falsify or support the SHM description in case the fluctuations and yields cannot be or are described by the same set of thermal parameters. They may also help decide which statistical ensemble is appropriate, and decouple the correlation of certain thermal model parameters. In the following, we introduce grand-canonical ensemble yields and fluctuations, see Section 2.1 and 2.4.

## 2. Statistical hadronization model in a nutshell

For correct evaluation of the final hadron state, one has to calculate the:

- primary particle yields at chemical freeze-out,
- charm hadron decays followed by
- decays of resonances.

### 2.1. Particle yields and fluctuations

Using the standard textbook approach for grand-canonical ensemble, every hadron of species  $i$  with energy  $E_i = \sqrt{m_i^2 + p_i^2}$  populates the energy states according to Fermi-Dirac or Bose-Einstein distribution function:

$$n_i \equiv n_i(E_i) = \frac{1}{\Upsilon_i^{-1} \exp(E_i/T) \pm 1}, \quad (1)$$

where the upper sign corresponds to fermions and the lower one to bosons. The fugacity  $\Upsilon_i$  of the  $i$ -th hadron species is described in detail below in Section 2.2. Then the hadron species  $i$  yield will correspond to the integral of the distribution function (Eq.1) over the phase space multiplied by the hadron spin degeneracy  $g_i = (2J_i + 1)$  and volume  $V$

$$\langle N_i \rangle \equiv \langle N_i(m_i, g_i, V, T, \Upsilon_i) \rangle = g_i V \int \frac{d^3 p}{(2\pi)^3} n_i. \quad (2)$$

The fluctuation of the yield (Eq.2) can be calculated as:

$$\langle (\Delta N_i)^2 \rangle = \Upsilon_i \left. \frac{\partial \langle N_i \rangle}{\partial \Upsilon_i} \right|_{T, V} = g_i V \int \frac{d^3 p}{(2\pi)^3} n_i (1 \mp n_i). \quad (3)$$

It is more practical for numerical computation to express the above equations (Eq.2,3) as an expansion in modified Bessel functions ( $W(x) \equiv x^2 K_2(x)$ ) as

$$\langle N_i \rangle = \frac{g_i V T^3}{2\pi^2} \sum_{n=1}^{\infty} \frac{(\pm 1)^{n-1} \Upsilon_i^n}{n^3} W\left(\frac{nm_i}{T}\right), \quad (4)$$

$$\langle (\Delta N_i)^2 \rangle = \frac{g_i V T^3}{2\pi^2} \sum_{n=1}^{\infty} \frac{(\pm 1)^{n-1} \Upsilon_i^n}{n^3} \binom{2+n-1}{n} W\left(\frac{nm_i}{T}\right). \quad (5)$$

These expansions can be calculated to any desired accuracy as long as the integrals (Eq.2,3) converge; for bosons one has to make sure that  $\Upsilon_i \exp(-m_i/T) < 1$ , otherwise the yield integral  $\langle N_i \rangle$  diverges. For heavy ( $m \gg T$ ) particles, such as charm hadrons, Boltzmann distribution is a good approximation, i.e., it is sufficient to evaluate the first term of the expansion in Eq. 4, which is indeed implemented in the CHARM module to reduce computation time at no observable loss of precision.

To evaluate the yield of hadron resonance with finite width  $\Gamma_i$ , one has to weigh the yield (Eq.2) by the resonance mass using the Breit-Wigner distribution:

$$\langle \tilde{N}_i^\Gamma \rangle = \int dM \langle N_i(M, g_i, T, V, \Upsilon_i) \rangle \frac{1}{2\pi} \frac{\Gamma_i}{(M - m_i)^2 + \Gamma_i^2/4} \longrightarrow \langle N_i \rangle \text{ for } \Gamma_i \rightarrow 0. \quad (6)$$

Using energy independent width implies a finite probability of the resonance being formed with unrealistically small mass. To mitigate this unphysical scenario, one has to use the energy dependent resonance width. The resonance decay energy threshold is a limiting factor in the accessible energy phase space. The partial width of a decay channel  $i \rightarrow j$  can be well approximated by

$$\Gamma_{i \rightarrow j}(M) = b_{i \rightarrow j} \Gamma_i \left[ 1 - \left( \frac{m_{ij}}{M} \right)^2 \right]^{l_{ij} + 1/2} \quad \text{for } M > m_{ij}, \quad (7)$$

where  $b_{i \rightarrow j}$  is the decay channel branching ratio,  $m_{ij}$  is the decay threshold (i.e., sum of the decay product masses) and  $l_{ij}$  is the angular momentum released in the decay. The total energy dependent width is then calculated using the partial widths (Eq. 7) for all decay channels of the resonance in question as

$$\Gamma_i(M) = \sum_j \Gamma_{i \rightarrow j}(M). \quad (8)$$

For a resonance with a finite width, we can then replace Eq. 6 by

$$\langle N_i^\Gamma \rangle = \frac{1}{A_i} \sum_j \int_{m_{ij}}^{\infty} dM \langle N_i(M, g_i, T, V, \Upsilon_i) \rangle \frac{\Gamma_{i \rightarrow j}(M)}{(M - m_i)^2 + \Gamma_i(M)^2/4}, \quad (9)$$

where  $A_i$  is a normalization constant equal to

$$A_i = \sum_j \int_{m_{ij}}^{\infty} dM \frac{\Gamma_{i \rightarrow j}(M)}{(M - m_i)^2 + \Gamma_i(M)^2/4}. \quad (10)$$

Eq. 9 is the form used in the program to evaluate hadron resonance yield whenever calculation with finite width is required. Note, that yield evaluation with finite width is implemented only for hadrons with no charm constituent quark, zero width ( $\Gamma_i = 0$ ) is used for all charm hadrons.

## 2.2. Quark chemistry of the hadron state

The fugacity of hadron states affects yields of different hadrons based on their quark content. It can be calculated from the individual constituent quark fugacities. In the most general case, for a hadron consisting of  $N_u^i, N_d^i, N_s^i$  and  $N_c^i$  up, down, strange and charm quarks respectively and  $N_{\bar{u}}^i, N_{\bar{d}}^i, N_{\bar{s}}^i$  and  $N_{\bar{c}}^i$  anti-quarks, the fugacity can be expressed as

$$\Upsilon_i = (\lambda_u \gamma_u)^{N_u^i} (\lambda_d \gamma_d)^{N_d^i} (\lambda_s \gamma_s)^{N_s^i} (\lambda_c \gamma_c)^{N_c^i} (\lambda_{\bar{u}} \gamma_{\bar{u}})^{N_{\bar{u}}^i} (\lambda_{\bar{d}} \gamma_{\bar{d}})^{N_{\bar{d}}^i} (\lambda_{\bar{s}} \gamma_{\bar{s}})^{N_{\bar{s}}^i} (\lambda_{\bar{c}} \gamma_{\bar{c}})^{N_{\bar{c}}^i}, \quad (11)$$

where  $\gamma_f$  is the phase space occupancy of flavor  $f$  and  $\lambda_f$  is the fugacity factor of flavor  $f$ . Note, that we allow for non-integer quark content to account for states like  $\eta$  meson, which is implemented as  $\eta = 0.55(u\bar{u} + d\bar{d}) + 0.45s\bar{s}$  in agreement with [10]. It can be shown that for quarks and anti-quarks of the same flavor

$$\gamma_f = \gamma_{\bar{f}} \quad \text{and} \quad \lambda_f = \lambda_{\bar{f}}^{-1}, \quad (12)$$

which reduces the number of variables necessary to evaluate the fugacity to a half.

It is a common practice to take advantage of the isospin symmetry and treat the two lightest quarks ( $q = u, d$ ) using light quark and isospin phase space occupancy and fugacity factors which are obtained via a transformation of parameters:

$$\gamma_q = \sqrt{\gamma_u \gamma_d}, \quad \gamma_3 = \sqrt{\frac{\gamma_u}{\gamma_d}}, \quad (13)$$

with straight forward backwards transformation

$$\gamma_u = \gamma_q \gamma_3, \quad \gamma_d = \gamma_q / \gamma_3, \quad (14)$$

and similarly for the fugacity factors

$$\lambda_q = \sqrt{\lambda_u \lambda_d}, \quad \lambda_3 = \sqrt{\frac{\lambda_u}{\lambda_d}}, \quad (15)$$

$$\lambda_u = \lambda_q \lambda_3, \quad \lambda_d = \lambda_q / \lambda_3. \quad (16)$$

Chemical potentials are closely related to fugacity, one can express an associated chemical potential  $\mu_i$  for each hadron species  $i$  via

$$\Upsilon_i = e^{\mu_i/T}. \quad (17)$$

It is more common to express chemical potentials related to conserved quantum numbers of the system, such as baryon number  $B$ , strangeness  $s$ , third component of isospin  $I_3$  and charm  $c$  :

$$\mu_B = 3T \log \lambda_q, \quad (18)$$

$$\mu_S = T \log \lambda_q / \lambda_s, \quad (19)$$

$$\mu_{I_3} = T \log \lambda_3, \quad (20)$$

$$\mu_C = T \log \lambda_c \lambda_q. \quad (21)$$

(Notice the inverse definition of  $\mu_S$ , which has historical origin and is a source of frequent mistake).

### 2.2.1. Charm chemistry

While charm hadrons are well described by the above framework along with the other three quark flavors, we follow slightly different approach in determining the charm chemical parameters. First, we consider only symmetric charm+anti-charm pair production (and/or annihilation). At LHC, for which SHARE with CHARM is optimized,  $\mu_B$  is very small and therefore the charm chemical potential is vanishing, and charm fugacity factor is effectively unity,  $\lambda_c = 1$ . This implies that the number of charm quarks and anti-quarks is the same,  $N_c = N_{\bar{c}} = N_{c+\bar{c}}/2$ . We determine the charm phase space occupancy  $\gamma_c$  following the approach of [11], where the number of charm quarks  $N_c$  is given (as a model parameter) and  $\gamma_c$  is found by solving

$$\begin{aligned} \langle N_{c+\bar{c}} \rangle = & \gamma_c \left( \gamma_q \langle N_{qc}^{eq} \rangle + \gamma_s \langle N_{sc}^{eq} \rangle + \gamma_q^2 \langle N_{qqc}^{eq} \rangle + \gamma_s \gamma_q \langle N_{cqs}^{eq} \rangle + \gamma_s^2 \langle N_{ssc}^{eq} \rangle \right) \\ & + \gamma_c^2 \left( \langle N_{cc}^{eq} \rangle + \gamma_q \langle N_{ccq}^{eq} \rangle + \gamma_s \langle N_{ccs}^{eq} \rangle \right) \\ & + \gamma_c^3 \langle N_{ccc}^{eq} \rangle, \end{aligned} \quad (22)$$

where  $\langle N_{ijk}^{eq} \rangle$  resp.  $\langle N_{kl}^{eq} \rangle$  is the sum of equilibrium yields of baryons with quark content  $ijk$  and  $\bar{i}\bar{j}\bar{k}$ , resp. mesons with quark content  $k\bar{l}$  and  $\bar{k}l$ . For instance,  $\langle N_{cu}^{eq} \rangle$  includes  $D^0$ ,  $\bar{D}^0$ ,  $D^*(2007)^0$ ,  $\bar{D}^*(2007)^0$ , etc. (Note that only in the Eq. 22,  $\langle N_{cc}^{eq} \rangle$  denotes the sum of charmonium yields, whereas  $N_{c\bar{c}}$  everywhere else in the text denotes the number of charm+anti-charm quarks.) Even though Eq. 22 is cubic in  $\gamma_c$  and has generally three solutions for  $\gamma_c$ , for physical values of all quantities involved, only one of the solutions is positive and real and is accepted as the value of  $\gamma_c$ .

The hadronization of charm itself is a new phenomenon in the physics of heavy-ion collisions and very little is known about this process. Predictions for the amount of charm created in heavy-ion collisions at LHC expect  $123 \pm 77$  charm+anti-charm quark pairs created in a central Pb–Pb collision [8]. We expect this amount to be slightly modified by annihilation and not very abundant thermal production of charm quarks during the expansion of the fireball. Massive charm quarks may expand slower outwards from the primary vertex of the collision. During hadronization, they may find themselves at a point within the fireball at slightly higher temperature. In this case, charm would populate the charm hadron phase space at a temperature above that of the light flavors. We introduce the charm hadronization temperature  $T_{charm}$  and use it in Eq. 4 to calculate charm hadron yields and in Eq. 22 when determining the value of  $\gamma_c$ . The ratio of charm to light hadronization temperature is a newly introduced model parameter, see Section 3.1.

### 2.3. Resonance decays

During the evaluation of hadron yields, the program first calculates the event-by-event average yields and fluctuations at hadronization treating resonances as particles with well defined mass. These quantities are in general different from experimentally observed yields and fluctuations. The resonances decay rapidly after the freeze-out and feed lighter resonances and stable particle yields. The final stable particle yields are obtained by allowing all resonances to decay sequentially from the heaviest to the lightest and thus correctly accounting for resonance cascades. Final yield of each hadron  $i$  is then a combination of primary production and feed from resonance decays

$$\langle N_i \rangle = \langle N_i \rangle_{\text{primary}} + \sum_{j \neq i} B_{j \rightarrow i} \langle N_j \rangle, \quad (23)$$

where  $B_{j \rightarrow i}$  is the probability (branching ratio) that particle  $j$  will decay into particle  $i$ . Applied recursively, Eq. 23 reproduces the experimentally observed yields.

For non-charm hadrons, all decay channels with branching ratio  $\geq 10^{-2}$  were accepted, but the higher number of charm hadron decays (a few hundred(!) in some cases) with smaller branching ratios required to accept all decay channels with branching ratio  $\geq 10^{-4}$ . Since charm hadrons in a lot of cases decay into more than three particles, a different approach in implementing them has to be used, see further in Section 3.3.3. There is still a lot of uncertainty in charm decay channels. Some of them are experimentally difficult to confirm, but required by, e.g., the isospin symmetry and had to be added by hand for several charm hadrons. For example, a measured  $\Lambda_c^+$  decay channel

$$\Lambda_c^+ \rightarrow p \bar{K}^0 \pi^0 \quad (3.3 \pm 1.0)\%, \quad (24)$$

is complemented by the unobserved isospin symmetric channel

$$\Lambda_c^+ \rightarrow n \bar{K}^0 \pi^+ \quad (3.3 \pm 1.0)\%, \quad (25)$$

with the same branching ratio.

The influence of resonance feed-down on fluctuations is the following:

$$\langle (\Delta N_{j \rightarrow i})^2 \rangle = B_{j \rightarrow i} (\mathcal{N}_{j \rightarrow i} - B_{j \rightarrow i}) \langle N_j \rangle + B_{j \rightarrow i}^2 \langle (\Delta N_j)^2 \rangle. \quad (26)$$

The first term corresponds to the fluctuations of the mother particle  $j$ , which decays into particle  $i$  with branching ratio  $B_{j \rightarrow i}$ .  $\mathcal{N}_{j \rightarrow i}$  is the number of particles  $i$  produced in the decay of  $j$  (inclusive production) so that  $\sum_i B_{j \rightarrow i} = \mathcal{N}_{j \rightarrow i}$ . For nearly all decays of almost all resonances  $\mathcal{N}_{j \rightarrow i} = 1$ , however, there are significant exceptions to this including production of multiple  $\pi^0$ , such as  $\eta \rightarrow 3\pi^0$ . The second term in Eq. 26 corresponds to the fluctuation in the yield of the mother particle (resonance).

#### 2.4. Fluctuations — volume fluctuations, fluctuations of ratios and finite acceptance

In most recent heavy-ion experiments, particle yields and fluctuations are measured in a limited kinematic domain, usually a well defined rapidity range around  $y = 0$  (central rapidity). Results are then reported per unit of rapidity, e.g., particle yields are  $dN_i/dy$ . The acceptance domain is in the boost invariant limit equivalent to a configuration space sub-volume [12] and it follows that both particle ratios and fluctuations satisfy:

$$\frac{\langle N_i \rangle}{\langle N_j \rangle} = \frac{dN_i/dy}{dN_j/dy}, \quad (27)$$

and the scaled variance  $\sigma_X^2$  of quantity  $X$  defined as

$$\sigma_X^2 = \frac{\langle (\Delta X)^2 \rangle}{\langle X \rangle} = \frac{\langle X^2 \rangle - \langle X \rangle^2}{\langle X \rangle}, \quad (28)$$

will be given by

$$\sigma_{N_i}^2 = \frac{d\sigma_{N_i}^2}{dy}. \quad (29)$$

The evaluation of grand canonical ensemble (GCE) fluctuations (Eq. 5) neglects the fluctuations of volume. These are accounted for by dividing the observed fluctuation into an extensive and intensive part as follows:

$$\langle(\Delta X)^2\rangle \approx \langle(\Delta x)^2\rangle\langle V\rangle^2 + \langle x\rangle^2\langle(\Delta V)^2\rangle, \quad (30)$$

where  $\langle x\rangle$  and  $\langle x^2\rangle$  can be calculated using the above equations in this section. Volume fluctuations  $\langle(\Delta V)^2\rangle$  are difficult to describe in a model independent way and thus the suggested procedure to avoid this problem is to choose observables independent of volume fluctuations. Observables for which  $\langle x\rangle^2 \ll \langle(\Delta x)^2\rangle$  are good candidates. Event-by-event fluctuations of particle ratios are even better choice as they are volume fluctuation independent by construction. With a complete decay tree, the fluctuations of particle ratios can be evaluated using the numerator's and denominator's fluctuations. However, one has to keep in mind that resonance decays produce both fluctuations and correlations, as the decays can feed both the numerator and the denominator. For the variance of a ratio of two particles  $N_1/N_2$ , one should use

$$\sigma_{N_1/N_2}^2 = \frac{\langle(\Delta N_1)^2\rangle}{\langle N_1\rangle^2} + \frac{\langle(\Delta N_2)^2\rangle}{\langle N_2\rangle^2} - 2\frac{\langle\Delta N_1\Delta N_2\rangle}{\langle N_1\rangle\langle N_2\rangle}. \quad (31)$$

The last correlation term depends on the resonance decays into both particles as

$$\langle\Delta N_1\Delta N_2\rangle = \langle N_1N_2\rangle - \langle N_1\rangle\langle N_2\rangle \simeq \sum_j B_{j\rightarrow 1,2}\langle N_j\rangle. \quad (32)$$

Even though  $\sigma_N^2$  is independent of the average system volume  $\langle V\rangle$ , the variance of a ratio acquires dependence on it since ratio fluctuations scale with  $\langle N\rangle^{-1}$ . An analysis incorporating particle fluctuations should therefore include some particle yields data and system volume is strongly suggested as a free fit parameter (see Section 3.1 for technical details on how to accomplish this).

Most common way to separate detector acceptance effects from physics is to evaluate the fluctuations in 'mixed' events, where particles from distinct events are combined. By construction, such fluctuations contain only detector acceptance effects as the particles themselves are not correlated in any other way. Hence, the normalized 'static' fluctuation  $\sigma_{\text{stat}}^2$  is determined only by a trivial Poisson contribution and the detector effects. In the SHM, the static fluctuation is

$$\left(\sigma_{N_i}^2\right)_{\text{stat}} = 1. \quad (33)$$

The correlation term,  $\langle\Delta N_1\Delta N_2\rangle$  of the particle ratio  $N_1/N_2$  in mixed events vanishes in Eq. 31 and hence the fluctuation of the ratio simplifies to

$$\left(\sigma_{N_1/N_2}^2\right)_{\text{stat}} = \frac{1}{\langle N_1\rangle} + \frac{1}{\langle N_2\rangle}. \quad (34)$$

The dynamical fluctuation  $\sigma_{\text{dyn}}^2$  defined by

$$\sigma_{\text{dyn}}^2 = \sqrt{\sigma^2 - \sigma_{\text{stat}}^2}, \quad (35)$$

corresponds to the difference of the directly measured fluctuation  $\sigma^2$  and the static fluctuation from mixed events  $\sigma_{\text{stat}}^2$  and can be shown to be independent of detector acceptance [13]. This makes the  $\sigma_{\text{dyn}}^2$  more robust to compare with fluctuation estimates from SHM.

Mixed event particles are uncorrelated and hence mixed event techniques cannot account for detector acceptance effects while evaluating particle correlations. The Eqs. 23 and 26 need to use a corrected branching ratios  $B_{j \rightarrow i} \rightarrow \alpha_{j \rightarrow i} B_{j \rightarrow i}$ , and consequently, Eq. 31 needs to be updated as well to read:

$$\sigma_{N_1/N_2}^2 = \frac{\langle(\Delta N_1)^2\rangle}{\langle N_1\rangle^2} + \frac{\langle(\Delta N_2)^2\rangle}{\langle N_2\rangle^2} - 2\alpha_{12} \frac{\langle\Delta N_1 \Delta N_2\rangle}{\langle N_1\rangle\langle N_2\rangle}. \quad (36)$$

The first correction factor we introduced,  $\alpha_{j \rightarrow i}$ , correspond to the probability that particle  $i$  will end up in the detector acceptance provided that particle  $j$  is also inside the region. The second correction,  $\alpha_{12}$ , corresponds to the probability that both decay products are within the detector acceptance. For boost invariant system with full azimuthal coverage,  $\alpha_{j \rightarrow i} = 1$ , since the particles leaving the detector acceptance will be balanced by those entering it. Unlike  $\alpha_{12}$ , which in general is  $\alpha_{12} < 1$ , since for resonances outside the detector acceptance with one of the decay products entering the detector acceptance, the other cannot enter it due to momentum conservation. In practice, this is necessary only at RHIC (much less at LHC) for some weak decays, which are experimentally distinguishable from primary particles. In the program, we offer the option to enter the correction factor  $\alpha_{12}$  for any resonance decay as an input parameter, see Section 3.3.2 for details how to accomplish this.

### 3. SHARE with CHARM program structure

The basic structure of the program is depicted in Figure 3. It requires a total of six input files containing list of particles, decay tree, and model parameters. The program can perform a multitude of commands, which are read at run time from the file (`sharerun.data`). The computational and fitting block will perform commands in the run file as entered one after another generally independently of each other. Each command produces an output into a separate file named by the user. The mandatory input files the user has to provide are (default filenames listed):

- `particles.data` (14-letter filename) — list of particle properties,
- `decays.data` (11-letter filename) — list of non-charm hadron decays,
- `HFfeed.data` (constant filename) — list of inclusive branching ratios of charm hadrons,
- `thermo.data` (11-letter filename) — list of model parameters,
- `ratioset.data` (13-letter filename) — list of model parameter ranges,
- `totratios.data` (14-letter filename) — experimental data and physical properties requested in the output
- `sharerun.data` (constant filename) — the driving file with a list of commands to perform,

and an optional input file with weak feed-down corrections

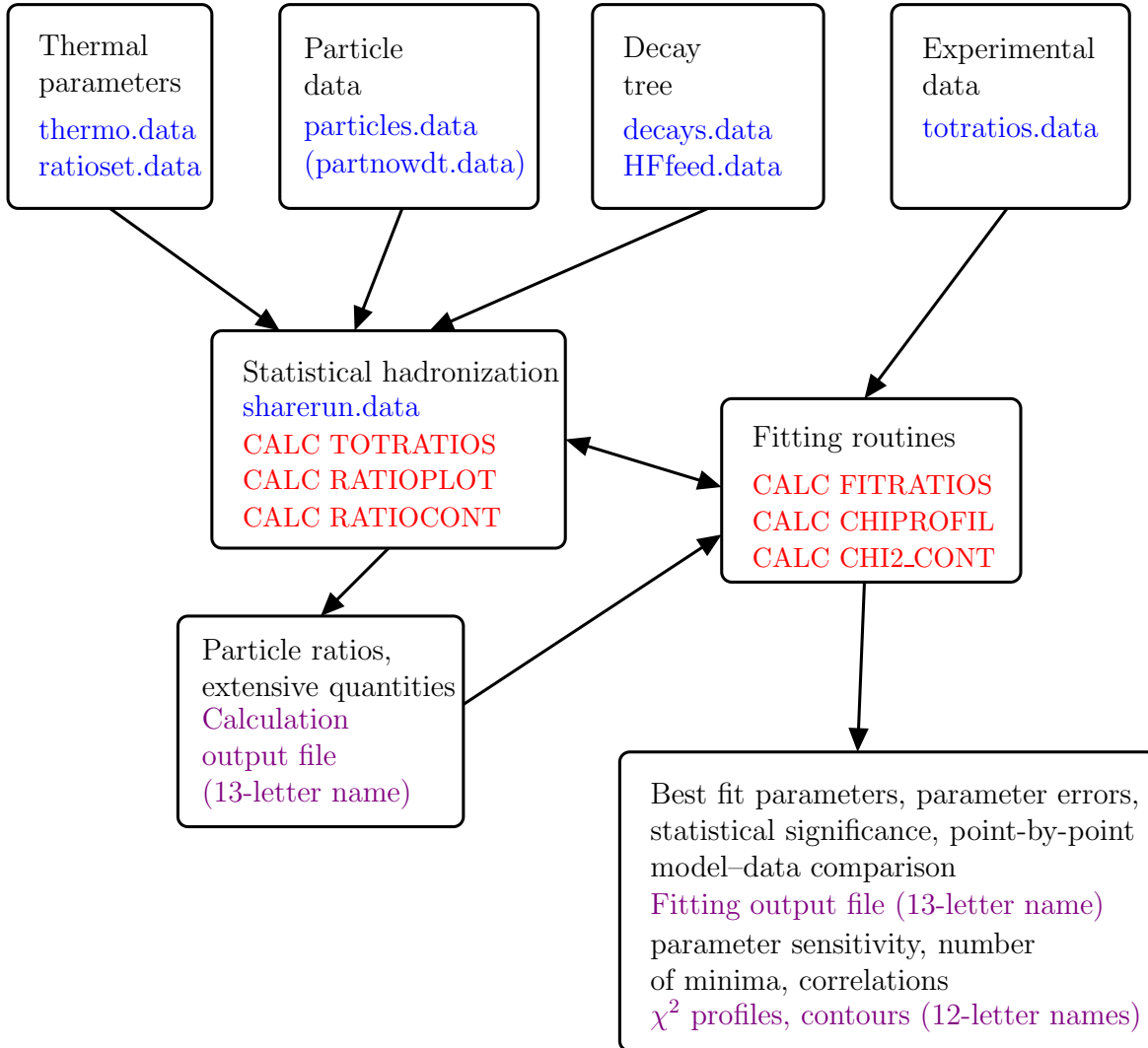


Figure 2: (color online) Schematics of the SHARE with CHARM program structure. Default input file names are written in blue, program commands in red and output files in purple.

- `weak.feed` (9-letter filename) — list of weak decay feed-down corrections  $\alpha_{12}$ , as described in Section 2.4.

If the user does not specify any of the mandatory input files explicitly, the program will look for the input file with the default name and will not run correctly if any of the mandatory input files is missing. In all of these files, the user can enter a comment by starting a line with the pound character, #. All subsequent characters after # on the line will be ignored. We will address the structure of each input files below in a separate section. It should be pointed out that all input files are read by the program as fixed format input and it is hence crucial to keep their structure

Table 1: Structure of the `thermo.data` file containing thermal parameters and their respective initial values.

Parameter	Initial Value	Parameter description
<code>norm</code>	2200.	absolute normalization in $\text{fm}^3$
<code>temp</code>	0.139	chemical freeze-out temperature $T$ in GeV
<code>lamq</code>	1.0055	light quark fugacity factor
<code>lams</code>	1.0	strangeness fugacity factor
<code>gamq</code>	1.0	light quark phase space occupancy
<code>gams</code>	1.0	strangeness phase space occupancy
<code>lmi3</code>	1.00	$I_3$ fugacity factor (Eq. 15)
<code>accu</code>	0.001	calculations accuracy
<code>dvol</code>	0.	statistical pressure ensemble fluctuations (Eq. 30)
<code>gam3</code>	1.	$I_3$ phase space occupancy (Eq. 13)
<code>lamc</code>	1.	charm fugacity factor ( <i>currently fixed to <math>\lambda_c = 1</math></i> )
<code>Ncbc</code>	0.	number of $c + \bar{c}$ quarks
<code>tc2t</code>	1.	ratio of charm to the light quark hadronization temperature $T_{charm}/T$

including the number of characters allocated for each record (including blank spaces between the records). The only exception is the charm hadron decay file `HFfeed.data`, which can include any positive number of blank characters (spaces or tabs) in between the records.

### 3.1. Thermal parameters

#### 3.1.1. List of thermal parameters (11-letter filename, default: `thermo.data`)

The thermal parameter file contains a list of parameters of the model together with their initial value. All parameter names are 4-letter tags. The `thermo.data` file has to contain the 12 parameters as in the provided program package. We show in Table 1 the typical contents of a sample file together with the description of each parameter. The units are GeV and  $\text{fm}^3$ , where applicable.

The fugacity factors  $\lambda_i$  ( $i = q, s, I_3$ ) may be replaced by their respective chemical potentials according to Eqs. 18–20. The respective tags are `mu_b`, `mu_s`, and `mui3`.

The parameter tags in this file are used throughout the program, so it is highly advisable *not* to change the parameter names, as it may result in unpredictable (if any) results. On the other hand, we encourage the user to change the initial parameter values in this file. The format of every line comprises a 4-letter parameter tag and 4 spaces followed by the initial value of the respective parameter. The relevant Fortran format statement is `(A4, 4X, F31.19)`.

#### 3.1.2. Fit parameter ranges (13-letter filename, default: `ratioset.data`)

The `ratioset.data` file defines the ranges of parameters that will be varied during a fit and which parameters will be kept constant. For each parameter, this file contains the lower and

Table 2: Structure of the `ratioset.data` file.

Tag	Lower limit	Upper limit	Initial step	Fit?=0/1
norm	9.	9999.	1.0	1
temp	0.1	0.3	0.1	1
lamq	0.1	90.	0.1	1
lams	0.9	90.	0.1	1
gamq	0.2	2.5	0.1	1
gams	0.1	9.	0.1	1
mui3	0.01	92.5	0.1	1
Ncbc	0.	400.	1.0	0
dvol	0.	10.	0.1	0
gam3	0.5	1.5	0.1	0
tc2t	0.5	4.	0.1	0
lamc	0.9	900.	0.1	0

upper limits of its range and the initial step size during minimization with MINUIT. Typical format of this file is shown in Table 2. The last column is each row states if the parameter is to be fitted within the specified range (1), or kept constant (0). All parameters defined in the thermal parameters file `thermo.data` have to be defined in the `ratioset.data` file as well, however, the parameters do not have to be in the same order in both files. Every line in this file must be compatible with the following format: (A4, 3X, 2F7.1, F7.5, I4)

If the upper and lower limits for a parameter are equal and the parameter is to be fitted, MINUIT will consider this parameter unconstrained during a fit. In case the user chooses to fit only experimental particle ratios and densities, the volume is automatically kept constant. We have found that the order of parameters, which is maintained during MINUIT calls, affect the quality (speed, reliability) of the resulting fit. The user is advised to input the most important fit parameters first, usually `temp` and `norm`. Second, highly correlated parameters should be placed one right after the other. Note, that some fit parameters (e.g., strangeness fugacity factor  $\lambda_s$ ) can be a result of a conservation law (e.g., of strangeness). For details about possible conservation law implementations, see Section 3.4.5.

### 3.2. Particle properties data file (14-letter filename, default: `particles.data`)

This input file contains the list of particles and its properties, specifically the particle name, mass, width, spin, isospin, quark content and Monte Carlo (MC) code where available. The structure of every line in the file is the following:

```
name mass width spin I I3 u d s au ad as c ac b ab MC
where
```

name	a nine character string identifying the particle,
mass	particle mass in $\text{GeV}/c^2$ ,
width	particle width in $\text{GeV}$ ,
spin	spin of the particle,
I	particle isospin,
$I_3$	the third component of the particle isospin,
$u, d, s, c, b$	number of particle constituent quarks, $u, d, s, c$ and $b$ respectively,
$au, ad, as, ac, ab$	number of particle constituent anti-quarks, $\bar{u}, \bar{d}, \bar{s}, \bar{c}$ and $\bar{b}$ respectively,
MC	particle MC identifier, where available. Note that not all hadron resonances have a MC code assigned in the standard scheme [1].

The particle name defined in the particle list is used as a unique particle identifier throughout the program and we strongly advice not to change the names of particles already provided in the input file that comes as a part of the program package. The following naming convention was chosen and is used for most particles; first two characters of the (9-letter) particle name is an abbreviation of the particle letter followed by 4 numbers representing particle approximate mass (in  $\text{MeV}/c^2$ ) and the last three letters reflect the particle electric charge, e.g.,  $\Lambda$  can be found in the program as `Lm1115zer`. The following 3-letter endings are being used:

zer	‘zero’	neutral particle, charge 0,
zrb	‘zero bar’	neutral anti-particle, charge 0 (neutral anti-baryons),
plu	‘plus’	positive particle, charge +,
plb	‘plus bar’	positive anti-particle, charge $-$ (anti-baryons, e.g., the antiproton $\bar{p}^-$ ),
min	‘minus’	negative particle, charge $-$ ,
mnb	‘minus bar’	negative anti-particle, charge + (e.g., $\bar{\Omega}^+$ ),
plp	‘plus plus’	doubly positive particle, charge ++ (e.g., $\Delta^{++}$ ),
ppb	‘plus plus bar’	doubly positive anti-particle, charge $--$ ,
nuc	‘nucleus’	(hyper-)nucleus with charge above the range of previous endings
anc	‘anti-nucleus’	(hyper-)anti-nucleus with charge above the range of previous endings

When editing the list of particles, the user is strongly encouraged to create a copy of a line in the particle properties file and edit the copied line replacing characters one-to-one to prevent formatting changes. The general expected format of a line is defined by the Fortran 77 format statement:

```
(A9, 2(4X, F10.7), 2X, 3(F5.1, 4X), 10(F6.3, 2X), I9)
```

where ‘A’ is a letter, ‘X’ is a space, ‘F’ is a real number and ‘I’ is an integer number. For more details about format specification as defined by the Fortran 77 standard, see, e.g., Ref. [14, section 13].

For example, motivated by our recent analysis of LHC data [15], we include a `**` resonance  $\Sigma(1560)$  in the particle list and decay tree as `Sg1560???`, but, as a 2-star resonance, we leave it commented out in both. In other words, this resonance is not included in the calculations by default. If the user chooses to include this resonance in the analysis, it is enough to remove the `#` character in front of the following lines in the particle list

```
#Sg1560min 1.5530000 ... → Sg1560min 1.5530000 ...
#Sg1560mnb 1.5530000 ... → Sg1560mnb 1.5530000 ...
```

. . . etc.

and same in the decay tree file to enable the  $\Sigma(1560) \rightarrow \Lambda\pi$  decay, see Section 3.3.1 below for details on the decay tree structure.

The  $\Delta(1232)^0$ , for instance, will appear in the list as:

```
D11232zer 1.232 0.12 1.5 1.5 -0.5 1. 2. 0. 0. 0. 0. 0. 0. 0. 0. 2114
```

We allow non-integer quark numbers to accommodate strong interaction flavor mixing, such as the  $\eta$  meson mentioned in Section 2.2. Since SHAREv2 [3], we enlarged the particle list to include all at least \*\*\* charm hadrons and resonances and updated those present and increased the total number of particles a user can specify to 1000. No bottom hadron is at the moment present in the particle list provided with this SHARE program release. The particle input file has been re-designed with future upgrade in mind, that would include calculation of bottom hadrons. Up to this day, no significant amount of bottom hadrons is expected in heavy-ion experiments and hence the list provided with the program does not contain any bottom hadrons.

SHARE with CHARM calculations are relevant for strongly interacting system, where  $K^0$  and  $\bar{K}^0$  are the relevant states. Electroweak mixing  $K^0 - \bar{K}^0$  occurs on a longer timescale and hence should be performed at the end of the calculation. For the convenience of the user, we implemented the following name ending shortcuts representing basic algebraic combinations of particles from the list.

sht	'short'	sht= $^{1/2}(\text{zer}+\text{zrb})$ , used to calculate mixed states, e.g., the often measured $K_S = \frac{1}{\sqrt{2}}(K^0 - \bar{K}^0)$ ,
lng	'long'	lng= $^{1/2}(\text{zer}+\text{zrb})$ , used to calculate mixed states, e.g., the less often measured $K_L = \frac{1}{\sqrt{2}}(K^0 + \bar{K}^0)$ ,
tot	'total'	tot=(zer+zrb), e.g., Lm1115tot for $\Lambda + \bar{\Lambda}$ ,
plt	'plus total'	plt=(plu+plb), e.g., pr0938plt for $p + \bar{p}$ ,
pbn	'plus bar net'	pbn=(plu-plb), e.g., pr0938pbn for $p - \bar{p}$ ,
mnt	'minus total'	mnt=(min+mnb), e.g., UM1672mnt for $\Omega + \bar{\Omega}$ ,
mnn	'minus net'	mnn=(min-mnb), e.g., UM1672mnn for $\Omega - \bar{\Omega}$ ,
plm	'plus minus'	plm=(plu+min), e.g., pi0139plm for $\pi^+ + \pi^-$ ,
pln	'plus minus net'	pln=(plu-min), e.g., pi0139pln for $\pi^+ - \pi^-$ ,
pmb	'plus minus bar'	pmb=(plb+mnb), e.g., Sg1189pmb for $\bar{\Sigma}^+ + \bar{\Sigma}^-$ .

Note, that these combinations are *not* in the particle list as separate entries, they are evaluated during the program run from the particle yields as one of the last steps of the calculation and they are printed in the output if so requested by the user (see Section 3.4).

### 3.3. Particle decays

Light hadron decays can be divided into two categories, light hadron ( $u, d, s$ ) 2-body and 3-body decays, and charm hadron decays.

#### 3.3.1. Light hadron decay tree (11-letter filename, default: decays.data)

The treatment of light hadron decays did not change since SHAREv1 [2]. Only 2 and 3-body decays are considered. Every line in decays.data contains one decay channel in the following

format:

```
Parent daughter1 daughter2 BR C-G?
```

for 2-body decays, and

```
Parent daughter1 daughter2 daughter3 BR C-G?
```

for 3-body decays, where `Parent` refers to the decaying particle producing daughter particles `daughterN` with branching ratio `BR`. The `C-G?` flag signalizes if the branching ratio should be corrected by a Clebsch-Gordan coefficient (0 = no, 1 = yes). For example, the decay  $K^{0*} \rightarrow K\pi$  reported to have a branching ratio of  $\sim 1.00$  in [1] appears in the decay tree file as two entries:

```
Ka0892zer   pi0139min   Ka0492plu   1.0   1
Ka0892zer   pi0135zer   Ka0492zer   1.0   1
```

whereas other decays, such as decays  $\phi \rightarrow K^+K^-$  and  $\phi \rightarrow \pi^+\pi^-\pi^0$ , do not need the Clebsch-Gordan coefficients correction, as each combination of daughter particles is reported separately;

```
ph1020zer   Ka0492plu   Ka0492min   0.49   0
ph1020zer   pi0139plu   pi0139min   pi0135zer  0.08   0
```

The general format of 2 and 3-body decays is

```
(A9,3X,A9,3X,A9,F9.4,I4)
```

and

```
(A9,3X,A9,3X,A9,3X,A9,F9.4,I4)
```

respectively. As a general rule, we again suggest that any modifications to this input file are made on one-to-one character replacement basis to prevent formatting discrepancies. Currently, the number of decay channels for each parent particle has been limited to 50.

### 3.3.2. Weak decay corrections (9-letter filename, e.g., *weak.feed*)

As discussed in Section 2.4, feed-down is an important feature of the experimental data to be accounted for within the statistical hadronization model. Limited acceptance of detectors requires experimental correction of the feed-down coefficients reflecting the probability of a resonance being produced within the detector acceptance and the decay product also being in within the detector acceptance region.

Weak decays, in particular, are susceptible to detector acceptance and efficiency corrections, as they happen at a macroscopic distance from the primary vertex. Weak decay corrections hence comprise a geometrical as well as momentum component. A significant portion of the final particle yield is oftentimes mostly feed-down, e.g., protons are mostly products of hyperon decay, such as  $\Lambda \rightarrow p\pi$ . At RHIC, careful evaluation of the correction factors for each weak decay product was a crucial element to fit the experimental data, whereas at LHC, thanks to a more precise tracking, virtually all weak decays are subtracted from the final hadron yields.

Decays defined in `decays.data` file, which violate conservation of strangeness and/or isospin are identified by the program as weak. The weak feed-down correction file can contain any number of weak decays defined in the decay tree (from 0 up to all the weak decays). Consequently,

no strong (or electromagnetic) decay corrections are allowed in this file, they are caught as input errors by the program, which exits after reporting the particular decay on screen. Each line in the weak decay file has the following structure for 2-body and 3-body weak decays respectively:

```
Parent daughter1 daughter2 all/1st/2nd/cor coefficient
Parent daughter1 daughter2 daughter3 all/1st/2nd/3rd/cor coefficient
```

formatted respectively:

```
(A9,3X,A9,3X,A9,3X,A3,F9.4)
(A9,3X,A9,3X,A9,3X,A9,3X,A3,3X,F9.4)
```

where `Parent` and `daughterN` are the names of particles involved in the decay, similarly to the decay tree file `decays.data` structure. The decay products do not have to be in the same order as in the decay tree, the program handles any permutation of the decay products (daughter particles). The following 3-letter tag specifies which of the decay products is being corrected. For example, the weak decay  $\Lambda \rightarrow p\pi^-$  can appear in the weak decay file multiple times specifying a different correction for each of the daughter particles:

```
Lm1115zer pr0938plu pi0139min 1st 1.0000
Lm1115zer pr0938plu pi0139min 2nd 0.0000
```

The STAR experiment at RHIC filters out the pion, but accepts the proton, as is seen in the above example. The user can specify, whether all daughters will have the same correction coefficient, or only one of them, referring to the 1st/2nd/3rd daughter on each line. The last 3-letter tag `cor` refers to the fractional contribution of the acceptance to the two particle correlation  $\langle \text{daughter1 daughter2} \rangle$  induced by a common parent resonance decay denoted by  $\alpha_{12}$  in Eq. 36 in Section 2.4. SHARE will then renormalize the branching ratio of `Parent`  $\rightarrow$  `all/1st/2nd/3rd/cor` by a `coefficient` when calculating all data points after a given `weakdecay` statement (see below).

The program may be run without any weak decay feed-down file, in which case the user has to choose from two cases:

1. All weak decays are accepted in the program, that is all particle yields contain contributions from weak decays. This scenario means, that the weak decays have not been corrected for in the experiment, hence the option is labeled `UNCORRECT`.
2. No weak decays are accepted, all weak decays are subtracted from the final experimental yields. This option is labeled `NOWK_FEED`. This is the default option, unless specified otherwise by the user.

This upgrade of SHARE is tailored to fit data from LHC measured by the ALICE experiment, which publishes results fully corrected for weak decays. The default treatment of weak decays is thus changed from SHAREv2 to ‘not to accept’ weak decay feed-down to any particle, the option `NOWK_FEED` described above.

All weak decay file options and user file names should be entered into the experimental data file (`totratios.data`) with the keyword `weakdecay` as `name1` (see Section 3.4) followed by one of the options above or user created weak decay feed-down correction file name as follows:

```

weakdecay  weak.feed
...
weakdecay  NOWK_FEED
...
weakdecay  UNCORRECT

```

Experimental data files are read in sequence and hence every `weakdecay` feed-down pattern applies to experimental data points below until another `weakdecay` statement is encountered. This allows the user to fit data points from multiple experiments with different weak decay feed-down corrections. For detailed information on the general structure of the experimental data file, see Section 3.4.

### 3.3.3. Charm decay tree (fixed filename `HFfeed.data`)

Although charm hadrons decay weakly, life times of charmed hadrons are very short due to the charm quark large mass. Therefore, all charm decays are very rapid and are treated separately from the weak decay methods described in the previous section (Section 3.3.2). The weakly decaying charmed hadrons can have up to several hundred decay channels with similar branching ratios and up to six decay products. Without any dominant decay channel present, we have to include all these concurrent decays. The treatment of light hadron decays described above was thus found unsuitable for the charm region.

In order to save computing time, inclusive branching ratios of charm hadron decays are specified in the charm decay tree. The yields of charm decay products still follows the logic of Eq. 23, however, the sum has significantly less terms because every daughter particle appears only once. Each line of the charm decay file specifies the `parent` particle followed by one `daughter` particle and the respective inclusive branching ratio `BR` in the following format:

```
Parent daughter BR
```

This file is the only exception among input files that can contain any amount of spaces between the columns.

On an example of  $D^{*0}(2007)$ , we show the organization of charm decays. The  $D^{*0}(2007)$  has two decay channels with branching ratios as follows [1]:

$$\begin{aligned}
 D^{*0} &\rightarrow D^0\pi^0, & \Gamma_1 &= 0.619 \pm 0.029, \\
 D^{*0} &\rightarrow D^0\gamma, & \Gamma_2 &= 0.381 \pm 0.029,
 \end{aligned}$$

which corresponds to the following in the `HFfeed.data` file:

```

Dc2007zer   Dc1800zer   1
Dc2007zer   pi0135zer   0.619
Dc2007zer   gam000zer  0.381

```

Every daughter particle type is on a separate line with its respective inclusive branching ratio. One can look at each line in the charm decay file from an equivalent perspective; how many daughter particles of a given type are produced on average after the decay of one parent particle.

### 3.4. (Experimental) Values to be calculated (14-letter filename, default: `totratios.data`)

Experimental data values and other values of interest to be calculated are defined in the file `totratios.data`. We provide an example of a typical experimental values file structure in Figure 3. The general format of every line is `(A9,2X,A9,3F12.7,I17)`. We would like to point out a common source of error which arises when the decimal point is omitted while entering experimental values in this file. Unfortunately, this is an intrinsic feature of Fortran 77 and cannot be easily mitigated.

#### 3.4.1. Particle ratios

Every line in the experimental data file should have the following format:

```
name1  name2  data  statistical  systematic  fit?(-1/0/1/2)
```

where

<code>name1</code>	The first particle (numerator of a ratio), 9-letter name as defined in the particle list (Section 3.2).
<code>name2</code>	The second particle (denominator of a ratio), or a tag indicating that the yield or density of <code>name1</code> is entered, 9-letter name.
<code>data</code>	The experimental value of this data point.
<code>statistical</code>	The statistical error of the data point.
<code>systematic</code>	The systematic error of the data point.
<code>fit?</code>	This flag specifies if this data point contributes to the evaluation of $\chi^2/\text{ndf}$ of the fit, when set to a positive value (1 or 2). When set to 0, the ratio is not fitted, but calculated and output to the graph file (see Section 4 for details). Values of <code>fit?=-1</code> or <code>2</code> mean that the data point will <i>not</i> be output to the graph file. Note, that under typical circumstances, the options 1 and 0 will be sufficient for typical program use.

#### 3.4.2. Particle yields and bulk source properties

Apart from particle ratios, the user have also the following options of quantities to be fitted, calculated, and printed out in the output.

**name2** can contain the following 9-letter tags:

<code>prt_yield</code>	The yield of the first particle, or collective extensive quantity
<code>prdensity</code>	The density of the first particle or quantity.
<code>solveXXXX</code>	Evaluation of the parameter XXXX based on first particle or quantity, see Section 3.4.5 for details.
<code>fluctXXXX</code>	Grand-canonical fluctuation, XXXX can contain one of the following: <code>_dyn</code> , <code>dynv</code> , <code>dnch</code> , <code>sgsm</code> . <code>fluct_dyn</code> to calculate $\sigma_{dyn} = \sqrt{\sigma_{tot}^2 - \sigma_{stat}^2}$ (see Eq. 35). <code>fluctdynv</code> to calculate $\sigma_{dyn} = \langle N_2 \rangle \sigma_{N_1/N_2}$ (see Eq. 36). <code>fluctdnch</code> to calculate $\sigma_{dyn} = \langle N_{ch} \rangle \sigma_{N_1/N_2}$ , the fluctuation scaled by the average number of charged particles $\langle N_{ch} \rangle$ . <code>fluctsgsm</code> to calculate $\sigma_{dyn} = \langle N_1 + N_2 \rangle \sigma_{N_1/N_2}$ (Other fluctuation options have been discontinued due to their sensitivity to acceptance effects.)

**name1** can contain the following 9-letter tags:

<code>negatives</code>	negative particles (weak decay corrections taken into account)
<code>positives</code>	positive particles (weak decay corrections taken into account)
<code>chargmult</code>	charged particles (weak decay corrections taken into account)
<code>neut_mult</code>	neutral particles (weak decay corrections taken into account)
<code>tot_multi</code>	total hadron multiplicity (weak decay corrections taken into account)
<code>tot_prime</code>	total primary particles multiplicity (no decays considered)
<code>totstrong</code>	total multiplicity including contributions from strong decays
<code>totstrang</code>	total strangeness $\langle s + \bar{s} \rangle$
<code>netstrang</code>	net strangeness $\langle s - \bar{s} \rangle$
<code>tot_light</code>	total number of light quarks (weak decay corrections taken into account)
<code>totcharge</code>	total charge $\langle Q + \bar{Q} \rangle$
<code>netcharge</code>	net charge $\langle Q - \bar{Q} \rangle$
<code>totbaryon</code>	total baryon number, i.e., sum of all baryons and anti-baryons, $\langle B + \bar{B} \rangle$
<code>netbaryon</code>	net baryon number, i.e., baryons minus anti-baryons $\langle B - \bar{B} \rangle$
<code>tot_charm</code>	total charm $\langle c + \bar{c} \rangle$ (corresponding to Ncbc, see Section 3.1)
<code>totenergy</code>	total energy (in GeV)

The above quantities are calculated *before* the weak decays have occurred. They do not take weak decay acceptances into account, which may produce an apparent violation of strangeness, charge or baryon number. To get values of the above quantities *after* weak decays, one should move the `net` and `tot` prefixes to the end of the respective quantity name tags. The equivalents of the above quantities *after* weak decays have occurred are: `chargetot`, `chargenet`, `baryonnet`, `baryontot`, `stragetot`, `strangnet`, `light_tot`. These are complemented by the following name tags:

<code>entropy_t</code>	total entropy $S$
<code>pressuret</code>	total pressure (in units of energy density, GeV/fm <sup>3</sup> )

and the auxiliary

Figure 3: A typical structure of a `totratios.data` file.

```

#----- Experimental data file -----
weakdecay weak.test
# -----
#netstrang solvelams 0. 0. 0. 0
netcharge prt_yield 0. 0. 0. 0
negatives prt_yield 900. 50. 0. 0
positives prt_yield 900. 50. 0. 0
02+03 prt_yield 1800. 100. 0. 0
netcharge netbaryon 0.384 0.02 0. 1
netstrang totstrang 0. 0.01 0. 1
totenergy tot_prime 0.75 0.002 0. 0
# -- BULK PROPERTIES MAYBE FITTED --
entropy_t prdensity 3.3 0.2 0. 0
totenergy prdensity 0.4 0.04 0. 0
totstrang entropy_t 0.072 0.004 0. 0
tot_charm entropy_t 0.0037 0.001 0. 0
totenergy T_entropy 1.015 0.015 0. 0
pressuret prdensity 0.0820 0.00050 0. 0
totstrang tot_charm 1.0 0.05 0. 0
#----- Particle Yields SOME MUST BE FITTED-----
pi0139plu prt_yield 733. 54. 0. 1
mu0000plu prt_yield 0. 0. 0. 0
pi0139min prt_yield 732. 52. 0. 1
mu0000min prt_yield 0. 0. 0. 0
pi0135zer prt_yield 0. 0. 0. 0
Ka0492plu prt_yield 109. 9. 0. 1

```

`T_entropy`  $TS$ , temperature times entropy

`T_____4`  $T^4/(\hbar c)^3$  (useful to evaluate, for example, the trace anomaly  $(\varepsilon - 3P)/T^4$ )

Weak decay feed-down correction file or option is indicated in the experimental file by the keyword `weakdecay`. When this keyword is encountered during the program run as `name1`, then `name2` must be either of `NOWK_FEED`, `UNCORRECT`, otherwise `name2` is treated as the weak decay feed-down filename. The weak decay scheme thus specified applies to all subsequent data points until new `weakdecay` statement or end of experimental data file.

### 3.4.3. Referring to data points and their combinations

We offer even more flexible handling of data points, we have implemented simple algebraic combinations of data points within a file. The user can refer to a data point defined in the same file by its two-digit line number (not counting comment lines starting with #). The following snippet of an input file shows how to refer to another data point; line number 8 refers to the  $\pi^-$  defined on line 7, however, calculates its density. We also show a more advanced example of how to define and fit the ratio of  $(p + \bar{p})/(\pi^- + \pi^+)$ . Note that line numbers are not part of the experimental data file, they are provided below for easier orientation in the example.

```

line #  input file
:      :
7      pi0139min  prt_yield  data  stat  syst  fit?
8      07          prdensity data  stat  syst  fit?
9      pi0139plu  prt_yield  data  stat  syst  fit?
10     pr0938plu  prt_yield  data  stat  syst  fit?
11     pr0938plb  prt_yield  data  stat  syst  fit?
      # this is a comment, line number does not increase.
12     10+11      07+09      data  stat  syst  fit?

```

The possible operations are addition, subtraction, multiplication and division accomplished by using `+`, `-`, `X`, `/` symbols respectively in between two two-digit line numbers as seen in the above example. Note the necessary trailing 0 for single digit line numbers. These operations are limited to two-digit line numbers, although the input file can in general have up to 200 entries (not counting commented lines). Note that this feature uses implicitly recursive code, which may be compiler dependent. It has been found to work as intended on several platforms and compilers we tested SHARE with CHARM on. We provide a sample data file with the program package.

#### 3.4.4. Statistical and systematic errors

The systematic and statistical errors can be entered as two separate quantities in SHARE as seen in the above example. This option is created since systematic error is not a random variable that the statistical error is. Systematic error originates from the experimental setup and/or data analysis methods and it can be common to several experimental results, e.g., the efficiency to track strange antibaryons and baryons has same systematic uncertainty, or there could be a strong (anti)correlation, e.g., if an observed particle track is a proton or  $K^+$  is not always possible to decide, but if it is one, it cannot be the other. By allowing for systematic and statistical error entry as matter of principle, we prepare for a more complete future treatment of the systematic error including an error correlation analysis.

Once the systematic error correlation matrix function is known, one must discover combinations of the data which suffer least from the systematic error. The fit than involves a data set in which some of the fitted quantities have a much reduced systematic error. At present, the systematic error correlation matrix is not made available by the experimental groups. Therefore, such more detailed error treatment in the fitting procedure is not included in this release of the SHARE with CHARM program suite as a procedure could neither be properly set-up nor tested.

In the current release of the program, if both errors are made available and have been entered separately, they will be added to obtain the total error `error` of the data point: `error = stat + syst`.

We note, that as outcome of this procedure, we often see in the study of the RHIC and LHC data that the overall normalization factor  $dV/dy$  shows a large and apparently common error of all data, suggesting that all results we interpreted had as input a common systematic tracking efficiency error.

### 3.4.5. Conservation Laws

SHARE with CHARM allows the user to solve for a thermal parameter based on a fixed (or experimental) value rather than fit it. The most common application of this feature would be exact conservation of strangeness,  $\langle s \rangle = \langle \bar{s} \rangle$ , which means numerically solving for  $\lambda_s$ . In this case,  $\lambda_s$  is not a fit parameter anymore, but rather an analytical function of the other parameters constrained by the experimental data point.

In order to solve for a parameter, the name2 in the experimental data file (`totratios.data`) should be in the form `solveXXXX`, where XXXX is one of the fit parameters. The parameter limits set in `ratio.set.data` still apply, every parameter solution outside of these limits is rejected. This helps rejecting unphysical solutions, such as  $\lambda_s < 0$ .

In principle, it is possible to solve for any parameter using any data point. However, many such combinations do not have a minimum, especially if the data point does not (or only marginally) depend on said parameter. If MINUIT takes a long time (e.g., many iterations) without converging to a minimum, there is a good chance that the minimization procedure will not work. It is thus advised to use this feature mainly to solve for the values of chemical potentials based on conservation laws. For instance, strangeness conservation can be assured in the system by solving for  $\lambda_s$  by using the following line in the `totratios.data` file requiring net strangeness  $\langle s - \bar{s} \rangle$  to vanish:

```
netstrang solvelams 0. 0. 0. 0
```

The baryochemical potential in a perfectly central Pb–Pb ( $Z=82$ ,  $A=207$ ) collision can be solved for using the baryon number and solving for  $\lambda_q$ :

```
netbaryon solvelamq 414. 0. 0. 0
```

and the corresponding charge conservation may be imposed on the fit with:

```
netcharge solvelmi3 164. 0. 0. 0
```

The `solve` statements have to come at the beginning of the experimental data file, otherwise the program will return an error.

An alternative to the exact solving for a parameter required by a conservation law is to require approximate conservation of a quantity. Treating a conservation law as a data point allows for detector acceptance corrections. A line such as:

```
netstrang totstrang 0. 0.01 0. 1
```

imposes strangeness conservation to within 1%. We often impose charge over baryon number conservation with the line

```
netcharge netbaryon 0.39 0.02 0. 1
```

The choice of implementing the conservation laws analytically or approximately (if at all) is left to the user. It is worth noting that exact solution is a more reliable procedure, however, it cannot be used very often considering the limited acceptance data from contemporary collider experiments.

## 4. Running the program — `sharerun.data`

This file contains the instructions which are executed one by one during a program run. Every line contains a separate operation, such as reading input files, assigning values to parameters, calculation of particle ratios, fitting model parameters to experimental data (i.e., minimizing  $\chi^2$ ), plotting contours and  $\chi^2$  profiles. The program will read one line at a time and execute the command until it reaches the end of the `sharerun.data` file. It is imperative that the user maintains the appropriate spacing of commands and values in this file, because this file is read as a formatted input, same as most of the input files described in previous sections. Any deviation from the expected number of characters may result in an unexpected behavior of the program ranging from a misinterpretation of a value to not recognizing the command at all and exiting prematurely with an error. Generally, there are two spaces between keywords and numbers. We specify the expected command format wherever necessary. Each command can be used multiple times with different input and output files. We shall now describe all the commands available to the user with a brief description.

### 4.1. Reading input files

**READ THERM\_INI** **<11-letter filename>**

Reads the specified file corresponding to the `thermo.data` file described in Section 3.1.

**READ FIT\_PARAM** **<13-letter filename>**

Reads a file containing parameter ranges equivalent to the `ratioset.data` file described in section 3.1.2.

**READ PARTICLES** **<14-letter filename>** **<11-letter filename>**

Reads the file containing list of particle properties and a second file of corresponding decay tree. The files are considered being equivalent to `particles.data` and `decays.data` files described in Section 3.2 and 3.3.1.

**READ TOTALDATA** **<14-letter filename>**

Reads experimental data file equivalent to the `totratios.data` file described in Section 3.4.

### 4.2. Parameter manipulation at run time

**PSET** **<4-letter tag>** **VALUE**

The PSET command sets the thermodynamic parameter specified by the 4-letter tag to a VALUE. A real number is expected in VALUE, hence decimal point is necessary even with integer values. When the `thermo.data` file is read, a series of PSET-like commands is performed using all parameters and values read from the file.

**PFIX** **<4-letter tag>**

Fixes the given model parameter to its current value. In all subsequent commands, this parameter will be kept fixed until released, or its value modified by another command.

There are 5 additional tags that are used to control the program options in connection with PFIX. The user can choose to use Boltzmann approximation and quantum (Fermi–Dirac and Bose–Einstein, as appropriate) statistics via the tags `bltz` and `fdbe` respectively. The

Figure 4: A typical sharerun.data file.

```

##### reading particle list and decay tree #####
#READ PARTICLES particles.data decays.data
#READ PARTICLES partnowdt.data decays.data
#
##### reading model parameters values and ranges #####
#READ THERM_INI thermo.data
#READ FIT_PARAM ratioset.data
#
##### fitting LHC data in 10-20% centrality - no charm #####
#READ TOTALDATA LHC1020MI.data
#CALC FITRATIOS fit1020ne.out
#
##### fix gamma_q, fit semi-equilibrium
#PSET gamq 1.0
#PFIx gamq
#CALC FITRATIOS fit1020se.out
#
##### release gamma_q, calculate sensitivity profile for Lambda yield
#PREL gamq 0.5 2.0 0.1
#CALC SNSPROFIL prof_SNSLamb gams 1.0 2.5 15 36
#
##### fit without the Lambda yield (datapoint #36)
#DFIT 36 0
#CALC FITRATIOS fit1020ne.noL
#
##### restore fitting Lambda yield
#DFIT 36 1
#
#
##### set D0 (Dc1800zer..datapoint #84) yield to a value 5. +/- 2. and fit it
#DSET 84 5.0 2.0
#DFIT 84 1
##### release the number of charm+anticharm quarks (Ncbc)
#PREL Ncbc 0.01 100. 1.0
##### ... and fit with the D0
#CALC FITRATIOS fit1020ch.out
##### calculate the chi2 profile in Ncbc
#CALC CHIPROFIL prof1020Ncbc Ncbc 5. 100. 19
#
##### plotting the the dependence of Dc1800zer
##### on number of charm+anticharm quarks (Ncbc) and charm temperature (tc2t)
#CALC RATIOCONT 84 ratioplt.out Ncbc 10. 200. 19 tc2t 1.0 3.0 10

```



**CALC RATIO PLOT** *<12-letter filename>* *<4-letter tag>* **L U P datapoint**

This command calculates a ratio, yield or quantity specified on the `datapoint`-th line in the experimental data file as a function of the thermal parameter specified by the 4-letter tag. The program will vary the parameter from L to H in P equidistant steps and record in the output file the varying parameter values in the first and the property values in the second column. The output file can then be used as input to an external plotting program, such as GNUPlot, PAW, Xmgrace or Mongo. The format of this command is

(A4, 2X, A9, 2X, A12, 2X, A4, 2X, 2F5.1, 2I5), i.e., two spaces between each word until the parameter tag, two spaces after the parameter tag, 5 characters reserved for each of the lower and upper limits followed by 5 characters for the number of points and last, 5 characters for the data point number.

**CALC RATIOCONT** *datapoint* *<12-letter filename>* *<tag1>* **L1 U1 P1...**  
**...<tag2>** **L2 U2 P2**

Calculates a ratio, yield or a thermodynamic quantity as a function of two parameters specified by `tag1` and `tag2` for parameter values ranging from L1 to U1 in P1 steps for the first parameter and from L2 to U2 in P2 steps for the second one. Similar to the above RATIO PLOT command, the data point is referred to by its line number (`datapoint`) in the experimental data file. (Note, that  $100 \times 100$  results in 10000 grid points to be calculated which may take a long time.) The general format of this command expected by the program is: (A4,2X,A9,I5,A12,2X,A4,2X,F5.1,2X,F5.1,2X,I3,2X,A4,2X,F5.1,2X,F5.1,2X,I3)

The output is written to a file with 13-letter filename specified by the user in a 3-column table and can be plotted by an external program capable of 3D plotting.

**CALC FITRATIOS** *<13-letter filename>*

This command minimizes  $\chi^2/\text{ndf}$  of the set of experimental data input by the last READ TOTALDATA command varying parameters within ranges specified in READ FIT\_PARAM starting with parameter initial values from READ THERM\_INI.

In our fitting procedure, we minimize the  $\chi^2$  value function as function of SHM parameters. The  $\chi^2$  function is the sum of squares of the relative difference between computed yields and experimental data.

$$\chi^2 = \sum_{i=1}^N \frac{(f_{i,\text{theory}} - f_{i,\text{experiment}})^2}{(\Delta f_{i,\text{systematic}} + \Delta f_{i,\text{statistical}})^2}, \quad (37)$$

where  $f_i$  is the  $i$ -th investigated quantity with experimental error  $\Delta f_i$  and  $N$  is the number of data points. We seek the best fit to experimental particle yields and ratios using MINUIT [4], an optimization package part of the CERNLIB computational libraries. We evaluate the statistical significance (also called either  $p$ -value, or confidence level – CL) of our fits. CL is defined as the probability that given a correct hypothesis (here the SHM model) and Gaussian ‘noise’ experimental errors (caution: we are dealing with significant systematic data errors),  $\chi^2$  would in repeated measurements assume a value that is at or above the considered value – clearly, the smaller  $\chi^2$  is, the higher CL is, asymptotically approaching 100%.

Values of statistical significance far below 50% suggest that the model is not appropriate for the task of describing the experimental data. Regarding  $\chi^2$  in the limit of many degrees of freedom  $N_{\text{data}} - N_{\text{parameter}} = N_{\text{dof}} \rightarrow \infty$ , it is well known that  $\chi^2/N_{\text{dof}} = 1$  corresponds to CL of 50%, see figure 36.2 in PDG [1]. For  $N_{\text{dof}} < 10$ , this figure shows that a considerably lower  $\chi^2/N_{\text{dof}}$  is necessary to reach CL of 50%. For more complete discussion of significance, see PDG [1] section 36.2.2.

In case the minimization package MINUIT [4] used by SHARE does not find a good reliable minimum via common strategies, or the parameter errors cannot be reliably evaluated, MINOS subroutine is called to evaluate the parameter errors and potentially find a better minimum. This, unfortunately, significantly increases the computation time.

The output in the 13-letter file provided by the user has the general format:

Header with time and date of minimization.

Final thermal parameter values ( ‘+/-’ error, when fitted),  
followed by chemical potentials  $\mu_B, \mu_S, \mu_{I_3}$   
and phase space occupancies for each flavor  $\gamma_u, \gamma_d, \gamma_s, \gamma_c$ .

Then, the detailed fit results are printed in a table format:

```
TOP BOTTOM THEORY EXP ERROR CHITERM FEED-DOWN
```

where TOP refers to the denominator and BOTTOM to the numerator of the quantities defined in the input file (`totratios.data`), THEORY states the model value, EXP states the experimental value as given in the input file, ERROR is the combined statistical and systematic error, CHITERM is the  $\chi$  contribution of the data point to the total  $\chi^2/\text{ndf}$  defined as:

$$\chi = \frac{f_{\text{theory}} - f_{\text{experiment}}}{\Delta f_{\text{statistical}} + \Delta f_{\text{systematic}}}, \quad (= 0 \text{ if not fitted}). \quad (38)$$

The  $\chi$  is reported before squaring to keep the sign, i.e., information about the resulting model theoretical value being above or below the experimental data point. FEED-DOWN states the weak decay feed-down scheme or filename used for this particular data point. The end of the output file reports the number of degrees of freedom, total  $\chi^2$ ,  $\chi^2/\text{ndf}$  and statistical significance of the fit.

At the end of each fit, two additional output files are created, `CharmFeedPrimary.data` and `CharmFeed.data`. The first one contains the primary yields of charm particles calculated by the CHARM module and the second one contains particle yields after charm decays, i.e., particle yields produced solely by charm. Note, that these two filenames are constant and the files get rewritten every time a fit is performed.

#### **CALC FITNMINOS <13-letter filename>**

This command is equivalent to the above FITRATIOS regarding both format of the command line and function. The only difference is that parameter error evaluation MINOS [4] is never called. Omitting the use of MINOS usually saves considerable amount of computing time, however, errors of the resulting thermal parameters will not be reliable and the minimum found has a higher chance of not being the global minimum.

**CALC PLOT\_DATA** <3 13-letter filenames>

Generates three files which are optimized to be graphed with an external 2D plotting package (GNUPlot, Xmgrace, PAW,...). The first file contains numerical list of ratios and quantities that were fitted, the second one contains a numerical list of ratios and quantities that were calculated and the last one will contain experimental values with errors. See the discussion in Section 3.4.1 on how to choose which file a quantity should be included in. The filenames on the command line should be separated by 2 spaces.

**CALC CHIPROFIL** <12-letter filename> tag L U P

This command calculates a  $\chi^2/\text{ndf}$  profile of a parameter specified by the tag. The program divides the parameter range between Lower limit and Upper limit in P equidistant intervals, fixes the given parameter at the boundary of each interval (i.e., P+1 values including L and U) and fits other free parameters to the data as specified in the `ratio.set.data` file or PSET/PFIX/PREL commands preceding this one. This procedure is equivalent to a sequence of PSET and CALC FITRATIOS commands.

The main output of this command is the filename with `.prof` extension, which contains a 2-column table with the given parameter values in the first and the resulting  $\chi^2/\text{ndf}$  in the second column. The full output of all performed fits is stored in a log file with `__log` extension. For each fitted parameter, a separate file is created containing 5 columns and has the parameter tag appended to its name. For instance, performing a temperature  $\chi^2/\text{ndf}$  profile with output file stored in 'profTempLHC1', the values of  $\gamma_q$  will be stored in 'profTempLHC1\_gamq' file (provided that  $\gamma_q$  is a free parameter of the fit). The first column of each parameter file contains values of the tag parameter (temperature in the above example), the second column the fitted parameter values ( $\gamma_q$  values in the above example), the third contains values of an associated bulk property (see Table 3 for a details), the fourth column states the  $\chi^2/\text{ndf}$  and the last column contains statistical significance.

The general format of this command is (A4, 2X, A9, 2X, A12, 2X, A4, 2X, 2F8.1, I5), in other words there has to be 2 spaces between the text strings up to the tag, after which there are 8 digits allocated for the Lower limit, 8 digits for the Upper limit and 5 digits for the number of P oints.

**CALC SIGPROFIL** <12-letter filename> tag L U P

This command is very similar to the above CHIPROFIL in terms of both the command format and functionality. The only difference is that in the main output file <filename>.prof, the statistical significance is printed in the second column rather than  $\chi^2/\text{ndf}$ .

**CALC FITPROFIL** <12-letter filename> tag L U P datapoint

This and the next two commands allow to study the fit parameter sensitivity to a particular data point in detail. The format of the command is the same as the one above, except for the extra integer datapoint identifier at the end (line number of the data point in the experimental data file). General format is (A4, 2X, A9, 2X, A12, 2X, A4, 2X, 2F8.1, 2I5). The command produces a parameter tag profile for a fitted datapoint model prediction rather than the overall fit quality, as the previous two commands do. For example, if datapoint corresponds to  $\pi/p$  ratio within the given data set, the program performs a  $\chi^2$

Table 3: Table of associated bulk properties with parameters printed in the profile output files.

Parameter tag	Associated bulk property
temp	totenergy prdensity
norm	pressuret prdensity
gamq	entropy_t prt_yield
lamq	netbaryon prt_yield
mu_b	netbaryon prt_yield
gams	totstrang prt_yield
lams	netstrang prt_yield
mu_s	netstrang prt_yield
lmi3	netcharge prt_yield
mui3	netcharge prt_yield

profile calculation with respect to the parameter `tag` fixing it at `P` values ranging from `L` to `U`.

The command creates several output files, namely `<filename>.prof`, which contains the values of parameter `tag` in the first column and the  $\chi$  term of the given `datapoint` defined by Eq. 38 in the second column. The output file with `.chi2` extension contains the overall  $\chi^2/\text{ndf}$  of the fits, and the extension `.stsg` represents statistical significance of the fits. For every fitted parameter other than `tag`, there is a correlation file with extension `_<tag2>` (e.g., `_gamq`) created, which has the same format and contents as for the `CHIPROFIL` command above. Full output for all the fits is stored in a log file with extension `__log`.

**CALC DATPROFIL <12-letter filename> tag L U P datapoint**

This command has the same command line structure, functionality and output files as the `FITPROFIL` command above, except the values of the `datapoint` (rather than its  $\chi$  term contribution to the overall  $\chi^2$  of the fits) is printed in the output file `<filename>.prof`.

**CALC SNSPROFIL <12-letter filename> tag L U P datapoint**

Same as the above two commands, except the output file `<filename>.prof` now contains the *sensitivity* of the given `datapoint` to the particular parameter `tag`. The sensitivity is defined as a ratio of the data point's SHM prediction for a given parameter `tag` value to the SHM prediction of the `datapoint` for the best fit value of that parameter.

**CALC CHI2\_CONT <9-letter filename> deviation tag1 tag2**

This command calculates the  $\chi^2/\text{ndf}$  contour for the parameters `tag1` and `tag2`. The program will output to the file `<filename>` pairs of parameter `tag1` and `tag2` values that correspond to  $\chi^2/\text{ndf} = \text{deviation} \times (\chi^2/\text{ndf})_{\text{bestfit}}$ . The general format of the command is `(A4, 2X, A9, 2X, A9, 1X, F4.1, 2X, A4, 2X, A4)`

#### 4.5. Run log (`sharerun.out`)

The complete 'log' for each run is saved in a file `sharerun.out`. This includes:

- The contents of each input file as read in by the program (useful for input file format check)
- A list of performed operations.
- MINUIT output. Parameter correlation matrix can be found here, for example.
- The content of each output file (in the same format as in the output file)

If the program does not encounter any problems during the run, a message:

RUN TERMINATED SUCCESSFULLY,

is printed on screen and at the end of the `sharerun.out` file. In case an error occurs during a run, the program reports it to the user on screen. More information about the error is reported in the `sharerun.out` file.

#### 4.6. Fitting pitfalls, parameter sensitivity to data

Convergence to the very same set of best parameters cannot be expected when one or more of the parameters is insensitive to any of the fitted experimental data points. In this case, the minimum of  $\chi^2$  function is a domain in the respective parameter space, and a point in this domain is chosen in a quasi-random manner. As an example of this situation, consider the data from LHC. When fitting particle yields and ratios, one can constrain the values of chemical non-equilibrium parameters  $\gamma_q$  and  $\gamma_s$  along with  $T, V$ , as these are constrained by the precisely measured numerous baryon and meson yields [19]. However, in the LHC environment, it is challenging to constrain the value of baryochemical potential  $\mu_B$ . This is especially the case when fitting with charm. While a measurement of any charm hadron yield, for instance  $D^0$  meson, with 10% precision constrains the charm yield to a narrow range in  $N_{c\bar{c}}$ , the charm feed-down introduces additional uncertainty in the value of  $\mu_B$  due to charm baryon production and decays. Moreover, feed-down impacts hadron yields and hence the other fitted parameters adjust accordingly. In order to measure the baryochemical potential  $\mu_B$ , one would need, for example, a relative baryon–antibaryon difference measurement,  $(\bar{B}_i - B_i)/(B_i + B_i)$  for a baryon  $B_i$  obtained with a precision comparable to the other input data.

We thus advise fixing insensitive parameters to most likely values, especially when fitting charm at LHC. Therefore, until additional data fixing  $\mu_B$  becomes available, one should proceed with zero baryochemical potential, that is fix  $\lambda_s = \lambda_q = 1$ , in the exploration of charm effect on hadronization.

## 5. Installation

### 5.1. Pre-requisites

Before you start installing SHARE with CHARM, make sure you have the following installed on your system:

- Fortran 77 compiler, we have tested GNU `gfortran` and Intel `ifort` compilers.
- C++ compiler (including C++ standard libraries), we have tested GNU `g++` and Intel `icpc` compilers.

- CERNLIB libraries. They are available in standard repositories for most GNU Linux distributions, alternatively, the source code is available for download at [18]. Debian based linux distribution (Ubuntu,...) users should locate and install the package `cernlib` from their system repository. Red Hat base (Fedora Project, SLC,...) can install `cernlib` from a rpm package available, for example, at [16].

### 5.2. Organization of the program package

The SHARE with CHARM program comes in a single `.zip` archive labeled `sharev3.zip`. The package is available at <http://www.physics.arizona.edu/~gtshare/SHARE/share.html>. After obtaining the program package, unpack it using the following command (it will create a folder called `sharev3` with all the files in it):

```
unzip sharev3.zip
```

The following files will be created in this directory from the archive contents. The files are enough for a ‘representative’ run of SHARE with CHARM.

**src/sharev3.0.0.F** SHARE source code in Fortran 77.  
**src/CharmDistribution\_v1.9.cpp** CHARM module source code in C++.  
**decays.data** The complete Particle Data Group decay tree of light hadrons (Section 3.3.1).  
**HFfeed.data** The complete Particle Data Group decay tree of charm hadrons (Section 3.3.3).  
**LHC1020MI.data** A representative input data files (Section 3.4) containing experimental yields data for centrality bin 10-20% based on data from the ALICE experiment as of August 2013, see [19] and references therein.  
**makefile** A makefile of the project, useful for program compilation, see Section 5.3 below.  
**particles.data** Particle properties with full widths (Section 3.2).  
**partnowdt.data** Particle properties with no widths (Section 3.2). Calculations with this input file require significantly less computational time, and the use of full widths has not yet been justified, see for example recent comparison in [15].  
**ratioset.data** The parameter ranges input file (Section 3.1.2).  
**ratioset.test** The parameter ranges input file for Quick Start test run.  
**sampleoutput** Directory containing sample output files resulting from a ‘representative’ sample run with input files we provide as part of the package.  
**sharerun.data** A ‘representative’ run input file (Section 4) including an analysis of hadron yields at LHC presented by members of our collaboration in [19].  
**thermo.data** The list of model parameters (Section 3.1).  
**weak.feed** A sample weak decay file (Section 3.3.2).

### 5.3. Recommended compilation — using make

The recommended way to compile SHARE with CHARM is to make use of the GNU `make` utility [17], available on most GNU Linux systems (if this is not your case, proceed to Section 5.4). The most common combination of available compilers is `gfortran` and `g++`. If this is your case, after unzipping the contents of the program package into a folder, use the command

```
make
```

in this directory to compile the program. If you are using different compilers, edit the header of the included `makefile` to specify compilers available on your system. When done, use `make` (as above) to compile SHARE with CHARM.

Using `make` with the included `makefile` processes the two source files in the `src` folder, compiles each of them into an object file, which is stored in the `obj` folder and then links the object files together with CERN libraries into an executable `share`, which is ready to be run from the command line. We provide the two most common targets in the `makefile`, `all` to compile the program and `clean` to remove objects and executable file. You may also need to specify the location of the CERN libraries on your system in the `makefile`, for instance,

```
LIBS = -L/usr/local/cernlib/2006/lib -lstdc++ ...
```

#### 5.4. Manual compilation

SHARE with CHARM consists of two source code files, both located in the `src` subdirectory. Manual compilation consists of three steps.

1. Compiling SHARE Fortran code into an object. For example, using the GNU Fortran compiler `gfortran`, this is done via the following command (in the `src` folder):

```
gfortran sharev3.0.0.F -c -o sharev3.0.0.o
```

Note the `-c` option to prevent linking. You may need to consult your Fortran compiler documentation for equivalent command line options.

2. Compiling the CHARM module written in C++ is accomplished similarly to the above step, using an example command line with GNU C++ compiler `g++`:

```
g++ CharmDistribution_v1.9.cpp -c -o CharmDistribution_v1.9.o
```

3. Linking all object files with the necessary libraries into an executable binary file `share` is accomplished using the Fortran compiler used in step 1 on the following command line :

```
gfortran sharev3.0.0.o CharmDistribution_v1.9.o \  
-lstdc++ -lkernlib -lmathlib -lpacklib -o share
```

In case you compiled CERN libraries manually, you may need to specify the location of the libraries on the last command line using the `-L/<cernlib location>/lib` option in order to link them properly. If necessary, consult your compiler and CERN libraries documentation for details.

When all three steps are completed without errors, move (copy) the executable binary of SHARE with CHARM (`share` in the above example) to the parent directory (i.e., one directory up) where all SHARE input files are located. The program is invoked with `./share` command (unless a different name was chosen by the user during compilation). The program opens the `sharerun.data` file located in the current directory and performs tasks specified therein. See Section 4 for details on how to run the program. The provided copy of `sharerun.data` should produce detailed output showing the program capabilities, which can be used to check correct program operation by comparing with the provided sample output in the `sampleoutput` directory. Tests were run on both 32 and 64 bit processors with two different versions of CERN libraries. Differences between platforms appear when fitted parameters are not constrained by data, see Section 4.6.

## 6. Summary of current SHM status

SHARE with CHARM is an analysis tool developed specifically to study particle production in relativistic heavy-ion collisions spanning an energy range from compact baryonic matter through the entire RHIC range up to top LHC energy. SHARE with CHARM is particularly suitable to address the following questions (*italic font show new features of this release*):

- What is chemical freeze-out temperature, chemical potentials, and volume?
- Which quark flavors are in chemical equilibrium at hadronization and those that are not, how abundant are they?
- What are the physical bulk properties of the hadronizing fireball?
- Are particle yield fluctuations compatible with hadron yields and ratios?
- *Is charm subject to statistical hadronization?*
- *How large is the contribution of charm hadron decays to the final light hadron yields?*
- *How does accounting for charm decay feed change the hadronization conditions?*
- *Does charm hadronize at the same temperature as the light hadron freeze-out?*

The need for the new version of SHARE with CHARM arises from the necessity of including charm hadrons into statistical hadronization model as they become significant in heavy-ion collision experiments at LHC energy range. In the upgraded program, a flexible treatment of charm hadrons has been introduced, and we provide full charm hadron list and, more importantly, a full decay tree compiled to the best of current knowledge of charm decays in a procedure that assures cross-particle symmetries and consistence.

At the time of preparing this publication, there is no charm hadron yield measured at LHC. With partial measurement of the  $D^0$ - $p_T$ -spectrum, we estimate its invariant yield  $dN/dy$  to be in the range of  $1.3 < dN_{D^0}/dy < 9.0$ , corresponding to  $N_{c\bar{c}} \in (6, 45)$ . However, in primary parton collisions a more generous result comes from scaling the total charm cross-section in  $pp$  collisions  $\sigma_{cc}$ , which implies  $N_{c\bar{c}} = 246 \pm 154$  [8], where most of the uncertainty is inherent from the  $\sigma_{cc}$  uncertainty. SHARE with CHARM is capable of exploring both of these regions. As soon as a single charm hadron yield data becomes available, fitting this hadron using SHARE with CHARM will help to constrain the total amount of charm present at hadronization allowing to cross check with the production models. With a second charm hadron yield, the difference between light and charm hadronization temperature can be constrained. And finally, with additional charm particle yields, we will be able to answer if charm hadronizes according to statistical hadronization principles.

We believe that at the time of writing, SHARE with CHARM is the only SHM implementation capable of:

- accounting for full chemical non-equilibrium of all four quark flavors,  $u$ ,  $d$ ,  $s$  and  $c$ ,
- characterizing and/or fitting bulk properties of the particle source,
- evaluating the produced hadron fluctuations,
- quantifying the charm hadron contribution to hadron abundances,

aside from providing the other features necessary to describe soft hadron production in relativistic heavy-ion collisions in the entire energy range.

## Acknowledgement

Work supported by the U.S. Department of Energy, Grants no. DE-FG02-04ER41318 (MP, JL, JR) and DE-FG02-93ER40764 (GT). Laboratoire de Physique Théorique et Hautes Energies, LPTHE, at University Paris 6 is supported by CNRS as Unité Mixte de Recherche, UMR7589. GT acknowledges financial support received from the Helmholtz International Centre for FAIR within the framework of the LOEWE program (Landesoffensive zur Entwicklung Wissenschaftlich-ökonomischer Exzellenz) launched by the State of Hesse.

## References

- [1] J. Beringer *et al.* [Particle Data Group Collaboration], Phys. Rev. D **86**, 010001 (2012).
- [2] G. Torrieri, S. Steinke, W. Broniowski, W. Florkowski, J. Letessier and J. Rafelski, Comput. Phys. Commun. **167**, 229 (2005) [nucl-th/0404083].
- [3] G. Torrieri, S. Jeon, J. Letessier and J. Rafelski, Comput. Phys. Commun. **175**, 635 (2006) [nucl-th/0603026].
- [4] F. James and M. Roos, Comput. Phys. Commun. **10**, 343 (1975).
- [5] J. Kapusta, B. Muller and J. Rafelski, “Quark-Gluon Plasma: Theoretical Foundations”, Elsevier Science, (2003).
- [6] J. Letessier and J. Rafelski, “Hadrons and quark–gluon plasma”, Camb. Monogr. Part. Phys. Nucl. Phys. Cosmol. **18**, 1 (2002).
- [7] P. Koch, B. Muller and J. Rafelski, Phys. Rept. **142**, 167 (1986).
- [8] R. E. Nelson, R. Vogt and A. D. Frawley, Phys. Rev. C **87**, 014908 (2013) [arXiv:1210.4610 [hep-ph]], and private communication with R. Vogt
- [9] M. Petran, J. Letessier, V. Petracek and J. Rafelski, Acta Phys. Polon. Supp. **5**, 255 (2012) [arXiv:1112.3189 [hep-ph]].
- [10] J. -W. Li and D. -S. Du, Phys. Rev. D **78**, 074030 (2008) [arXiv:0707.2631 [hep-ph]].
- [11] I. Kuznetsova and J. Rafelski, Eur. Phys. J. C **51**, 113 (2007) [hep-ph/0607203].
- [12] G. Torrieri, S. Jeon and J. Rafelski, Phys. Rev. C **74**, 024901 (2006) [nucl-th/0503026].
- [13] C. Pruneau, S. Gavin and S. Voloshin, Phys. Rev. C **66**, 044904 (2002) [nucl-ex/0204011].
- [14] Fortran 77 Standard, [http://www.fortran.com/F77\\_std/rjcnf0001.html](http://www.fortran.com/F77_std/rjcnf0001.html), Accessed 20 Sept 2013, (or any F77 reference manual).
- [15] M. Petran, J. Letessier, V. Petracek and J. Rafelski, arXiv:1309.6382 [hep-ph].
- [16] CERNLIB rpm package list, <http://rpmfind.net/linux/rpm2html/search.php?query=cernlib>, Accessed 6 Oct 2013.
- [17] Homepage of the ‘make’ utility, <http://www.gnu.org/software/make/>, Accessed 30 Sept 2013.
- [18] Homepage of CERNLIB, <http://cernlib.web.cern.ch/cernlib/>, Accessed 30 Sept 2013.
- [19] M. Petran, J. Letessier, V. Petracek and J. Rafelski, Phys. Rev. C **88**, 034907 (2013), [arXiv:1303.2098 [hep-ph]].

## APPENDIX G

### CHARM DECAY AS A SOURCE OF MULTISTRANGE PARTICLES

M. Petran, J. Letessier, V. Petracek, J. Rafelski, Pending publication as proceedings of Strangeness in Quark Matter (SQM), 22-27 July 2013, Birmingham, UK, in IOP Conference series

E-print available as: arXiv:1310.2551 [hep-ph]

#### Summary

We evaluate the effect of including charm flavor hadrons produced in heavy-ion collisions at RHIC and LHC. Based on charm cross section measurement (publication reference [1]), we estimate the amount of charm produced in central Au–Au collisions at the top RHIC energy 200 GeV to be  $N_{c\bar{c}} = 8.6$  at mid-rapidity. Our study shows that charm effect at RHIC is negligible in terms of the resulting influence on SHM parameters and bulk physical properties of the source. However, at LHC the expected amount of charm is much greater. Theoretical charm cross section prediction leads to  $N_{c\bar{c}} = 246 \pm 154$  at mid-rapidity in central Pb–Pb collisions (publication reference [2]). We complement this estimate with the incomplete  $p_{\perp}$ -spectrum of  $D^0$  meson measured by the ALICE collaboration (publication reference [7]), which leads to  $dN_{D^0}/dy \in (1.3, 9.0)$ . The  $D^0$  yield estimate translates to a range of  $N_{c\bar{c}} \in (6, 45)$  in 0–20% centrality Pb–Pb collisions at  $\sqrt{s_{NN}} = 2.76$  TeV, much lower than the theoretical expectation. We evaluate the charm effect in a range of  $N_{c\bar{c}}$  covering both scenarios. We confirm a previous result (publication reference [6]), that charm decays are a significant source of multistrange particles and we show that for  $N_{c\bar{c}} > 50$ , the charm effect on the yield of  $\Xi$ , for example, is larger

than experimental error and hence charm is relevant to achieve precise description of particle production at LHC. We show that fitted charm hadron decays replace strange hadron production from QGP and effectively reduce the strangeness phase space occupancy  $\gamma_s$  as a function of charm abundance. Physical properties of the fireball are only marginally different.

During preparation of this proceedings, I was responsible for all calculations, result analysis and preparation of graphic presentation. My original draft was revised before submission with my co-authors, and the final version below contains about 70% of my original text.

# Charm decay as a source of multistrange hadrons

M Petran<sup>1</sup>, J Letessier<sup>2</sup>, V Petracek<sup>3</sup> and J Rafelski<sup>1</sup>

<sup>1</sup> Department of Physics, University of Arizona, Tucson, AZ 85719, USA

<sup>2</sup> Laboratoire de Physique Theorique et Hautes Energies, Universite Paris 6, F-75005

<sup>3</sup> Czech Technical University in Prague, Brehova 7, 115 19 Praha 1, Czech Republic

**Abstract.** We describe a newly formulated approach to account for charm production and decay in Statistical Hadronization approach. Considering Pb–Pb collisions at  $\sqrt{s_{NN}} = 2.76$  TeV at LHC we show that charm hadron decays can be a significant contributor to the multistrange hadron abundance. We discuss the magnitude of expected effects as a function of charm yield.

## 1. Charm Production and Decay in Heavy Ion Collisions

We demonstrate that in a precise analysis of hadron abundances within, e.g., the statistical hadronization model (SHM), it is necessary at LHC to allow for contribution to hadron yields from charm decays. In order to accomplish this we need to know: 1) total charm quark yield in QGP at hadronization; 2) charm hadronization pattern into hadrons; and 3) charm hadron decay distribution.

Initial state charm production can be estimated by folding the  $pp$  cross section with the number of initial nucleon-nucleon collisions. To be specific, we recall that in central Au–Au collisions at RHIC, the total charm cross-section has been measured to be  $d\sigma_{c\bar{c}}/dy|_{y=0} = 175 \pm 12 \pm 23 \mu b$ , and shown to scale with the number of binary collisions [1]. Thus, in most central 0%–5% centrality bin RHIC reactions, one finds  $N_{cc}^{\text{RHIC}} \equiv dN_{c+\bar{c}}/dy \simeq 4.3$  for  $y \in (-0.5, 0.5)$  measured in the CM frame.

For the LHC energy in Pb–Pb collisions at  $\sqrt{s_{NN}} = 2.76$  TeV at LHC, theoretical considerations lead to  $N_{cc} = 246 \pm 154$  ( $123 \pm 77$  pairs), where the error is due to uncertainty in charm production cross section [2]. It is believed that most of these charm pairs survive the parton thermalization and the sequel QGP evolution to the hadronization stage. However, if the prediction of such high abundance is true, one must expect some significant charm reannihilation. This can be checked in near the future within our kinetic flavor evolution model [3].

At QGP hadronization, all surviving charm hadronizes, producing heavy particles with hidden, open single charm, and multiple charm content. After traveling at most a few hundred  $\mu m$ , all these particles have decayed. For nearly all decay channels, it is practically impossible to tell which final state hadrons originate in a charm decay. This means that the hadron yields one measures contain input from post-hadronization charm decay. If all particles were fed by charm decay with a strength that is similar to the SHM model production, the contribution of charm would simply be a shift in overall normalization. The principal objective we pursue here is to show that this is not the case. We show that charm and strangeness are strongly correlated, and thus charm replaces some of strangeness production in QGP. Given  $N_{cc}$ , we predict yields of all charmed hadrons using the statistical hadronization method.

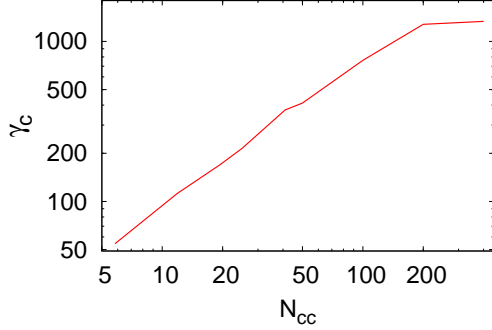


**Figure 1.** The charm phase space occupancy as a function of total charm present at hadronization.

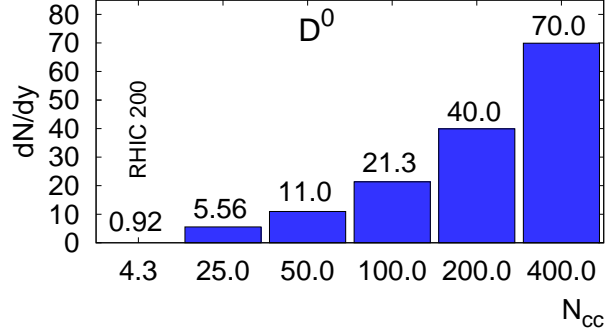


**Figure 2.** The  $D^0$  meson yield as a function of total charm abundance  $N_{cc}$  at hadronization.

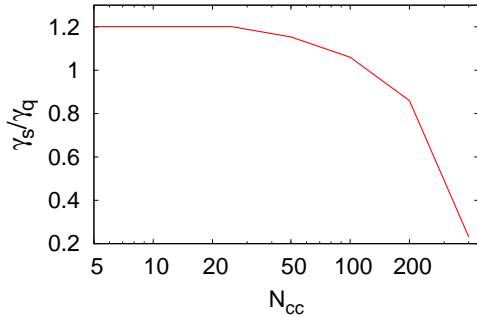
## 2. SHARE with CHARM

We have developed a new program predicting the contribution of charm hadron decays and allowing a fit with charm feed accounted into all hadron abundance. This program comprises a CHARM module which adds charm decay hadron multiplicity into SHARE, the statistical hadronization model implementation we use [4, 5]. The new SHARE with CHARM utility uses  $N_{cc}$  as an additional fit parameter when analyzing hadron production in heavy-ion collisions. SHARE with CHARM further allows the differentiation of the temperature of charm hadronization  $T_c$  from the temperature  $T$  of other hadron production. However, for reason of space we refrain here from showing results with this refinement.

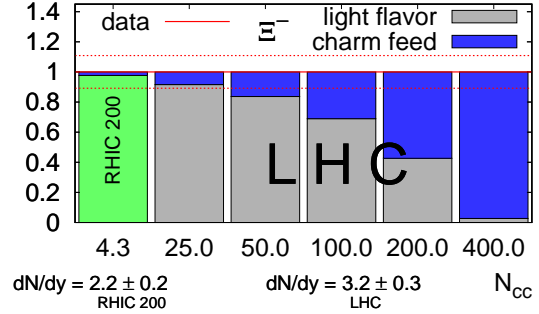
SHARE with CHARM functions as follows: for a given  $N_{cc}$  in the first step we compute the distribution of charm among all charm hadrons following the principles of statistical hadronization at a prescribed temperature  $T_c$ . To describe the normalization of charm yield, the phase space occupancy  $\gamma_c$  has been introduced. Given  $N_{cc}$ ,  $\gamma_c$  is solved for using methods described in [6]. Charm production is not thermal, but is due to the initial hard parton scattering. Therefore it is expected to be strongly out of chemical equilibrium. In Figure 1 we see the magnitude of  $\gamma_c$  as a function of  $N_{cc}$  for hadronization temperature  $T_c = T$ . We note that for  $N_{cc} > 50$ , the magnitude of  $\gamma_c > 500$  implies that some of the charm produced will reannihilate. This effect may explain how the large initial predicted yield can be consistent with the more realistic yield obtained in direct experimental effort, as we now describe.

Figure 2 shows the expected  $dN_{D^0}/dy$  yield (number above each column) for a prescribed value of  $N_{cc}$ . Charmed hadrons in general show dependence on  $N_{cc}$  proportional to the number of constituent (anti-)charm quarks with small variations due to changes in statistical parameters such as  $T$  and  $\gamma_s$  arising when a fit is performed. The ALICE experiment at LHC has the capability of recognizing the charm decay in specific channels and thus can measure the charmed hadron yields. The  $D^0$  meson  $p_\perp$ -spectrum has been presented [7] for the 0-20% centrality bin. Due to the uncertain low  $p_\perp$  bin, the yield  $dN/dy$  cannot be reliably integrated. However, the other points allow us to estimate by extrapolation to  $p_\perp = 0$  a yield  $dN/dy|_{D^0} \in (1.3, 9.0)$ .

Considering the results presented in Figure 2, this implies a 5 times larger total yield  $N_{cc} \simeq 6 - 45$  charm and anti-charm quarks. Scaling from 0-20% to the 0-5% centrality by a factor 1.35 we find  $N_{cc}^{\text{LHC}} \in (10, 60)$  as the best direct experiment-based estimate, much less than the central point of the initial production evaluation  $N_{cc} = 246 \pm 154$  [2]. Still, we choose to show expected yields for up to a value  $N_{cc} = 400$ , and the yield of  $D^0$  mesons clearly is not compatible even with  $N_{cc} = 100$ .



**Figure 3.** Strangeness over light quark phase space occupancy as a function of total charm present at hadronization.



**Figure 4.** The relative contribution of charm decays to the yield of  $\Xi^-$  as a function of charm abundance, see text for details.

In the next SHARE with CHARM step, each of the produced charm hadrons is allowed to decay. Based on experimental decay data [8], symmetry principles, and plausibility arguments, we prepared a complete charmed hadron decay table. This task took much effort, required to study of many additional theoretical references, and further improvements will certainly be necessary. One must see our present effort as a first step to be as complete as the current understanding of charm hadron decays.

In the final SHARE with CHARM step, the produced hadrons and their resonances are added to the SHARE initial SHM yields obtained for a set of chosen SHM parameters. Hadron resonances are decayed; the total hadron yields are compared to the experimental data input field, and  $\chi^2$  computed. An improved set of statistical parameters is proposed by MINUIT routine embedded in SHARE. The cycle of computations is carried out until SHARE concludes that the best local minimum of  $\chi^2$  is achieved.

### 3. Charm decay feed

We quantify the charm hadron decay contributions in the final hadron yields using previous analysis of central Au–Au collisions at RHIC [9] and for LHC, we perform our study using the same input data as in our recent analysis of Pb–Pb collisions at LHC [10, 11]. In order to quantify the expected effect in the absence of a measured charm hadron yield at LHC we perform a parametric study prescribing a value of  $N_{cc} \in (0, 400)$  while fitting the yields of observed hadrons. Charm feed–down of light hadrons generally has a different pattern than the light hadron production in QGP hadronization. Therefore, although the charm contribution may be hidden within the experimental errors of light hadrons, a very large abundance introduces a tension in the SHM fit of multiple hadron species with different strangeness content.

In Figure 3, we show the change of the statistical parameter  $\gamma_s/\gamma_q$ , characterizing the strangeness present at time of hadronization, resulting from the fit. For the value  $N_{cc} = 0$ , the results of our prior fit apply [10, 11]. There is a nominal change up to  $N_{cc} < 50$ . For  $N_{cc} > 50$  the charm decay feed replaces in a significant way the strangeness abundance, and for  $N_{cc} = 400$  strangeness in QGP at hadronization would be practically erased. Naturally, this is impossible, and it is clear that  $N_{cc} > 150$  is an unpalatable result also inconsistent with the  $D^0$  spectral results as we discussed.

During our study, we confirm a previous result [6], that charm decays contribute substantially to multistrange hadrons,  $\phi$ ,  $\Xi$  and  $\Omega$ . In Figure 4, we show as an example the relative contribution to  $\Xi^-$  yield as a function of total charm abundance  $N_{cc}$  normalized to the experimental value indicated at the bottom for RHIC and LHC. The red dotted lines represent

the experimental error, the blue part shows the contribution to  $\Xi^-$  yield from charm decays. One can see that at RHIC-200, the charm contribution presents an insignificant part of the total yield. However, at LHC-2760, the contribution to  $\Xi^-$  yield (and similarly other multistrange particles) exceeds the experimental error for  $N_{cc} > 25$  (that is 13 or more pairs).

We further study the effect of charm on the thermal parameters of the SHM fit. Volume  $dV/dy$ , chemical freeze-out (hadronization) temperature  $T$  and light hadron phase space occupancy  $\gamma_q$  show a very slow, but steady decrease within their respective errors. As discussed, charm decays are a significant source of strangeness and hence the strange phase space occupancy  $\gamma_s$  decreases significantly upon the introduction of a relatively large charm yield. This is the cause why multistrange particles are affected the most by charm decays.

We investigated the effect of including the charm degree of freedom on the bulk properties of the particle source. We found that the physical bulk properties, such as energy density  $\varepsilon$ , entropy density  $\sigma$ , and pressure  $P$  remain unchanged. Therefore, the charm contribution to particle yields does not affect our previous findings about universality of hadronization condition [10].

#### 4. Outlook

Using the new SHM program, SHARE with CHARM, we found that in RHIC Au–Au collisions at 200 GeV, the amount of charm has very little direct effect on hadron yields, whereas in LHC Pb–Pb collisions at 2.76 TeV, charm has an observable effect on hadron yields. We have shown that the present best estimate of the total  $c + \bar{c}$  yield  $N_{cc} \simeq 250 \pm 150$  seems too large compared to the reported  $D^0$  spectrum. We have shown that  $N_{cc} \simeq 100$  (50 pairs) will contribute nearly 3sd to the yield of  $\Xi$  and thus analysis of the hadron yields should include charm decays once such a yield is confirmed.

A precise yield of at least one of the charmed hadrons is necessary for an analysis of hadron yields with SHARE with CHARM to be possible. Without charmed hadrons we find that a fit of  $N_{cc}$  does not lead to a clear  $\chi^2$  minimum: we find a nearly totally flat  $\chi^2$  as a function of  $N_{cc}$ . This is of course good news in the sense that any acceptable in size measured charmed hadron yield will “work”. If and when we have more than one charmed hadron yield measured directly, we can determine the difference in hadronization temperature  $\delta T \equiv T_c - T$ . With more than two charmed hadron yields available we begin to test the hypothesis that statistical hadronization applies to charmed hadron production. We noted that based on future experiment further refinements in our charm hadron decay tables are needed. To conclude, there is still much to do in preparation for the charm hadron era of relativistic heavy ion collisions.

#### Acknowledgments

This work has been supported by a grant from the U.S. Department of Energy, grant DE-FG02-04ER41318, Laboratoire de Physique Théorique et Hautes Energies, LPTHE, at University Paris 6 is supported by CNRS as Unité Mixte de Recherche, UMR7589.

#### References

- [1] D. Thusty [STAR Collaboration], Nucl. Phys. A **904-905**, 639c (2013) [arXiv:1211.5995 [hep-ex]].
- [2] R. E. Nelson, R. Vogt and A. D. Frawley, Phys. Rev. C **87**, 014908 (2013) and R. Vogt, private communication.
- [3] J. Letessier and J. Rafelski, Phys. Rev. C **75**, 014905 (2007).
- [4] G. Torrieri, et al Comput. Phys. Commun. **167**, 229 (2005).
- [5] G. Torrieri, S. Jeon, J. Letessier and J. Rafelski, Comput. Phys. Commun. **175**, 635 (2006).
- [6] I. Kuznetsova and J. Rafelski, Eur. Phys. J. C **51**, 113 (2007).
- [7] B. Abelev *et al.* [ALICE Collaboration], JHEP **1209**, 112 (2012).
- [8] J. Beringer *et al.* [Particle Data Group Collaboration], Phys. Rev. D **86**, 010001 (2012).
- [9] J. Rafelski, J. Letessier and G. Torrieri, Phys. Rev. C **72**, 024905 (2005).
- [10] M. Petran and J. Rafelski, Phys. Rev. C **88**, 021901(R) (2013)
- [11] M. Petran, J. Letessier, V. Petracek and J. Rafelski, Phys. Rev. C **88**, 034907 (2013).

## REFERENCES

- [1] B. V. Jacak and B. Muller, *The exploration of hot nuclear matter*, Science, **337**:310–314, 2012, DOI:10.1126/science.1215901.
- [2] J. Letessier and J. Rafelski, *Hadrons and quark - gluon plasma*, volume 18, Camb.Monogr.Part.Phys.Nucl.Phys.Cosmol., 2002.
- [3] J. Rafelski and J. Letessier, *Sudden hadronization in relativistic nuclear collisions*, Phys.Rev.Lett., **85**:4695–4698, 2000, DOI:10.1103/PhysRevLett.85.4695.
- [4] P. Koch, B. Muller, and J. Rafelski, *Strangeness in Relativistic Heavy Ion Collisions*, Phys.Rept., **142**:167–262, 1986, DOI:10.1016/0370-1573(86)90096-7.
- [5] J. Beringer et al., *Review of Particle Physics (RPP)*, Phys.Rev., **D86**:010 001, 2012, DOI:10.1103/PhysRevD.86.010001.
- [6] J. Rafelski and B. Muller, *Strangeness Production in the Quark - Gluon Plasma*, Phys.Rev.Lett., **48**:1066, 1982, DOI:10.1103/PhysRevLett.48.1066.
- [7] I. Kuznetsova and J. Rafelski, *Heavy flavor hadrons in statistical hadronization of strangeness-rich QGP*, Eur.Phys.J., **C51**:113–133, 2007, DOI:10.1140/epjc/s10052-007-0268-9.
- [8] B. Abelev et al., *Suppression of high transverse momentum D mesons in central Pb-Pb collisions at  $\sqrt{s_{NN}} = 2.76$  TeV*, JHEP, **1209**:112, 2012, DOI:10.1007/JHEP09(2012)112.
- [9] D. Tlusty, *Open charm hadron production via hadronic decays at STAR*, Nucl.Phys., **A904-905**:639c–642c, 2013, DOI:10.1016/j.nuclphysa.2013.02.097.
- [10] B. Abelev et al., *Systematic Measurements of Identified Particle Spectra in pp, d+ Au and Au+Au Collisions from STAR*, Phys.Rev., **C79**:034 909, 2009, DOI:10.1103/PhysRevC.79.034909.
- [11] Y. Zhang, *D<sup>0</sup> meson yield in Au–Au collisions*, 2013, personal communication.
- [12] J. Rafelski, *Strange anti-baryons from quark - gluon plasma*, Phys.Lett., **B262**:333–340, 1991, DOI:10.1016/0370-2693(91)91576-H.

- [13] M. Aggarwal et al., *Strange and Multi-strange Particle Production in Au+Au Collisions at  $\sqrt{s_{NN}} = 62.4$  GeV*, Phys.Rev., **C83**:024901, 2011, DOI:10.1103/PhysRevC.83.024901.
- [14] M. L. Miller, et al., *Glauber modeling in high energy nuclear collisions*, Ann.Rev.Nucl.Part.Sci., **57**:205–243, 2007, DOI:10.1146/annurev.nucl.57.090506.123020.
- [15] J. Rafelski and J. Letessier, *Critical Hadronization Pressure*, J.Phys., **G36**:064017, 2009, DOI:10.1088/0954-3899/36/6/064017.
- [16] M. Ivanov, *Identified charged hadron production measured with ALICE at the LHC*, Nucl.Phys., **A904-905**:162c–169c, 2013, DOI:10.1016/j.nuclphysa.2013.01.058.
- [17] J. Rafelski and J. Letessier, *Particle Production in  $\sqrt{s_{NN}} = 2.76$  TeV Heavy Ion Collisions*, Phys.Rev., **C83**:054909, 2011, DOI:10.1103/PhysRevC.83.054909.
- [18] B. Abelev et al., *Centrality dependence of  $\pi$ ,  $K$ ,  $p$  production in Pb-Pb collisions at  $\sqrt{s_{NN}} = 2.76$  TeV*, 2013.
- [19] S. Singha, *Strange hadron and resonance production in Pb-Pb collisions at  $\sqrt{s_{NN}} = 2.76$  TeV with ALICE experiment at LHC*, Nucl.Phys., **A904-905**:539c–542c, 2013, DOI:10.1016/j.nuclphysa.2013.02.071.
- [20] J. Aichelin and K. Werner, *Centrality Dependence of Strangeness Enhancement in Ultrarelativistic Heavy Ion Collisions: A Core-Corona Effect*, Phys.Rev., **C79**:064907, 2009, DOI:10.1103/PhysRevC.79.064907, 10.1103/PhysRevC.81.029902.
- [21] B. Abelev et al., *Pion, Kaon, and Proton Production in Central Pb-Pb Collisions at  $\sqrt{s_{NN}} = 2.76$  TeV*, Phys.Rev.Lett., **109**:252301, 2012, DOI:10.1103/PhysRevLett.109.252301.
- [22] I. Karpenko, Y. Sinyukov, and K. Werner, *Uniform description of bulk observables in hydrokinetic model of  $A + A$  collisions at RHIC and LHC*, Phys.Rev., **C87**:024914, 2013, DOI:10.1103/PhysRevC.87.024914.
- [23] G. Torrieri, et al., *Statistical hadronization with resonances*, Acta Phys.Polon., **B35**:2911–2927, 2004.
- [24] G. Torrieri, et al., *SHAREv2: Fluctuations and a comprehensive treatment of decay feed-down*, Comput.Phys.Commun., **175**:635–649, 2006, DOI:10.1016/j.cpc.2006.07.010.